A HYBRID SYSTEMS STRATEGY FOR AUTOMATED SPACECRAFT TOUR DESIGN AND OPTIMIZATION

A Dissertation
Submitted to the Faculty
of
Purdue University
by
Jeffrey R. Stuart

In Partial Fulfillment of the
Requirements for the Degree
of
Doctor of Philosophy

August 2014
Purdue University
West Lafayette, Indiana

"We were just a lot of kids. With cut fingers, lumpy heads and whining tenor voices. We liked our game of mibs as well as the next rumple hair... But we liked the rockets more."

- Ray Bradbury, "King of the Grey Spaces", 1943

This work is dedicated to my family: past, present, and future.

ACKNOWLEDGMENTS

The people in my life have always helped me far more that I truly deserve; my Grandpa Tom would call it “Stuart Luck”. Through their patience, forbearance, and kindness, my family, teachers, friends, and colleagues have given me more than my fair share of opportunity and good fortune. To paraphrase Isaac Newton, these are the giants upon whose shoulders I stand.

First and foremost, I want to thank, from the bottom of my heart, my fiance Ashwati Das, for her love, patience, and support. She constantly inspires me to be a better person, and if it were not for her always looking out for me I might have missed many wonderful opportunities. I am also extremely grateful for my family, including my parents James and Mary, my brother Phill, all of my aunts, uncles, cousins, and my grandparents. Their love, support, and humor have been a constant source of strength and comfort throughout my life. Unfortunately, my Grandpas Chuck and Tom and my Grandma Gong-Gong passed away before I finished this work. I hope, wherever they are, that I have made them proud.

Professor Kathleen Howell is a superb mentor as well as teacher and as an advisor has helped me more than I can possibly express. She has always challenged me academically and has given me numerous opportunities for improvement and advancement. I owe much of my success as a student of astrodynamics to her tutelage and patience. In addition, her attitude toward teaching and respect for her students are a continuous inspiration to myself as well as to countless others.

I would also like to thank my committee members, Professors William Crossley, James Longuski, and Inseok Hwang, as well as Dr. Roby Wilson of the Jet Propulsion Laboratory, California Institute of Technology. Though I did not know it when I took their courses, my committee prepared me for my current work. Professor Longuski first introduced me to functional optimization, and his courses have rounded out my

education in dynamics and astrophysics. I learned parameter and global optimization from Professor Crossley, and I always enjoyed the jokes he told in class. Professor Hwang reinforced my knowledge of optimal control as well as estimation and first introduced me to the concept of hybrid systems. Dr. Wilson served as my mentor while on-site at JPL and provided guidance on many aspects of the algorithm development and trade-studies contained in this work. Additionally, I would like to acknowledge Professor Seokcheon Lee of the School of Industrial Engineering for introducing me to several of the search and coordination algorithms used in this work.

I have several mentors outside of my formal education, and I cannot thank them enough for their guidance, inspiration, and patience. Steve “Flo” Florence has taught me much about leadership and has instilled in me the confidence to be a mentor myself, in both FIRST and other fields. He and his wife, Nancy, have looked out for me so much over the past ten years; they are truly my “other” parents. Bob Lashbrook and his wife Shirley, who it was my great good fortune to meet during my high school years, have taught me more about “true” engineering, that is, humble problem-solving, than any number of classes ever could. Shirley’s recent passage is a loss felt by all who knew her, and her as well as her family are in our hearts and minds. Last but not least, Gary Stair, and his wife Betsy Blair, have been a true inspiration and a gentle reminder that there is more to life than engineering. Perhaps most importantly, they have taught me that the most important aspect of responsibility is who chooses to accept it. To all of these, and others, I owe a debt far greater than I can ever repay.

I also owe a great debt of gratitude to my fellow students, past and present. Marty Ozimek first set me on my research path and has been an invaluable source of advice and help through all my work; I hope all my future colleagues are of his caliber. Many of the images throughout this work have benefited from the advice of Wayne Schlei, whose tireless work with the visualization software Avizo© is a great benefit to all of his fellow students. Furthermore, Wayne was a wonderful companion in my forays into the search and coordination algorithms in this work, and it is

entirely due to his influence that I took that fateful course from Professor Lee. Tom Pavlak has consistently diagnosed problems with my codes and offered pointers on targeting algorithms and has therefore saved me large amounts of time. My friends during my undergraduate studies, my fellow graduate students in the research group, and AAE as a whole, for that matter, the people of Purdue FIRST Programs, the Bujinkan Yanagi Dojo, and so many others, have made my time at Purdue a joy with their friendship and open heartedness, and I cannot thank any of them enough. Furthermore, the staff of the School of Aeronautics and Astronautics have been kind, patient, and put up with more of my antics than they really should have: they are saints, every one.

Finally, I thank the School of Aeronautics and Astronautics and the College of Engineering for funding me during my Master's studies. I truly enjoyed my work as a teaching assistant, and I hope I was able to teach my students as much as I learned myself. At various times during my term as a doctoral student, I was supported the Indiana Space Grant Consortium, the Purdue Research Fund, and the NASA Space Research Technology Fellowship, NASA Grant NNX12AM61H. I hope that my work is worthy of the remarkable level of support it has received over the years.

TABLE OF CONTENTS

LIST OF TABLES

LIST OF FIGURES

Figure Page

Figure Page

Figure Page

ABSTRACT

Stuart, Jeffrey R. Ph.D., Purdue University, August 2014. A Hybrid Systems Strategy for Automated Spacecraft Tour Design and Optimization. Major Professor: Kathleen C. Howell.

As the number of operational spacecraft increases, autonomous operations is rapidly evolving into a critical necessity. Additionally, the capability to rapidly generate baseline trajectories greatly expands the range of options available to analysts as they explore the design space to meet mission demands. Thus, a general strategy is developed, one that is suitable for the construction of flight plans for both Earth-based and interplanetary spacecraft that encounter multiple objects, where these multiple encounters comprise a “tour”. The proposed scheme is flexible in implementation and can readily be adjusted to a variety of mission architectures. Heuristic algorithms that autonomously generate baseline tour trajectories and, when appropriate, adjust reference solutions in the presence of rapidly changing environments are investigated. Furthermore, relative priorities for ranking the targets are explicitly accommodated during the construction of potential tour sequences. As a consequence, *a priori*, as well as newly acquired, knowledge concerning the target objects enhances the potential value of the ultimate encounter sequences. A variety of transfer options are incorporated, from rendezvous arcs enabled by low-thrust engines to more conventional impulsive orbit adjustments via chemical propulsion technologies. When advantageous, trajectories are optimized in terms of propellant consumption via a combination of indirect and direct methods; such a combination of available technologies is an example of hybrid optimization. Additionally, elements of hybrid systems theory, i.e., the blending of dynamical states, some discrete and some continuous, are integrated into the high-level tour generation scheme. For a preliminary investigation, this strategy is applied to mission design scenarios for a Sun-Jupiter Trojan asteroid tour as well as orbital debris removal for near-Earth applications.

1. INTRODUCTION

Autonomous spacecraft guidance, navigation, and control (GNC) systems are increasingly attractive for ground operations and, also, for the complex scenarios envisioned to meet space-based commercial, scientific, and exploration goals. For example, autonomous GNC systems can assist ground-based human operators supporting mission design as well as flight operations and enable mission scenarios wherein spacecraft, either singly or as part of a multiple-spacecraft network, are required to operate independently from external commands. The distinguishing feature of such autonomous procedures is comparatively little human-in-the-loop interaction as compared to traditional mission design and navigation scenarios; this increased autonomy is advantageous at all stages of mission formulation and operation. Additionally, self-reliant GNC systems possess the potential to reduce spacecraft response times where delays are introduced by communications lags and human-in-the-loop interactions. Autonomy is particularly important for deep space missions where there is significant response-time delay and sporadic communication due to the physical distance between the vehicle and the Earth. A strategy that independently and adaptively accommodates the GNC requirements, from generating baseline trajectories to active control schemes relative to the reference path in an effort to satisfy specified mission objectives, is therefore highly desirable.

1.1 Problem Definition

A framework is proposed for the general strategy of automating generation of trajectories wherein at least one spacecraft (variously termed “chaser”, “servicer”, “surveyor”, or “probe”) completes a series of rendezvous encounters with various celestial objects, or “tours”. Specific implementations of the tour construction framework call upon a variety of schemes and algorithms to address the processes required for complete trajectory design. While many missions are limited to one spacecraft, several near-future applications require the coordination of multiple independently acting vehicles. Thus, while this investigation focuses primarily upon the construction of high-value tours for a single vehicle, options for multiple spacecraft are explored. Note that operations in close proximity to the target objects are not modeled; rather, the selection of the visited targets, the ordering of the encounter sequence, and the transfer from the vicinity of one object to the next are the focus of this investigation. This process for the construction of encounter sequences may be applied to a variety of mission architectures and to different dynamical force environments. In this investigation, the removal of artificial debris objects near the Earth and the surveying of primordial asteroids serve to demonstrate the flexibility of the general framework. The automated procedure incorporates several key considerations including:

- the definition of the mathematical model governing the natural motion of the target objects and the chaser vehicle,
- the generation of individual transfer options,
- the search or coordination method used to construct the encounter sequences,
- the relative priority ranking of the target objects, and
- the transition of the resulting trajectories to higher-fidelity models as well as flight operations scenarios,

where a variety of algorithms or schemes may be applied to components of the design process. These considerations are addressed for specific mission concepts by incorporating elements of direct and indirect optimization techniques, numerical methods, hybrid systems theory, dynamical systems theory, evolutionary search algorithms, multi-agent coordination methods, and, when necessary, minimal human-in-the-loop interaction. The automated schemes within this framework are each flexible in implementation and are readily adapted to a variety of spacecraft mission scenarios.

1.2 Previous Work

The construction of tour trajectories along which robotic spacecraft encounter several celestial bodies has a rich history, dating from the time of the Mariner 10 spacecraft [1] and the conception of the Planetary Grand Tour by Gary Flandro [2] as well as Michael Minovitch. [3,4] Furthermore, automation has been a key enabling capability in the design of spacecraft trajectories, however, most advances in automation have focused upon the generation and optimization of individual transfer arcs between targets of interest or pre-specified end-to-end sequences. For example, the software package STOUR reliably aids in the construction of specific flyby sequences, however many key aspects of the trajectory must be defined and pre-determined by human operators. [5] Thus, the generation of individual end-to-end trajectories has historically required significant human-in-the-loop interaction and intuition; one recent example is the tour of Saturn's moons completed by the Cassini spacecraft. [6] In recent years, however, there has been a growing interest in mission concepts that involve vast design spaces that are generally intractable for adequate exploration via traditional trajectory design techniques. Furthermore, these trajectory design problems typically incorporate both discrete and continuous variables in their formulation, where this challenging mixture of variables is a specific example of a "hybrid system". [7] Accordingly, several recent investigations have focused on automating the process for constructing potential reference trajectories in support of particular mission scenarios, in particular, the selection of high-value encounter sequences. For instance, the Global Trajectory Optimization Competition has posed a variety of tour scenarios for its design challenges, usually eliciting a wide variety of solution approaches in response. [8] In some instances, the solution approaches developed during the course of the competition have been extended and published in peer-reviewed journals. [9–12] On the other hand, the recently developed software package EMTG reliably produces potential interplanetary trajectories comprised of brief flyby encounters. [13] Additionally, Ceriotti and Vasile incorporated an ant colony optimization algorithm within a scheme to generate interplanetary gravity-assist trajectories. [14] Furthermore, several independent investigations have sought to automate the generation involving flyby sequences of planetary satellites, for example, various proposed missions to Europa [15] and the other Galilean satellites. [16,17] However, the encounters in the majority of these studies have been brief flybys, rather than full rendezvous allowing for an extended loiter time near the target object. Furthermore, transfers are usually computed using simplified gravity models with analytical conic solutions. While relatively few investigations focus on rendezvous options or environments requiring higher-fidelity dynamical models, graph-based methods that generate paths between discretely defined nodes have been applied to the selection of transfer options between orbits in multi-body regimes. [18]

Two specific mission scenarios, asteroid survey tours and debris mitigation, are considered as test cases for the general rendezvous tour construction framework. While no spacecraft missions have targeted these objects to date, several preliminary efforts have sought to automate the construction of tour trajectories of the respective bodies. Investigations have been completed into the construction of Trojan asteroid survey tours by Izzo [19], Canalias [20], and Matsumoto [21], though these authors implement global search algorithms that produce single tours comprised of brief flyby encounters, optimized end-to-end. Perozzi [22] investigates the construction of Main Belt and near-Earth asteroid tour trajectories incorporating both rendezvous and flyby options, while Barbee [23] considers rendezvous and flyby opportunities as two different mission architectures. However, both investigations use Lambert arcs to approximate the timing and propellant costs to transfer between target asteroids. In contrast, scenarios wherein the targets and order are not pre-defined have, thus far, rarely been applied to the particular problem of debris mitigation, though recently Missel and Mortari have applied a genetic algorithm to path pre-planning [24] and Barbee et al. examined a model of the Traveling Salesman Problem. [23]

1.3 Overview of Present Work

Within this investigation, a systematic, general framework is developed for the construction of tour sequences, and subsequently, trajectories. A variety of rendezvous tour architectures, as well as techniques that enable the generation of encounter sequences, are examined. The body of this investigation is organized as follows:

- Chapter 2: The general formulation of the rendezous tour design process is summarized and the tasks associated with the automated generation of trajectories are described. The selection of appropriate dynamical models, the determination and ranking of potential targets, the computation of transfer options, and the selection of a search strategy for tour generation are introduced. Baseline models and algorithms that are readily adapted to specific mission scenarios are presented.

- Chapter 3: The scheme for generating rendezvous sequences is applied to the active removal of debris objects near to the Earth. Analytical approximations for the propellant cost to transfer between targets are developed, and algorithms suitable for the coordination of multiple operating spacecraft are adapted for use within the context of the general tour design process. High value targets for removal are detailed.

- Chapter 4: Specific debris mitigation and removal scenarios incorporating multiple independently operating chaser spacecraft are investigated. The limitations of near-term mitigation strategies are explored and specific high-value encounter sequences are suggested.

- Chapter 5: The tour construction scheme is adapted for the scenario wherein a single robotic spacecraft is used to survey the population of Trojan asteroids. Rendezvous arcs connecting specific target asteroids are enabled by a novel low-thrust propulsion system. A search scheme balancing propellant consumption, loiter time at the asteroids, and potential scientific return is implemented. An automated process to transition feasible encounter sequences constructed using lower-fidelity models to higher-accuracy, end-to-end trajectories is developed.

- Chapter 6: A variety of scenarios for survey missions of the Trojan asteroid swarms are considered. Preliminary results generated using lower accuracy approximations are transitioned to higher fidelity simulations and several options for end-to-end, that is, Earth-departure to mission termination, are explored.
- Chapter 7: A summary of the investigation and concluding remarks are presented. Potential avenues for future investigation are offered.

2. OVERVIEW: THE TOUR CONSTRUCTION PROCESS

The construction of a feasible tour trajectory and, ultimately, successful flight along the path is a non-trivial task necessitating a careful blend of human-in-the-loop interactions with automated processes that aid in the exploration of potential solutions. Once a particular mission concept has been selected for investigation, there are typically several interrelated tasks, as parts of the larger trajectory design problem, that must be accomplished before a detailed reference path is generated incorporating a model fidelity and design maturity that is sufficient for operations or for more in-depth study. These tasks within the trajectory design process must, in general, be adjusted with respect to one another and can be automated to varying degrees. In general, the automated construction of tour trajectories proceeds consistent with four high-level functions:

1. *Mission conception*: the formulation of the mission goals and constraints;
2. *Definition of natural dynamical models*: the selection of a minimal dynamical model suitable for rapid preliminary analysis while retaining sufficient dynamical fidelity;
3. *Automated tour generation*: the automated process whereby potential trajectories are constructed, composed of three sub-tasks:
    (a) *Relative target value assessment*: determining a set of potential individual targets and assessing their relative priority, if any;
    (b) *Rendezvous computation*: computing and applying the propellant costs as well as the timing required for transfer from one object to another;
    (c) *Search strategy implementation*: the ordered selection of targets for individual spacecraft and the production of encounter sequences; and,

4. *Mission operations*: the transition of preliminary trajectory results to higher fidelity models suitable for eventual mission operations.

A notional diagram of the design flow and the high-level functions, including the design tasks, in a proposed rendezvous tour mission architecture is displayed in Fig. 2.1. The three circles representing the design tasks, as sub-components of a tour generation strategy, are overlapped to reflect the interrelated nature of the tasks. Design considerations within one category can significantly influence available options in another element. Techniques and algorithms comprising the various design tasks of the tour creation process are developed and applied to two specific mission scenarios. The algorithmic procedures are not tailored to the specific test cases, however, and are readily adapted to a wide variety of other trajectory design architectures. Overviews of the tour generation components are introduced, along with general solution processes for specific tour design tasks.

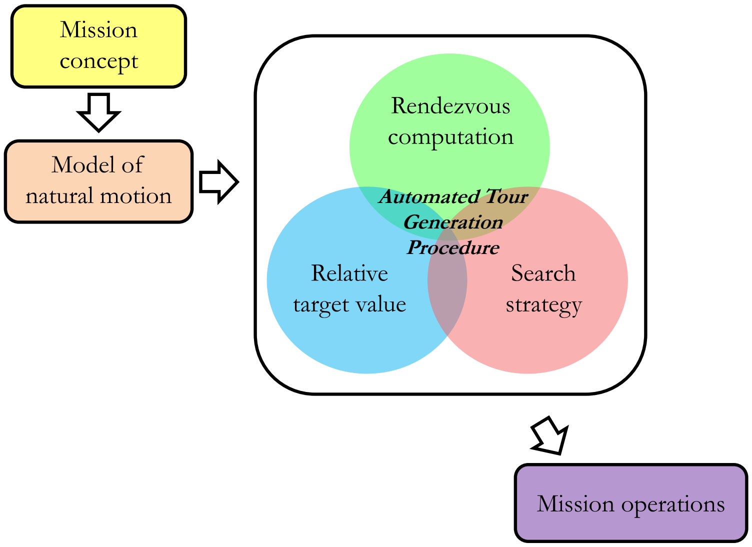

Figure 2.1.. Conceptual schematic of the tour design framework

2.1 Mission conception

Any spacecraft mission is proposed to satisfy a specific set of goals, from the gathering of valuable scientific information to the demonstration of a key technical capability. Specific, measurable objectives for the mission are then formulated such that, when the objectives are met, the mission goals are also satisfied. These objectives, along with pertinent technical and economic restrictions, then drive the design of the spacecraft, trajectory, and other mission operations. While a large variety of current and future missions are under investigation by a variety of government agencies, universities, and private companies, an element common to several proposed mission concepts is the desire to encounter multiple objects of interest, where each encounter involves an extended duration in the near vicinity of the target body. Two specific mission scenarios, the active removal of debris objects near to the Earth and surveys of the enginmatic Trojan asteroids, are explored in this analysis.

2.2 Definition of natural dynamical models

A mathematical model incorporating the natural dynamics governing the motion of the target objects as well as the operating spacecraft is a critical component of an automated trajectory design process. Of course, the specific mission application and the desired level of fidelity drives the development of this model. At the core of this investigation is the general formulation of a strategy to generate rendezvous tours, thus, the mathematical representation of the dynamical model leads directly to the construction of initial and target states for departure and arrival at the desired target bodies. Accordingly, a basic dynamical model is developed that is suitable for adaptation to assess the motion of the target debris objects as well as the Trojan asteroids for the two sample architectures.

2.2.1 Basis for natural motion: the N-body problem

Though humanity has puzzled for millenia on the motion of the stars and planets, Newton's law of universal gravitation supplied a firm physical and mathematical basis for Kepler's earlier kinematical observations of planetary motion. Indeed, Newton's law is fundamental and remains a widely applied concept in preliminary mission design, even though Einstein's theory of general relativity, a more detailed model of gravity, is now readily available. Using modern vector notation, the model for universal gravitation is written

$$\boldsymbol{F}_g = -\frac{GMm}{d^3}\boldsymbol{d} \tag{2.1}$$

where $\boldsymbol{F}_g$ is the vector gravitational force due to a point mass P_M, of mass M, acting on point mass P_m, with mass m, the relative position vector is $\boldsymbol{d}$ (directed from P_M to P_m), and the scalar G is the Universal Gravitational Constant. Note that vectors are indicated by bold-type. Also included in Newton's *Philosophiæ Naturalis Principia Mathematica* [25] are his equally famous three laws of motion. The well-known second law states that the change in the momentum of a particle is directly proportional to the sum of the forces acting on the particle. This relationship is mathematically represented as

$$\boldsymbol{F} = m\ddot{\boldsymbol{r}} \tag{2.2}$$

where $\boldsymbol{F}$ is the vector force resultant, $\boldsymbol{r}$ is the position vector of the particle with respect to an inertially fixed base point, and dots indicate a derivative with respect to time from the perspective of an inertial observer. From the law of motion in Eq. (2.2), and incorporating the gravity force representation in Eq. (2.1), the system is expanded to include N point masses. As a result, the motion of a particle P_i in inertial space is written

$$m_i\ddot{\boldsymbol{r}}_i = -G\sum_{\substack{j=1\\ j\neq i}}^{n}\frac{m_i m_j}{d_{ji}^3}\boldsymbol{d}_{ji}. \tag{2.3}$$

In Eq. (2.3), the vector $\boldsymbol{r}_i$ denotes the position of particle P_i with respect to an inertially fixed base point and the vectors $\boldsymbol{d}_{ji}$ denote relative displacements such that

$\boldsymbol{d}_{ji} = \boldsymbol{r}_i - \boldsymbol{r}_j$. This system of N particles is represented in Fig. 2.2, with the vectors $\boldsymbol{r}_i$ and $\boldsymbol{d}_{ji}$ annotated.

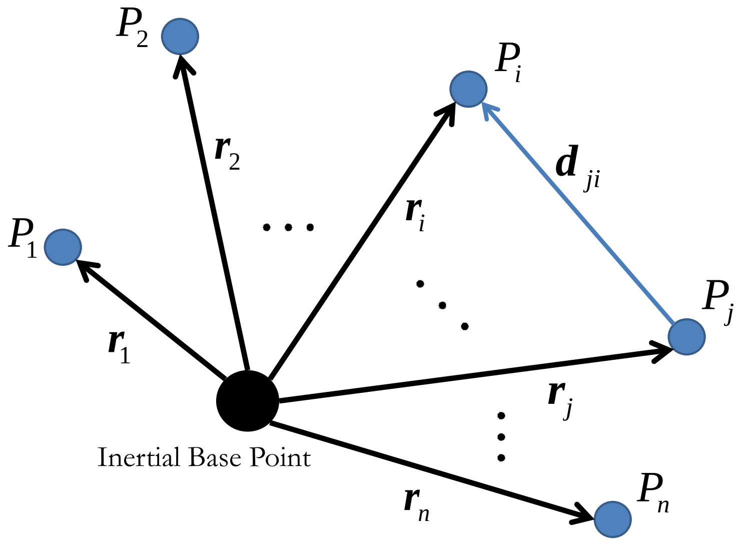

Figure 2.2.. Diagram of N-body problem

In mission scenarios, the gravitational environment is frequently dominated by a massive central body while offering perturbations due to smaller and / or more distant gravitating bodies. Thus, an accurate model for point masses moving under the influence of gravity is supplied by the relative vector equation of motion for a particle P_i moving with respect to a central body P_q:

$$\ddot{\boldsymbol{r}}_{qi} + \frac{G(m_i + m_q)}{r_{qi}^3}\boldsymbol{r}_{qi} = G \sum_{\substack{j=1 \\ j \neq i,q}}^{n} m_j \left(\frac{\boldsymbol{r}_{ij}}{r_{ij}^3} - \frac{\boldsymbol{r}_{qj}}{r_{qj}^3} \right) \tag{2.4}$$

where additional bodies are denoted by the subscript j. The ephemerides, i.e., positions and velocities of the celestial bodies, are available from the Jet Propulsion Laboratory's HORIZONS database [26]. The relative position vector $\boldsymbol{r}_{ij}$ is defined

$$\boldsymbol{r}_{ij} = \boldsymbol{r}_{qj} - \boldsymbol{r}_{qi} \tag{2.5}$$

where all positions are known relative to the central body q. Therefore, the natural dynamics of the spacecraft in an inertial frame are mathematically modeled as

$$\boldsymbol{f}_n(t, \boldsymbol{r}_{qi}) = -\frac{G(m_i + m_q)}{r_{qi}^3}\boldsymbol{r}_{qi} + G\sum_{\substack{j=1 \\ j \neq i,q}}^{n} m_j \left(\frac{\boldsymbol{r}_{ij}}{r_{ij}^3} - \frac{\boldsymbol{r}_{qj}}{r_{qj}^3}\right) \tag{2.6}$$

where the system is time varying and the symbol $\boldsymbol{f}_n$ represents the net gravitational acceleration governing the position vector $\boldsymbol{r}_{qi}$. Numerical integration of these vector equations of motion is readily adjusted for any number of gravitating bodies, where the number does not, in general, alter other aspects of the rendezvous tour generation function such as the target-to-target transfer model and the implementation of the optimization algorithm.

2.3 Tour generation: relative target value assessment

The selection and prioritization of a set of target bodies is a critical step in the formulation, construction, and analysis of potential rendezvous trajectory development. This relative ranking of targets can encompass a variety of factors and could, in fact, be re-ordered during the path planning process or during the actual operations. For example, an imminent conjunction with a high probability of collision might be detected between two debris objects, necessitating the near-term removal of one or both targets. Assuming some identified scope for the analysis, subsets of target bodies are selected from the full target populations via several heuristic methods; while this winnowing process is intrinsically human-in-the-loop, a variety of filtering processes are readily automated. Once target sub-sets are defined, individual target objects are assigned a scalar priority ranking that, in general, represents the value of an encounter with an object relative to others. Recall that the two sample scenarios in this investigation represent very different problems, i.e., (i) tour design for a Trojan asteroid mission, and (ii) a debris mitigation strategy for Earth-based objects. Thus, a priority value metric may represent either the expected scientific return from the asteroid encounters or a simulated hazard level posed by an individual debris object.

2.4 Tour generation: rendezvous computation

The accurate and efficient computation of transfer links between target objects plays a key role in the construction of viable encounter sequences that satisfy typical rendezvous mission objectives. Often, simplified cost estimates or models can be used to speed computation during initial searches through the available design space. However, results from any "simplified" search must retain sufficient fidelity such that potential tour sequences may be successfully transferred to higher fidelity models while retaining the desirable tour characteristics. A variety of propulsive technologies are available to effect changes in the natural motion of the touring, or chaser, spacecraft. Such capabilities range from well-established chemical engines to more efficient electric thrusters to advanced technologies such as solar sails. However, each propulsive technique offers unique advantages and challenges in terms of both the physical capability as well as the required analysis and computational methods to simulate spacecraft operation. Multiple propulsive models are investigated to assess their potential within the context of multiple-encounter rendezvous missions while simultaneously demonstrating the adaptability of the general framework for the construction of viable tour sequences. In particular, a variety of low-thrust models are adapted for use in the construction of asteroid encounter surveys while simplified cost estimates, analogous to chemical and electrical thruster performance, are implemented for the mitigation of debris near to the Earth. Furthermore, a general procedure for differential corrections is developed, where this scheme is adaptable to a wide variety of trajectory design scenarios.

2.4.1 Basis for rendezvous computation: a general corrections procedure

The determination of trajectories and transfers within a multi-body regime is a natural example of a two-point boundary value problem (2PBVP). Though many techniques for numerically computing solutions to 2PBVPs exist, an algorithm comprised of constraints and free variables [27], based on a generalization of Newton's method, is employed here because of its simplicity in formulation and a recent history of successful applications [28]. Begin with a general design vector $\boldsymbol{X}$ of n free variables X_i, that is, a vector of design variables,

$$\boldsymbol{X} = \begin{Bmatrix} X_1 \\ X_2 \\ \vdots \\ X_n \end{Bmatrix} \tag{2.7}$$

where the objective is to determine a solution vector that satisfies a set of m constraints of the form

$$\boldsymbol{F}(\boldsymbol{X}) = \begin{Bmatrix} F_1(\boldsymbol{X}) \\ F_2(\boldsymbol{X}) \\ \vdots \\ F_m(\boldsymbol{X}) \end{Bmatrix} = \mathbf{0}. \tag{2.8}$$

One possible set of design variables that is applicable in this problem is position, velocity, and time while potential constraints include path restrictions on position and velocity as well as limits on the energy level of an orbit. When the constraint vector $\boldsymbol{F}(\boldsymbol{X})$ includes quantities downstream from $\boldsymbol{X}$ as a result of numerical simulation, the algorithm can be used to implement a shooting process [29].

After the free variables are selected and the constraints are defined, an algorithm is developed that iterates from an initial guess of the solution, $\boldsymbol{X}_0$, toward a true solution. To construct this algorithm, the constraint vector $\boldsymbol{F}(\boldsymbol{X})$ is expanded to first order in a Taylor series about the initial guess $\boldsymbol{X}_0$

$$\boldsymbol{F}(\boldsymbol{X}) \approx \boldsymbol{F}(\boldsymbol{X}_0) + D\boldsymbol{F}(\boldsymbol{X}_0)(\boldsymbol{X} - \boldsymbol{X}_0) \tag{2.9}$$

where $\boldsymbol{X}$ is assumed close to $\boldsymbol{X}_0$. The Jacobian matrix $D\boldsymbol{F}(\boldsymbol{X})$ is an $m \times n$ gradient matrix

$$D\boldsymbol{F}(\boldsymbol{X}) = \frac{\partial \boldsymbol{F}(\boldsymbol{X})}{\partial \boldsymbol{X}} = \begin{bmatrix} \frac{\partial F_1}{\partial X_1} & \frac{\partial F_1}{\partial X_2} & \cdots & \frac{\partial F_1}{\partial X_n} \\ \frac{\partial F_2}{\partial X_1} & \frac{\partial F_2}{\partial X_2} & \cdots & \frac{\partial F_2}{\partial X_n} \\ \vdots & \vdots & \ddots & \vdots \\ \frac{\partial F_m}{\partial X_1} & \frac{\partial F_m}{\partial X_2} & \cdots & \frac{\partial F_m}{\partial X_n} \end{bmatrix} \tag{2.10}$$

that relates changes in the constraint vector $\boldsymbol{F}(\boldsymbol{X})$ to changes in the state vector $\boldsymbol{X}$. Recalling the goal to satisfy the constraints such that $\boldsymbol{F}(\boldsymbol{X}) = \boldsymbol{0}$, Eq. (2.9) is reformulated as an iterative function, that is

$$\boldsymbol{F}(\boldsymbol{X}_i) + D\boldsymbol{F}(\boldsymbol{X}_i)(\boldsymbol{X}_{i+1} - \boldsymbol{X}_i) = \boldsymbol{0} \tag{2.11}$$

and $\boldsymbol{X}_{i+1}$ is computed until the constraint vector falls below a certain specified tolerance $\|\boldsymbol{F}(\boldsymbol{X}_{i+1})\| < \epsilon$. The norm of the full constraint vector may not always yield the best performance and such criteria can be adjusted as necessary. When the number of constraints and free variables are equal, $m = n$, then the update process is straightforward and the multi-dimensional Newton's method [29] is employed such that at each step

$$\boldsymbol{X}_{i+1} = \boldsymbol{X}_i - D\boldsymbol{F}(\boldsymbol{X}_i)^{-1}\boldsymbol{F}(\boldsymbol{X}_i) \tag{2.12}$$

where the Jacobian matrix $D\boldsymbol{F}(\boldsymbol{X}_i)$ is square and, so long as it is non-singular, invertible. If $n > m$, there are infinitely many solutions, so a single solution is determined from among many options by computing the vector $\boldsymbol{X}_{i+1}$ nearest to $\boldsymbol{X}_i$. This Minimum-Norm solution [30] is evaluated

$$\boldsymbol{X}_{i+1} = \boldsymbol{X}_i - D\boldsymbol{F}(\boldsymbol{X}_i)^T\left[D\boldsymbol{F}(\boldsymbol{X}_i)D\boldsymbol{F}(\boldsymbol{X}_i)^T\right]^{-1}\boldsymbol{F}(\boldsymbol{X}_i) \tag{2.13}$$

where Eq. (2.13) uses an orthogonal projection of $D\boldsymbol{F}(\boldsymbol{X}_i)$ to compute $\boldsymbol{X}_{i+1}$ and, thus, the solution $\boldsymbol{X}_{i+1}$ typically retains the properties of the previous solution $\boldsymbol{X}_i$.

Differential corrections is a powerful tool in orbit and transfer design, as well as other aspects of spacecraft mission analysis and operations, and the implementation of the process in terms of a general constraint-variable corrections procedure is the primary algorithm used in this analysis. The general algorithm is summarized as follows:

1. Determine all free variables and all functional dependencies, construct the variable vector $\boldsymbol{X}$, and generate an initial guess $\boldsymbol{X}_0$.

2. Define all constraints in the problem, formulate them in terms of equality constraints, and fill the constraint vector $\boldsymbol{F}(\boldsymbol{X}) = \boldsymbol{0}$.

3. Calculate the Jacobian matrix $D\boldsymbol{F}(\boldsymbol{X}) = \frac{\partial \boldsymbol{F}(\boldsymbol{X})}{\partial \boldsymbol{X}}$, that is, the gradient of the constraints with respect to the free variables.
4. Use Newton's method (Eq. (2.12)), a Minimum-Norm solution (Eq. (2.13)), or an acceptable alternative, to iterate until the constraint falls below an acceptable tolerance, $\|\boldsymbol{F}(\boldsymbol{X}_{i+1})\| < \epsilon$.

Assuming all constraints are formulated as equality constraints and the initial guess $\boldsymbol{X}_0$ is sufficiently close to a true solution, this algorithm converges quadratically [29]. The constraint-variable procedure is used to generate all orbits and unconstrained low-thrust transfers in this analysis.

2.4.1.1 Variational equations and the state transition matrix

For many applications in the astrodynamics, the corrections algorithm includes the evaluation of the elements of a constraint vector from states obtained via numerical integration. The update equation is then based on a Jacobian matrix which, for its construction, requires some method to map variations in the initial states to variations in the final states. The first step in determining these variational relationships is a baseline solution $\boldsymbol{x}^*(t)$ to the equations of motion (the symbol $*$ here indicates a reference trajectory). For nonlinear systems, determination of a baseline solution entails numerical integration of a scalar set of n first-order ordinary differential equations (ODE). Thus, the equations of motion $\dot{\boldsymbol{x}} = \boldsymbol{f}(\boldsymbol{x})$ are propagated for some time interval $[t_0, t]$ from an initial state $\boldsymbol{x}_0^*$ to obtain $\boldsymbol{x}^*(\boldsymbol{x}_0^*, t)$. Several ODE solvers are available, for example, MATLAB®'s `ode45` and `ode113` functions or Adams-Bashforth-Moulton integrators in Fortran [31].

With the known trajectory $\boldsymbol{x}^*(\boldsymbol{x}_0^*, t)$, nearby solutions are generated by employing a continuation process. Variations between the final state along the known trajectory and the positions and velocity vectors corresponding to the nearby solutions are determined by approximating the impact of variations in the initial state on $\boldsymbol{x}^*(\boldsymbol{x}_0^*, t)$. To model a nearby path, define a new initial state

$$\boldsymbol{x}_0 = \boldsymbol{x}_0^* + \delta\boldsymbol{x}_0 \tag{2.14}$$

where $\delta\boldsymbol{x}_0$ is a small variation. The variation at the terminal time, t, is then

$$\begin{aligned} \delta\boldsymbol{x}(t) &= \boldsymbol{x}(\boldsymbol{x}_0, t) - \boldsymbol{x}^*(\boldsymbol{x}_0^*, t) \\ &= \boldsymbol{x}(\boldsymbol{x}_0^* + \delta\boldsymbol{x}_0, t) - \boldsymbol{x}^*(\boldsymbol{x}_0^*, t). \end{aligned} \tag{2.15}$$

The process of representing a neighboring arc relative to a reference trajectory is illustrated in Fig. 2.3. Expanding the term $\boldsymbol{x}(\boldsymbol{x}_0^* + \delta\boldsymbol{x}_0, t)$ and linearizing about the reference trajectory for an assumed small initial variation yields

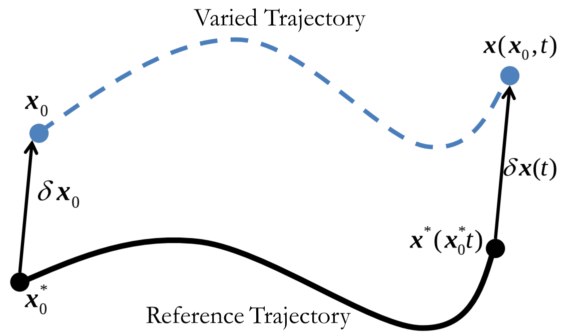

Figure 2.3.. A reference trajectory with nearby path

$$\delta\boldsymbol{x}(t) = \frac{\partial\boldsymbol{x}}{\partial\boldsymbol{x}_0}\delta\boldsymbol{x}_0 \tag{2.16}$$

as in Kahlil [32]. The matrix derivative $\frac{\partial\boldsymbol{x}}{\partial\boldsymbol{x}_0}$ is evaluated along the reference path and linearly maps variations in the initial state $\boldsymbol{x}_0$ to changes in the state downstream, $\boldsymbol{x}(\boldsymbol{x}_0, t)$. This transformation matrix is denoted the State Transition Matrix (STM) and is defined

$$\boldsymbol{\Phi}(t, t_0) = \frac{\partial\boldsymbol{x}}{\partial\boldsymbol{x}_0}. \tag{2.17}$$

When $t = t_0$ and, thus, $\boldsymbol{x} = \boldsymbol{x}_0$, Eq. (2.17) indicates that $\boldsymbol{\Phi}(t_0, t_0) = \mathbf{I}$, that is, the initial STM is the identity matrix. Differentiating Eq. (2.16) with respect to time produces

$$\frac{d}{dt}(\frac{\partial \boldsymbol{x}}{\partial \boldsymbol{x}_0}) = \frac{\partial}{\partial \boldsymbol{x}_0}\frac{d\boldsymbol{x}}{dt} = \frac{\partial \boldsymbol{f}}{\partial \boldsymbol{x}_0} = \frac{\partial \boldsymbol{f}}{\partial \boldsymbol{x}}\frac{\partial \boldsymbol{x}}{\partial \boldsymbol{x}_0} = \frac{\partial \dot{\boldsymbol{x}}}{\partial \boldsymbol{x}}\frac{\partial \boldsymbol{x}}{\partial \boldsymbol{x}_0} \tag{2.18}$$

where the partial differential matrix is defined $\frac{\partial \dot{\boldsymbol{x}}}{\partial \boldsymbol{x}} = \mathbf{A}(t)$. Substituting Eq. (2.17) into Eq. (2.18) produces the matrix differential equation

$$\dot{\boldsymbol{\Phi}}(t, t_0) = \mathbf{A}(t)\boldsymbol{\Phi}(t, t_0). \tag{2.19}$$

Thus, a system with n state variables requires the integration of n^2 additional differential equations for the availability of the STM. However, if the system is time-invariant, the matrix $\mathbf{A}$ is constant, the analysis simplifies and the STM is evaluated as $\boldsymbol{\Phi}(t) = e^{\mathbf{A}t}$ [33].

2.4.1.2 Finite differencing

In some instances, numerical simulations using the STM to evaluate the elements of the Jacobian matrix are not productive, prohibitively difficult in a large-scale problem, or computationally expensive. Therefore, an alternative approach to calculate these values is useful. Numerical finite-differencing is common when a slight loss in accuracy is offset by an increase in computational efficiency which is acceptable. Central differencing is the most popular of the finite-differencing options because of the balance between accuracy and the number of function evaluations as well as the ease of implementation [29]. In central differencing, the derivative of the j^{th} scalar constraint F_j with respect to the i^{th} scalar state variable X_i is approximated as

$$\frac{\partial F_j}{\partial X_i} \approx \frac{F_j(X_i + h) - F_j(X_i - h)}{2h} \tag{2.20}$$

where h is a “small” step in the value of the variable. In this investigation, a step size of $h = 10^{-5}$ nondimensional units typically supplies an acceptable trade-off between truncation error and round-off error.

2.4.1.3 Single and multiple shooting

In astrodynamics trajectory design problems, targeting or shooting methods are common. A shooting scheme typically involves numerical integration along one or more arcs; the initial state along each arc is generally corrected to achieve a specified objective. Any shooting procedure can be implemented in a corrections algorithm. The general corrections procedure used in this investigation does not place restrictions on the selection of either the variables in the state vector $\boldsymbol{X}$ or the constraints in the vector $\boldsymbol{F}(\boldsymbol{X})$. However, some terminology to distinguish between various applications of the process is helpful. Consider the vector $\boldsymbol{X} = \{\boldsymbol{x}_0, t\}^T$ that includes the initial 6D vector state $\boldsymbol{x}_0$ and the propagation time t along a path. Then, the arc possesses a target terminal point, $\boldsymbol{x}_T$, such that the constraint is expressed $\boldsymbol{F}(\boldsymbol{X}) = \boldsymbol{x}^t - \boldsymbol{x}_T$. The vectors $\boldsymbol{x}^t$ and $\boldsymbol{x}_T$, defined via the constraint $\boldsymbol{F}$, can involve a complete state vector or a subset of the states. All free variables correspond to a single initial state and time and all constraints are evaluated by a progapation from that specified initial state for the predetermined time interval t (denoted by the superscript t). This application of the corrections algorithm is labeled “single shooting”; a diagram appears in Fig. 2.4.

A general corrections procedure is not restricted to single states and one time interval to define a trajectory; in fact, segmenting a single arc into several sub-arcs offers many advantages. For example, an end-to-end trajectory might require one or many close passages of a primary, necessitating a complex path with high numerical sensitivity. Then, the linear corrections procedure is more successfully applied to shorter arcs that each represent a small time interval along the entire path. Corrections of the state and, possibly time corresponding to each arc, are evaluated simultaneously using a shooting method. Simultaneously updating the interior points is denoted “multiple shooting” and the procedure can be implemented using a free variable-constraint algorithm. The scheme is implemented in this analysis by adding the interior points to the design vector $\boldsymbol{X}$. For example, collect a set of n points $\boldsymbol{x}_i$ that represent a

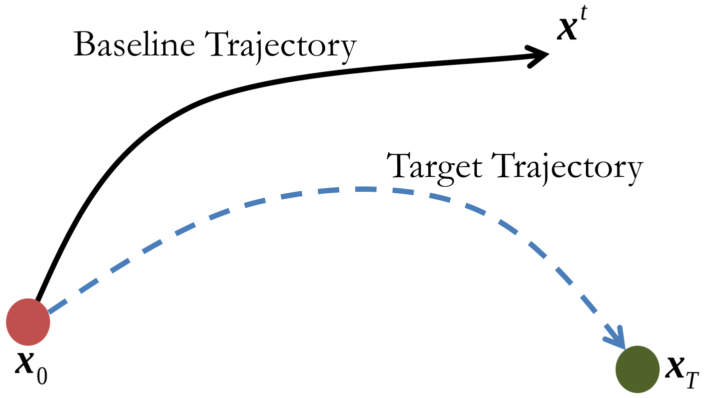

Figure 2.4.. Diagram of single shooting

sequential series of arcs and define the initial states corresponding to each arc to seed n numerical propagations of possibly varying duration t_i. The goal is the construction of a smooth trajectory connecting all n points in series to a terminal point $\boldsymbol{x}_T$; this case is illustrated in Fig. 2.5. Then, the constraint vector $\boldsymbol{F}(\boldsymbol{X})$ includes elements of the form $\boldsymbol{x}_i - \boldsymbol{x}_{i-1}^t$ that ensure continuity between the terminal point of one arc and the initial point of the following arc. Thus, the algorithm corrects a state vector $\boldsymbol{X}$ including the n state vectors $\boldsymbol{x}_i$ and, if desired, the progapation times t_i. In addition to state constraints, other types of constraints are often implemented in a corrections process; specific constraints pertinent to this analysis are discussed in subsequent chapters.

2.5 Tour generation: search strategy

Even in the most simplified form, tour design is an NP-hard problem, meaning that the solution space grows exponentially with a linear growth in the number of potential targets. Therefore, once targets are selected and transition options, with

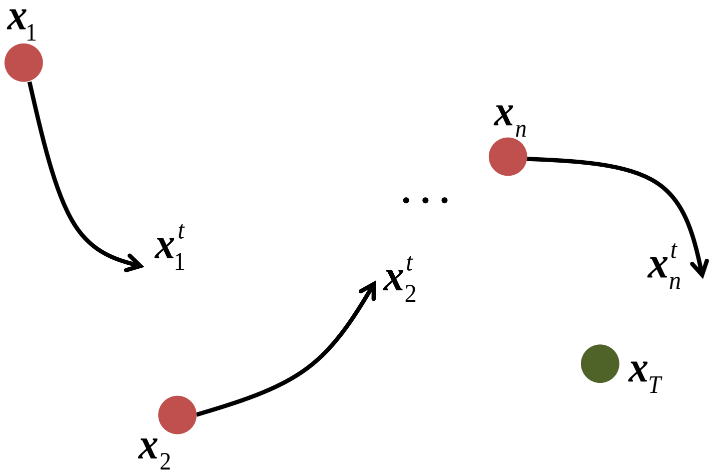

Figure 2.5.. Illustration of a series of arcs in a multiple shooting scheme

the associated costs, are computed (if pre-computation of these links is even feasible), a computationally efficient search method must still be implemented. While strict tree enumeration is a practical scheme for very small scale problems, this solution method quickly becomes intractable for even moderately-sized problems. Thus, many graph search methods, such as Dijkstra's algorithm [34] and branch-and-bound tree searches [35], have been developed over the last century. Furthermore, given that the construction of spacecraft tour trajectories can be posed as a specific example of the classic Traveling Salesman Problem (TSP), a wide variety of solution techniques are available. [36] One heuristic algorithm based upon the foraging behavior of ants, ant colony optimization (ACO), [37] has gained much interest as a solution scheme for a wide variety of applications, from the classic Traveling Salesman Problem (TSP) to the routing of information in data networks to the organization of jobs within a factory. [38] In particular, ACO is easy to implement as well as relatively computationally efficient such that trade studies may be rapidly performed. While ACO has a history of successful implementation in discrete system formulations, the algorithm also has the potential to be adapted to scenarios with continuous trade-spaces, such as astrodynamics. The ACO implementations in this preliminary investigation are intended as illustrative examples, not rigorous examinations of the performance of the search method and the effect of varying search parameters.

2.5.1 Basis for search strategies: traditional ant colony optimization

Standard ant colony optimization (SACO) is a stochastic route-finding algorithm patterned after the foraging behavior of ant colonies wherein ants alternately explore for food and follow pheromone trails to known food sources. Once a source of food is discovered, the ants instinctively locate a route that is near-optimal in terms of travel distance to the food source while retaining the ability to adapt to changing environments and opportunities. The process relies on the continued laying and dissipation of pheromone trails such that favorable trails are reinforced while other routes decay as their use declines. This process is inherently robust while ensuring near optimal performance as well as allowing for a variety of static and dynamic applications. [39]

Typical SACO applications assume a discrete set of N targets, or nodes, with single, bi-directional links, such that an "ant" traveling from location A to location B can travel equally easily in the opposite direction for the same cost. As illustrated in Fig. 2.6, these networks are usually sparse, that is, not every pair of nodes is connected. In most applications, the goal is to traverse the network from one node to another or to create a circuit of all nodes, both for the least cost. Many SACO applications simplify the model to represent one cost, for example, the travel time between cities in the classic Traveling Salesman Problem (TSP). The ant colony algorithm mimics the foraging behavior of ant colonies by performing a series of parallel searches wherein sets of virtual ants construct individual routes through the network. During each round of parallel searches, termed a "generation", multiple ants are released such that the individual ants construct independent sets of encounter

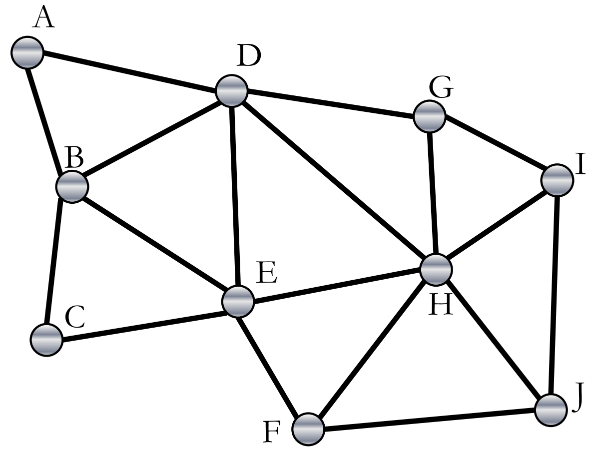

Figure 2.6.. Schema of sample network on which ant colony optimization can be applied. Links between objects can be traveled in both directions.

sequences. To construct routes during the k^{th} generation, each individual ant, after placement at a random initial object, travels from node to node, following these behavioral rules at each encountered node:

1. *Exploration*: With some "exploration" probability γ, travel to a randomly selected new node, where the parameter γ decreases from 1 to some steady-state value $0 < \gamma_{ss} < 1$ over succeeding generations; else,

2. *Following*: Stochastically select an unvisited node with the "following" probability
$$P_{i,j} = \frac{\tau_{i,j} B_{i,j}^{\beta}}{\sum \tau_{i,j} B_{i,j}^{\beta}} \tag{2.21}$$
where $P_{i,j}$ is the probability for traveling from the i^{th} node to the j^{th} node, $\tau_{i,j}$ is the pheromone level on the link, $B_{i,j}$ is the quality of the connection, and β is a weighting parameter consistent across all connections.

3. When the ant reaches the desired target destination, terminate search.

The number of ants, i.e., N_a, is an adjustable parameter in the algorithm. For the applications in this investigation, the exploration probability in the k^{th} generation is defined to be

$$\gamma = \gamma_{ss} + (1 - \gamma_{ss})e^{-\frac{k-1}{\ln N_g}} \tag{2.22}$$

where γ_{ss} is the lowest desired exploration probability and N_g is the total number of generations over which the search is enacted. This definition of exploration probability ensures a smooth exponential decay from a probability of 1 in the first generation to the base probability, γ_{ss}. The term involving the natural logarithm yields a consistent decay of exploration likelihood regardless of the number of generations. After each succeeding ant generation, the pheromone levels along each individual link are updated via

$$\tau_{i,j} = (1 - \rho)\tau_{i,j} + Q_{i,j} \tag{2.23}$$

with the decay rate ρ and pheromone update parameter $Q_{i,j}$. Note that this pheromone increase, $Q_{i,j}$, corresponding to a given link is often either zero (if only the best routes and, therefore, the best links, are reinforced) or some function that is dependent on the performance metric associated with those tours that include the particular leg in question. A common pheromone update procedure involves an increase of the pheromone level on each link of the best tour by the summed quality of each link on said tour, that is

$$Q = \sum_{j=2,i=j-1}^{N_e} B_{i,j} \tag{2.24}$$

where $Q = Q_{i,j}$ for each (i, j) link along the best tour and N_e is the total number of nodes traversed. Under this update model, the best tour acquires the highest Q value. A variation on this update strategy assigns this same pheromone increase across all tours. After a pre-determined number of generations, this procedure is terminated and the best tour is returned. Due to the stochastic features of the algorithm and the recognized tendency of ACO algorithms to quickly “lock” onto potential solutions, several runs are typically completed and the best route from among the runs is returned as the solution. For ACO algorithms as a whole, local information is supplied by the link quality, $B_{i,j}$, while global "goodness" information is preserved in the pheromone concentrations, $\tau_{i,j}$. Thus, in most SACO applications, the number of generations, number of ants, γ, β, ρ, and selection criteria for pheromone updates are all adjustable parameters. However, the determination of the best set of search parameters is highly problem dependent and, particularly for multi-objective problems, requires operator intuition and judgment of desirable outcomes. For this preliminary investigation, example sets of search parameters sufficient to produce sample results are chosen for each mission scenario considered.

2.6 Mission operations

Estimated rendezvous costs may be suitable for preliminary searches, but higher fidelity dynamical and spacecraft performance models are required for detailed analysis and, ultimately, flight operations. Thus, given estimated performances of potential encounter sequences, a straightforward and, ideally, automated transition to detailed trajectory plans must be accomplished. This transition process can be as simple as an ordered list of encountered objects between analysis tools. However, transmission of higher-level information, for example, mission epochs and nominal thrust profiles, is desirable. Some aspects of the transition of preliminary mission plans to both higher fidelity models as well as dynamic, flight operations scenarios are addressed. Specifically, Trojan asteroid tour trajectories, enabled by low-thrust propulsion and constructed using a simplified models of natural dynamics, are optimized end-to-end within the context of higher fidelity gravity simulations for a variety of electrical power sources for the thruster. Likewise, the behavior of debris removal spacecraft are re-evaluated and, when necessary, re-ordered via auction and bidding [40,41] algorithms that dynamically adapt pre-planned encounter sequences to a changing environment.

3. POTENTIAL DEBRIS MITIGATION SEQUENCES - SOLUTION APPROACH

The general automated procedure to produce rendezvous tours is adapted for an active debris removal campaign. However, due to the number of debris objects currently in Earth orbit, multiple spacecraft or “chasers” will be required to encounter and operate upon multiple debris objects in order to engender a significant reduction in the debris population. To support the goal of active debris removal, several objectives for the automated tour construction strategy are formulated for this preliminary analysis:

- a rapid and accurate procedure to compute estimated transfer costs between Earth-centered orbits;
- a search strategy that supplies information relevant to the complete mitigation of hazardous debris populations; and,
- a systematic approach to coordinate the actions of multiple operating spacecraft within the context of a rapidly evolving debris environment.

The tasks of the general tour design framework are adapted to satisfy these objectives, as displayed in Fig. 3.1. After an overview, each task in the trajectory design process is explored in depth. To support active debris mitigation, the trajectory design scenario for a single spacecraft is modeled as a vehicle routing problem (VRP) where the objective is a spacecraft that encounters a large number of debris objects while being constrained in terms of available propellant. However, since a single chaser can only encounter a limited number of debris objects, the use of multiple spacecraft operating as independent agents within a larger system is investigated. In particular, ant colony optimization as well as auction and bidding processes are examined as methods to coordinate the operation of the debris-mitigating satellites for both pre-

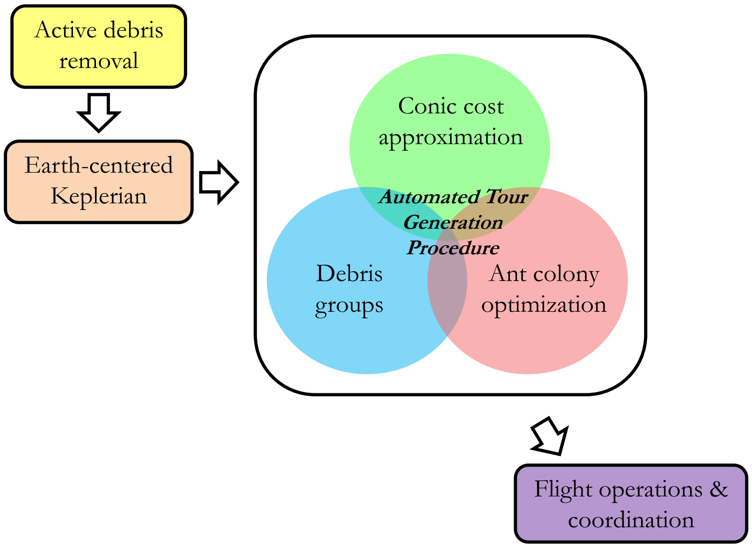

Figure 3.1.. Conceptual schematic of the tour design procedure, adapted for the generation of multiple-spacecraft debris removal campaigns

mission planning and real-time adjustments to baseline designs. The chaser employs either a chemical or electrical propulsion system while debris mitigation operations require some finite time interval within the close vicinity of the object, so transfer duration and spacecraft loiter time must also be addressed. Proximity operations at the debris objects are not explicitly modeled in this analysis but some assumed cost is applied at each encounter to represent these activities. Though this penalty potentially entails some additional propellant expenditure, the exact form of this cost depends heavily upon the objects under consideration. For example, a small object may be collected by a servicer spacecraft and, thus, increase the inert mass of the system. Alternatively, the main vehicle may deploy de-orbit packages at the larger objects, where this decrease in vehicle mass can incur an additional penalty to the propellant expenditure. Furthermore, the servicer spacecraft is typically restricted to relatively short-term missions, as opposed to multi-year operations. Short-term responses imply that large changes in the motion of the spacecraft must be generated via the on-board propulsion systems rather than natural, but slow, perturbations in the motion of the orbiting bodies. Though this analysis employs a simplified computational scheme that abstracts many of these considerations, preliminary target sequences and the expected mitigation costs may still be assessed. Furthermore, while this investigation does not explicitly incorporate launch or on-orbit resupply considerations, the proposed approaches are readily modified for application to scenarios where the mitigation architecture includes a supply station or other "home-base" in addition to the chaser spacecraft.

3.1 Mission concept and historical background

The current population of debris objects in Earth orbit, and the projected growth in the size of this population, are concerns to many governmental agencies, private companies, and other participants in the space industry. Debris objects pose a hazard to active spacecraft, often necessitating maneuvers to avoid dangerous close approaches, while collisions between debris objects have the potential to create a cascading build-up of debris in near-Earth orbit. [42] Indeed, in February 2009, an on-orbit collision occurred between an active Iridium communications satellite and a defunct Cosmos satellite wherein the Iridium satellite was lost and large amount of new debris objects were released. [43] At the same time, active anti-satellite system tests, such as the Fengyun-1C [44] and USA-193 [45], have contributed greatly to the debris environment. The Fengyun-1C test was particularly disruptive as it generated a large amount of debris in an already relatively highly-populated orbit. [46] On the other hand, because of careful planning of the American anti-satellite test, the fragments from USA-193 quickly decayed into the atmosphere. Accordingly, satellite disposal policy and active debris removal campaigns are a topic of international discussions.

The long-term evolution of debris populations has been the focus of many analyses, and the improved accuracy in collision prediction and error estimation is a topic of on-going investigation. For example, Liou, [47] Loftus, [48] and Lewis [49] have demonstrated the positive effect of active debris mitigation on long-term debris populations. Likewise, many advancements have occurred in the detection, tracking, characterization, and prioritization of artificial objects orbiting the Earth. [50–54] Less attention, however, has focused on trajectory design and analysis to mitigate the existing debris objects, though Peterson [55] has published preliminary results that include the identification of high-priority debris objects and a ΔV cost analysis for disposal missions; furthermore, Castronuovo [56] and Braun et al. [57] have proposed preliminary debris mitigation mission concepts. Additionally, Healy [58] analyzes the capability of a rapid-response architecture wherein an orbiting spacecraft is deployed in response to a specific collision event. These studies, however, typically presuppose a fixed order of target encounters or are restricted to general order-of-magnitude analyses. As noted previously, however, some investigations have incorporated automated vehicle routing processes into the construction of viable debris encounter sequences. [23, 24] On the other hand, market-based auction algorithms have been successfully applied to spacecraft constellation design and operations, [59–61] though they have yet to be employed in mitigation strategies for space debris or for similar spacecraft routing problems.

Potential mitigation strategies may be classified in terms of a variety of elements of the mission architecture. While an exhaustive survey of all currently proposed mitigation approaches has yet to be completed, an overview sufficient for the current investigation is included in Table 3.1. Red text indicates the assumed architectures for this particular investigation. Since not all mitigation strategies are technologically feasible for all debris types, multiple debris mitigation architectures are required to significantly reduce the debris population. Furthermore, even when a mitigation plan is crafted to target a specific portion of the debris population, economic realities may limit the full impact that such a strategy might realize. For example, an architecture based on chaser spacecraft rendezvous and subsequent deployment of de-orbit packages to multiple large debris objects within a short time frame entails relatively high propellant costs and, therefore, necessitates either a large number of spacecraft or the presence of on-orbit supply depots for the chaser vehicles. Thus, while preliminary results indicate that the proposed mitigation strategy is capable of a significant reduction in the hazard posed by debris objects within a relatively short time frame, the full impact is necessarily limited in scope and must be supplemented by alternate approaches for debris removal.

3.2 Natural motion: Earth-centered Keplerian orbits

High-fidelity numerical models, such as the planetary ephemerides, as well as simulations provide accuracy and precision when predicting the motion of celestial objects, albeit at a sometimes prohibitive computational expense. Thus, analytical models and simplified numerical simulations are of great utility, particularly in the preliminary stages of mission analysis and design. The simplest model of orbital motion is the relative motion of two gravitating bodies under their mutual attraction, also known as Kepler's Problem. One advantage of this formulation is that it admits an analytical solution to the nonlinear equations of motion and, thus, enables rapid analysis and computation for a wide variety of mission scenarios. While many classic treatises rigorously develop the analytical solution to Kepler's Problem from the laws posed in Newton's *Principia*, [25] references that are readily accessible to modern audiences include *Oribital Mechanics* by Prussing & Conway, [62] *Fundamentals of Astrodynamics and Applications* by Vallado & McClain, [63] and *Fundamentals of Astrodynamics* by Bate, Mueller, & White. [64] The present investigation omits the full mathematical derivation of the analytical expressions for the two-body problem, however key concepts and relations are summarized.

The law of motion from Eq. 2.3 for two gravitating point masses moving under their mutual influence ultimately simplifies to the relative equation of motion

$$\ddot{\boldsymbol{d}} = -\frac{\mu_C}{d^3}\boldsymbol{d} \tag{3.1}$$

where $\boldsymbol{d}$ is the relative displacement vector between the two celestial objects. The gravitational parameter is defined $\mu_C = G(M_1 + M_2)$ where M_1 and M_2 are the masses of the two particles. In this system, the barycenter B, or center of mass, of

Table 3.1. Potential components of debris mitigation architectures.

Descriptor	**Classification**				
Platform	spacecraft	launch vehicle	ground-based	balloon	aircraft
Time scale	<1 day	<1 year (short)	>1 year (long)		
TRL	9 - flight proven	7	5 - component validation	3	1 - basic principle
On-orbit propulsion	chemical	electric	solar sail	electrodynamic	none / NA
Disposal	atmospheric	graveyard orbit	reclamation		
Approach	rendezvous	fly-by	none / NA		
Interaction method	collision	dissipative	capture	deployable	
interaction method sub-descriptors	*destructive* *controlled*	*propellant exhaust* *gas cloud* *laser*	*tug* *scow* *slingshot* *net*	*tracker* *propulsive* *drag inducing* *solar sail* *electrodynamic tether*	

the two gravitating bodies is taken as the origin of the inertially fixed reference frame defined by unit vectors $\hat{X}, \hat{Y}, \hat{Z}$ forming a right-hand coordinate system. The symbol '$\hat{\ }$' denotes a unit vector. Under this simplified dynamical regime, the motion of the two gravitating bodies reduce to conic paths where one focus of each conic section is collocated with the barycenter B of the two bodies.[1] However, when the second body is negligibly small compared to the primary body, i.e., $M_2 \ll M_1$, then the center of mass of the larger gravitating body approaches the system barycenter and, consequently, the inertial base point of the coordinate frame. The larger particle is then termed the "central body". The gravitational parameter the two-body motion then reduces to $\mu_C \approx GM_C$, where $M_C = M_1$. This approximation holds for many cases of interest, including the motion of a spacecraft near to the Earth.

3.2.1 Definition of the conic orbital elements

The N-body problem possesses 10 conserved quantities, or integrals of motion, namely the scalar energy of the system, the 3-vector angular momentum of the two particles, and two 3-vectors defining the system linear momentum. But, the relative motion of two gravitating bodies reduces to a set of 6 governing differential equations. Thus, Kepler's problem admits an analytical solution wherein the relative motion of the two bodies is completely described without the need for numerical propagations of the equations of motion. By combining the momentum vectors, another conserved vector quantity, the eccentricity vector

$$\boldsymbol{e} = \frac{\dot{\boldsymbol{d}} \times \boldsymbol{h}}{\mu_C} - \hat{\boldsymbol{r}}, \tag{3.2}$$

a special form of the Laplace-Runge-Lenz vector, [65] is revealed. The angular momentum vector $\boldsymbol{h} = \boldsymbol{d} \times \boldsymbol{v}$, where $\boldsymbol{v} = \dot{\boldsymbol{d}}$ with respect to an inertial observer, and the eccentricity vector $\boldsymbol{e}$ determine the size, shape, and orientation of the motion with respect to the barycenter. However, as these two vector quantities are interrelated,

---

[1] A special instance of this latter scenario forms the basis for the circular restricted three-body problem, as discussed in Section 5.2.

the specific energy of the system must also be incorporated into the description of motion.

While Cartesian coordinates are a general, and very useful, formulation for expressing the motion of spacecraft or other celestial objects, two-body motion is equivalently described using a set of elements defining conic sections, the Keplerian orbital elements. This set of variables allows the time-varying position and velocity states to be expressed as a function of five constants and one time-dependent variable, greatly simplifying the procedure for modeling the motion of the object through space. Six classical conic elements, along with several related values, are illustrated in Figs. 3.2 and 3.3 and are defined as follows:

- *Semi-major axis*, a: determines the size, and therefore the energy, of the orbit and, for closed elliptical orbits, is defined to be the median distance of the orbiting body from the central body.

- *Period*, $\mathbb{P}$: the time taken to travel one full circuit around the orbit, directly related to the semi-major axis.

- *Mean motion*, n: the average angular rate of change of the particle moving along the orbit, directly related to the semi-major axis.

- *Eccentricity*, e: the magnitude of the eccentricity vector $\boldsymbol{e}$. This quantity defines the shape of the orbit, where $e = 0$ indicates a perfectly circular orbit and $0 < e < 1$ an elliptical orbit. For values of $e \geq 1$, the orbit is unbound from the central body and has either a parabolic ($e = 1$) or hyperbolic ($e > 1$) shape.

- *Inclination*, i: the angle between the orbital plane and the XY-plane of the inertial reference frame, i.e., the angle between the inertial Z-axis and the orbital angular momentum $\boldsymbol{h}$. Defined to be $i \in [0°, 180°]$.

- *Righ Ascension of the Ascending Node (RAAN)*, Ω: specified to be the angle between a fixed direction in the inertial frame (where the inertial frame is typically defined such that this direction is the X-axis) and the point where the orbit crosses the XY-plane from negative to positive Z values. Defined to be $\Omega \in [0°, 360°)$.

- *Argument of periapse*, ω: the angular displacement of the origin-periapse vector $\boldsymbol{e}$ from the line of nodes (the intersection of the orbital plane of motion and the XY-plane). Defined to be $\omega \in [0°, 360°)$.
- *True anomaly*, θ^*: the time dependent angle between the current position vector of the orbiting object $\boldsymbol{d}$ and the line of apsides $\boldsymbol{e}$. Defined to be $\theta^* \in [0°, 360°)$.
- *Argument of latitude*, θ: the angle between the line of nodes and the position vector $\boldsymbol{d}$, such that $\theta = \omega + \theta^*$. Defined to be $\theta \in [0°, 360°)$.
- *Eccentric anomaly*, E: the angle between the line of apsides and the line from the center of the elliptical orbit to a point on the auxiliary circle. This secondary point is defined such that it is colinear with the true position of the smaller body and this formed line is perpendicular to the line of apsides.
- *Mean anomaly*, M: the angle swept out around the center of the elliptical path by the mean motion as time advances, i.e.,

  $$M = n(t - t_p) \tag{3.3}$$

  where t is the time since the most recent periapse passage t_p.

The semi-major axis and eccentricity describe the size and shape of the orbit, whereas the inclination, RAAN, and argument of periapse orient the orbit with respect to the inertial coordinate frame with origin at the barycenter. The remaining time dependent variables θ^*, E, M, and θ are interchangable from a computational (but not necessarily operational) viewpoint and are used to define the state of the orbiting body at any instant in time. Only six independent constants from the list of conic elements are necessary to uniquely define the state of the orbiting body. Thus, many transformations between the orbital elements, as well as the Cartesian coordinates $\boldsymbol{d}$ and $\boldsymbol{v}$, are available. A complete process for transforming between Keplerian orbital elements and Cartesian coordinates is detailed by Vallado. [63]

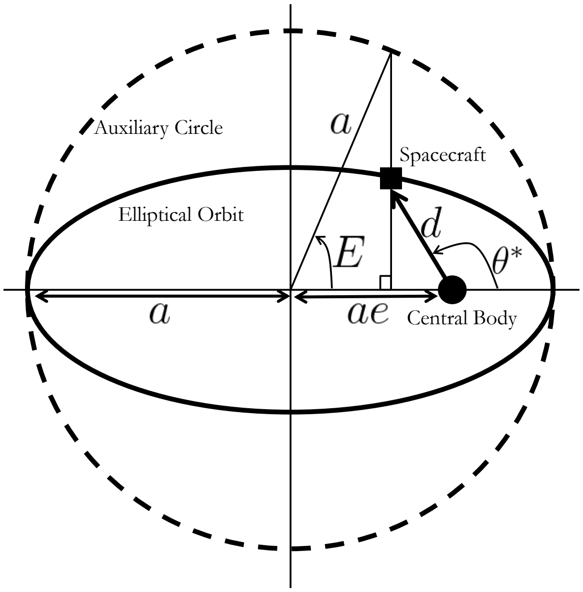

Figure 3.2.. Conic orbital elements in plane of motion.

3.2.2 Relationships involving the conic elements

While no single scalar value conveys all the information required to fully describe the orbital motion of a spacecraft or other small body, certain subsets of the Keplerian elements can, with the appropriate transformations, offer valuable insight into the behavior of the orbiting particle. For instance, the semi-major axis and eccentricity predict the lowest and highest points in the orbit via

$$d_p = a(1 - e) \tag{3.4}$$

$$d_a = a(1 + e) \tag{3.5}$$

where d_p and d_a are, respectively, the radii of periapse (closest approach) and apoapse (furthest recession) of the orbiting particle with respect to the central body. These two equations combine to produce

$$a = \frac{1}{2}(d_p + d_a) \tag{3.6}$$

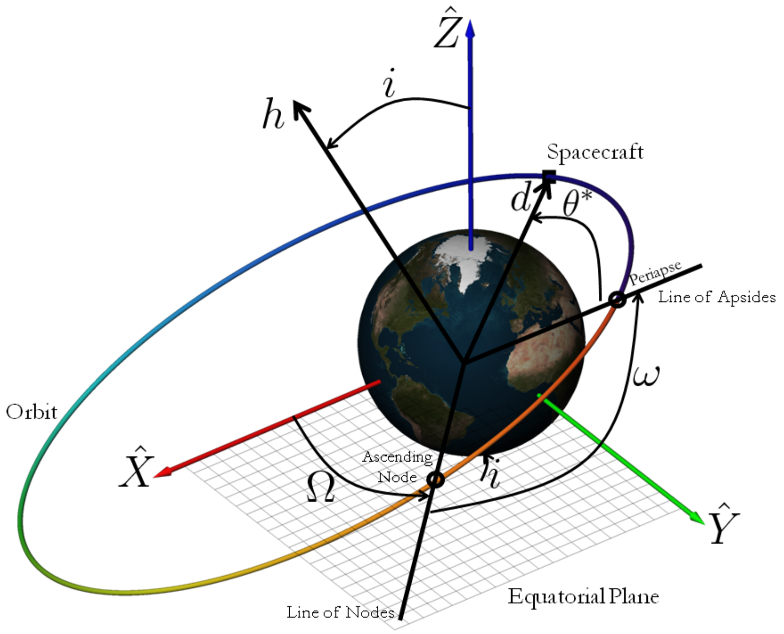

Figure 3.3.. Conic orbital elements with respect to inertially fixed frame. Earth is used as central body for illustrative purposes; conic elements are defined identically for any central body.

where this relation is consistent with the definition of the semi-major axis. Furthermore, the semi-major axis fully defines the time dependency of the motion about the gravitating body via the relations

$$\mathbb{P} = 2\pi\sqrt{\frac{a^3}{\mu_C}} \tag{3.7}$$

and

$$n = \sqrt{\frac{\mu_C}{a^3}} \tag{3.8}$$

where the orbital period and mean motion are functions only of the semi-major axis and the gravitational parameter. Recall that the gravitational parameter μ_C is commonly approximated using only the mass of the central body when the secondary body is negligibly small, for example spacecraft or debris objects.

Any one of the time-varying angular variables θ^*, E, M, or θ can be tracked over a given time interval to construct the full state history of the particle however, in practice, the mean anomaly is the most easily computed value, from Eq. (3.3). Once the mean anomaly is determined for a particular epoch, the equivalent eccentric anomaly is obtained via Kepler's Equation

$$M = E - e\sin E \tag{3.9}$$

where both the mean and eccentric anomalies are expressed in radians. In general, Eq. (3.9) must be numerically solved since no closed form solution exists. The true anomaly is recovered from the eccentric anomaly by using the relation

$$\tan\frac{\theta^*}{2} = \sqrt{\frac{1+e}{1-e}}\tan\frac{E}{2} \tag{3.10}$$

with the argument of latitude θ readily obtained thereafter. The scalar values for the current radius and velocity are obtained from the standard conic expressions

$$d = \frac{p}{1 + e\cos\theta^*} \tag{3.11}$$

$$v = \sqrt{\frac{2\mu_C}{d} - \frac{\mu_C}{a}} \tag{3.12}$$

where the semi-latus rectum is defined by

$$p = \frac{h^2}{\mu_C} \tag{3.13}$$

with h the scalar magnitude of the angular momentum vector $\boldsymbol{h} = \boldsymbol{d} \times \boldsymbol{v}$, a conserved quantity for two-body motion. For the special case of circular orbits ($e = 0$), the anomaly values are equivalent, i.e., $\theta^* = E = M$, and the magnitudes of the radius and velocity become constants, although the vector quantities $\boldsymbol{d}$ and $\boldsymbol{v}$ vary with time.

3.3 Relative target priority: debris groups and collision threat

The build-up of defunct satellites and rocket bodies as well as fragmentary objects poses a hazard to all currently operating and future satellite missions. Two distinct hazards are posed by these objects: i) direct collision with an active object, wherein even a small fragment can disable an operating satellite, and ii) a collision between defunct objects leading to the generation of still more debris fragments. In fact, if several collisions occur, a runaway cascade of collisions could disable a large number of active satellites and completely obstruct access to entire regions of Earth orbit. Such a runaway chain of collisions is termed the "Kessler effect". [42] While the removal of large, defunct objects is the preferable method to reduce fragmentation events, there are enough fragments currently in orbit that schemes dedicated to removing these smaller objects is also desirable.

3.3.1 Debris classification taxonomies

One critical element of debris mitigation is the identification and classification of potential target objects. While the technology to identify and track objects orbiting the Earth has existed for several decades, only recently have attempts been made to produce a systematic classification scheme for artificial debris objects. [50–52] These taxonomic schemes draw upon many physical characteristics, from orbit regime to size and shape to material composition, for determining the origin, current status, and potential orbital evolution of the debris objects. A modified set of Früh's taxonomic categories for artificial satellites is detailed in Table 3.2; note that many of these classifications are available using remote observation techniques. Once the observed and inferred physical characteristics of an object have been collected, the long-term evolution and hazard level of the artificial satellite may be assessed. As in Table 3.1, red text in Table 3.2 indicates specific debris classifications that serve as a focus of this preliminary investigation. In particular, large objects that are likely to contribute to the future growth of the debris population, due to shedding and fragmentation events, are preferentially targeted for removal. Furthermore, if a collision event occurs, the expedited removal of the resulting fragments from Earth orbit is desirable, therefore, medium-sized objects (that is, larger than 10 cm and, thus, able to be tracked using current observation capabilities) are also targeted for disposal.

Note that since proximity operations are not explicitly modeled, no restrictions apply to certain descriptor categories.

Table 3.2. Physical characteristics for taxonomic classification of artificial debris objects.

Descriptor	**Classification**			
Orbit regime	LEO	MEO	GEO	HEO
Orbit control	controlled / active		uncontrolled / defunct	
Attitude	controlled	spinning	tumbling	
Fragmentation	intact	fragment		
Material	single	few	composite of many	
Size	large (>1.5m)	medium	small (<10cm)	micro (<1cm)
Shape	regular convex	regular with concavities		irregular
Area to mass ratio (AMR)	high (HAMR) >2 m^2/kg	medium (MAMR)	low (LAMR) >0.8 m^2/kg	

3.3.2 Selection of target debris groups

Given the tens of thousands of debris objects in Earth orbit, careful selection of potential targets of interest is a necessary step in the formulation of a feasible mitigation strategy. Investigations by Peterson [55] and Lewis et al. [66] identify specific debris objects and categories that pose the highest long-term threat in terms of probability and severity of collision. These objects are typically large, intact objects, e.g., defunct satellite buses or rocket bodies from the upper stages of launch systems. Furthermore, as demonstrated by Peterson, these high-risk objects usually form a taxonomic group in terms of physical characteristics such as orbit regime as well as body size and shape. In particular, the LEO regime is of particular concern because of the high density of objects with large relative velocities and correspondingly high-energy collision events. In contrast, LEO altitudes readily allow for the definitive termination of debris objects via atmospheric re-entry. Thus, a viable mitigation strategy for large LEO objects is the attachment of de-orbit packages such as propulsive modules or drag-inducing devices.

Based upon Peterson's analysis, a test case in this investigation is the active mitigation of the SL-8 / Kosmos upper stage rocket bodies. The identical size and shape of each of these target objects enables the easy replication of any chaser spacecraft attachment mechanism as well as the deployable de-orbit package. Indeed, the major distinguishing factor among the SL-8 rocket bodies is the orbital behavior of the objects. The vast majority of the 295 currently extant Kosmos upper stages (as of July 4^{th}, 2013) reside in nearly circular orbits with three distinct altitude / inclination groupings at roughly 760 km / 74°, 970 km / 83°, and 1570 km / 74°, as illustrated in Fig. 3.4. But, the target rocket bodies are widely distributed in right ascension of the ascending node (RAAN) and phase within their respective orbit planes.

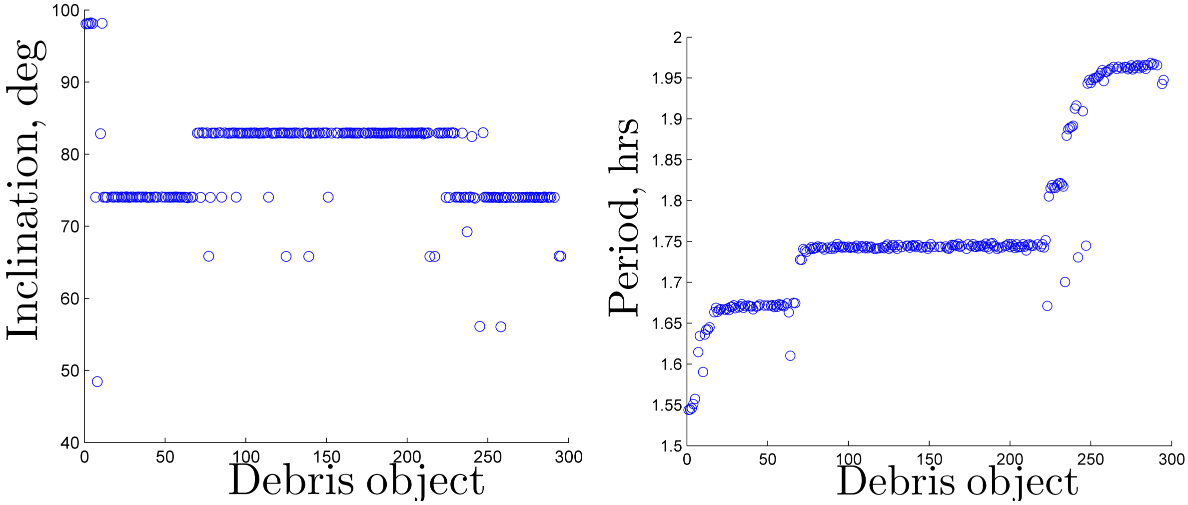

Figure 3.4.. Orbital period and inclination with respect to the equator of the target SL-8 / Kosmos upper stage rocket bodies. Elements extracted from public NORAD Two-Line Element set dated July 4, 2013. [67]

While the preventative removal of a relatively small number of large debris objects is logistically easier than the removal of small objects after a fragmentation event, enough such events have occurred that a feasibility analysis of the disposal of fragments is also desirable. For example, the Iridium-Kosmos collision in February 2009 [43] and the Fengyun-1C anti-satellite test [44] produced a large number of fragments that, over time, have necessitated many avoidance manuevers from operating satellites, for instance, the Earth observatories comprising the A-Train constellation. [68] While many fragments have decayed since the collision events, the majority of the small objects remain in orbit, roughly 69% from Iridium 33, 77% from Kosmos 2251, and 88% from Fengyun-1C. The bulk of the fragments from these events reside within a 700-900 km altitude band and are closely grouped in orbit inclination, as evident in Figs. 3.5, 3.6, and 3.7. However, the fragment orbits do vary in eccentricity and orbit plane, the latter due to nodal drift caused by zonal harmonics in the Earth's gravity field. While no convenient fragment groups are readily apparent, the objects are filtered for orbital characteristics that are amenable to a preliminary transfer cost analysis. Therefore, only objects residing in nearly circular orbits (eccentricity lower than or equal to 0.025) and above 700 km altitude are considered in the test cases examined. Objects lower than this critical altitude are typically moving along orbits that are rapidly decaying and, thus, active removal is not required. The mitigation techniques for these small objects generally fall into two broad categories: (i) the collection and storage of the debris object on-board the servicer spacecraft, or (ii) the alteration of the orbital path of the fragment such that an eventual decay into Earth's atmosphere is assured. In the event that no consumable resource is used for these mitigation operations, the number of objects mitigated by a single spacecraft may then be arbitrarily large assuming sufficient propellant remains to transfer from one object to another.

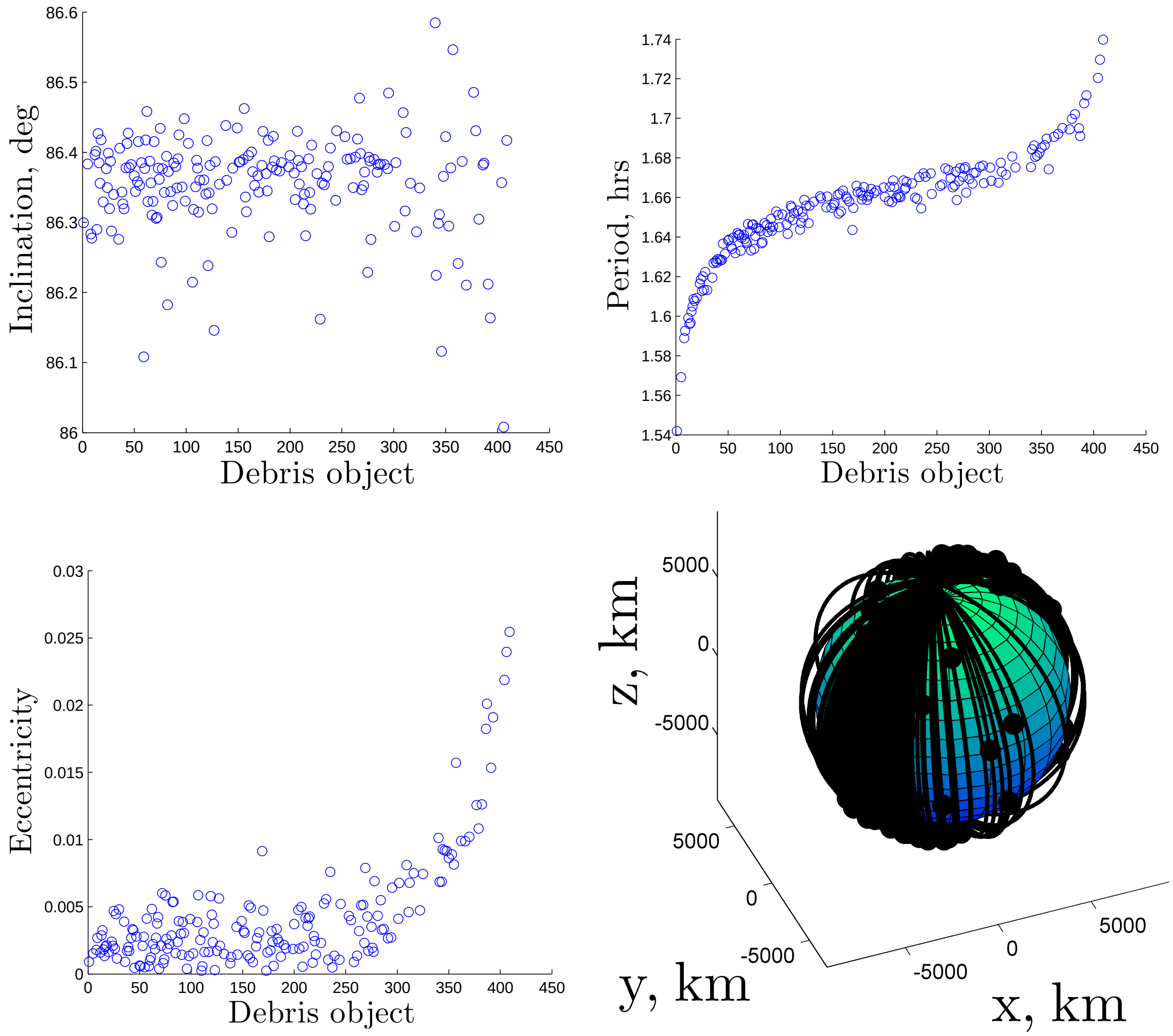

Figure 3.5.. Orbital period, inclination, eccentricity, and orbits of the target Iridium 33 fragments. Orbits display grouping in right ascension of ascending node. Elements extracted from public NORAD Two-Line Element set dated April 24, 2014. [67]

3.3.3 Collision threat posed by individual objects

Extensive research has been conducted into the analysis of collision risks between orbiting bodies; Chan [69] supplies a summary of many modern collision prediction techniques while the National Research Council offers periodic assessments of the

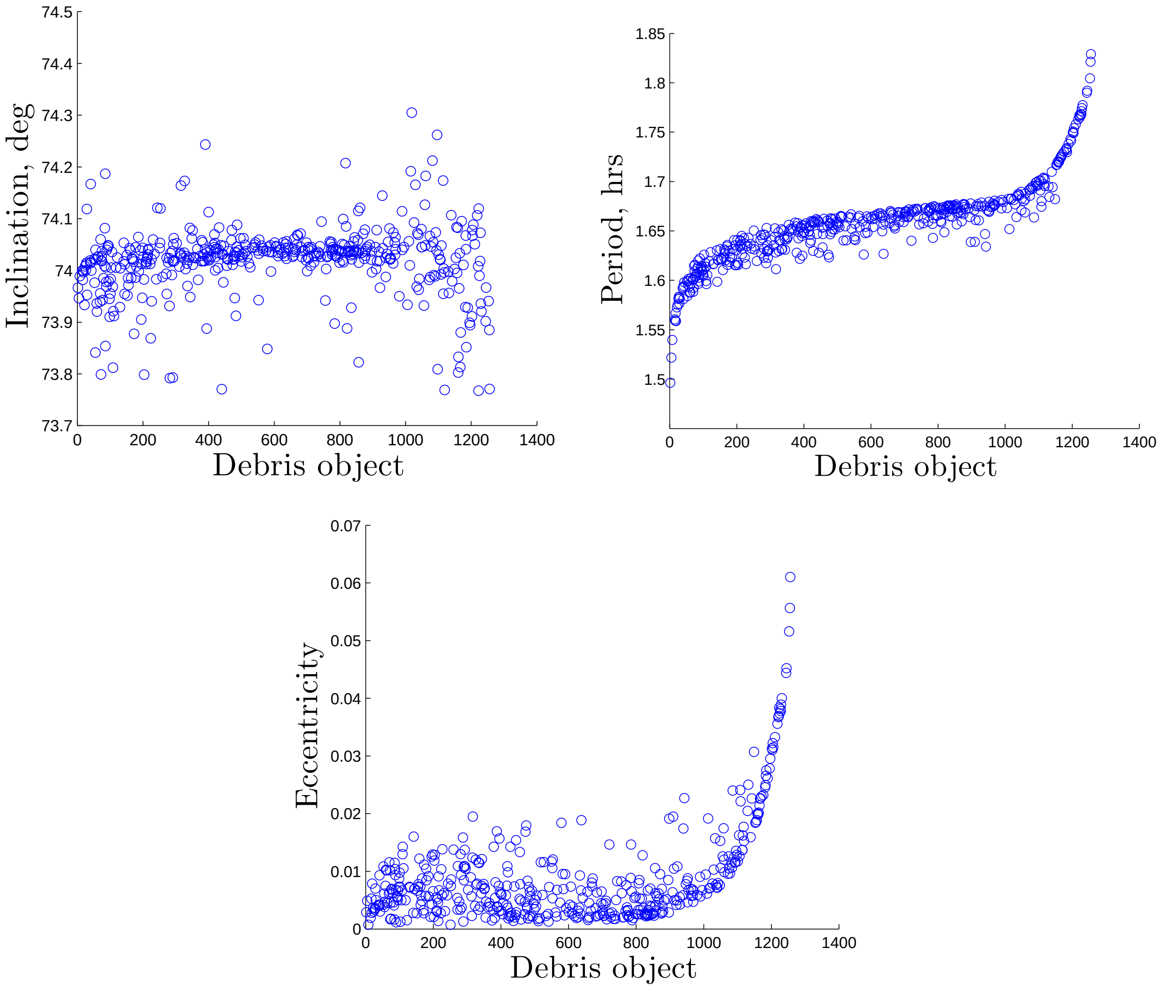

Figure 3.6.. Orbital period, inclination, eccentricity, and orbits of the target Kosmos-2251 fragments. Orbit plot omitted. Elements extracted from public NORAD Two-Line Element set dated April 24, 2014. [67]

debris mitigation capabilies of NASA. [70] The computation of the collision risk posed by individual close approaches between orbiting bodies is beyond the scope of the current investigation, but, such information is readily incorporated into the process for the generation of debris removal tours. When necessary, the hazard posed by an individual debris object is randomly assigned a value w on the interval [0.5,1.5], where this value is easily updated with time to simulate a dynamic environment wherein collision risks are continually assessed and updated.

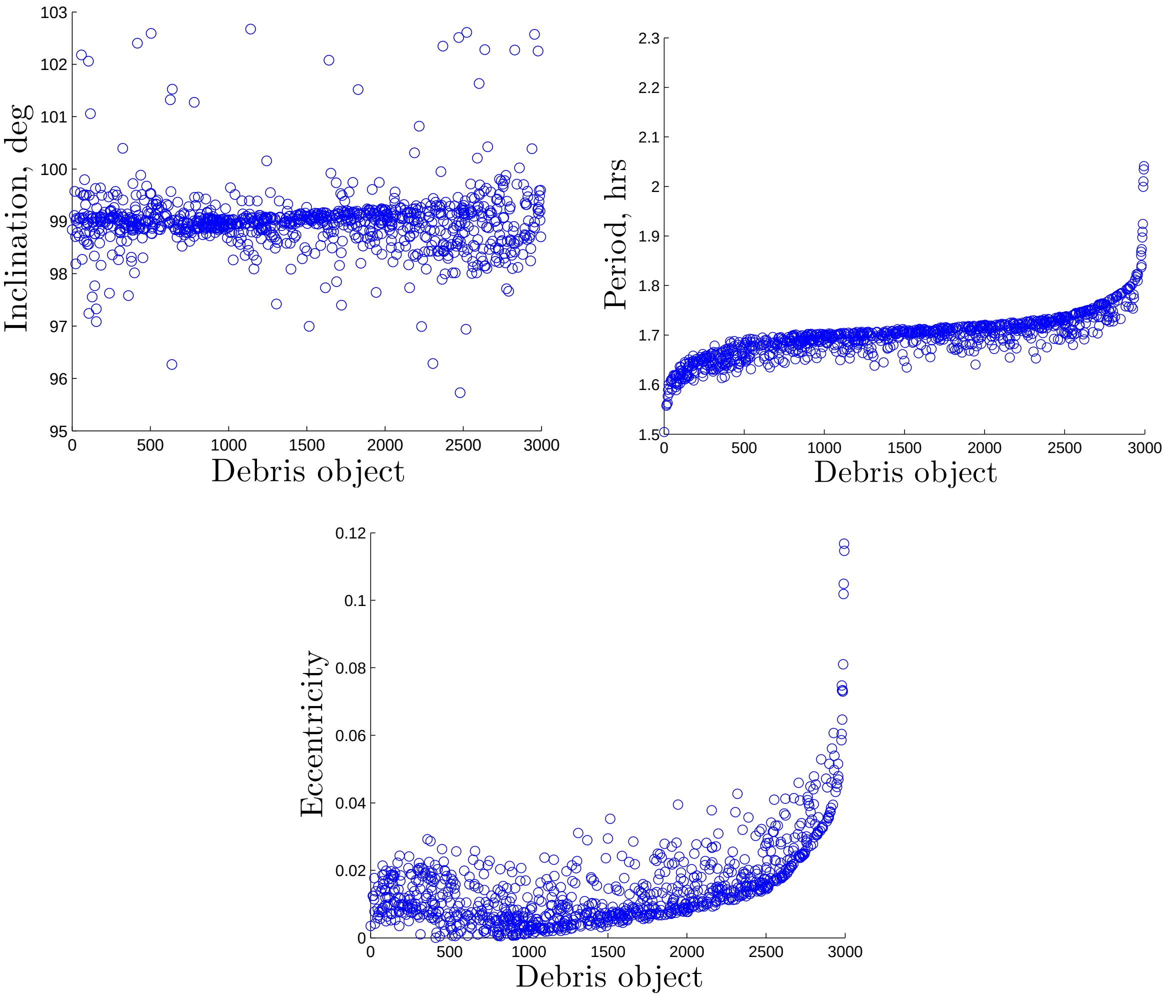

Figure 3.7.. Orbital period, inclination, eccentricity, and orbits of the target Fengyun-1C fragments. Orbit plot omitted. Elements extracted from public NORAD Two-Line Element set dated April 24, 2014. [67]

3.4 Rendezvous computation: conic cost approximations

For this preliminary investigation, only a simplified, rapidly-computed cost approximation is desired for the debris mitigation mission scenario. Thus, the general corrections procedure detailed in Section 2.4.1 is omitted and analytical rendezvous propellant cost estimates are developed. Some form of the corrections procedure is, however, necessary for the construction of true rendezvous solutions between the target debris objects. Due to the clustering of the debris object orbits in terms of inclination and the near-circularity of the motion, the majority of the propellant is expended to adjust the size and orientation of the orbit. For a chaser spacecraft traveling from one target to another within the same group, maneuvers are necessary to adjust the altitude, change the orbital plane, and to match the phase of the destination object. That is, the total rendezvous cost is approximated via

$$\Delta V = \Delta V_{alt} + \Delta V_{pc} + \Delta V_{ph} \tag{3.14}$$

where ΔV_{alt} is the cost to alter the spacecraft altitude, ΔV_{pc} reflects the maneuver to change the orbit plane, and the cost of the phasing maneuvers are represented by ΔV_{ph}. The propellant expenditure for each purpose is assumed to be decoupled and only a simplified cost model is desired. Hence, analytical expressions estimating the maneuver magnitude for the chaser rendezvous with the debris objects are readily developed for this preliminary analysis.

The analytical cost estimates assume an impulsive maneuver capability, i.e., thrust is delivered by a high impulse system that operates only for short durations. Since engines using chemical propellants are the only technology capabable of delivering this performance within the near-term, the analytical approximations are best suited for analyzing mission scenarios enabled by chemical propulsion. However, for architectures where a more efficient low-thrust system is desirable, the transfer cost for electrical thrusters is approximated from the impulsive cost estimates. Peterson [55], using Edelbaum's low-thrust optimization methods, [71] demonstrates that the ΔV cost for small changes in altitude (i.e., less than 5,000 km) are nearly equivalent using either impulsive- or continuous-thrust models. Thus, changes to the servicer spacecraft orbit phase are also roughly equal using the phasing method implemented. In contrast, the cost to shift the plane of motion is comparable in terms of an 8/5 ratio, that is, low-thrust / impulsive systems. For clarity, note that an impulsive maneuver equal to 1 km/s in ΔV changes the orbital plane by approximately 8°, whereas an equal amount of ΔV delivered by an electrical engine alters the plane by only 5°.

Therefore, the total cost for the transfer effected by a low-thrust system from one debris object to another is easily summarized

$$\Delta V_{lt} = \Delta V_{alt} + \frac{8}{5}\Delta V_{pc} + \Delta V_{ph} \tag{3.15}$$

where the impulsive transfer costs are defined as in Eq. (3.14).

3.4.1 Altitude adjustment ΔV cost

The most efficient method within a two-body environment to transfer between co-planar, circular orbits of differing altitudes is the Hohmann transfer, i.e., an elliptical transfer orbit with a periapse altitude equal to the altitude of the smaller orbit and an apoapse radius equivalent to the semi-major axis of the larger orbit. [72] The Hohmann transfer between two orbits is illustrated in Fig. 3.8. Accordingly, recalling Eq. (3.6), the semi-major axis of the Hohmann ellipse is defined as

$$a_H = \frac{1}{2}(d_{CD} + d_{CT}) \tag{3.16}$$

where $d_{CD} = a_{CD}$ and $d_{CT} = a_{CT}$ are the radii of the circular departure and arrival orbits, respectively. Thus, from Eq. (3.12), the velocity magnitude within the circular orbits is

$$v_C = \sqrt{\frac{\mu_C}{d_C}} \tag{3.17}$$

where $\mu_C = 3.986 \times 10^5 \frac{km}{s}$, the gravitational parameter for the Earth, and the velocity at the apses of the transfer ellipse are

$$v_H = \sqrt{\frac{2\mu_C}{d_C} - \frac{\mu_C}{a_H}} \tag{3.18}$$

where the radius d_C is that of either the departure or target orbit. Since the maneuver is tangential, the magnitude required to shift from one of the circular orbits to the equivalent point on the Hohmann ellipse is then

$$\Delta V_H = \|v_H - v_C\| \tag{3.19}$$

and, therefore, the total estimated cost for the change in the orbit altitude is

$$\Delta V_{alt} = \Delta V_{HD} + \Delta V_{HT}. \tag{3.20}$$

Note that the Hohmann transfer is reversable, i.e., the cost to transfer from an orbit with a higher altitude to an orbit with a lower altitude is exactly equal to the transfer from the smaller to the larger orbit. Using the fragments from the Iridium 33 satellite as a demonstration, one fragment is selected and the ΔV cost to change the orbit of a chaser spacecraft from the selected object to all other Iridium 33 fragments is computed. The resulting costs are displayed in Fig. 3.9. Note the nearly linear relationship between the change in semi-major axis and the required propellant expenditure.

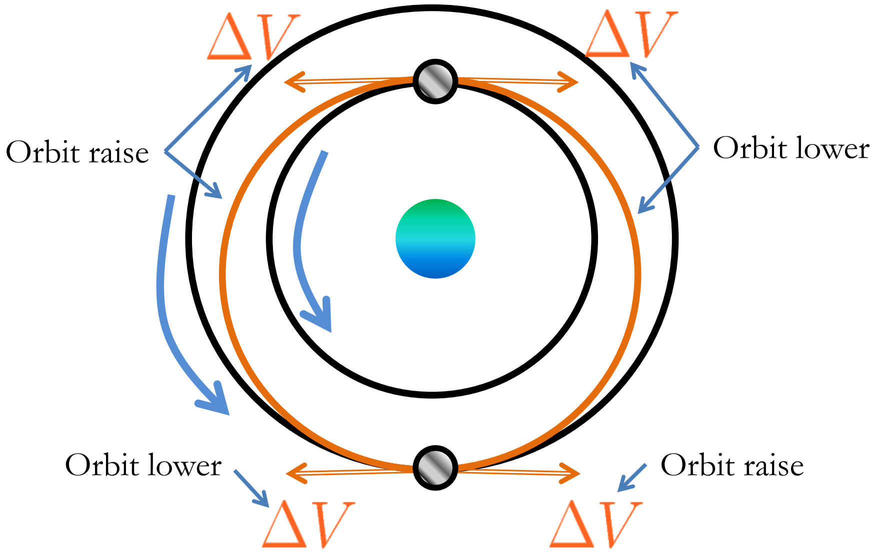

Figure 3.8.. Sketch of Hohmann transfer between circular orbits. Hohmann cost to transfer from lower to upper orbit is identical to reverse tranfser, apart from direction of applied velocity change. Raising the orbit requires tangential burns in the velocity direction while lowering the altitude necessitates maneuvers anti-parallel to orbital velocity.

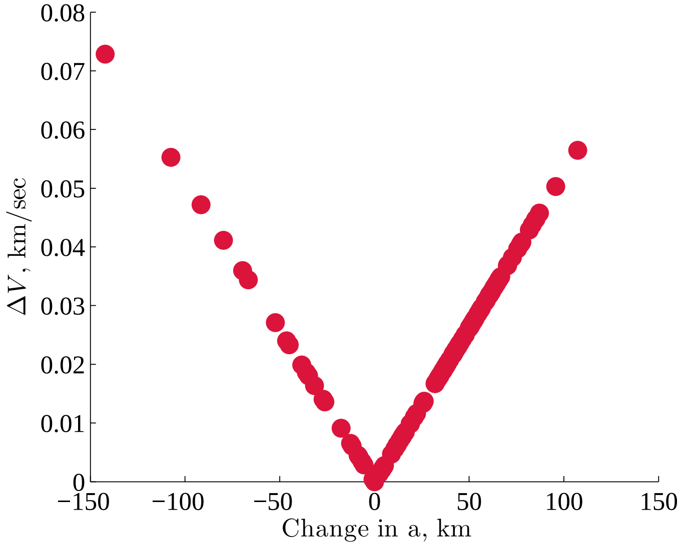

Figure 3.9.. Altitude (semi-major axis) change costs for Iridium 33; for low changes in altitude the cost is approximately linear.

3.4.2 Plane change ΔV cost

In short-duration mitigation missions for which zonal drift and other pertubative effects are negligible, changes in the orbit plane are likely to be accomplished via the expenditure of propellant. If the current and destination orbits intersect in physical space, then the transfer may be implemented using a single impulse. Note that, generally, the required magnitude of a single impulse ΔV_{si} maneuver when the orbits interest is evaluated as

$$\Delta V_{si}^2 = V_D^2 + V_T^2 - 2V_D V_T \cos\eta \tag{3.21}$$

where V_D and V_T are the speeds along the departure and target orbits at the point of intersection, respectively, and it is assumed that the velocity vectors are in the same plane. The angle η is the angle between the velocity vectors. Note that in the case when departure and destination orbits are identical but the planes of motion differ, reflected in different nodal crossings (i.e., RAAN), the shift in the orbit plane is accomplished by a single impluse at one of the two intersections along the orbital tracks. Furthermore, given the nearly circular orbits in which the target debris objects reside, the cost to transfer between orbit planes is easily approximated as

$$\Delta V_{pc} = 2V_c \sin\frac{\Delta\Omega}{2} \tag{3.22}$$

where $\Delta\Omega$ is the difference in RAAN between the initial and arrival orbit planes and V_c is the circular orbit velocity, as illustrated in Fig. 3.10. Using this formulation, the cost of the transfer maneuver is estimated simply from the classical elements describing the target orbits without any requirement to locate the intersection points between the spacecraft paths. Recall the three groupings of SL-8 rocket bodies in Fig. 3.4. One object from each group is selected, where the plane change maneuver from the selected target orbit to any other upper stage within its own group yields Fig. 3.11. For all three families or groups, the cost associated with small values of $\Delta\Omega$ results in a nearly linear relationship between $\Delta\Omega$ and ΔV, as expected, and requires approximately 1 km/s to enable about an 8° change in RAAN.

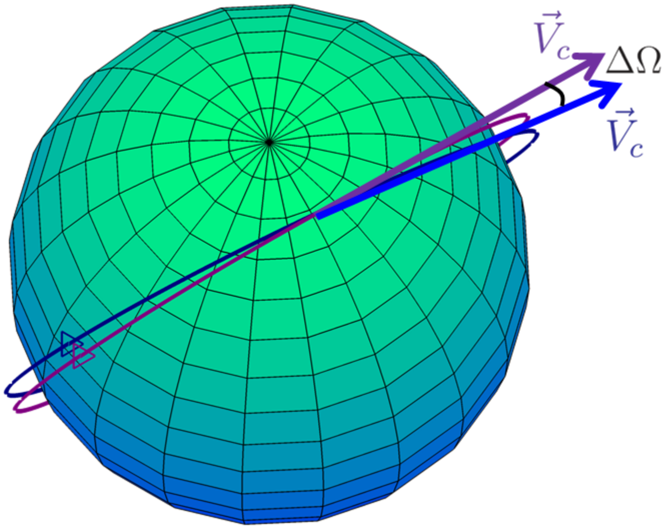

Figure 3.10.. Intersection velocities along departure (blue) and target (purple) debris orbits. Note that difference in RAAN $\Delta\Omega$ is equal to the angular difference between the two velocities.

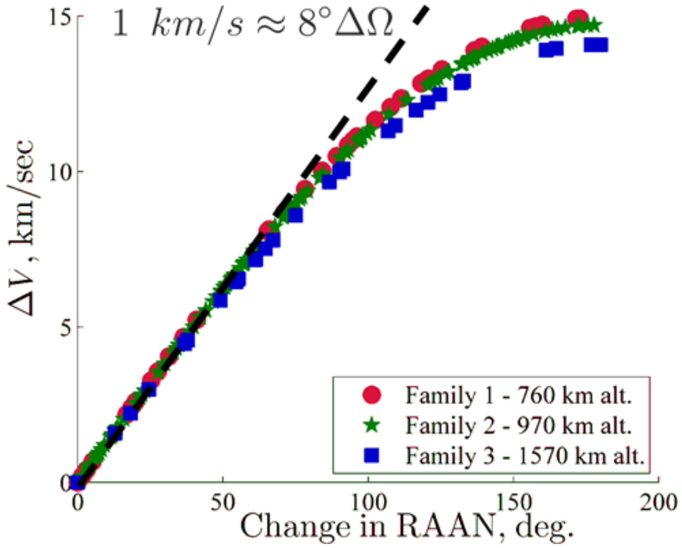

Figure 3.11.. Plane change costs for three SL-8 rocket body groupings. For low changes in RAAN, the cost is approximately linear.

3.4.3 Phasing ΔV cost

While shifting the orbital plane and the altitude of the chaser spacecraft to that of the debris objects is a necessary step in the rendezvous process, the required maneuver that is necessary to match the phase of the target object must also be incorporated into the cost model. Due to the low eccentricity of the orbits for the selected debris objects, differences in phase are straightforwardly expressed in terms of changes in the argument of latitude, $\Delta\theta$, that is, the varying times associated with the object's crossing of the equatorial plane of Earth. One strategy to match the phase of the chaser to that of the target is a boost of the chaser spacecraft into a loiter orbit with a different period from that of the debris object; then, after some wait interval, the differences in mean motion will bring the chaser and target within close proximity. After any difference in the argument of latitude is eliminated, a second burn returns the chaser spacecraft to a circular orbit matching the orbit of the debris object. A notional respresentation of this process appears in Fig. 3.12, where the number of revolutions, n, of the chaser spacecraft along the phasing ellipse and, m, the target object on its circular path are independently adjustable. The required period of the phasing orbit that is occupied by the chaser, $\mathbb{P}_E$, is computed via

$$n\mathbb{P}_E = \mathbb{P}_C\left(m + \frac{\Delta\theta}{2\pi}\right) \tag{3.23}$$

where $\mathbb{P}_C$ is the period of the debris object in the circular orbit and the difference in the argument of latitude, $\Delta\theta$, between the chaser and target varies between $\pm\pi$ radians. The integers n and m represent the number of revolutions n of the chaser spacecraft along the phasing orbit and the revolutions m of the debris object in the target orbit. Once an appropriate size for the phasing orbit is determined, the total propulsive cost for the phasing maneuvers is

$$\Delta V_{ph} = 2\|V_E - V_C\| \tag{3.24}$$

where V_E is the speed on the phasing ellipse at the circular orbit altitude, i.e., at either periapse or apoapse depending upon whether the debris object is trailing or leading the chaser spacecraft, respectively. Recall that two burns are required for phasing, hence the factor of 2 in Eq. (3.24). The relevant apse speed on the phasing orbit is obtained from

$$V_E = \sqrt{\frac{2\mu}{a_C} - \frac{\mu}{a_E}} \tag{3.25}$$

where the elliptical and circular semi-major axes a_E and a_C are calculated via

$$\left(\frac{\mathbb{P}}{2\pi}\right)^2 = \frac{a^3}{\mu_C}. \tag{3.26}$$

Recall that the gravitational parameter of the Earth is $\mu_C = 3.986 \times 10^5 \frac{km}{s}$.

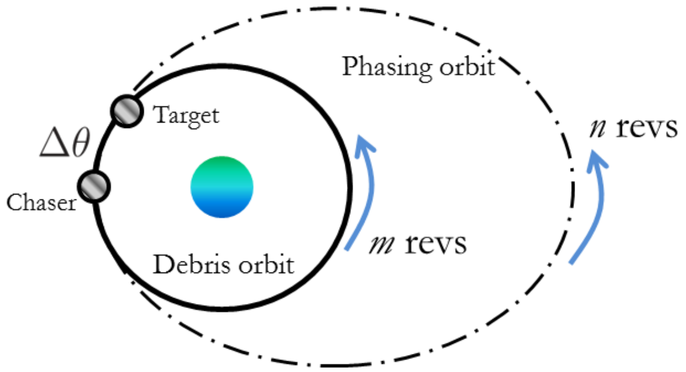

Figure 3.12.. Illustration of debris object orbit and phasing orbit for the spacecraft. If the debris object leads the chaser spacecraft, a phasing orbit smaller than the debris orbit is used.

A trade-off between the phasing and debris orbital periods and propellant cost is available for the phasing portion of the rendezvous maneuvers. The revolution numbers n and m in Eq. (3.23) can be independently adjusted, but, if more than one phasing revolution about the Earth is incorporated, the most successful strategy maintains $n = m$ so that differences in orbital periods and, consequently, the required propellant expenditures, are reduced. Thus, the trade-space for a single shift in orbit phasing from one debris object to another is reduced to simply the balancing of the duration, represented by the number of phasing revolutions n, and the required ΔV from the propulsion system. The phasing maneuver costs across the three target groupings of the SL-8 rocket bodies and for two phasing durations, $n = 10$ and

$n = 100$, are plotted in Fig. 3.13. Note the linear relationship between ΔV and number of phasing revolutions as well as cost and the required change in argument of latitude. These linear relationships break down if the phasing maneuver is attempted for a low number of orbital periods. For this preliminary investigation, the revolution number n is fixed for any particular solution run, however more sophisticated search methods incorporating both transfer time and cost could be implemented. [73]

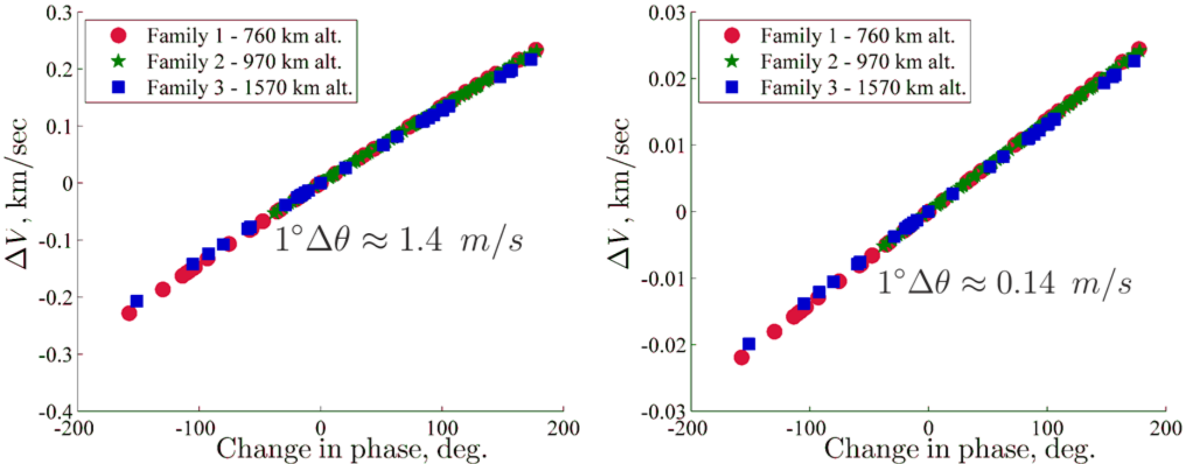

a. ΔV cost for 10 periods, $n = m = 10$. b. ΔV cost for 100 periods, $n = m = 1$.

Figure 3.13.. Phase change cost for three SL-8 upper stage families.

3.5 Search strategy: ant colony optimization and the vehicle routing problem

Many search strategies are capable of reliably producing potential trajectories for spacecraft operations of a single vehicle without the need to coordinate actions with other vehicles. Ant colony optimization, however, offers the added advantage that it is readily adaptable for scenarios where multiple spacecraft must interact and coordinate behavior. One natural application for ACO is the solution of vehicle routing problems (VRP); [38, 74] the generation of debris mitigation tours is a specific example. However, one critical factor incorporated into any search strategy is the fact that the chaser spacecraft is not infinitely capable but instead possesses limited propulsive reserves and mitigation capability, here represented by the on-board number of de-orbit packages or a limited carrying capacity for fragmented pieces of satellites.

In most ACO applications, the objective is to traverse the network from one node to another or to create a circuit of all nodes, in both cases, for the least cost. However, for debris mitigation spacecraft with limited capability, the network-spanning route is split into discrete sequences that can be addressed by one individual vehicle. In this case, an "ant" representing a chaser spacecraft traverses all potential debris targets with a "reset" after a chaser spacecraft has exhausted either its propellant (ΔV_{cap}) or de-orbit package (p_{cap}) reserves. For an individual ant, the number of resets is equivalent to the number of chaser spacecraft that are required to implement all encounter sequences. This concept is notionally presented in Fig. 3.14, where the dashed, colored links indicate sequences followed by individual chaser spacecraft (the "ant", in turn, travels all dashed connections). For this investigation, the target-to-target transfer model is simplified to one equivalent ΔV cost as evaluated by Eq. (3.14) or (3.15). Thus, once an initial debris target is specified, the set of accessible targets is readily computed. However, the construction of the optimal encounter sequence, particularly when coordinated with other nearby chaser spacecraft, is a non-trivial process for all but the the simplest models of transfer cost. Recall that the altitude and plane-change costs are determined entirely by the geometry of the target debris orbits while the phasing cost is dependent upon the selection of the phasing number n. Consequently, because two factors contribute to the transfer cost, the total ΔV requirements for a chaser to transfer from target A to B to C is not necessarily equivalent to the associated cost if target B is omitted, e.g., A to C.

Recall from Section 2.5.1 that the ant colony algorithm mimics the foraging behavior of ant colonies by performing a series of parallel searches wherein sets of virtual ants construct individual routes through the network. However, the rules that the ants obey when traversing the network are extended as follows:

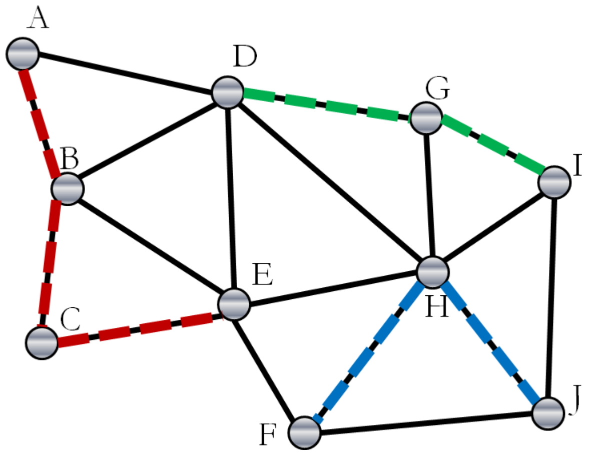

Figure 3.14.. Schema of a sample debris network on which ant colony optimization can be applied. Links between objects can be traveled in both directions. Colored, dashed connections are traversed by specific chaser vehicles.

1. *Exploration*: With some "exploration" probability γ, the "ant" travels to a randomly selected new node, where the parameter γ decreases from 1 to some steady-state value $0 < \gamma_{ss} < 1$ over succeeding generations; else,

2. *Following*: Stochastically select an unvisited node with the "following" probability

$$P_{i,j} = \frac{\tau_{i,j} B_{i,j}^{\beta}}{\sum \tau_{i,j} B_{i,j}^{\beta}} \tag{3.27}$$

   where $P_{i,j}$ is the probability for travel from the i^{th} node to the j^{th} node, $\tau_{i,j}$ is the pheromone level on the link, $B_{i,j}$ is the quality of the connection, and β is a weighting parameter.

3. *Reset*: If the chaser spacecraft exhausts either its set of de-orbit packages or propellant capacity, place the ant at a randomly selected, but unvisited, debris object with full mitigation and propellant capacities.

4. When all nodes / debris objects have been traversed, terminate the search for the individual ant. The total number of resets that the ant must perform

represents the number of chaser spacecraft required to effect the constructed mitigation sequences.

Once each individual ant has completed its search during the k^{th} generation, global information on successful routes is conveyed to succeeding generations via the creation and dissipation of virtual pheromones. For the mitigation of artificial debris objects, the individual link quality is defined

$$B_{i,j} = \Delta V_{a:i \rightarrow j} = \Delta V_{cap} - \sum \Delta V_p \tag{3.28}$$

where $\Delta V_{a:i \rightarrow j}$ is the remaining propulsive capability of the chaser spacecraft at arrival at the target object, ΔV_{cap} is the initial mitigation spacecraft propellant reserve, and $\sum \Delta V_p$ is the summed propellant expenditure for the links previously followed by the spacecraft. Note that while the link quality is simplified to an evaluation of the ΔV cost for this mission scenario, the travel time and the importance of the target objects have been successfully incorporated into the link quality metric for other mission scenarios; [73] this expanded capability is discussed in greater detail in the solution approach to the construction of asteroid survey tours.

Global information on beneficial routes through the network are conveyed to individual ants via the creation and dissipation of pheromone values associated with specific object-to-object transfer options. This updated pheromone represents a transfer of information from one generation of ants to the next such that ants in later generations possess a higher probability of producing higher-value encounter sequences. After each succeeding generation of ants, the pheromone levels along each individual link are updated via Eq. (2.23). Furthermore, if the pheromone level on an individual link falls below a certain threshold, ρ_L, the pheromone level on that transfer option is set to zero. This logic removes the need to explicitly compute travel probabilities that are already nearly zero as compared to trails with higher reinforcement levels. Note that the pheromone increase, $Q_{i,j}$, corresponding to a given link is either zero (if only the best routes and, therefore, the best links, are reinforced) or some function that is dependent on the performance metric associated with tours that include the particular leg in question. For the debris mitigation scenario, the pheromone update procedure increases the pheromone on each link of the current best tour over all previous generations by the value $1/Q$ where the quality value Q is defined to be

$$Q = C_{sc}N_{sc} + \sum_{k=1}^{N_{sc}} \Delta V_k \tag{3.29}$$

and where N_{sc} is the number of spacecraft or, equivalently, the number of "resets" required to encounter all debris objects, C_{sc} is a constant scaling factor, and ΔV_k is the propellant consumed by the k^{th} chaser spacecraft. The scaling constant C_{sc} is essentially a weighting factor that, if set sufficiently high, allows the number of required chaser spacecraft to dominate the propellant consumption, that is the total ΔV expenditure, of the individual spacecraft. Under this update model, the best tour acquires the lowest Q value. After a pre-determined number of generations, this procedure is terminated and the best tour is returned.

3.6 Mission operations: coordination of flight operation for multiple vehicles

A bidding and auction process is applied to the coordination and modification of the debris removal sequences for multiple service spacecraft within the context of real-time flight operations. The auction scheme reduces the necessity for constant human-in-the-loop monitoring of the debris mitigation spacecraft while simultaneously assisting in the assignment of time-critical targets to the operating vehicles. In the auctions, individual spacecraft bid to remove specific debris objects through simple serial auctions where all available spacecraft bid to select the next object to visit. Under nominal conditions, the top bid collected from each spacecraft is then the next target object along their baseline routes as determined by the ACO scheme. However, for certain contingencies, e.g., a particular debris object poses an imminent threat of collision or a chaser spacecraft becomes deactivated, the auction process alters the operation of the spacecraft swarm in real time. Generally, for the type of auctions in this investigation, no advantage ensues by under-bidding but over-bidding may offer benefits (e.g., a servicer can increase the attractiveness of its bid by underestimating the propellant cost). Therefore, this general process is not currently "incentive compatible", i.e., honesty may not be the best bidding strategy for an individual spacecraft. [40] However, in this investigation, the mitigation spacecraft are assumed to be honest, a reasonable assumption when all chasers are operated by the same company or agency. In the event that the spacecraft are operated by competing entities, a system of salvage rights could be instituted in which the "owner" of the debris object sells the rights to recover valuable resources to the highest bidder, a system that would be incentive compatible, but that is not currently implemented here.

A key element of the auction process is the bidding function; an appropriate choice incorporates one or more performance metrics from the current problem. For tours that encounter and mitigate debris objects, several important considerations include: the propulsive capability of the chaser spacecraft, the ability of the spacecraft to physically handle the object, the relative threat posed by the debris objects, and the time-to-rendezvous and mitigate the target object in question. Recall that the phasing duration is pre-selected and, therefore, translated into an equivalent ΔV cost. Accordingly, a bidding function is defined for the case when the k^{th} spacecraft bids upon the j^{th} object, namely

$$B_{j,k} = w_j^W p_k^R \Delta V_{k:i\to j}^M \tag{3.30}$$

where the bid B is a function of the relative threat posed by the object (w), the number of de-orbit packages remaining on the servicer spacecraft (p) after mitigating the subject target object, and the remaining propulsive capability (ΔV_k) after the servicer transfers from its current (debris object) orbit to the target orbit, as computed by Eq. 3.28.[2] The weighting parameters W, R, and M are adjusted to modify the relative importance of each metric on the overall bid. Note, also, that if one of

---

[2] Note that this bidding function could potentially be used as the link quality metric in the ACO implementation. However, as the target threat is highly variable over time, it could, in fact, be unknown at the time of the construction of the preliminary encounter sequence. Accordingly, individual target threat was omitted during the construction of initial target sequences.

the weighting parameters is equal to zero, the bidding function is then insensitive to that particular metric. If equal weighting is employed in this bidding function, the auction process favors the removal of the highest threat objects using the most capable spacecraft, i.e., the vehicle assuring the highest likelihood of success.

A serial, simple auction is implemented, wherein bids are solicited at periodic intervals Υ. The simple auction process is advantageous in that it is decentralized as well as relatively flexible and robust in the event of a chaser spacecraft failure or the addition of debris objects. Furthermore, updates to the object threat w are readily computed and incorporated into the bidding process. The process for the simple auction during each bidding period is implemented as follows:

1. All hazard levels posed by the target objects are reassessed and communicated to the chaser spacecraft, also termed "agents".
2. If a chaser spacecraft is busy, either traveling between debris objects or currently mitigating a target object, it does not bid.
3. If a chaser is not busy, it then constructs bids for all debris objects that can be accessed given the remaining propellant.
4. The agent then reports its top n bids, where n is the number of other chaser spacecraft participating in the auction process.
5. Each spacecraft that bids is first assigned its top bid. If another spacecraft places a higher winning bid on the same object, then the losing agent is assigned to its second highest bid, etc.
6. In the event that several bids are equal, the assignment of targets is random.

Once an agent has been awarded a specific target, the spacecraft transfers to the orbit of the specified debris object, expending the required propellant ΔV. Furthermore, the mitigation capability of the chaser spacecraft is updated, representing the usage of consumable resources to remove the targeted debris object. Note that, in the bidding process, debris objects that have been assigned to a specific servicer spacecraft are then removed from future bids, even if the rendezvous and mitigation of the rocket body has not been completed. Larger values of Υ increase the likelihood of simultaneous bids. For this investigation, the value of Υ is set to a value such that all chaser spacecraft complete the mitigation of their respective targets before a new round of bidding is announced. Though not specifically modeled, one intriguing application is a modification of the auction implementation process such that an auction is called only when a high collision risk conjunction event is detected. The spacecraft all follow their nominal routes, constructed from the ACO process, and only adjust behavior at the appearance of an imminent threat. The simple auction process is advantageous because it is decentralized and relatively flexible and robust in the event of a chaser spacecraft failure or the emergence of additional debris objects. Furthermore, updates to the object threat value w are readily computed and incorporated into the bidding process.

4. POTENTIAL DEBRIS MITIGATION SEQUENCES - RESULTS

A variety of debris mitigation architectures are investigated and potential removal options enabled by near-term technologies are detailed. A diverse set of debris objects are targeted for removal, from large intact bodies to smaller debris fragments. Preliminary tour options generated by the automated tour construction scheme reveal the infrastructure needed for complete removal of the target objects. Enhancements to spacecraft autonomy are demonstrated, particularly when the actions of multiple spacecraft must be coordinated. Feasible target sets are indentified for mission architectures using near-term technologies while potential avenues for enhanced future capabilities are discussed.

4.1 Preliminary searches with multiple spacecraft

Potential tour sequences are generated and analyzed in terms of the required number of mitigation spacecraft as well as the performance of individual chasers. Ant colony optimization is employed to create preliminary encounter paths and determine the required number of spacecraft for complete mitigation of the target families. The ACO algorithm is employed to generate potential tour sequences for each set of target debris objects.

4.1.1 SL-8 rocket body groups

The ACO algorithm is employed to generate potential tour sequences for each of the three sets of expended SL-8 rocket bodies. Since a short-term, i.e., less than one year, mitigation mission is desired, the chaser spacecraft are assumed to have a chemical propulsion system on-board. Furthermore, at each encounter with an SL-8 upper stage, the servicer spacecraft affixes module capable of altering the orbit of the debris object onto a rapidly decaying path, where each mitigation spacecraft carries with a limited number of these de-orbit packages. For this investigation, the same search parameters (e.g., spacecraft propellant capacity, number of ants, decay rate) are applied to each large debris grouping. These parameters are detailed in Table 4.1; note that these search parameters are selected as representative examples, while more detailed analysis is required to determine the optimal set of search criterion. Recall that the altitude of the rocket bodies is consistent across each family, such that propellant costs to alter the chaser spacecraft altitude within each family is negligible.

Table 4.1. Spacecraft, tour, and ACO parameter values, common to all runs targeting large debris bodies.

Quantity	**Value**
Propellant capacity of chaser spacecraft (ΔV_{cap}), km/s	2
Number of de-orbit packages per chaser spacecraft (p_{cap})	8
Phasing revolution number ($n = m$)	30
Number of generations (N_g)	100
Number of ants (N_a)	20
Link quality weight in link probability (β)	1
Pheromone decay rate (ρ)	0.05
Pheromone lower threshold (ρ_L)	10^{-5}
Base exploration probability (γ_{ss})	0.1
Spacecraft number scaling factor (C_{sc})	10

4.1.1.1 Family 1 - 760 km altitude

Tours are generated for the mitigation of the 39 SL-8 rocket bodies residing in 760 km altitude orbits. Recall that each tour, or "ant", respresents mitigation sequences for multiple chaser spacecraft. The performance of individual ants is examined in Fig. 4.1, where the required number of spacecraft for full removal of the target grouping as well as the average propellant per chaser are plotted for the last generation of the ACO run. The "Tour Number" is, in fact, the "ant" number. Across all the tours (ants), note the variance in the number of spacecraft required to accomplish the goal. Furthermore, there is an inverse relationship between the average ΔV expended per ant and the required number of chasers. This result supports the intuitive notion that chaser spacecraft with higher propulsive capability could generally reduce the required number of spacecraft for full mitigation. Similar trends are observed for the other target groupings at 970 and 1570 km altitudes. Recall that, as with most stochastic algorithms, the ACO search is typically run several times in order to improve the likelihood of discovery of the true global optimum. However, as the goal of this investigation is the generation of high-value prospective tours that are subsequently optimized in higher fidelity models, even singular runs provide valuable insight into the characteristics of optimal spacecraft tours. Furthermore, in instances were several runs of ACO are performed with identical parameters, the resulting best solutions from each run typically require the same number of chaser spacecraft for complete mitigation.

Examination of the best mitigation tour, as produced by the ACO algorithm in the 45^{th} generation, reveals that a minimum of 13 spacecraft are necessary for complete, short-term mitigation of all members of the 760 km altitude family. While this number is economically infeasible, a smaller set of mitigation spacecraft could still result in a significant reduction in the population of upper stages. Figures 4.2 and 4.3 aid in identifying particular high-return-on-investment sequences; information on the individual performance of specific spacecraft is conveyed in Fig. 4.2 whereas Fig. 4.3

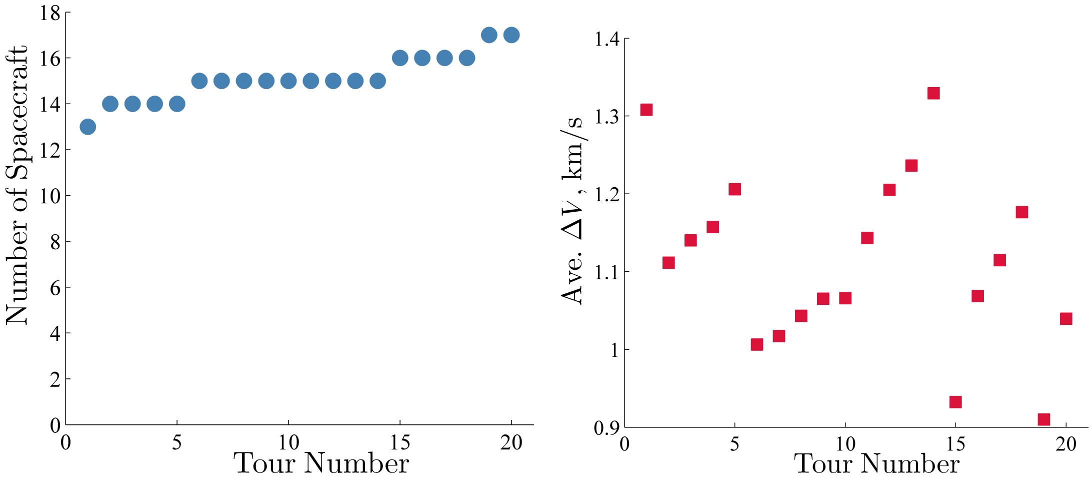

(a) (b)

Figure 4.1.. “Ant” performance at last generation of ACO tour generation for 760 km altitude SL-8 rocket bodies.

illustrates the clustering in the orbit planes for the encounter sequences. Note that average phases and altitudes are not displayed as the plane change dominates the ΔV rendezvous cost for these upper stages. Two particular spacecraft, numbers 5 and 6 in the figures, encounter 4 and 5 debris objects in two distinct RAAN regions, 17° and 262°, respectively. Note that neither chaser reaches the propellant cap of 2 km/s or the de-orbit package capacity of 8. Yet, these two sequences present the best options for short-term, chemical-enabled mitigation of the selected objects; other mission architectures could increase the performance of the chaser spacecraft by incorporating more efficient propulsion systems, by exploiting long-term drifts due to spherical harmonics, or incorporating resupply depots for the chaser spacecraft.

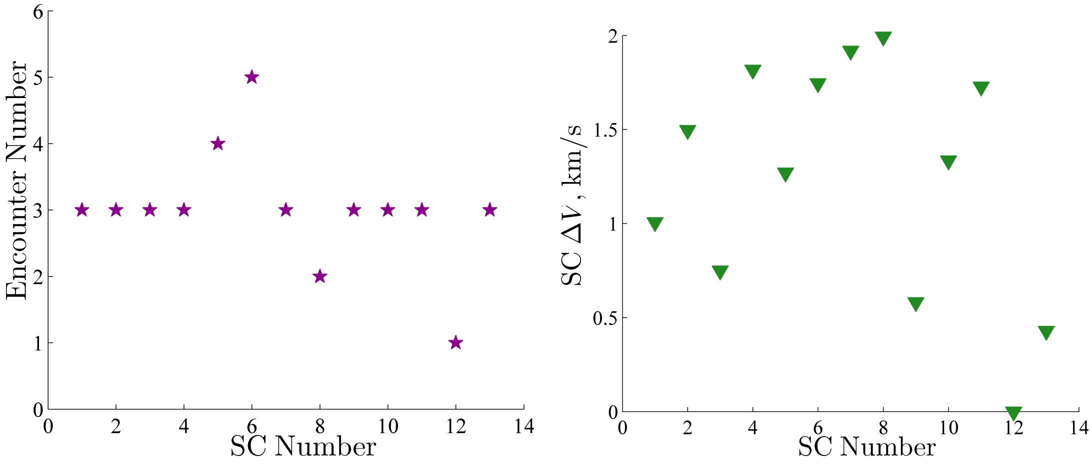

(a) (b)

Figure 4.2.. Number of encountered debris objects and ΔV expenditure for each chaser spacecraft along the best found tour of 760 km family.

4.1.1.2 Family 2 - 970 km altitude

The ACO heuristic selection strategy is applied to the mitigation of the 114 upper stages in the 970 km altitude regime, where the best constructed tour, from the 98^{th} generation, requires 26 chaser spacecraft for full removal of the targets. As before,

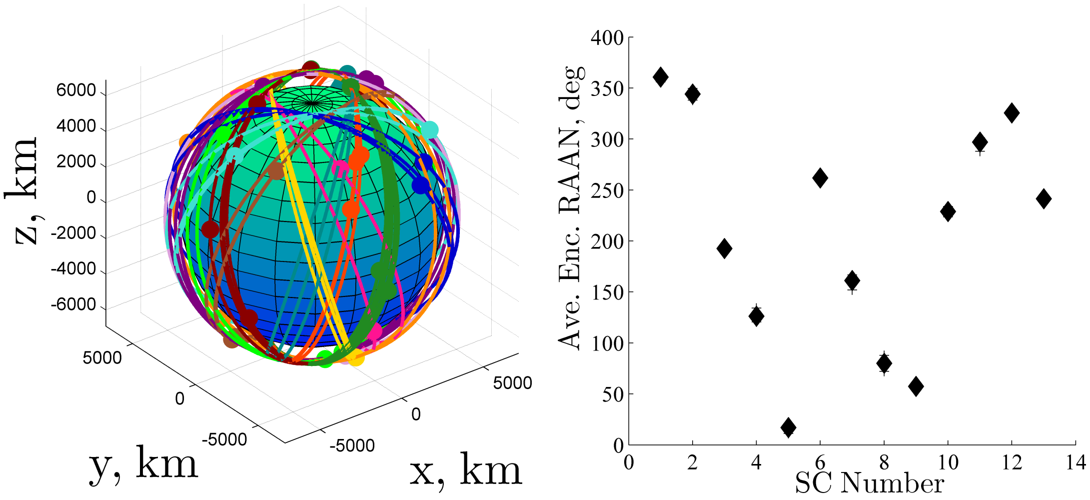

(a) (b)

Figure 4.3.. Orbits and mean RAAN of encountered debris objects for each chaser spacecraft along the best found tour of 760 km family. Color of orbit indicates mitigation by different chaser spacecraft. Diamonds are average RAAN across all encounters while crosses indicate specific RAAN values.

this number of spacecraft is currently not realizable, however Figs. 4.4 and 4.5 reveal several possibilities for high-return mitigation progressions. Two sequences exhaust all de-orbit packages on their respective carrier spacecraft, while nearly half of the followed routes actually encounter 5 or more debris objects. Furthermore, most of the tour sequences expend more that three-quarters of the chaser propellant reserves, indicating that a moderate increase in propulsive capability could significantly reduce the number of spacecraft required. Likewise, mitigation of this target grouping, in particular, may benefit heavily from the use of refueling stations or other home-base architectures.

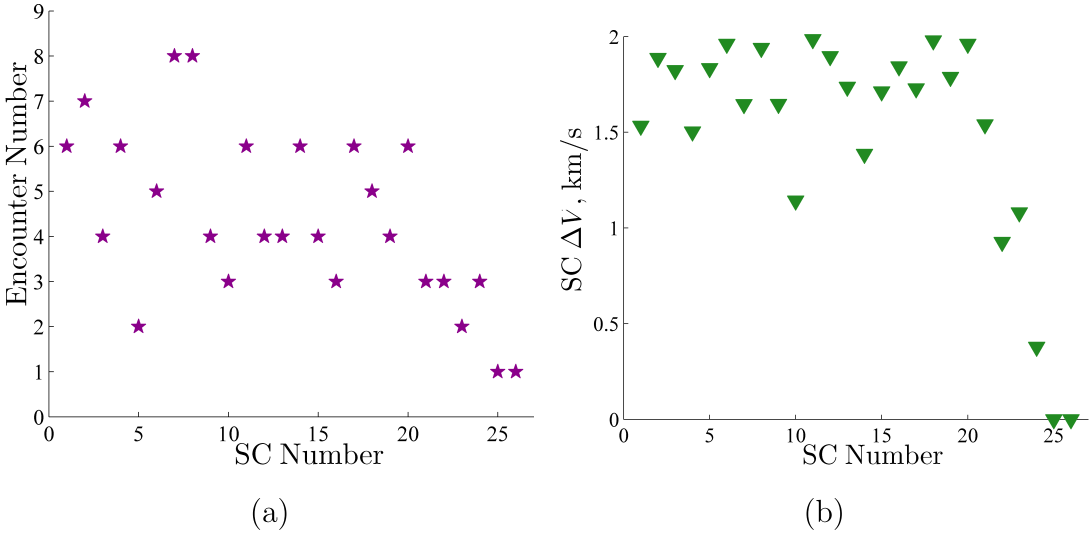

(a) (b)

Figure 4.4.. Number of encountered debris objects and ΔV expenditure for each chaser spacecraft along the best found tour of 970 km family.

4.1.1.3 Family 3 - 1570 km altitude

The 29 target objects at the 1570 km altitude are examined for potential mitigation tours. The best tour emerged from the ACO procedure in the 52nd generation and requires 13 chaser spacecraft for complete mitigation. Similar to the previous examples, Figs. 4.6 and 4.7 reveal the best potential for high-return encounter sequences.

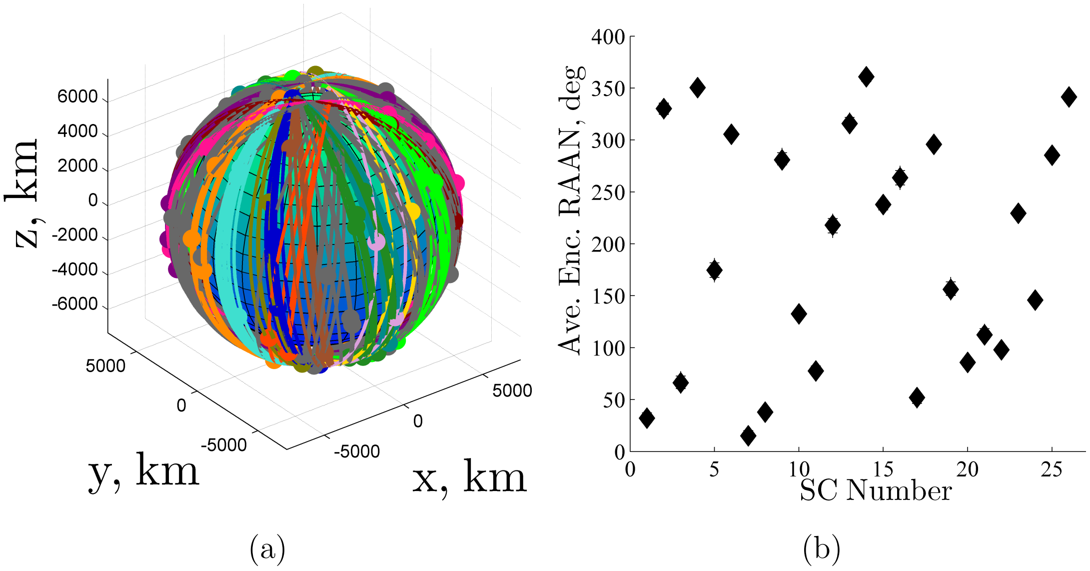

Figure 4.5.. Orbits and mean RAAN of encountered debris objects for each chaser spacecraft along the best found tour of 970 km family. Color of orbit indicates mitigation by different chaser spacecraft, up to the 15^{th} chaser. All subsequent encounters are plotted in grey. Diamonds are average RAAN across all encounters while crosses indicate specific RAAN values.

As in the mitigation tours for the first target family, two spacecraft encounter 5 and 4 debris objects, respectively, in two distinct RAAN regions, centered on 341° and 47°. Other than these two moderate encounter counts, all other potential spacecraft progressions in this region encounter a maximum of 2 upper stages, indicating a critical need to incorporate either long-term relative RAAN drift or a similar enabling architecture for the full depletion of this debris reservoir.

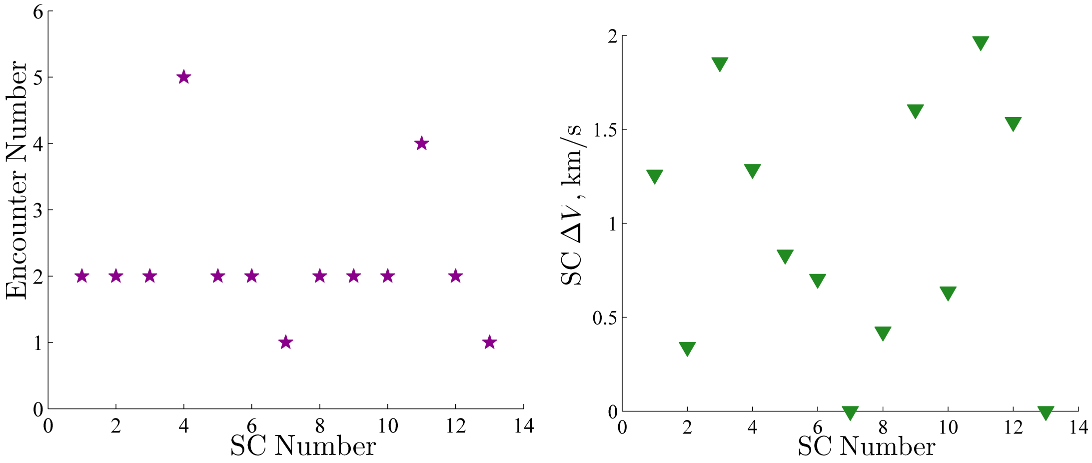

(a) (b)

Figure 4.6.. Number of encountered debris objects and ΔV expenditure for each chaser spacecraft along the best found tour of 1570 km family.

4.1.1.4 Combined families 1 and 3

Two of the SL-8 rocket body groups, specifically those at 760 km and 1570 km altitudes, reside in orbits with nearly identical inclinations of 74°, reducing the plane change necessary for rendezvous. Accordingly, transfer costs between these target debris objects may be achievable using chemical propulsion systems, even with the significant altitude change required to transfer between the debris groups. Therefore, a search for mitigation sequences of these combined debris object sets is performed via the ACO algorithm. The best tour, constructed in the 44^{th} generation, removes

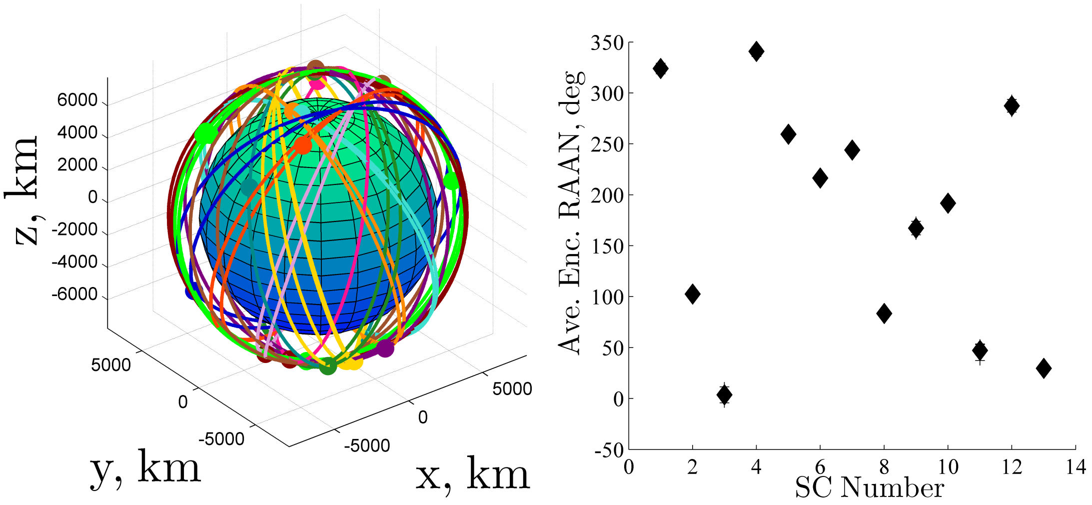

(a) (b)

Figure 4.7.. Orbits and mean RAAN of encountered debris objects for each chaser spacecraft along the best found tour of 1570 km family. Color of orbit indicates mitigation by different chaser spacecraft. Diamonds are average RAAN across all encounters while crosses indicate specific RAAN values.

all 68 rocket bodies using 22 chaser vehicles, with the performance of individual spacecraft displayed in Figs. 4.8 and 4.9. Recall that 26 total spacecraft are required for complete removal of the two groups when targeted separately. Note that, in general, the chaser spacecraft readily switch between altitudes and no consistent grouping in phase is exhibited. On the other hand, the RAAN of the encountered objects remains tightly grouped for each individual spacecraft, indicating that the plane change cost dominates over other components of the rendezvous. Seven chaser spacecraft encounter 4 or more empty upper stages, though there is no discernable clustering in the average operating RAAN or altitude of these specific vehicles.

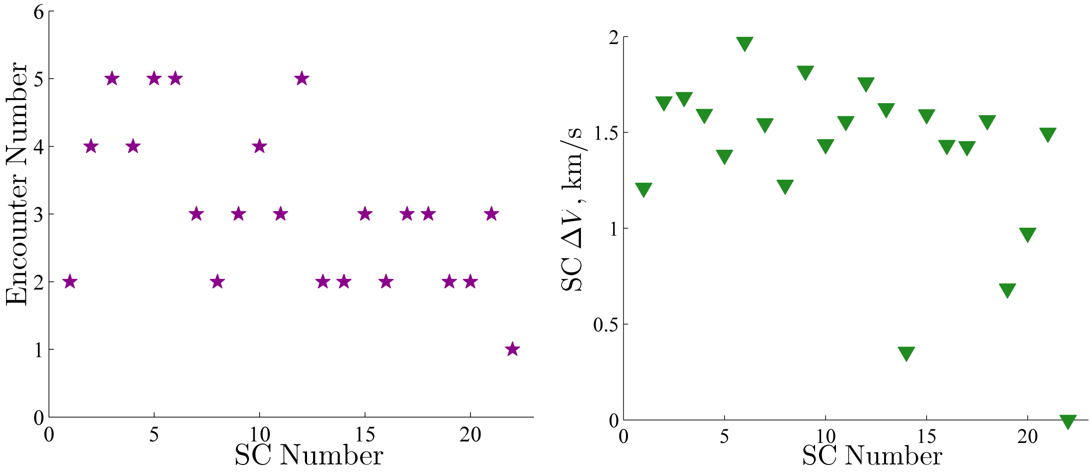

(a)

(b)

Figure 4.8.. Number of encountered debris objects and ΔV expenditure for each chaser spacecraft along the best found tour of combined 760 km and 1570 km altitude families of SL-8 upper stages.

4.1.2 Small debris fragments

The complete removal of the fragments emanating from the Iridium-Kosmos collision and the Fengyun 1-C anti-satellite test is assessed using the ant colony heuristic. Recall that the ACO algorithm, in addition to creating routes for individual chaser

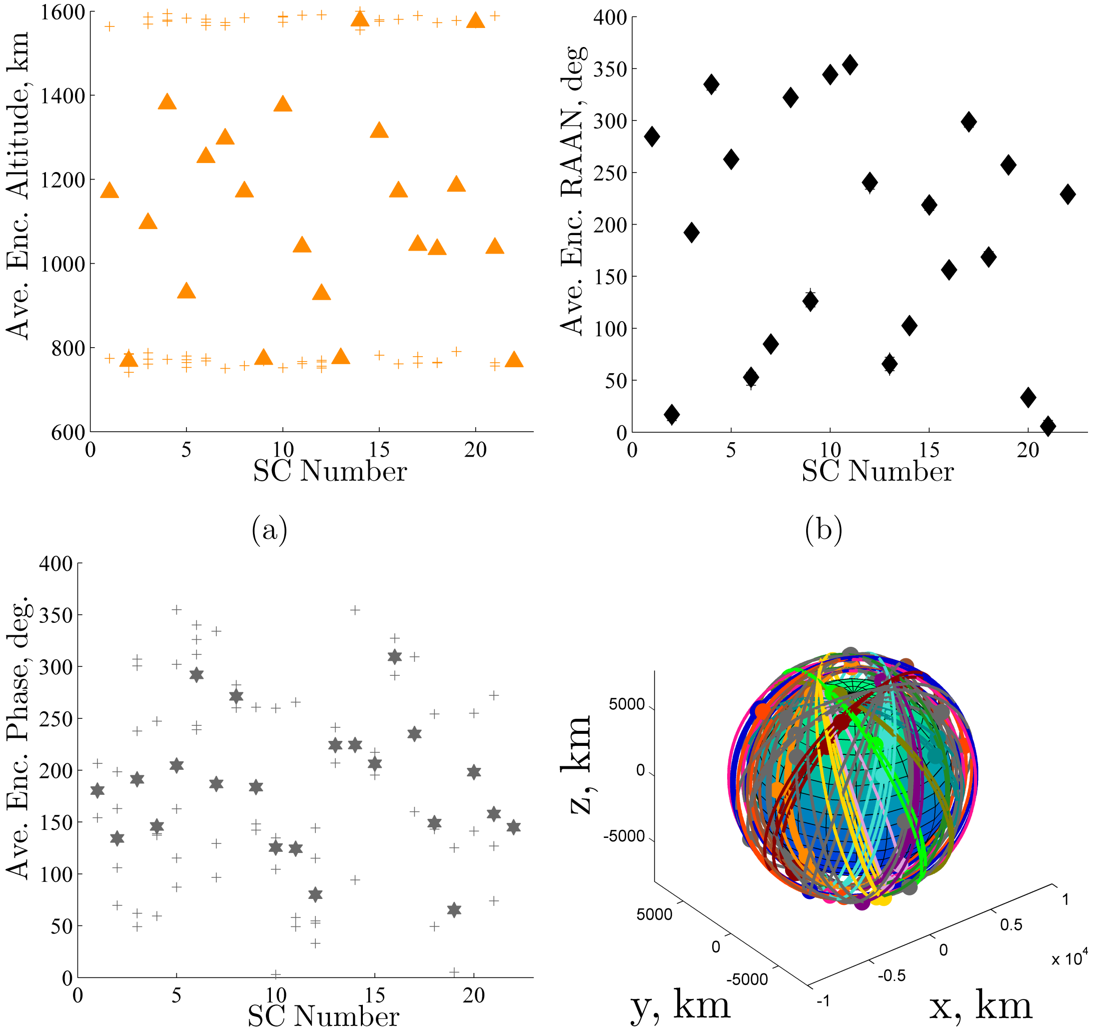

(a) (b)

(c) (d)

Figure 4.9.. Orbits and orbital elements of encountered debris objects for each chaser spacecraft along the best found tour of combined 760 km and 1570 km altitude families. Color of orbit indicates mitigation by different chaser spacecraft. Triangles, diamonds, and hexagrams are average altitude, RAAN, and phase, respectively, across all encounters while crosses indicate specific orbital element values of encountered objects.

spacecraft, provides the total number of spacecraft that are necessary to mitigate all the debris objects in a given family. A high-efficiency, low-thrust electrical propulsion system enables the chaser spacecraft to transfer from the orbit of one debris to another. While such a mission architecture necessarily entails spacecraft operation over multiple years, the simplified rendezvous cost analysis omits any long-term natural effects such as secular drifts in the orbital line of nodes. The parameters relevant to the mitigation of the small debris fragments are detailed in Table 4.2. The current orbits of the fragments are extracted from the NORAD Two-Line Element (TLE) set dated April 24, 2014, however some objects originating from the fragmentation events are omitted from this repository due to limitations on tracking capability. Thus, the debris groups targeted in this analysis represent only a fraction of the total population of the Iridium 33, Kosmos-2251, and Fengyun 1-C fragments currently in orbit.

Table 4.2. Spacecraft, tour, and ACO parameter values, common to all runs targeting fragmented debris objects.

Quantity	**Value**
Propellant capacity of chaser spacecraft (ΔV_{cap}), km/s	3.4
Maximum number of fragments (p_{cap})	100
Phasing revolution number, ($n = m$)	30
Number of generations (N_g)	100
Number of ants (N_a)	20
Link quality weight in link probability (β)	1
Pheromone decay rate (ρ)	0.05
Pheromone lower threshold (ρ_L)	10^{-6}
Base exploration probability (γ_{ss})	0.1
Spacecraft number scaling factor (C_{sc})	100

4.1.2.1 Iridium 33 fragments

The TLE is filtered for low-eccentricity (that is, $e < 0.025$), high-altitude ($a > 700$ km) fragments originating from the Iridium 33 communications satellite. The resulting 126 fragments are then set as the targets for the ant colony heuristic. The performance of the individual ants is examined in Fig. 4.10, where the required number of spacecraft for full removal of the target grouping as well as the average propellant per chaser are plotted for the last generation of the ACO run. As before, the "Tour Number" is the "ant" number. As with the mitigation tours of the SL-8 rocket bodies, there is an inverse relationship between the average ΔV expended per ant and the required number of chasers. Similar trends are observed for the other fragmented debris objects. Note that, generally speaking, the tours of the debris fragments enabled by a low-thrust system require fewer resets and, consequently, fewer chaser vehicles than the best performing tour of the 114 SL-8 rocket bodies at 970 km altitude. This is attributable, in part, to the clustering in orbital plane of the Iridium fragments. However, the higher efficiency of electrical thrusters over chemical engines also plays a significant role, even with the higher plane change costs of low-thrust propulsion.

The best mitigation tour, from the 87^{th} generation of the ACO scheme, requires 18 spacecraft for complete mitigation of all fragments from the Iridium 33 satellite. As before, Figs. 4.11 and 4.12 reveal beneficial encounter sequences. Five servicer spacecraft encounter and mitigate more than 10 debris objects while nearly half of the required vehicles approach the maximum propulsive capability of 3.4 km/s ΔV. Examination of the orbital elements of the encountered fragments for each of the chaser spacecraft reveals distinct clustering in RAAN with comparatively larger spreads in the object altitude and phase. This close clustering indicates that the plane change dominates the propellant cost of the object-to-object transfer. Accordingly, rendezvous schemes that exploit the relative nodal drift of inclined orbits under the influence of zonal harmonics are of great interest to improve the operational efficiency of the individual spacecraft.

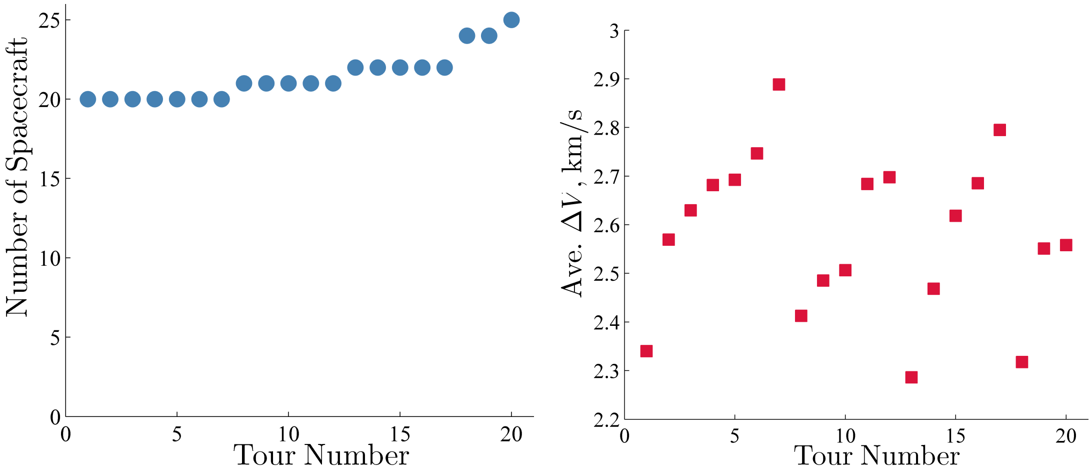

(a) (b)

Figure 4.10.. “Ant” performance at last generation of ACO tour generation for Iridium 33 fragments.

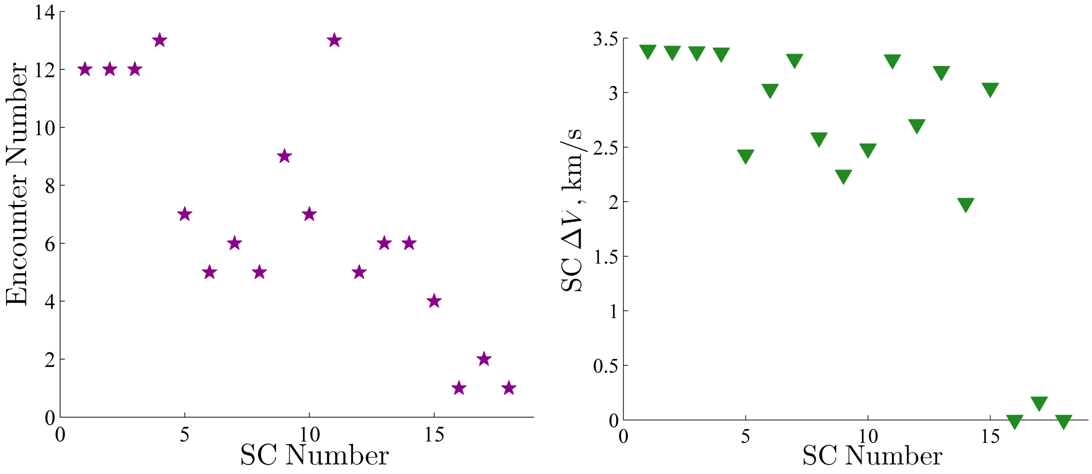

(a) (b)

Figure 4.11.. Number of encountered debris objects and ΔV expenditure for each chaser spacecraft along the best found tour of Iridium 33 fragments.

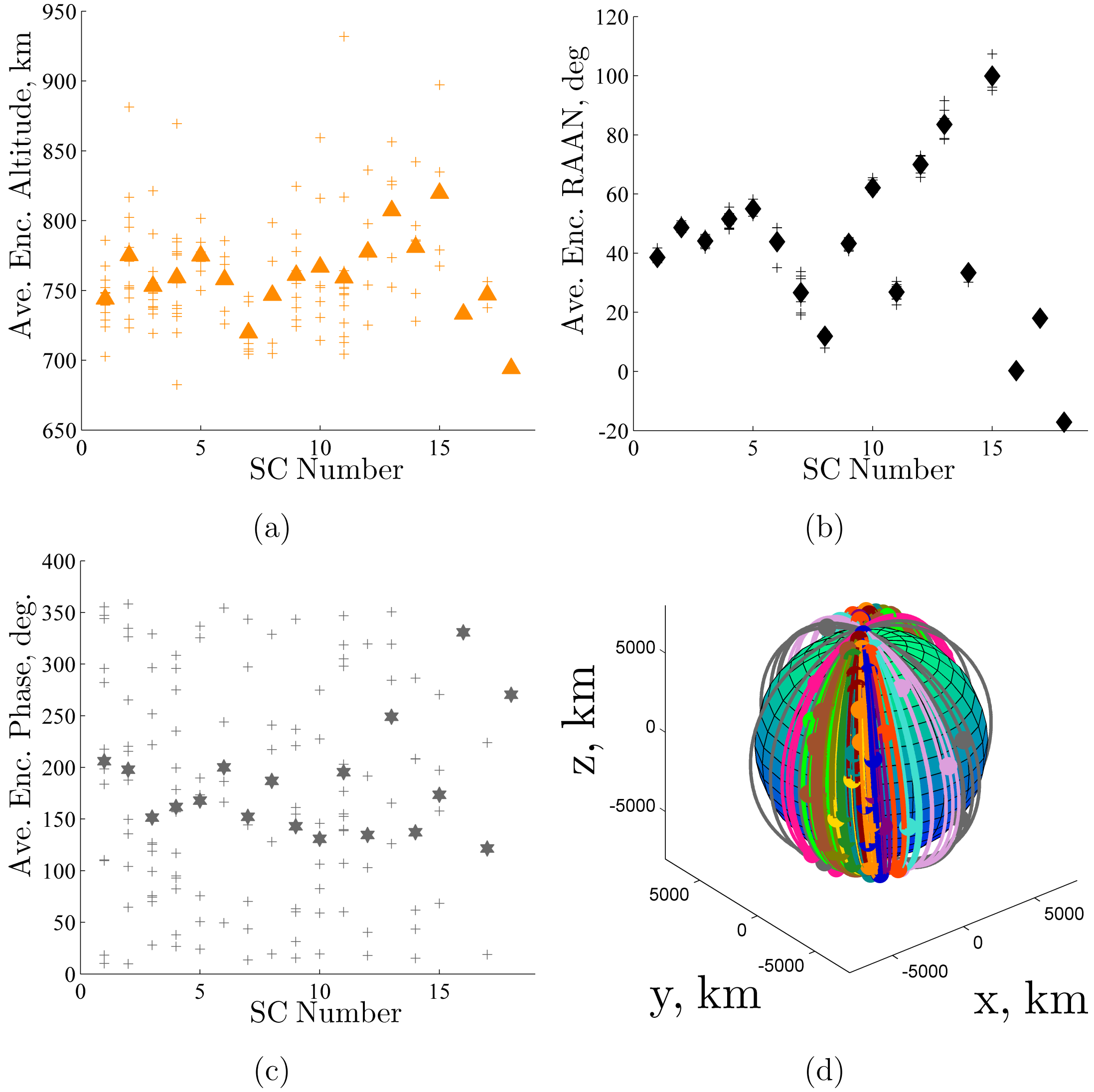

(a)

(b)

(c)

(d)

Figure 4.12.. Orbits and orbital elements of encountered debris objects for each chaser spacecraft along the best found tour of Iridium 33 fragments. Color of orbit indicates mitigation by different chaser spacecraft. Triangles, diamonds, and hexagrams are average altitude, RAAN, and phase, respectively, across all encounters while crosses indicate specific orbital element values.

4.1.2.2 Kosmos-2251 fragments

Encounter sequences are generated for the 270 nearly circular, high-altitude Kosmos-2251 fragments from the satellite catalog. The best mitigation tour emerges from the 54^{th} generation of the ACO scheme and requires 42 spacecraft for the removal of all fragments. High-value routes followed by specific chaser spacecraft are displayed in Figs. 4.13 and 4.14. As with the Iridium 33 fragments, five servicer spacecraft encounter and mitigate 10 or more debris objects. However, a larger proportion, nearly three-quarters, of the required vehicles approach the maximum propulsive capability of 3.4 km/s ΔV. As before, the RAAN of the encountered orbits are tightly grouped for each individual vehicle whereas the altitude and phase exhibit wide dispersions.

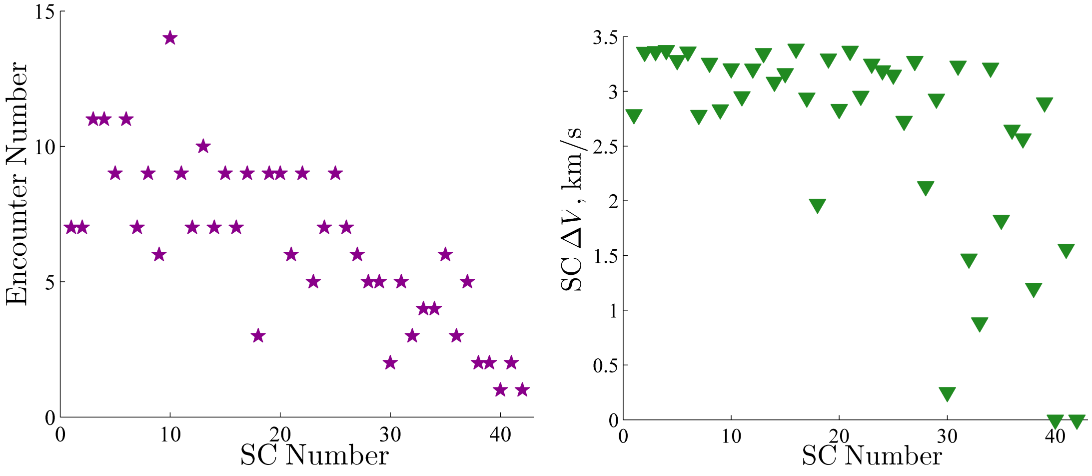

(a) (b)

Figure 4.13.. Number of encountered debris objects and ΔV expenditure for each chaser spacecraft along the best found tour of Kosmos-2251 fragments.

4.1.2.3 Fengyun 1-C fragments

The ant colony heuristic is applied to the removal of the 970 most recently tracked fragments from the Fengyun 1-C anti-satellite test.The best mitigation tour arises

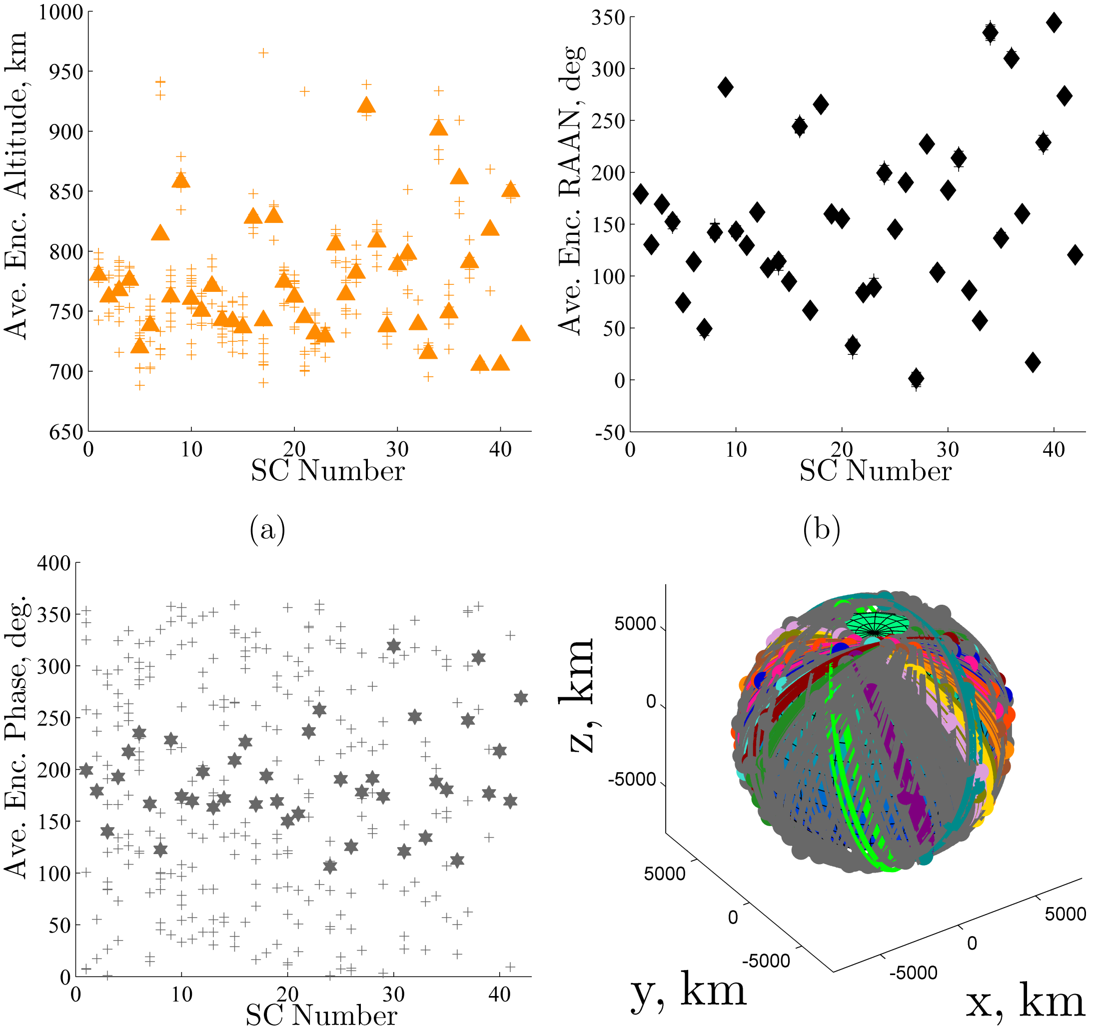

(a) (b)

(c) (d)

Figure 4.14.. Orbits and orbital elements of encountered debris objects for each chaser spacecraft along the best found tour of Kosmos-2251 fragments. Color of orbit indicates mitigation by different chaser spacecraft. Triangles, diamonds, and hexagrams are average altitude, RAAN, and phase, respectively, across all encounters while crosses indicate specific orbital element values.

from the 40^{th} generation of the ACO scheme and requires 97 spacecraft for complete mitigation of all targets. While this is an impractically large number of required spacecraft, certain vehicles follow high-value trajectories, as displayed in Figs. 4.15 and 4.16. Three chasers encounter and mitigate 15 or fragments while nearly all of the vehicles consume the maximum propulsive capability of 3.4 km/s ΔV. As with the previous scenarios targeting medium-sized debris fragments, phase and altitude considerations do not restrict target selection. However, the plane change continues to dominate the transfer cost, indicating a critical need for more efficient rendezvous schemes.

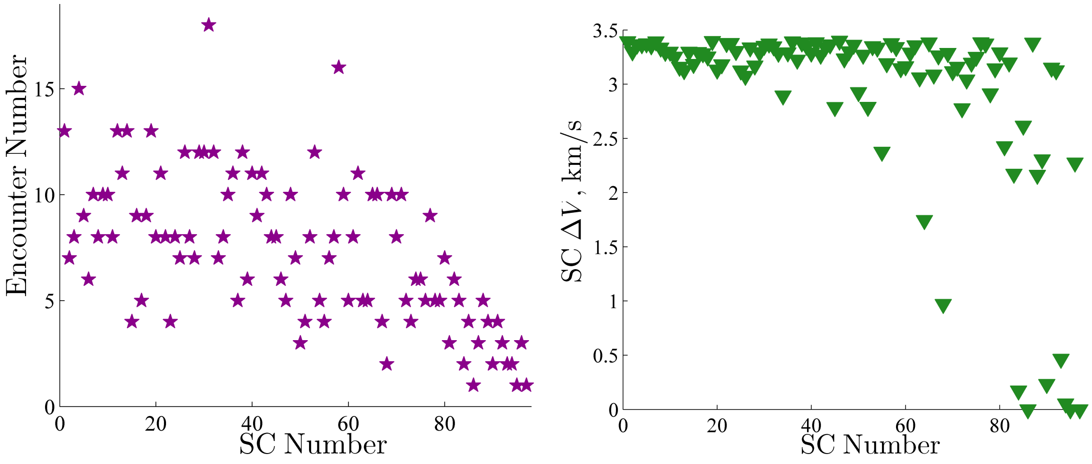

(a) (b)

Figure 4.15.. Number of encountered debris objects and ΔV expenditure for each chaser spacecraft along the best found tour of Fengyun 1-C fragments.

4.2 Flight operations for multiple spacecraft coordinated with auctions

While the ACO search algorithm reliably produces high-value target sequences, the auction coordination method readily re-routes chaser spacecraft to address contingencies such as the detection of an imminent conjunction with a high probability

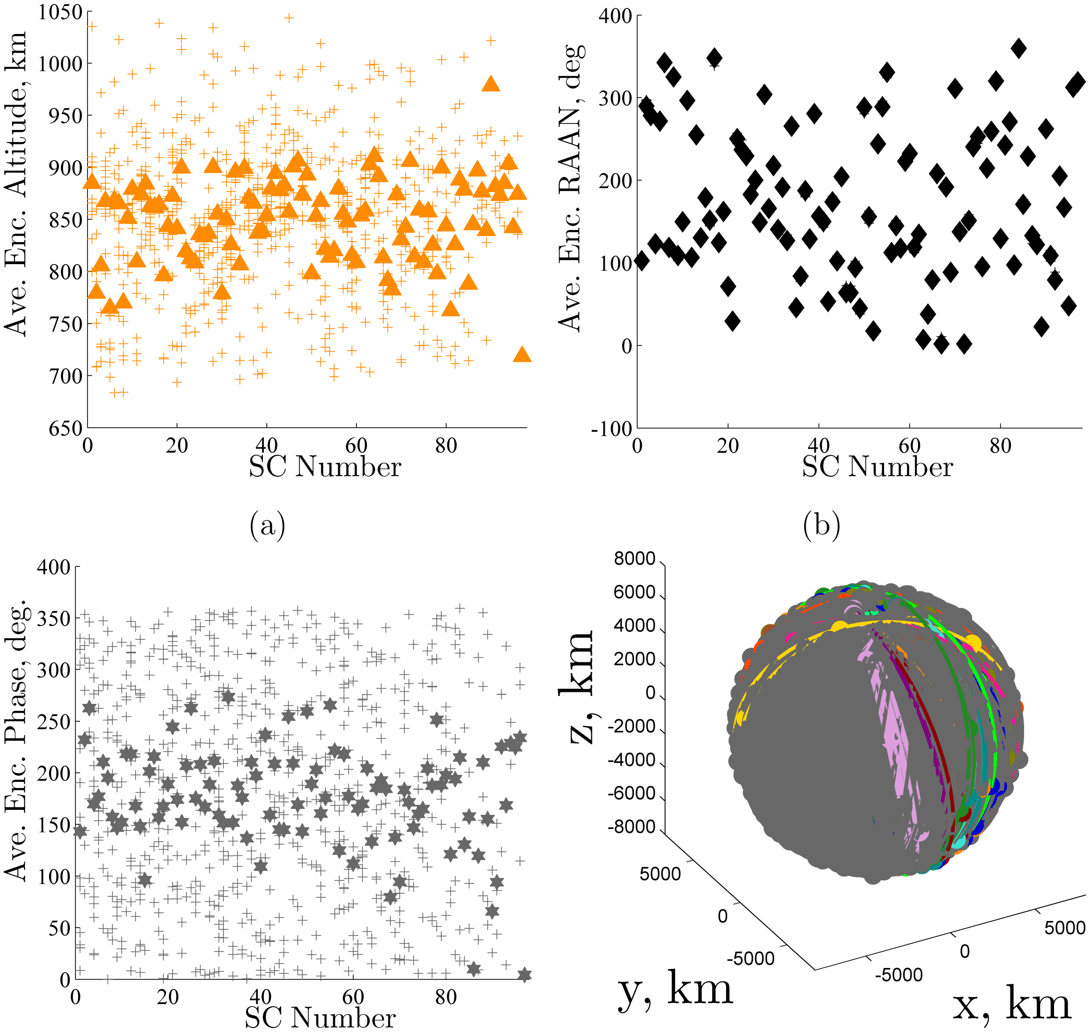

(a) (b)

(c) (d)

Figure 4.16.. Orbits and orbital elements of encountered debris objects for each chaser spacecraft along the best found tour of Fengyun 1-C fragments. Color of orbit indicates mitigation by different chaser spacecraft. Triangles, diamonds, and hexagrams are average altitude, RAAN, and phase, respectively, across all encounters while crosses indicate specific orbital element values.

of physical collision. Two sample cases are considered for the auction process: (i) the mitigation of rocket bodies in the median altitude grouping at 970 km, and (ii) the removal of Iridium 33 fragments. Whereas the ACO algorithm typically requires a large fleet of chaser spacecraft for complete mitigation of the target objects, a more feasible set of 6 mitigation spacecraft is used in the auction algorithm. While this number of chasers is still somewhat large, the resulting interactions between the six spacecraft highlight several of the advantages of the auction and bidding process. For the auction runs, the initial targets of the highest performing chaser spacecraft from the previously conducted ACO searches are also specified as the initial target objects of the bidding spacecraft. The subsequent path of the chaser spacecraft is determined solely by the auction and bidding process. For each test case, two auction scenarios are considered: (i) one incorporating only the propellant and mitigation capability margins of the chaser spacecraft as well as (ii) one case that additionally includes the current debris hazard level. In both cases, the appropriate weighting factors M, R, and W in Eq. (3.30) are set to either 1 or 0 depending on the case. At the initiation of each round of bidding, the threat level w_j posed by each debris object is randomly assigned from a uniform distribution on the interval [0.5, 1.5]. This changing target importance, selected as an extreme example, is formulated on purpose to illustrate the capability of the auction algorithm to address a highly dynamic problem space.

4.2.1 SL-8 rocket bodies - family 2

As a sample case, the auction process is applied to the mitigation of SL-8 rocket bodies in the median altitude grouping at 970 km. Recall that the chaser spacecraft targeting these upper stages use chemical propulsion and have a limited number of de-orbit packages to affix to the target debris objects. Information on the 6 selected baseline sequences is summarized in Table 4.3. Note that a few chaser spacecraft operate within relatively close orbital planes and, therefore, could potentially target the same debris objects during the course of operations.

Table 4.3. Baseline target sequences from ACO tour generation within target family of SL-8 upper stages at 970 km altitude.

Auction SC Num.	**ACO SC Num.**	**Num. Enc.**	**Average RAAN, deg.**	**ΔV, km/s**
1	7	8	16	1.646
2	8	8	38	1.940
3	2	7	330	1.887
4	1	6	32	1.533
5	4	6	350	1.503
6	11	6	78	1.985

The results of the auction algorithm are summarized in Table 4.4, along with a comparison of the equivalent results from the ACO sequence generation process. As is apparent, the auctioned sequences without incorporation of the threat level outperform the ACO progressions in terms of propellant consumption and the number of rocket body encounters. This improved outcome highlights two key considerations when using this particular implementation of ACO: i) while good target sets might be identified, the possibility always exists that individual spacecraft performance might be improved by adjusting its encounter sequence; and ii) even though the total required number of spacecraft are reliably predicted, individual targets may potentially be shifted from one chaser queue to another. In contrast, when the hazard level is incorporated into the bidding, the chaser spacecraft encounter fewer rocket bodies, but at a higher ΔV cost. However, those objects that are encountered are, on average, those with the highest removal priority. The performance of the individual chaser spacecraft is illustrated in Figs. 4.19 and 4.20. Two chaser spacecraft, in particular, auction spacecraft numbers 2 and 4, are the source of all the conflicting bids that must be resolved via the auction algorithm. These two chaser spacecraft operate largely within the same RAAN region - at nominal RAAN values of 38° and 32°, respectively - and often target the same debris objects, particularly when threat level is incorporated into the bid. The respective targets orbits are colored orange and blue in Figs. 4.19 and 4.20.

4.2.2 Debris fragments - Iridium 33

The auction and bidding scheme is implemented to coordinate the mitigation actions of six chaser spacecraft targeting fragments originating from the Iridium 33 satellite. The chaser spacecraft use high-efficiency electrical propulsion systems and possess the capability to encounter and mitigate a large number of debris fragments. As before, the bidding spacecraft are seeded from the six best performing vehicles from the ant colony heuristic, with characteristics highlighted in Table 4.5. For this

Table 4.4. Performance comparison of ACO and auction methods, 6 chaser spacecraft, target family of SL-8 upper stages at 970 km altitude.

	Solution method		
		Auction	**Auction**
Quantity	**ACO**	**M=R=1,W=0**	**M=R=W=1**
Total number of objects mitigated*	41	43	40
Average consumed ΔV, km/s	1.749	1.694	1.842
Average threat mitigated†	–	1.04	1.18
Number of conflicting bids	–	1	3

*From total of 114 orbiting debris objects.

†From uniform distribution over range [0.5,1.5].

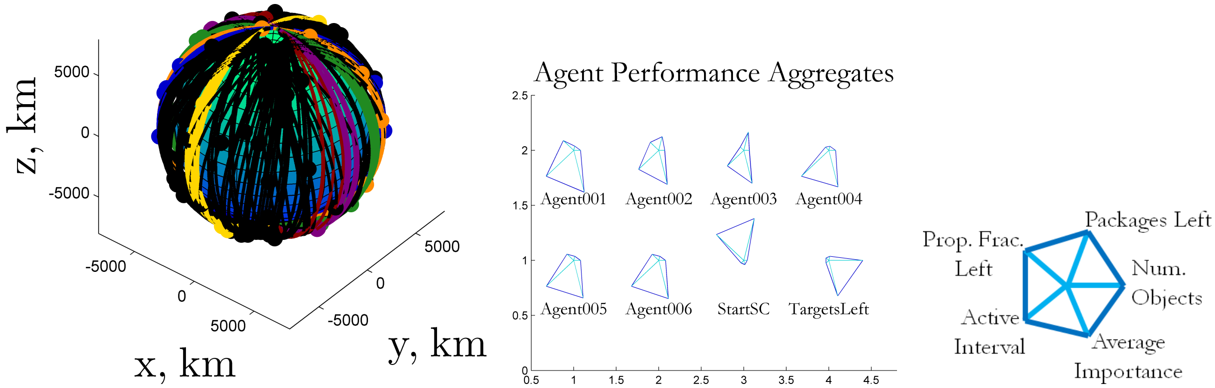

(a) Orbits

(b) Relative Performance

(c) Key

Figure 4.17.. Mitigation sequences and agent performance resulting from auction process for 970 km altitude SL-8 rocket bodies, threat omitted from bid (M=R=1,W=0). Glyphs indicate performance relative to other chaser spacecraft (“agents”) as well as a spacecraft before any mitigation actions and the remaining debris population.

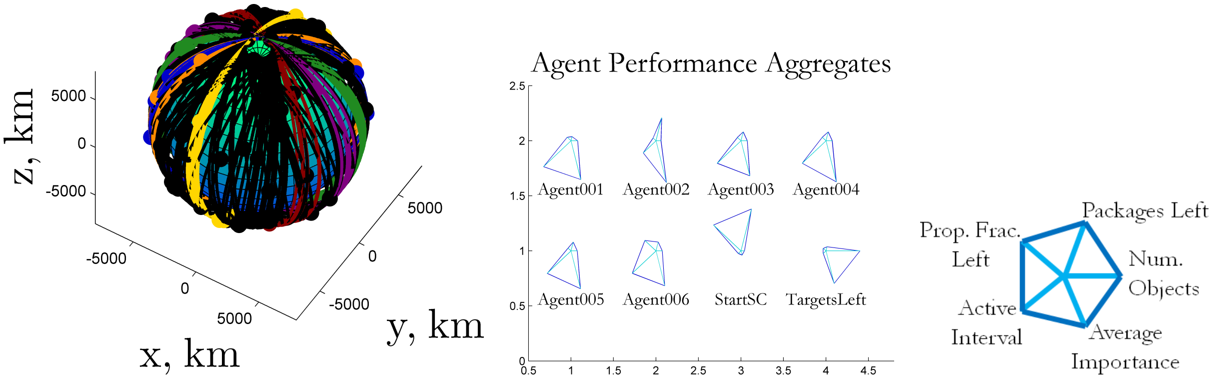

(a) Orbits (b) Relative Performance (c) Key

Figure 4.18.. Mitigation sequences and agent performance resulting from auction process for 970 km altitude SL-8 rocket bodies, threat included in bid (M=R=W=1). Glyphs indicate performance relative to other chaser spacecraft ("agents") as well as a spacecraft before any mitigation actions and the remaining debris population

mitigation scenario, the average operating planes of all chaser spacecraft are grouped within relatively close proximity, recalling the large concentration of target fragments from the Iridium 33 satellite.

Table 4.5. Baseline target sequences from ACO tour generation within target Iridium 33 fragments.

Auction SC Num.	**ACO SC Num.**	**Num. Enc.**	**Average RAAN, deg.**	**ΔV, km/s**
1	4	13	52	3.364
2	11	13	27	3.302
3	1	12	39	3.392
4	2	12	49	3.381
5	3	12	44	3.376
6	9	9	43	2.246

As before, the ACO sequences are compared to the equivalent results from the auction algorithm, as displayed in Table 4.6. The auctioned sequences that do not assess the threat level greatly outperform the ACO progressions in terms of the fragments encountered. However, due to the much larger number of encounters, the average consumed propellant per chaser vehicle is also higher. For the case when hazard level is reflected in the spacecraft bids, the bidding vehicles still encounter more fragments than the equivalent ACO sequences, with a lower ΔV cost as well. As with the previous auction incorporating relative threat levels, objects with higher removal priority are preferentially targeted. Furthermore, because the 6 chaser spacecraft operate in orbit planes that are relatively close to one another, a large number of conflicting target selections were resolved via the auction algorithm. The performance of the individual chaser spacecraft is illustrated in Figs. 4.19 and 4.20.

Table 4.6. Performance comparison of ACO and auction methods, 6 chaser spacecraft, target Iridium 33 fragments.

	Solution method		
		Auction	**Auction**
Quantity	**ACO**	**M=R=1,W=0**	**M=R=W=1**
Total number of objects mitigated[*]	71	93	76
Average consumed ΔV, km/s	3.177	3.252	3.149
Average threat mitigated[†]	–	0.995	1.258
Number of conflicting bids	–	23	31

[*] From total of 126 orbiting debris objects.

[†] From uniform distribution over range [0.5,1.5].

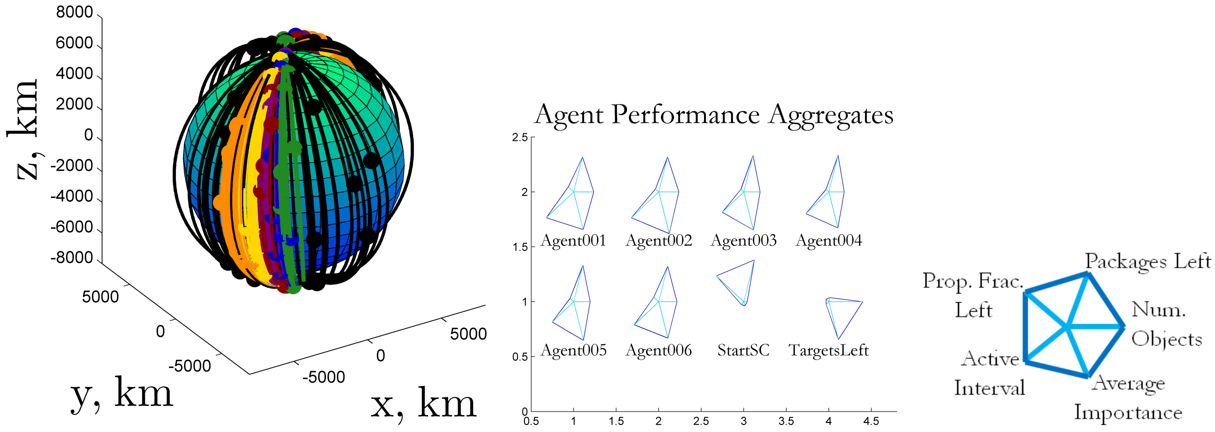

(a) Orbits (b) Relative Performance (c) Key

Figure 4.19.. Mitigation sequences and agent performance resulting from auction process for Iridium 33 fragments, threat omitted from bid (M=R=1,W=0). Glyphs indicate performance relative to other chaser spacecraft ("agents") as well as a spacecraft before any mitigation actions and the remaining debris population.

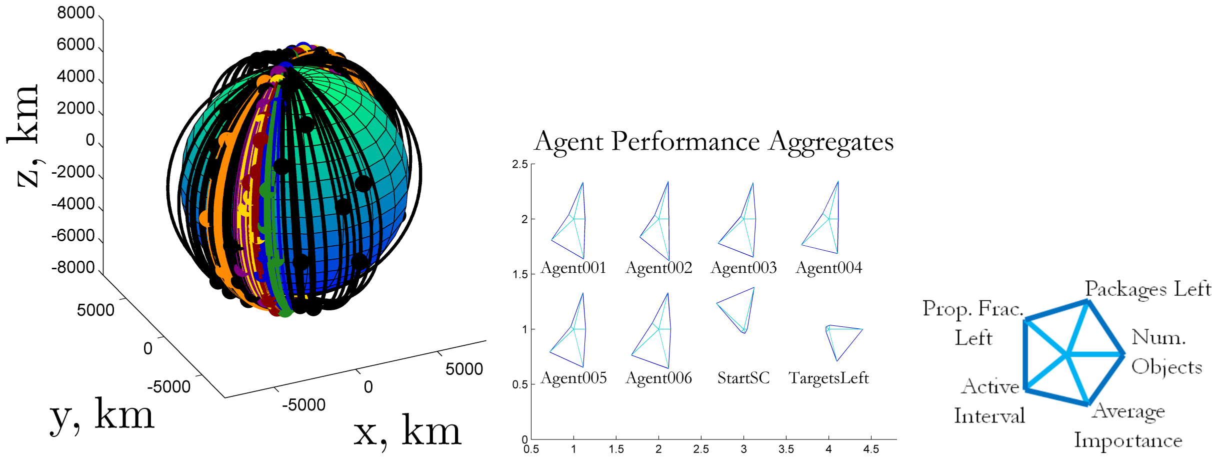

(a) Orbits (b) Relative Performance (c) Key

Figure 4.20.. Mitigation sequences and agent performance resulting from auction process for Iridium 33 fragments, threat including in bid (M=R=W=1). Glyphs indicate performance relative to other chaser spacecraft ("agents") as well as a spacecraft before any mitigation actions and the remaining debris population

4.3 Potential debris mitigation sequences - summary and conclusions

The general rendezvous trajectory desgin framework is adapted to the mitigation of debris in orbit about the Earth and a classification scheme for space debris mitigation architectures is proposed. While no one mitigation method is suitable for all types of debris objects, strategic selection of target objects and enabling technologies can yield a significant positive impact on the current size and future growth of the debris population. Specifically, the expended upper stages of the SL-8 launch system as well as the fragments originating from the Iridium-Kosmos collision and the Fengyun 1-C anti-satellite tests are preferentially targeted for removal. The natural dynamics of the chaser spacecraft are simplified to the two-body problem, for which analytical solutions to the equations of motion are available. Further, by selectively targeting objects residing in low eccentricity orbits, analytical approximations to the object-to-object transfer costs are developed for both chemical and electrical propulsion systems. These simplified costs, applicable to both chemical and electrical propulsion, are readily computed and allow for the rapid estimation of the performance of the debris removal vehicles. Since multiple spacecraft are needed to mitigate a significant portion of population of debris objects near to the Earth, trajectory design and reconfiguration schemes that directly address multiple operating vehicles are investigated. The ant colony heuristic search algorithm generates baseline encounter sequences for chaser spacecraft and reliably predicts the minimum number of spacecraft needed for complete removal of the target populations. Short-term mitigation of entire debris families using current technologies requires an infeasible number of chaser spacecraft, but a more moderate number of vehicles may still make significant reductions in the population of debris objects. While searches enabled by the ACO method produce high-value rendezvous chains, the highly dynamic nature of the near-Earth debris population may necessitate the adjustment of the flight paths of the mitigation spacecraft. Thus, an auction and bidding algorithm is instituted wherein the mitigation actions of multiple chaser vehicles, seeded by the best encounter sequences from the ACO results, are coordinated without any need for human-in-the-loop interaction. In general, the encounter sequences composed by the auction algorithm improve upon the equivalent tours arising from the ACO algorithm in both propellant consumption as well as number of debris object mitigated with the additional benefit that imminent threats posed by individual debris objects may be swiftly addressed upon detection. In fact, proper formulation of the auction process, combined with an appropriate update scheme for target priority, potentially retains both the positive features of the combined ant colony / auction approach.

4.3.1 Debris mitigation - recommendations for future investigation

Traditional technologies, assisted by novel search and coordination methods, can enable a nontrivial reduction in the current debris population near to the Earth. However, there are many potential avenues for further investigation and development. One critical capability is an improved scheme for the transfer between debris objects; a technique exploiting long-term differential drifts in orbital plane could supplement current chemical and electrical propulsion systems, whereas near-term technologies such as solar sails may obviate propellant requirements, and limitations, entirely. Furthermore, easing restrictions on the eccentricity of the target objects could enable a more complete survey of the available tour options. On the other hand, the automated tour construction scheme can be readily extended to incorporate the concept of resupply of individual chasers or the presence of a “home base” for the operating spacecraft.

5. END-TO-END ASTEROID SURVEY TOURS - SOLUTION APPROACH

The tour trajectory design framework for application to the construction of survey tours of the Sun-Jupiter L_4 Trojan asteroids is enabled by a low-thrust propulsion system. As with active debris mitigation, objectives are formulated that support the goal of exploration of the Trojan asteroids:

- a method to rapidly compute low-thrust transfers within the asteroid swarm;
- the direct incorporation of potential scientific merit in the construction of asteroid encounter sequences; and,
- an automated process to transition from simplified dynamical models to higher fidelity regimes.

Considering these objectives, the specific modifications to the process to encompass asteroid tours are illustrated in Fig. 5.1. The target asteroids are clustered in dynamically stable regions associated with specific equilibrium solutions available only in the restricted three-body problem. Therefore, the influence of multiple gravitating bodies is explicitly modeled at the lowest reasonable fidelity to ultimately deliver accurate results. The generation of end-to-end tour trajectories, that is, from Earth departure to termination of operations within the asteroid swarm, is decomposed into several distinct steps, each of which individually benefits from automation. First, locally optimal low-thrust arcs, comprised of the spacecraft departure path from one asteroid and the rendezvous with another asteroid, are independently generated using a hybrid optimization scheme. The hybrid optimization method blends (i) the low-dimensionality of indirect, calculus of variations approaches with (ii) the numerically robust computation of solutions by direct, gradient-based methods. Next, subsets

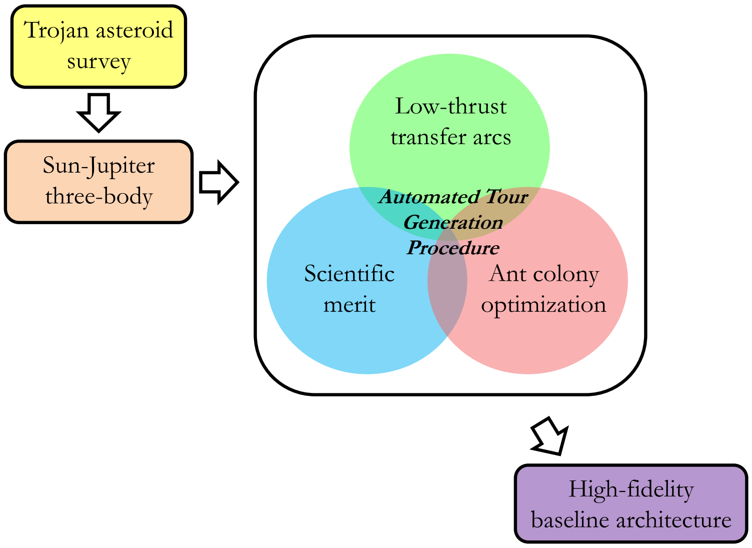

Figure 5.1.. Conceptual schematic of the tour design procedure, adapted for the construction of Trojan asteroid surveys

of these rendezvous arcs are sequenced with coast arcs in the vicinity of the target asteroids to produce a tour trajectory within the asteroid swarm. Tour generation within the asteroid swarm is accomplished via either (i) an enumerated tree search that generates all potential tour solutions for a pre-determined thrust arc duration or (ii) an ant colony optimization algorithm that has been extended for use in routing problems with continuous solution spaces and offers a trade-off between timing and propellant consumption. Furthermore, the ant colongy search scheme directly incorporates potential scientific value into the selection of target asteroids whereas the tree search approach enables the inclusion of scientific merit as a post-processing step. The resulting tours exploit natually advantageous departure and arrival conditions while simultaneously providing ample coast time in close proximity to the encountered asteroids. Sample outbound legs from the Earth to the asteroid swarm are then joined to the pre-determined asteroid sequences resulting in prospective end-to-end baseline trajectories. While the optimization of end-to-end trajectories is a non-trivial task with numerous solution approaches, the VSI engine model that is employed in this investigation enables a scheme wherein the full trajectory optimization is split into a series of individual thrust arc optimizations. This optimization approach of separating the spacecraft path into individual thrust arcs has been demonstrated to yield the overall optimal rendezvous trajectory. [75] The automated algorithm includes a variety of electrical power sources for the low-thrust propulsion system as well as criteria for the use of natural dynamical models of varying fidelity.

5.1 Mission concept and historical background

Asteroids located in all regions of the solar system are objects of past, present and proposed future missions. Such examples include NASA's Dawn mission to the Main Belt asteroids Vesta and Ceres [76], the Hayabusa [77] and OSIRIS-REx [78] sample return missions to Near-Earth Objects (NEOs), and the NASA Decadal study proposing a mission to the Sun-Jupiter Trojan asteroid swarm at a projected cost of less than $900M in fiscal year 2015 dollars. [79] Most recently, NASA's Asteroid Redirect Initiative is a high priority, i.e., the plan to retrieve a small near-Earth asteroid and return it to a stable orbit within the Earth-Moon system for further study. [80] Desjean [81] offers another high-level perspective on a potential mission to the Sun-Jupiter Trojan asteriods. Typical asteroid tour design and analysis investigations are automated searches to narrow the selection of candidate objects of interest [19] or the analyses produce tours effected by conventional chemical engines. [20] However, the inclusion of low-thrust propulsion technology into asteroid tours has emerged as a possibly enabling capability as well. [82, 83]

While a variety of optimal control approaches reliably produce feasible low-thrust trajectories, these techniques often include an *a priori* assumption for the form of the spacecraft trajectory or thrust control law, frequently employ patched conic models, and/or are typically limited to brief fly-by encounters of the objects of interest. In contrast, low-thrust trajectories implemented with a VSI engine generally entail optimal engine operation time histories and, accordingly, no assumed form for the thrust profile. [84] Therefore, a variable specific impulse (VSI) engine that varies the optimal thrust magnitude is selected to simplify the construction of rendezvous solutions. [85] As a consequence, no coasting arcs are required for rendezvous and the initial generation of optimal trajectories is less restrictive in terms of thrust duration. Examples of VSI engines include the Variable Specific Impulse Magnetoplasma Rocket (VASIMR) currently under development by the Ad Astra Rocket Company [86] and the Electron and Ion Cyclotron Resonance (EICR) Plasma Propulsion Systems at Kyushu University in Japan. [87] Optimal control laws applied to the operation of VSI thrusters are typically based upon Lawden's Primer Vector Theory [88] and Pontryagin's Minimum/Maximum Principle. [89] However, most VSI studies, such as those completed by Volle [90], Senent et al., [91] and Stuart et al., [92] focus on the generation of point solutions for individual transfer or rendezvous arcs. More recent work by Stuart et al. places the operation of a VSI engine within the context of end-to-end (flight initiation to termination) rendezvous tour trajectory generation. [75, 93–95]

Optimization strategies are generally decomposed into two types: (i) indirect methods that apply the calculus of variations, [96, 97] and (ii) direct methods that are either gradient-based, e.g., sequential quadratic programming, [98] or hueristic, such as the genetic algorithm. [99] However, recent advances in trajectory design approaches have combined these disparate optimization algorithms into so-called "hybrid" optimization schemes that retain the key advantages of the base algorithms while alleviating the respective weaknesses. For example, Gao and Kluever [100] as well as Stuart and Howell [94] blend low-dimensioned indirect methods, supplying a thrust control law, with more robust direct optimization of a cost function. Much work has also been completed to hybridize global heuristic methods with gradient-based schemes. [101–103]

Hybrid systems theory is the study of dynamical systems incorporating both discrete and continuous variables. [7] Typical applications within the discipline of astrodynamics include the combination of two or more propulsion systems, e.g., low-thrust engines and solar sails, [104, 105] or switching between dynamical regimes. [106] Of particular interest, however, are hybrid propulsion systems combining conventional high-impulse thrusters with low-thrust engines, such as those investigated by Edelbaum [107], Johnson, [108] and others. [109–111]

5.2 Natural motion: Sun-Jupiter restricted three-body problem

A Keplerian model is not always sufficient to adequately describe the motion of a spacecraft or celestial object, even when perturbative effects can be analytically expressed, and the gravitational influence of multiple bodies must be directly modeled. In compensation for modeling and computational difficulties, these multi-body systems afford solutions that emerge only when more than one gravity field is present. For instance, the motion of the Trojan asteroids leading and trailing Jupiter in its motion around the Sun are clustered in the vicinity of the L_4 and L_5 libration points, pseudo-equilibrium solutions not available in two-body models. Given the many successful results from applications of the two-body problem, the next step is an expansion of the trajectory options by exploring the motion of three bodies under their mutual gravitational attraction. In 1967, Victor Szebehely authored an in-depth analysis of the Three-Body Problem (3BP) in his book, *Theory of Orbits* [112]. Much of the problem formulation here follows that in Szebehely.

The model for the general equation of motions (EOM), Eq. (2.3), is initially focused on three masses in the model, i.e., $N = 3$. So, reducing Eq. (2.3) to three particles and selecting the point P_3 as the body of interest results in

$$\ddot{\boldsymbol{r}}_3 = -G\frac{m_1}{d_{13}^3}\boldsymbol{d}_{13} - G\frac{m_2}{d_{23}^3}\boldsymbol{d}_{23} \tag{5.1}$$

where the mass m_3 has been factored from both sides of the equation. To solve this equation analytically requires knowledge of the motion of P_1 and P_2, and without a priori time histories for $\boldsymbol{r}_1$ and $\boldsymbol{r}_2$, the motion for all three bodies must be evaluated simultaneously. Such a complete set of vector differential equations represents 18 scalar first-order differential equations (DE). Thus, 18 integrals are required for a complete closed-form solution. However, only ten integrals of motion are known:

six from conservation of system linear momentum, three from conservation of system angular momentum, and one from conservation of system energy. Since an insufficient number of analytical constants are available, the three-body problem must, of necessity, be investigated primarily through numerical methods. But, a few simplifying assumptions produce much insight without the loss of significant fidelity.

The first simplifying assumption in the 3BP involves the mass of the third particle P_3; the mass of P_3, i.e. m_3, is assumed neglegible in comparison to the masses of the other two bodies, m_1 and m_2. Therefore, the motion of the massive points P_1 and P_2, generally termed the "primaries", are unaffected by the motion of P_3. Such an assumption reflects a wide variety of interesting systems. For example, P_3 might be a spacecraft while P_1 and P_2 are more massive bodies forming a two-body system (e.g., Sun/Earth/spacecraft or Jupiter/Io/spacecraft). Merely for convenience, it is further assumed that $m_1 > m_2$; then, P_1 is labeled the larger primary while P_2 denotes the primary of smaller mass. Since the motions of P_1 and P_2 no longer depend on P_3, they represent a two-body system with a known conic solution, as discussed in Section 3.2. For most systems of interest, this conic is closed and, for simplicity, can be approximated as circular. So, one additional simplification assumes P_1 and P_2 move in circular orbits around their common barycenter, B. This selection of a circular orbit, in constrast to an elliptical path for the primaries, is not necessary but reasonably represents many cases of interest. One notable representative example is a primary system comprised of the Sun and one of the planets. These simplifications reduce the general three-body problem to the Circular Restricted Three-Body Problem (CR3BP).

The differential equation in Eq. (5.1) specifies the motion of P_3 relative to an inertially fixed observer, but an inertially fixed view is not always the most appropriate for problem formulation or visualization. An inertial frame, I, is defined with the unit vectors $\hat{X}, \hat{Y}, \hat{Z}$ forming a right-hand coordinate system with origin at the barycenter of the primaries, B. For convenience, frame I is constructed such that the plane containing the conic motion of the primaries is spanned by the unit vectors $\hat{X}$ and

$\hat{Y}$. The unit vector $\hat{Z}$ is then directed along the orbital angular momentum vector of the primary orbit. A rotating frame, R, is defined relative to the inertial frame by a rotation through an angle θ about the $\hat{Z}$ axis; unit vectors $\hat{x}, \hat{y}, \hat{z}$ represent this coordinate frame, with $\hat{Z} \parallel \hat{z}$. The angle θ is constrained such that the unit vector $\hat{x}$ remains directed from P_1 to P_2 at all times. Therefore, a coordinate transformation from frame R to frame I has the form

$$\begin{Bmatrix} \hat{X} \\ \hat{Y} \\ \hat{Z} \end{Bmatrix} = \begin{bmatrix} \cos\theta & -\sin\theta & 0 \\ \sin\theta & \cos\theta & 0 \\ 0 & 0 & 1 \end{bmatrix} \begin{Bmatrix} \hat{x} \\ \hat{y} \\ \hat{z} \end{Bmatrix} \tag{5.2}$$

where the rotation matrix is labeled the Direction Cosine Matrix (DCM). Because the transformation from R to I consists of only a simple rotation about the common $\hat{z}, \hat{Z}$ axis, the XY-plane is the same as the xy-plane. Figure 5.2 supplies a schematic representing the system in the CR3BP, with the rotating and inertial frames as well as the paths of the primaries illustrated.

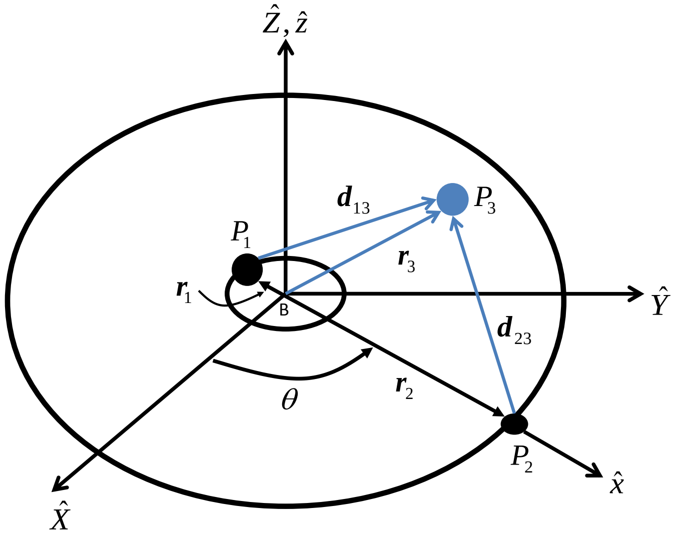

Figure 5.2.. Schematic representing the circular restricted three-body problem

With the previous simplifications, it is convenient to nondimensionalize the equations of motion in Eq. (5.1). The fundamental properties of length, mass, and time generate the characteristic quantities. To denote length, define

$$l^* = r_1 + r_2 \tag{5.3}$$

where $r_i = |\boldsymbol{r}_i|$, the magnitude of the position vector locating the primaries relative to B. Because the primaries move in closed circles, the quantities r_1, r_2, and l^* are constant. A second characteristic quantity involves mass, that is, the sum of the primary masses

$$m^* = m_1 + m_2 \tag{5.4}$$

where m_1 and m_2 are the dimensional masses of the larger and smaller primaries, respectively. Finally, the characteristic time, t^*, is constructed such that the value of the nondimensional universal gravitational constant, G, becomes unity, thus

$$t^* = \sqrt{\frac{(r_1 + r_2)^3}{G(m_1 + m_2)}} = \sqrt{\frac{l^{*3}}{Gm^*}}. \tag{5.5}$$

Given the characteristic quanties, some useful nondimensional parameters are then defined, i.e.

$$\mu = \frac{m_2}{m^*} = \frac{r_1}{l^*} \tag{5.6}$$

$$1 - \mu = \frac{m_1}{m^*} = \frac{r_2}{l^*} \tag{5.7}$$

$$\boldsymbol{r} = \frac{\boldsymbol{r}_3}{l^*} \tag{5.8}$$

$$\boldsymbol{d}_i = \frac{\boldsymbol{d}_{i3}}{l^*} \tag{5.9}$$

where Eq. (5.6) yields the nondimensional distance of the larger primary with respect to the system barycenter and Eq. (5.7) defines the nondimensional distance of P_2 from the barycenter. The characteristic quantities in the Sun-Jupiter system, used to model the behavior of the Trojan asteroids, appear in Table 5.1. Note that the primary mass ratio μ for the Sun-Jupiter system is representative of many other natural systems (e.g., $\mu = 0.0002366$ for the Saturn-Titan system).

Table 5.1. Trojan asteroid and Sun-Jupiter system parameter values.

Quantity	**Value**
Solar mass (M_S), kg	1.9891×10^{30}
Jupiter mass (M_J), kg	1.8986×10^{27}
Gravitational Constant (G), $\frac{\text{km}^3}{\text{kg}\cdot\text{sec}^2}$	6.67428×10^{-20}
Mass parameter (μ_{SJ})	9.53816×10^{-4}
Sun-Jupiter distance (l^*), km	7.78412×10^{8}
Characteristic Time (t^*), sec	5.95911×10^{7}
Characteristic Time (t_d^*), days	6.89712×10^{2}

The equations of motion for P_3 are then reformulated within the context of a rotating reference frame. Because the characteristic time t^* is also the inverse of the mean motion, n, of the primaries in their respective orbits, the angle θ between the inertial frame and the rotating reference frame is simply the nondimensional time t, thus $\theta = nt = t$. The frame R is centered on the system barycenter, so the vector $\boldsymbol{r} = (x, y, z)^T$ is easily defined as the nondimensional displacement vector of particle P_3 from the system barycenter, represented in terms of the rotating coordinates. Therefore, the variables in $\boldsymbol{r}$ are displacements in the directions of the corresponding unit vectors $(\hat{x}, \hat{y}, \hat{z})$, i.e., $\boldsymbol{r} = x\hat{x} + y\hat{y} + z\hat{z}$. Then, the relative displacement vectors

$$\boldsymbol{d}_1 = \begin{Bmatrix} x+\mu \\ y \\ z \end{Bmatrix} \qquad \boldsymbol{d}_2 = \begin{Bmatrix} x+\mu-1 \\ y \\ z \end{Bmatrix} \tag{5.10}$$

reflect the distances of P_3 from the two primaries, with corresponding distances

$$d_1 = \sqrt{(x+\mu)^2 + y^2 + z^2} \tag{5.11}$$

$$d_2 = \sqrt{(x+\mu-1)^2 + y^2 + z^2} \tag{5.12}$$

in nondimensional units. Now, the six-dimensional state vector corresponding to the particle P_3, expressed in terms of the rotating reference frame is defined

$$\boldsymbol{x} = \begin{Bmatrix} \boldsymbol{r} \\ \boldsymbol{v} \end{Bmatrix} \tag{5.13}$$

where $\boldsymbol{r}$ has been previously defined. The three-element vector $\boldsymbol{v}$ is the velocity of body P_3 with respect to the barycenter, as viewed by an observer in R, so $\boldsymbol{v} = \dot{x}\hat{x} + \dot{y}\hat{y} + \dot{z}\hat{z}$. The equations of motion (EOM), derived by non-dimensionalizing Eq. (5.1), are then written in the form

$$\dot{\boldsymbol{x}} = \boldsymbol{f}(\boldsymbol{x}) = \begin{Bmatrix} \dot{\boldsymbol{r}} \\ \dot{\boldsymbol{v}} \end{Bmatrix} = \begin{Bmatrix} \boldsymbol{v} \\ \boldsymbol{f}_n(\boldsymbol{r}, \boldsymbol{v}) \end{Bmatrix} \tag{5.14}$$

where $\boldsymbol{f}_n$ represents the acceleration of the spacecraft. The scalar elements of $\boldsymbol{f}_n$, in terms of the rotating coordinates, that is

$$\boldsymbol{f_n} = \begin{Bmatrix} 2\dot{y} + x - \frac{(1-\mu)(x+\mu)}{d_1^3} - \frac{\mu(x+\mu-1)}{d_2^3} \\ -2\dot{x} + y - \frac{(1-\mu)y}{d_1^3} - \frac{\mu y}{d_2^3} \\ -\frac{(1-\mu)z}{d_1^3} - \frac{\mu z}{d_2^3}, \end{Bmatrix} \tag{5.15}$$

are relative to a rotating observer and, thus, include centrifugal and Coriolis terms in addition to the gravitational terms. The acceleration representing these natural dynamics is formulated in terms of a pseudo-potential function, that is

$$U^* = \frac{1-\mu}{d_1} + \frac{\mu}{d_2} + \frac{1}{2}(x^2 + y^2) \tag{5.16}$$

containing only position, not velocity, terms. Equation (5.15) can then be expressed

$$\boldsymbol{f_n} = \begin{Bmatrix} 2\dot{y} + \frac{\partial U^*}{\partial x} \\ -2\dot{x} + \frac{\partial U^*}{\partial y} \\ \frac{\partial U^*}{\partial z} \end{Bmatrix} \tag{5.17}$$

where the dynamical terms containing only position states have been replaced by partials of the psuedo-potential.

The pseudo-potential function is particularly useful. The function U^* supplies a succinct expression for an integral of motion, that is, the Jacobi Constant C. To determine an expression for Jacobi Constant, begin with expressions for the nondimensional kinetic energy

$$K = \frac{1}{2}(\dot{x}^2 - 2\dot{x}y + y^2 + \dot{y}^2 + 2x\dot{y} + x^2 + \dot{z}^2) \tag{5.18}$$

and the nondimensional gravitational potential energy

$$U = -\frac{1-\mu}{d_1} - \frac{\mu}{d_2} \tag{5.19}$$

corresponding to the particle P_3. Split the kinetic energy expression into separate terms such that

$$K = K_0 + K_1 + K_2 \tag{5.20a}$$

$$K_0 = \frac{1}{2}(x^2 + y^2) \tag{5.20b}$$

$$K_1 = x\dot{y} - \dot{x}y \tag{5.20c}$$

$$K_2 = \frac{1}{2}(\dot{x}^2 + \dot{y}^2 + \dot{z}^2). \tag{5.20d}$$

Since the potential energy in Eq. (5.19) includes no time derivatives, then, according to Lanczos [113], there exists an integral of motion

$$C_I = K_2 + U - K_0 = \frac{1}{2}(\dot{x}^2 + \dot{y}^2 + \dot{z}^2) - \frac{1-\mu}{d_1} - \frac{\mu}{d_2} - \frac{1}{2}(x^2 + y^2) \tag{5.21}$$

where C_I is a constant of integration. Recall the definition of the pseudo-potential from Eq. (5.16), and this constant is also expressed

$$v^2 = 2U^* - C, \tag{5.22}$$

where C is the Jacobi Constant.

5.2.1 Equilibrium solutions and stability

Computation of equilibrium solutions is a sensible first step in the analysis of nonlinear dynamical systems such as the CR3BP. Equilibrium solutions are often available analytically and may be the only particular solutions that are immediately apparent. If the velocity of P_3 relative to the rotating frame is set equal to zero, equilibrium points are then determined as the locations where relative acceleration is also zero. Thus, from Eq. (5.17), the partials

$$\frac{\partial U^*}{\partial x} = \frac{\partial U^*}{\partial y} = \frac{\partial U^*}{\partial z} = 0 \tag{5.23}$$

determine the location of any points with zero relative motion. As a matter of notation, the symbol U_q^* indicates a partial of the psuedo-potential with respect to the variable q (e.g., $U_x^* = \frac{\partial U^*}{\partial x}$). Five equilibrium points, typically labelled the libration or Lagrange points, exist in the CR3BP, all lying in the xy-plane of primary motion, such that the state vector for these equilibrium solutions is $\boldsymbol{x}_{eq} = (x_i, y_i, 0, 0, 0, 0)^T$ where x_i and y_i are the coordinates of the i-th equilibrium point. These five points appear in Fig. 5.3 relative to the Sun-Jupiter rotating frame, with locations to scale. The points L_4 and L_5 are located analytically such that

$$x_{4,5} = \frac{1}{2} - \mu \tag{5.24a}$$

$$y_{4,5} = \pm\frac{\sqrt{3}}{2} \tag{5.24b}$$

and are commonly termed the equilateral or triangular points since they form equilateral triangles with the two primaries. Unfortunatly, the collinear points L_1, L_2, and L_3 do not possess such closed-form solutions and must be determined numerically in an iterative process. Because the collinear points lie on the x-axis, the coordinates y and z are equal to zero, while the x coordinates are typically expressed as the functions

$$x_1 = 1 - \mu - \iota_1 \tag{5.25}$$

$$x_2 = 1 - \mu + \iota_2 \tag{5.26}$$

$$x_3 = -\mu + \iota_3 \tag{5.27}$$

where the variables ι_i are defined as displacements from the nearest primary (Earth for L_3 and the Moon for L_1 and L_2). The precise locations of the collinear points are then determined by solving the following nonlinear relationships

$$f_1(\iota_1) = \iota_1 + \mu - 1 + \frac{1-\mu}{(1-\iota_1)^2} - \frac{\mu}{\iota_1^2} = 0 \tag{5.28}$$

$$f_2(\iota_2) = \iota_2 + \mu - 1 - \frac{1-\mu}{(1-\iota_2)^2} - \frac{\mu}{\iota_2^2} = 0 \tag{5.29}$$

$$f_3(\iota_3) = \iota_3 + \mu - 1 - \frac{1-\mu}{\iota_3^2} - \frac{\mu}{(1-\iota_3)^2} = 0. \tag{5.30}$$

Given a reasonably accurate initial guess, Newton's method [114] is used to iteratively solve for ι_i using the following update equation

$$\iota_i^{(k+1)} = \iota_i^{(k)} - \frac{f_i(\iota_i^{(k)})}{f_i'(\iota_i^{(k)})} \tag{5.31}$$

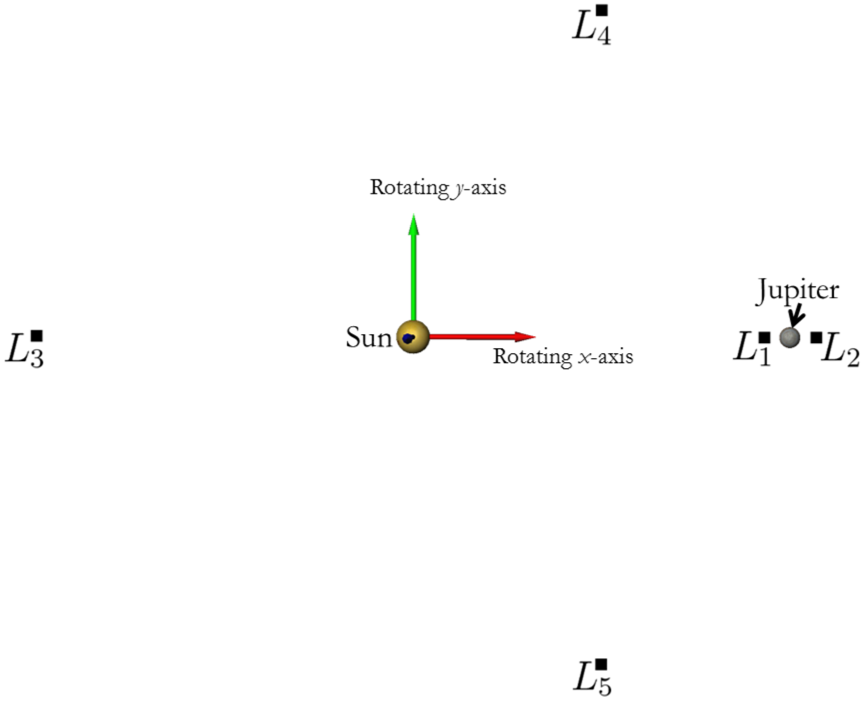

Figure 5.3.. Libration points in the Sun-Jupiter system (Sun and Jupiter size not to scale)

where $\iota_i^{(k)}$ is the approximation of ι_i associated with the k-th iteration and iteration is terminated when $|\iota_i^{(k+1)} - \iota_i^{(k)}|$ falls below a certain tolerance ϵ. The computed locations, in both dimensional and nondimensional units, of the five libration points in the Sun-Jupiter system are summarized in Table 5.2.

Table 5.2. Sun-Jupiter libration point locations

	Non-dimensional		**Dimensional, km** $(\times 10^8)$	
Point	x	y	x	y
L_1	0.93236701	0	7.25765684	0
L_2	1.06882909	0	8.31989414	0
L_3	-1.00039742	0	-7.78721379	0
L_4	0.49904618	0.866025404	3.88463548	6.74124584
L_5	0.49904618	-0.866025404	3.88463548	-6.74124584

The five libration points are equilibrium solutions and, by definition, possess zero relative motion with respect to the primaries. Thus, they are often proposed as respositories of natural bodies as well as potential sites for communications or observational spacecraft. However, the stability of the equilibrium solutions is a key component in evaluating the viability of long-term stability for celestial objects as well as station-keeping and transfer costs. Before stability is determined, the motion near an equilibrium solution is formulated in a systematic way. To this end, define a state $\boldsymbol{x}$ near an equilibrium solution $\boldsymbol{x}_{eq}$ as

$$\boldsymbol{x} = \boldsymbol{x}_{eq} + \delta\boldsymbol{x} \tag{5.32}$$

where the vector $\delta\boldsymbol{x}$ is a small perturbation. Given the EOMs in Eq. (5.14), expanding the vector $\boldsymbol{f}$ in terms of the six-dimensional state $\boldsymbol{x}$ in a Taylor series yields

$$\boldsymbol{f}(\boldsymbol{x}) = \boldsymbol{f}(\boldsymbol{x}_{eq} + \delta\boldsymbol{x}) = \boldsymbol{f}(\boldsymbol{x}_{eq}) + \frac{\partial \boldsymbol{f}(\boldsymbol{x})}{\partial \boldsymbol{x}_{eq}}\delta\boldsymbol{x} + H.O.T. \tag{5.33}$$

but, since $\dot{\boldsymbol{x}} = \dot{\boldsymbol{x}}_{eq} + \delta\dot{\boldsymbol{x}}$ and $\boldsymbol{f}(\boldsymbol{x}) = \dot{\boldsymbol{x}}$, Eq. (5.33) reduces to

$$\delta\dot{\boldsymbol{x}} = \frac{\partial \boldsymbol{f}(\boldsymbol{x})}{\partial \boldsymbol{x}_{eq}}\delta\boldsymbol{x} = \mathbf{A}_6(t)\delta\boldsymbol{x} + H.O.T. \tag{5.34}$$

where the higher-order terms converge to zero as $\boldsymbol{x}$ appoaches $\boldsymbol{x}_{eq}$. The 6×6 matrix $\mathbf{A}_6(t)$ contains the linearized dynamics relative to the reference

$$\mathbf{A}_6(t) = \left.\frac{\partial \boldsymbol{f}(\boldsymbol{x}_{eq})}{\partial \boldsymbol{x}}\right|_{\boldsymbol{x}=\boldsymbol{x}_{eq}} = \begin{bmatrix} 0 & 0 & 0 & 1 & 0 & 0 \\ 0 & 0 & 0 & 0 & 1 & 0 \\ 0 & 0 & 0 & 0 & 0 & 1 \\ U^*_{xx} & U^*_{xy} & U^*_{xz} & 0 & 2 & 0 \\ U^*_{xy} & U^*_{yy} & U^*_{yz} & -2 & 0 & 0 \\ U^*_{xz} & U^*_{yz} & U^*_{zz} & 0 & 0 & 0 \end{bmatrix} \tag{5.35}$$

where $U^*_{\nu\varrho}$ indicates the second-partial derivatives with respect to the variables ν and ϱ; that is, $U^*_{xy} = \frac{\partial^2 U^*}{\partial x \partial y}$, etc. Evaluated at the libration points, this matrix is constant since the reference solution $\boldsymbol{x}_{eq}$ is constant and does not evolve with time.

The stability of the libration points is investigated using Lyapunov stability analysis. A solution is considered stable when it remains bounded in a small region as the system evolves in time. Mathematically, this criterion is equivalent, in a scalar sense, to stating that a solution to Eq. (5.14), $\psi(t)$, is stable if for any small initial perturbation $\delta > 0$ there is a solution $\phi(t)$ such that

$$|\phi(t_0) - \psi(t_0)| < \delta \tag{5.36}$$

that stays bounded with respect to $\psi(t)$

$$|\phi(t) - \psi(t)| < \epsilon \tag{5.37}$$

for $t \geq t_0$ and a small perturbation $\epsilon > 0$. Since the equilibrium points are stationary, the vector solutions $\boldsymbol{x}_{eq}$ are Lyapunov stable if there is a $\epsilon > 0$ for a specified $\delta > 0$ such that

$$|\boldsymbol{x}(t_0) - \boldsymbol{x}_{eq}| < \delta \tag{5.38}$$

and

$$|\boldsymbol{x}(t) - \boldsymbol{x}_{eq}| < \epsilon \tag{5.39}$$

for $t \geq t_0$. If this condition is not satisfied, then the point is unstable. Alternatively, if

$$\lim_{t \to \infty} \boldsymbol{x}(t) = \boldsymbol{x}_{eq} \tag{5.40}$$

the point is asymptotically stable.

The Lyapunov stability of the libration points is then determined via linear analysis and the constant matrix $\mathbf{A}_6$. Define the eigenvalues γ_i for $i = 1, 2, \ldots, 6$ with associated eigenvectors $\tilde{\gamma}_i$. In general, the eigenvalues are complex with the real part determining the stability of the equilibrium point:

- if $\Re[\gamma_i] < 0$ for all i, the point is asymptotically stable,
- if $\Re[\gamma_i] > 0$ for *any* i, the point is unstable,
- if $\Re[\gamma_i] = 0$ for some i and $\Re[\gamma_i] < 0$ for the remaining i, then the linear motion is oscillatory, the point is "marginally stable" in the linear system, and the nonlinear behavior is indeterminate.

If more than one of these conditions on the real part of the eigenvalues is satisfied for any given $\mathbf{A}_6$, then motion near the equilibrium point will exhibit some combination of contracting, expanding, and oscillatory terms. As an example from the Sun-Jupiter system, motion near the collinear points L_1, L_2, and L_3 can exhibit stable, unstable, *and* oscillatory behavior, since the matrix $\mathbf{A}_6$ has one negative real eigenvalue, one positive real eigenvalue, and four purely imaginary eigenvalues associated with each of these locations. In contrast, the Sun-Jupiter equilateral points possess purely imaginary eigenvalues so the linear motion is marginally stable and the nonlinear behavior must be determined using higher-order stability analysis. Szebehely [112] discusses the stability of the triangular points in detail and concludes that the two points are stable for $0 < \mu < 0.03852$. Thus, the Sun-Jupiter L_4 and L_5 are nonlinearly stable, a result verified by the presence of the long-term, stable population of the Trojan asteroids in the close vicinity of these points. The Sun-Jupiter libration point stability behavior is typical of most of the solar system CR3BPs because of their relatively low values for the parameter μ.

5.3 Relative target priority: potential scientific merit of an asteroid encounter

For asteroid tour scenarios, an important consideration is the relative scientific value attached to particular asteroids or specified combinations of asteroids, that is, the relative value in terms of scientific data or resource discovery for specific asteroid sequences. Thus, tour design schemes that incorporate a relative priority or importance metric, either within the sequence generation procedure or as part of data post-processing, can be a valuable tool in satisfying scientific or economic mission objectives as well as technical requirements. All primordial celestial bodies are of great scientific interest and offer insight into the formation and evolution of the solar system. In fact, Near-Earth and Main Belt asteroids have already been visited [76, 77] and several missions currently under development plan to encounter still more. [78, 80] However, one high priority for a future mission is a visit to the Sun-Jupiter Trojan asteroid swarm. [79] This latter case serves as a motivating example for this investigation.

The Trojan asteroids as a whole offer great potential for valuable scientific insight; however, specific target asteroids may possess uncommon or even unique characteristics that warrant higher priority in mission planning scenarios. The Trojan asteroids reside in two clusters around the Sun-Jupiter L_4 and L_5 libration points, the more numerous "Greek" and smaller "Trojan" camps, respectively. Twelve target asteroids from the larger L_4 swarm are selected for this preliminary investigation, where the asteroids all reside in generally low inclination orbits with respect to the solar system ecliptic plane. However, these objects still possess a range of physical characteristics that serve to distinguish them and allow for a relative ranking of potential scientific merit. Indeed, two target asteroids, 624 Hektor and 3548 Eurybates, are included specifically because they offer the possibility of higher than average scientific returns. Table 5.3 lists the target asteroids along with their osculating orbital elements on October 3, 2021 and the relative priority ranking used in this investigation.[1] The following sections detail the scientific considerations that aid in distinguishing higher priority targets among the selected asteroids.

Table 5.3. Asteroids selected as bodies of potential scientific interest in the L_4 Trojan asteroid swarm. Osculating orbital elements at epoch 3 Oct. 2021, with relative priority w.

Name	a, **AU**	e	i, **deg**	Ω, **deg**	ω, **deg**	θ^*, **deg**	w
624 Hektor	5.25	0.023	18.16	342.9	187.7	236.8	2
659 Nestor	5.14	0.116	4.53	350.8	342.3	69.4	1
1143 Odysseus	5.21	0.090	3.14	221.3	239.3	277.0	1
1869 Philoctetes	5.16	0.064	3.98	43.9	325.2	8.9	0.5
3548 Eurybates	5.19	0.088	8.06	43.6	27.0	342.7	2
4057 Demophon	5.22	0.118	2.88	24.3	61.6	288.2	0.5
4138 Kalchas	5.15	0.043	2.10	208.1	162.8	36.0	1
5012 Eurymedon	5.24	0.084	5.00	34.8	333.6	25.6	0.5
5652 Amphimachus	5.19	0.074	1.90	281.8	102.7	11.7	0.5
7152 Euneus	5.13	0.061	3.71	113.1	307.7	332.0	0.5
8241 Agrius	5.15	0.044	4.34	22.7	264.6	132.1	0.5
8317 Eurysaces	5.30	0.047	0.94	208.2	113.2	92.9	0.5

---

[1] A more complete discussion of the motion of bodies in orbit about a single central body, e.g., the Sun, is provided in Sect. 3.2

5.3.1 Asteroid spectral types

The Sun-Jupiter Trojan asteroid swarm is composed of two distinct spectral groupings, D-type asteroids that are a dark burgundy hue (the so-called “redder” group) as well as C- and P-type asteroids that possess a more blue-grey color (the “less-red” set). [115,116] These observations from the NASA Infrared Telescope Facility and the WISE telescope indicate that the L_4 Trojan asteroid swarm is composed of primordial bodies with a composition that may be distinct from the brighter red main belt asteroids as well as the icy Kuiper belt objects. In fact, these asteroids are among the oldest extant bodies in the solar system and may be the only remaining samples from this region of the early accretion disk. Any prospective spacecraft tour of the Trojan swarm that encounters at least one object from each spectral group, therefore, offers a much greater potential for scientific return than a comparable tour that encounters objects of only one, or of unknown, spectral type. Of the twelve target asteroids in this preliminary investigation, two (624 Hektor and 1143 Odysseus) are D-type, redder objects and three (659 Nestor, 3548 Eurybates, and 4138 Kalchas) are in the less-red group. Thus, these asteroids have been assigned a slightly higher priority value of 1 (or higher, in the special cases of 624 Hektor and 3548 Eurybates), above the 0.5 scientific metric assigned to asteroids of unknown spectral type.

5.3.2 624 Hektor - contact binary

In addition to its classification in terms of spectral type, the redder asteroid 624 Hektor garners interest because it is the only known example of a contact binary in the “Greek” camp in the vicinity of the L_4 Sun-Jupiter libration point. [117, 118] This highly oblong object is also larger than most other Trojan asteroids, equivalent in size to a 225-km diameter spheroid. Furthermore, observations from the Keck telescope have confirmed the presence of a 15-km diameter moonlet in orbit around the main body. [119] The roughly 1,200-km altitude, 2.98-day orbit of this moonlet suggests an estimated bulk density of 1.8-3.5 g/cm^3 for the main body of asteroid

624 Hektor. Proximity operations at 624 Hektor can offer valuable insight into the nature of binary systems as well as an evaluation of the bulk density estimates. Thus, a rendezvous encounter with Hektor is given an elevated priority of 2 in this preliminary investigation.

5.3.3 3548 Eurybates - collision family

Similarly to 624 Hektor, less-red 3548 Eurybates is prioritized as a high-value target because it is believed to be the main remnant of an asteroid-asteroid collision. [120] Even though this collision is estimated to have occured 1-4 Gyr in the past, at least 150 asteroids are still grouped by physical and orbital properties such as spectral type and semi-major axis in the vicinity of 3548 Eurybates, indicating a significant collision event. Thus, a spacecraft encounter with Eurybates can offer key insights into such asteroid-asteroid collisions. Furthermore, the approach and departure for the main collision body can also afford fly-by opportunities with collision ejecta, further increasing the scientific value of a rendezvous with 3548 Eurybates. Though these fly-by opportunities are not explicitly modeled in this investigation, the increased fly-by potential and opportunity to examine a large collision fragment does warrant an higher priority level of 2 for encounters with 3548 Eurybates.

5.4 Rendezvous computation: low-thrust transfer arcs

The construction of rendezvous options enabled by a Variable Specific Impulse (VSI), low-thrust system requires two key steps: (i) the optimization of the engine performance time history, and (ii) the detection and usage of conditions amenable to locally optimal solutions. A local hybrid optimization scheme is implemented wherein indirect procedures are blended with direct methods to retain low-dimensionality and, therefore, computational efficiency, while increasing the robustness of the convergence characteristics. The application of techniques from the calculus of variations supplies conditions on optimal operation of the engine while requiring only the solution for an initial set of co-states. In addition to reducing the number of function evaluations per iteration, this indirect approach also ensures a smooth and continuous control history while not restricting engine operation time histories to an assumed form. A spacecraft mass objective function is locally optimized using a gradient-based procedure, removing a requirement to derive and employ the sensitive transversality conditions of indirect methods. State continuity constraints ensuring arrival at the targets of interest as well as constraints on the operation of the rendezvous arcs are implemented using the general corrections procedure detailed in Sect. 2.4.1. Initial guesses for locally optimal departure and arrival conditions are given by local close approaches between the respective asteroids. Global and heuristic algorithms, though not addressed in this investigation, can also be used to optimize fuel performance.

The effect of the electrical power source is examined within the context of the trajectory design and optimization procedures as well as the resulting propellant consumption and engine operation histories. Three types of electrical power sources are compared: (i) constant power Nuclear Electric Propulsion (NEP) systems; (ii) varying power Solar Electric Propulsion (SEP) thrusters; and (iii) hybrid constant/varying power Power-Limited SEP (PLS) engines. Constant power systems typically employ an on-board source, such as radioisotope thermoelectric generators (RTGs), to deliver a consistent, but limited, supply of electrical power. In contrast, SEP systems use photons emitted by the Sun, and collected by solar cells affixed to the spacecraft, to provide electrical power. However, the Sun is also a potential challenge for SEP spacecraft as a power source, i.e., (i) photon density is inversely proportional to the square of the distance from the Sun and (ii) extended periods of shadow must be avoided along the baseline path and incorporated in any guidance algorithm. Within the context of this investigation, the drop-off in photon density is addressed in the design of the Earth-to-asteroid outbound legs while shadow effects are neglected as close proximity operations are not included in this analysis. A further concern for any low-thrust propulsion system is the usual upper bound on engine power for safe operation or a peak engine efficiency power level. In either case, a limit exists upon the maximum power available to the engine, even though the solar panels on a SEP spacecraft may collect more than sufficient electricity to exceed this bound. Thus, a power-limited SEP thruster is also investigated, where this engine type is modeled as a hybrid system of constant- and varying-power engines. In this investigation, each propulsion system is defined such that all possess the same reference power level within the Sun-Jupiter L_4 asteroid swarm and, therefore, the selection of the power source has a correspondingly large effect on the resulting Earth-to-asteroid leg with minimal impact on the performance of the asteroid-to-asteroid thrust arcs. Three distinct low-thrust propulsion scenarios offer a variety of challenges and opportunities, especially when implemented in the overall automated trajectory generation procedure.

5.4.1 Optimization of low-thrust engine operation

Optimal thruster operation conditions suitable for inclusion into a hybrid local optimization method are developed for a general dynamical model. Thus, the equations of motion arising from natural forces such as gravity are readily adjusted without the need to re-derive the engine performance criteria.

5.4.1.1 General equations of motion incorporating thrust

General spacecraft motion is governed by the gravity fields of massive bodies such as the Sun, the Earth, and other gravitational sources and is additionally perturbed by non-gravitational effects such as solar radiation pressure (SRP) and atmospheric drag. Incorporated into the forces that influence the motion in this system are terms that arise from the thrusting of the VSI engine. The system of equations are nondimensionalized to aid numerical integration efficiency: computed results are converted to dimensional quantities by the proper use of the characteristic quantities and spacecraft parameter values. The spacecraft state vector is then defined as:

$$\boldsymbol{\chi} = \begin{Bmatrix} \boldsymbol{r} \\ \boldsymbol{v} \\ m \end{Bmatrix} \tag{5.41}$$

where $\boldsymbol{r}$ is the position vector relative to a fixed point, $\boldsymbol{v}$ is the velocity vector, i.e., the derivative of $\boldsymbol{r}$, within the context of the defined coordinate frames, and m is the instantaneous scalar mass of the spacecraft. Note that bold type indicates vector quantities. The equations of motion are then derived with the result:

$$\dot{\boldsymbol{\chi}} = \begin{Bmatrix} \dot{\boldsymbol{r}} \\ \dot{\boldsymbol{v}} \\ \dot{m} \end{Bmatrix} = \begin{Bmatrix} \boldsymbol{v} \\ \boldsymbol{f}_n(t, \boldsymbol{r}, \boldsymbol{v}) + \frac{T}{m}\boldsymbol{u} \\ -\frac{T^2}{2P} \end{Bmatrix} \tag{5.42}$$

where T is thrust magnitude, P is engine power, $\boldsymbol{u}$ is a unit vector defining the thrust direction, and $\boldsymbol{f}_n$ represents the natural acceleration of the spacecraft. In general, $\boldsymbol{f}_n$ will encompass both gravitational and other terms and may be time-varying, with the exact form dependent on the dynamical model. Furthermore, denote the six-dimensional vector that includes position $\boldsymbol{r}$ and velocity $\boldsymbol{v}$ by the vector $\boldsymbol{x}$, where $\boldsymbol{x} = \begin{bmatrix} x \; y \; z \; \dot{x} \; \dot{y} \; \dot{z} \end{bmatrix}^T$. The power P is defined as a scalar value between zero and a maximum available power level specified by the engine model, such that

$$0 \leq P \leq P_{\text{max}}. \tag{5.43}$$

For this investigation, the value of P_{max} is specified in terms of a reference power level P_{ref} for NEP and SEP systems while an engine power limit P_{lim} is employed to further define a PLS system. Then, the engine thrust T is evaluated via

$$T = \frac{2P}{I_{sp} g_0} \tag{5.44}$$

where I_{sp} is the engine specific impulse and $g_0 = 9.80665$ m/s^2, the gravitational acceleration at the surface of the Earth. Furthermore, the equivalent ΔV cost of a low-thrust arc is readily compute via

$$\Delta V = \int_{t_0}^{t_1} \frac{T}{m} dt \tag{5.45}$$

provided the thrust and mass profiles are available. In cases were no analytical solution to Eq. (5.45) is admissable, numerical quadrature readily provides accurate estimates of the equivalent ΔV cost. [29]

5.4.1.2 The Euler-Lagrange theory

The first-order variational approach that approximates system behavior relative to a reference trajectory arc, as discussed in Section 2.4.1.1, essentially serves as an introduction to a powerful analytical approach, the Calculus of Variations (CoV). The rich history of CoV in the development of dynamical analysis and optimization techniques, as well as the insight offered into the workings of the physical world, creates great interest. A brief discussion of the CoV and its relationship to optimization is presented here, but more general and complete treatments are available in Bolza [97] and Lanczos [113]. In this investigation, the CoV is used to convert a functional optimization problem into a two-point boundary value problem (2PBVP).

Functional optimization is associated with a class of problems where the optimal solution is a continuous time history rather than a discrete set of variables. The objective of functional optimization is the determination of an extremum (maximum or minimum) of a scalar cost functional of the general scalar form

$$J = J_e(\boldsymbol{x}_f, t_f) + \int_{t_0}^{t_f} L(\boldsymbol{x}, t, \boldsymbol{\eta})dt \tag{5.46}$$

where the function J_e is the end cost and the evaluation of the integral yields the path cost. The integrand L is denoted the Lagrangian, and $\boldsymbol{\eta}$ is an m-dimensional vector of control variables. With a cost functional of the form in Eq. (5.46), the optimization problem is labelled the Bolza Problem with two special cases. If only the end-cost term is present, the Problem of Mayer emerges; while, if only the path cost appears, the problem is, appropriately, the Problem of Lagrange. The functional optimization problem, in addition to dynamical equations such as those in Eq. (5.14), usually includes boundary conditions of the form

$$\boldsymbol{\psi}(\boldsymbol{x}, t) = \boldsymbol{0} \tag{5.47}$$

with the time and state $\boldsymbol{x}$ evaluated at the beginning or end of the trajectory arc. Then, an optimal control history $\boldsymbol{\eta}^*(t)$ and an optimal set of free initial conditions $\boldsymbol{x}_0^*$ is determined using indirect optimization.

Lawden [88], as well as Bryson and Ho [121], each offer a full development and proof of the Euler-Lagrange Theorem; another source, with more modern notation, is available in Longuski, et al. [122]. The Euler-Lagrange Theorem states that, for an extremum of the scalar cost functional J, when $dJ = 0$, the following necessary conditions must follow, that is

$$\dot{\boldsymbol{x}} = \boldsymbol{f}(\boldsymbol{x}, t, \boldsymbol{\eta}) = H_{\boldsymbol{\lambda}} \tag{5.48a}$$

$$\dot{\boldsymbol{\lambda}} = -H_{\boldsymbol{x}} \tag{5.48b}$$

$$H_{\boldsymbol{\eta}} = \boldsymbol{0} \tag{5.48c}$$

where H represents the Hamiltonian and the elements of the vector $\boldsymbol{\lambda}$ reflect the co-states that correspond to the states in $\boldsymbol{x}$. Subscripts on H indicate a gradient of the Hamiltonian with respect to one of the vectors $\boldsymbol{x}$, $\boldsymbol{\eta}$, or $\boldsymbol{\lambda}$ (i.e., $H_{\boldsymbol{\eta}} = \frac{\partial H}{\partial \boldsymbol{\eta}}$). The Hamiltonian, H, for the problem is then written as

$$H(\boldsymbol{x}, t, \boldsymbol{\eta}, \boldsymbol{\lambda}) = L(\boldsymbol{x}, t, \boldsymbol{\eta}) + \boldsymbol{\lambda}^T \boldsymbol{f}(\boldsymbol{x}, t, \boldsymbol{\eta}). \tag{5.49}$$

Additional transversality conditions, that is

$$H dt - \boldsymbol{\lambda}^T d\boldsymbol{x} + dJ_e = 0 \tag{5.50}$$

are constructed to apply at the beginning or the end of the trajectory arc. These transversality relationships match the number of free variables (e.g., states and times) to the number of boundary conditions. Because the boundary conditions $\boldsymbol{\psi}$ are specified end states for the optimization problem, the variational vector relationship

$$d\boldsymbol{\psi} = \boldsymbol{\psi}_{t_f} dt_f + \boldsymbol{\psi}_{\boldsymbol{x}_f} d\boldsymbol{x}_f = \boldsymbol{0} \tag{5.51}$$

is used to reduce Eq. (5.50) to a sum of differentials whose coefficients are set equal to zero. The boundary value problem then possesses a full set of parameters and boundary conditions; thus, extremizing H with respect to $\boldsymbol{\eta}$ extremizes J. For the optimal path $\boldsymbol{x}^*(\boldsymbol{x}_0^*, t)$, the Hamiltonian then satisfies one of the following two statements,

$$H\left[\boldsymbol{x}^*(t), t, \boldsymbol{\eta}^*(t), \boldsymbol{\lambda}(t)\right] \leq H\left[\boldsymbol{x}^*(t), t, \boldsymbol{\eta}(t), \boldsymbol{\lambda}(t)\right] \tag{5.52a}$$

$$H\left[\boldsymbol{x}^*(t), t, \boldsymbol{\eta}^*(t), \boldsymbol{\lambda}(t)\right] \geq H\left[\boldsymbol{x}^*(t), t, \boldsymbol{\eta}(t), \boldsymbol{\lambda}(t)\right] \tag{5.52b}$$

representing the minimum or maximum cost functional, respectively. The statement in Eq. (5.52), i.e., the Minimum or Maximum Principle depending on the problem formulation, is proven by, and often named for, Pontryagin [89].

5.4.1.3 Indirect optimization of constant power thrust arcs

When the on-board propulsion system is powered by a self-contained power source, as is the case with a NEP engine, or by solar panels delivering approximately constant power, such as SEP systems in the Earth-Moon region, the maximum engine power $P_{\max}$ is assumed to be a constant value over the duration of the trajectory. For all such trajectories in this investigation, the maximum engine power is specified to be $P_{\max} = P_{\text{ref}}$ unless otherwise noted. To fully define the optimization problem, the performance index and the boundary conditions must also be specified. To arrive at the target object with the maximum final spacecraft mass for a specified thrust duration, the performance index J is defined

$$\max J = m_f. \tag{5.53}$$

The boundary conditions and the Hamiltonian are adjoined to the performance index, such that Eq. (5.53) is expanded to become the Bolza function

$$\max J' = m_f + \boldsymbol{\nu}_0^T \boldsymbol{\psi}_0 + \boldsymbol{\nu}_f^T \boldsymbol{\psi}_f + \int_{t_0}^{t_f} [H - \boldsymbol{\lambda}^T \dot{\boldsymbol{\chi}}] dt \tag{5.54}$$

where H is the problem Hamiltonian, $\boldsymbol{\lambda}$ is a co-state vector, the terms $\boldsymbol{\psi}$ are vectors comprised of boundary conditions, and the vector terms involving $\boldsymbol{\nu}$ are Lagrange multipliers corresponding to the boundary conditions. The co-state vector is then

$$\boldsymbol{\lambda} = \begin{Bmatrix} \boldsymbol{\lambda_r} \\ \boldsymbol{\lambda_v} \\ \lambda_m \end{Bmatrix} \tag{5.55}$$

where $\boldsymbol{\lambda_r}$ and $\boldsymbol{\lambda_v}$ are three-dimensional vectors comprised of the position and velocity co-states, respectively, and the scalar λ_m is the mass co-state. The initial and final vector boundary conditions are

$$\boldsymbol{\psi}_0 = \boldsymbol{x}_I - \boldsymbol{x}_I(\tau_0) = \mathbf{0} \tag{5.56}$$

and

$$\boldsymbol{\psi}_f = \boldsymbol{x}_T - \boldsymbol{x}_T(\tau_0 + TD) = \mathbf{0} \tag{5.57}$$

where the subscripts I and T indicate the states associated with the current object and the target object, respectively. The parameter τ_0 defines the epoch of thrust initiation while TD is defined to be the duration of engine operation, i.e., thrust. Equation (5.56) is implicitly satisfied by defining $\boldsymbol{x}_I$ as the state along the current object trajectory as defined by the parameter τ_0. The final, or target, boundary conditions in Eq. (5.57) are satisfied by solving the boundary value problem.

The calculus of variations, specifically the Euler-Lagrange Theorem as detailed in Sect. 5.4.1.2, is employed to define several properties of the 2PBVP and to acquire the derivatives of the co-states. The problem Hamiltonian is

$$H = \boldsymbol{\lambda}^T \dot{\boldsymbol{\chi}} = \boldsymbol{\lambda_r}^T \boldsymbol{v} + \boldsymbol{\lambda_v}^T \left[\boldsymbol{f}_n(t, \boldsymbol{r}, \boldsymbol{v}) + \frac{T}{m} \boldsymbol{u} \right] - \lambda_m \frac{T^2}{2P} \tag{5.58}$$

where the value of H is constant over the trajectory for the time-invariant systems. For time-varying models, H is no longer a constant value. The optimal control strategy emerges by maximizing the Hamiltonian with respect to the controls T, P, and $\boldsymbol{u}$ such that

$$P = P_{\text{max}} \tag{5.59}$$

$$T = \frac{\lambda_v P_{\text{max}}}{\lambda_m m} \tag{5.60}$$

$$\boldsymbol{u} = \frac{\boldsymbol{\lambda_v}}{\lambda_{\boldsymbol{v}}} \tag{5.61}$$

where $\lambda_{\boldsymbol{v}}=||\boldsymbol{\lambda_v}||$. Given these control expressions, the Hamiltonian is reformulated and Eq. (5.58) is rewritten as

$$H = \boldsymbol{\lambda}_{\boldsymbol{r}}^T \boldsymbol{v} + \boldsymbol{\lambda}_{\boldsymbol{v}}^T \boldsymbol{f}_n + S \cdot T \tag{5.62}$$

where S is the switching function

$$S = \frac{\lambda_{\boldsymbol{v}}}{m} - \frac{\lambda_m T}{2P_{\text{max}}}. \tag{5.63}$$

The Euler-Lagrange conditions for optimality modify the performance index in Eq. (5.54). With the reformulated Hamiltonian, that is, Eq. (5.62), the following equations of motion for the co-states emerge

$$\dot{\boldsymbol{\lambda}} = -\left(\frac{\partial H}{\partial \boldsymbol{\chi}}\right)^T = \left\{\begin{matrix} -\boldsymbol{\lambda}_{\boldsymbol{v}}^T \left(\frac{\partial \boldsymbol{f}_n}{\partial \boldsymbol{r}}\right) \\ -\boldsymbol{\lambda}_{\boldsymbol{r}}^T - \boldsymbol{\lambda}_{\boldsymbol{v}}^T \left(\frac{\partial \boldsymbol{f}_n}{\partial \boldsymbol{v}}\right) \\ \lambda_{\boldsymbol{v}} \frac{T}{m^2} \end{matrix}\right\} \tag{5.64}$$

where the initial state for λ_m is set equal to unity to reduce the number of variables to be determined. Note that: (a) a similar procedure to minimize the initial mass for a given target mass results in identical conditions for engine operation, and (b) the differential equations for the co-states do not change form based upon the underlying natural dynamics; thus, $\frac{\partial \boldsymbol{f}_n}{\partial \boldsymbol{r}}$ and $\frac{\partial \boldsymbol{f}_n}{\partial \boldsymbol{v}}$ are freely substituted when using models of varying fidelity.

When the co-states are included in the set of design variables for a corrections procedure (see Sect. 2.4.1), the constraint gradient is determined using the previously defined 6×6 STM $\boldsymbol{\Phi}(t, t_0)$ (Section 2.4.1.1) as well as a new 14×14 STM $\boldsymbol{\Psi}(t, t_0)$

incorporating the seven states (position, velocity, mass) and the corresponding co-states. To create the new STM, define the combined state and co-state vector

$$\boldsymbol{\xi} = \begin{Bmatrix} \boldsymbol{\chi} \\ \boldsymbol{\lambda} \end{Bmatrix} \tag{5.65}$$

with the associated vector derivative

$$\boldsymbol{a} = \dot{\boldsymbol{\xi}} = \begin{Bmatrix} \dot{\boldsymbol{\chi}} \\ \dot{\boldsymbol{\lambda}} \end{Bmatrix} \tag{5.66}$$

where the vectors $\boldsymbol{\chi}$ and $\boldsymbol{\lambda}$ include the states and co-states, respectively. A new linear dynamical matrix of partials $\mathbf{A}_{14}(t)$ is evaluated as

$$\mathbf{A}_{14}(t) = \frac{d\boldsymbol{a}(\boldsymbol{\xi})}{d\boldsymbol{\xi}} = \begin{bmatrix} \mathbf{0}_3 & \mathbf{I}_3 & \mathbf{0}_{3,1} & \mathbf{0}_3 & \mathbf{0}_3 & \mathbf{0}_{3,1} \\ \frac{\partial \boldsymbol{f}_n}{\partial \boldsymbol{r}} & \frac{\partial \boldsymbol{f}_n}{\partial \boldsymbol{v}} & -\frac{2P_{\max}}{m^3\lambda_m}\boldsymbol{\lambda}_{\boldsymbol{v}} & \mathbf{0}_3 & \frac{P_{\max}}{m^2\lambda_m}\mathbf{I}_3 & -\frac{P_{\max}}{m^2\lambda_m^2}\boldsymbol{\lambda}_{\boldsymbol{v}} \\ \mathbf{0}_{1,3} & \mathbf{0}_{1,3} & \frac{P_{\max}\lambda_{\boldsymbol{v}}^2}{m^3\lambda_m^2} & \mathbf{0}_{1,3} & -\frac{P_{\max}}{m^2\lambda_m^2}\boldsymbol{\lambda}_{\boldsymbol{v}}^T & \frac{P_{\max}\lambda_{\boldsymbol{v}}^2}{m^2\lambda_m^3} \\ -\mathbf{W} & \mathbf{0}_3 & \mathbf{0}_{3,1} & \mathbf{0}_3 & -\left(\frac{\partial \boldsymbol{f}_n}{\partial \boldsymbol{r}}\right)^T & \mathbf{0}_{3,1} \\ \mathbf{0}_3 & \mathbf{0}_3 & \mathbf{0}_{3,1} & -\mathrm{I}_3 & -\left(\frac{\partial \boldsymbol{f}_n}{\partial \boldsymbol{v}}\right)^T & \mathbf{0}_{3,1} \\ \mathbf{0}_{1,3} & \mathbf{0}_{1,3} & -\frac{3P_{\max}\lambda_{\boldsymbol{v}}^2}{m^4\lambda_m} & \mathbf{0}_{1,3} & \frac{2P_{\max}}{m^2\lambda_m}\boldsymbol{\lambda}_{\boldsymbol{v}}^T & -\frac{P_{\max}\lambda_{\boldsymbol{v}}^2}{m^3\lambda_m^2} \end{bmatrix} \tag{5.67}$$

where the subscripts on $\mathbf{0}$ and $\mathbf{I}$ indicate the size of the zero or identity matrix.[2] The 3×3 sub-matrix

$$\mathbf{W} = \begin{bmatrix} W_{11} & W_{12} & W_{13} \\ W_{21} & W_{22} & W_{23} \\ W_{31} & W_{32} & W_{33} \end{bmatrix} \tag{5.68}$$

---

[2] The individual subscript ‘3’ indicates a 3×3 matrix; the subscript combination ‘3,1’ denotes a 3-element column vector, and ‘1,3’ a 3-element row vector.

incorporates the third partials of the psuedo-potential function U^* from Eq. (5.16)

$$\begin{aligned}
W_{11} &= \lambda_{v_x} U^*_{x^3} + \lambda_{v_y} U^*_{x^2 y} + \lambda_{v_z} U^*_{x^2 z} \\
W_{12} &= \lambda_{v_x} U^*_{x^2 y} + \lambda_{v_y} U^*_{x y^2} + \lambda_{v_z} U^*_{xyz} \\
W_{13} &= \lambda_{v_x} U^*_{x^2 z} + \lambda_{v_y} U^*_{xyz} + \lambda_{v_z} U^*_{x z^2} \\
W_{21} &= \lambda_{v_x} U^*_{x^2 y} + \lambda_{v_y} U^*_{x y^2} + \lambda_{v_z} U^*_{xyz} \\
W_{22} &= \lambda_{v_x} U^*_{x y^2} + \lambda_{v_y} U^*_{y^3} + \lambda_{v_z} U^*_{y^2 z} \qquad (5.69) \\
W_{23} &= \lambda_{v_x} U^*_{xyz} + \lambda_{v_y} U^*_{y^2 z} + \lambda_{v_z} U^*_{y z^2} \\
W_{31} &= \lambda_{v_x} U^*_{x^2 z} + \lambda_{v_y} U^*_{xyz} + \lambda_{v_z} U^*_{x z^2} \\
W_{32} &= \lambda_{v_x} U^*_{xyz} + \lambda_{v_y} U^*_{y^2 z} + \lambda_{v_z} U^*_{y z^2} \\
W_{33} &= \lambda_{v_x} U^*_{x z^2} + \lambda_{v_y} U^*_{y z^2} + \lambda_{v_z} U^*_{z^3}.
\end{aligned}$$

Then, the new 14 × 14 STM is defined such that

$$\delta\boldsymbol{\xi}(t) = \frac{\partial \boldsymbol{\xi}}{\partial \boldsymbol{\xi}_0}\delta\boldsymbol{\xi}_0 = \boldsymbol{\Psi}(t,t_0)\delta\boldsymbol{\xi}_0 \qquad (5.70)$$

$$\dot{\boldsymbol{\Psi}}(t,t_0) = \frac{\partial \boldsymbol{a}}{\partial \boldsymbol{\xi}}\boldsymbol{\Psi}(t,t_0) = \mathbf{A}_{14}(t)\boldsymbol{\Psi}(t,t_0) \qquad (5.71)$$

where the initial STM is equal to the identity matrix, $\boldsymbol{\Psi}(t_0,t_0) = \mathbf{I}$. Note that the 14×14 STM $\boldsymbol{\Psi}$ reduces to the 6×6 STM $\boldsymbol{\Phi}$ when the spacecraft mass and the co-states are removed as variables (e.g., the VSI engine is turned off or a thrust profile is specified).

5.4.1.4 Indirect optimization of varying power thrust arcs

The development of the operational conditions for a varying engine power level, e.g., a SEP system operating at changing distances from the Sun, proceeds similarly to the indirect method for NEP thrusters. In contrast, however, the maximum available engine power is now determined via

$$P_{\max} = \frac{P_{\text{ref}}}{d_s^2} \qquad (5.72)$$

where d_s is the nondimensional distance between the spacecraft and the Sun. For a pure SEP system, the available engine power is not constrained by any upper or lower limits.

The objective function and constraints for a SEP system are the same as for NEP systems, so Eqs. (5.53)-(5.57) are unchanged in the definition of the 2PBVP. Recalling from Eq. (5.59) that the most efficient engine operation occurs at the maximum available power level, the new problem Hamiltonian is then

$$H = \boldsymbol{\lambda}^T \dot{\boldsymbol{\chi}} = \boldsymbol{\lambda}_{\boldsymbol{r}}^T \boldsymbol{v} + \boldsymbol{\lambda}_{\boldsymbol{v}}^T \left[\boldsymbol{f}_n(t, \boldsymbol{r}, \boldsymbol{v}) + \frac{T}{m} \boldsymbol{u} \right] - \lambda_m \frac{T^2 d_s^2}{2 P_{\text{ref}}}. \tag{5.73}$$

As before, maximizing the Hamiltonian produces the primer vector in Eq. (5.61) and the control, in terms of the thrust magnitude,

$$T = \frac{\lambda_v P_{\text{ref}}}{\lambda_m m d_s^2} \tag{5.74}$$

while the Euler-Lagrange conditions yield the co-state equations of motion

$$\dot{\boldsymbol{\lambda}} = -\left(\frac{\partial H}{\partial \boldsymbol{\chi}} \right)^T = \left\{ \begin{array}{c} -\boldsymbol{\lambda}_{\boldsymbol{v}}^T \left(\frac{\partial \boldsymbol{f}_n}{\partial \boldsymbol{r}} \right) + \lambda_m \frac{T^2}{P_{\text{ref}}} \boldsymbol{d}_s \\ -\boldsymbol{\lambda}_{\boldsymbol{r}}^T - \boldsymbol{\lambda}_{\boldsymbol{v}}^T \left(\frac{\partial \boldsymbol{f}_n}{\partial \boldsymbol{v}} \right) \\ \lambda_{\boldsymbol{v}} \frac{T}{m^2} \end{array} \right\} \tag{5.75}$$

where $\boldsymbol{d}_s$ is the nondimensional distance vector from the Sun to the spacecraft (recall that bold-face indicates vector quantities such that $d_s = \|\boldsymbol{d}_s\|$). The 14×14 linear dynamical matrix of partials $\mathbf{A}_{14}(t)$ is now evaluated as

$$\mathbf{A}_{14}(t) = \frac{d\boldsymbol{a}(\boldsymbol{\xi})}{d\boldsymbol{\xi}} =$$

$$\begin{bmatrix} \mathbf{0}_3 & \mathbf{I}_3 & \mathbf{0}_{3,1} & \mathbf{0}_3 & \mathbf{0}_3 & \mathbf{0}_{3,1} \\ \mathbf{P}_{\boldsymbol{fr}} & \frac{\partial \boldsymbol{f}_n}{\partial \boldsymbol{v}} & -\frac{2P_{\text{ref}}}{d_s^2 m^3 \lambda_m} \boldsymbol{\lambda}_{\boldsymbol{v}} & \mathbf{0}_3 & \frac{P_{\text{ref}}}{d_s^2 m^2 \lambda_m} \mathbf{I}_3 & -\frac{P_{\text{ref}}}{d_s^2 m^2 \lambda_m^2} \boldsymbol{\lambda}_{\boldsymbol{v}} \\ \frac{P_{\text{ref}} \lambda_v^2}{m^2 \lambda_m^2 d_s^4} \boldsymbol{d}_s^T & \mathbf{0}_{1,3} & \frac{P_{\text{ref}} \lambda_{\boldsymbol{v}}^2}{m^3 \lambda_m^2 d_s^2} & \mathbf{0}_{1,3} & -\frac{P_{\text{ref}}}{m^2 \lambda_m^2 d_s^2} \boldsymbol{\lambda}_{\boldsymbol{v}}^T & \frac{P_{\text{ref}} \lambda_{\boldsymbol{v}}^2}{m^2 \lambda_m^3 d_s^2} \\ -\tilde{\mathbf{W}} & \mathbf{0}_3 & \mathbf{0}_{3,1} & \mathbf{0}_3 & -\mathbf{P}_{\boldsymbol{fr}}^T & \mathbf{0}_{3,1} \\ \mathbf{0}_3 & \mathbf{0}_3 & \mathbf{0}_{3,1} & -\mathrm{I}_3 & -\left(\frac{\partial \boldsymbol{f}_n}{\partial \boldsymbol{v}} \right)^T & \mathbf{0}_{3,1} \\ -\frac{2P_{\text{ref}} \lambda_{\boldsymbol{v}}^2}{m^3 \lambda_m d_s^4} \boldsymbol{d}_s^T & \mathbf{0}_{1,3} & -\frac{3P_{\text{ref}} \lambda_{\boldsymbol{v}}^2}{m^4 \lambda_m d_s^2} & \mathbf{0}_{1,3} & \frac{2P_{\text{ref}}}{m^2 \lambda_m d_s^2} \boldsymbol{\lambda}_{\boldsymbol{v}}^T & -\frac{P_{\text{ref}} \lambda_{\boldsymbol{v}}^2}{m^3 \lambda_m^2 d_s^2} \end{bmatrix} \tag{5.76}$$

where the submatrix $\tilde{\mathbf{W}}$ is defined as

$$\tilde{\mathbf{W}} = \mathbf{W} - \frac{\lambda_v^2 P_{\text{ref}}}{m^2 \lambda_m d_s^4} \mathbf{I}_3 + \frac{4\lambda_v^2 P_{\text{ref}}}{m^2 \lambda_m d_s^6} \boldsymbol{d}_s \boldsymbol{d}_s^T \tag{5.77}$$

with $\mathbf{W}$ provided by Eq. (5.68). The new partial derivative sub-matrix $\mathbf{P}_{\boldsymbol{fr}}$ is defined to be

$$\mathbf{P}_{\boldsymbol{fr}} = \frac{\partial \boldsymbol{f}_n}{\partial \boldsymbol{r}} - \frac{2P_{\text{ref}}}{m^2 \lambda_m d_s^4} \boldsymbol{\lambda_v} \boldsymbol{d}_s^T. \tag{5.78}$$

Consistent with a constant-power thrust arc, the engine operating conditions and the differential equations are unchanged if the initial mass is minimized or if differing models representing the natural dynamics are incorporated.

5.4.1.5 Adjoint control transformation

Dixon [123] developed the Adjoint Control Transformation (ACT) to supply more intuitive variables as a basis to generate an initial guess for the co-states and to increase the convergence radius of the locally optimal solutions. To accomplish these goals, the ACT relates the thrust direction in a vehicle-centered frame to the initial co-states $\boldsymbol{\lambda}_0$. The spacecraft-centered frame V is defined with the right-handed triad

$$\hat{V} = \frac{\boldsymbol{v}}{|\boldsymbol{v}|} \qquad \hat{n} = \frac{\boldsymbol{r} \times \boldsymbol{v}}{|\boldsymbol{r} \times \boldsymbol{v}|} \qquad \hat{b} = \hat{n} \times \hat{V} \tag{5.79}$$

where $\hat{V}$ is a unit vector in the direction of the spacecraft velocity, $\hat{n}$ is the instantaneous orbit normal, and $\hat{b}$ completes the orthonormal set of unit vectors. Two spherical angles, α and β, specify the thrust direction in this frame. These two angles, the unit vectors defining frame V, and the thrust vector $\boldsymbol{T}$ are all illustrated in Fig. 5.4.

The thrust direction is now expressed in terms of the angles α and β and then transformed to the rotating frame R. In terms of the angles, the unit vector that defines the thrust direction in frame V is written

$$\boldsymbol{u}_V = \begin{Bmatrix} \cos\alpha\cos\beta \\ \sin\alpha\cos\beta \\ \sin\beta \end{Bmatrix}. \tag{5.80}$$

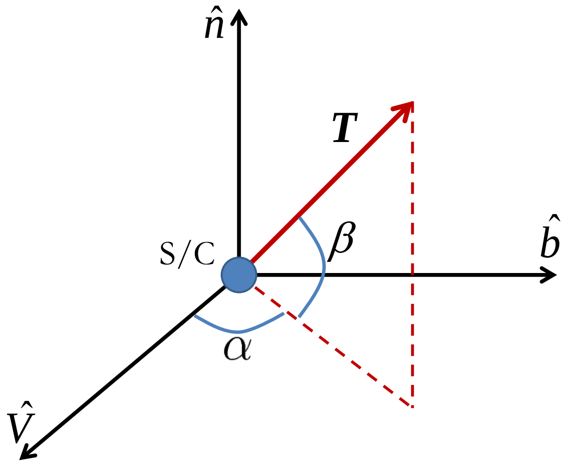

Figure 5.4.. Spacecraft-centered frame V with thrust vector

Then, the differential vector

$$\dot{\boldsymbol{u}}_V = \begin{Bmatrix} -\dot{\alpha}\sin\alpha\cos\beta - \dot{\beta}\cos\alpha\sin\beta \\ \dot{\alpha}\cos\alpha\cos\beta - \dot{\beta}\sin\alpha\sin\beta \\ \dot{\beta}\cos\beta \end{Bmatrix} \tag{5.81}$$

represents the rate of change of the thrust direction as observed from the vehicle frame. The transformation of the thrust direction vector from frame V to frame R is accomplished via

$$\boldsymbol{u}_R = \mathbf{D}\boldsymbol{u}_V \tag{5.82}$$

where the rotation DCM $\mathbf{D}$ is defined

$$\mathbf{D} = \begin{bmatrix} \hat{x}\cdot\hat{V} & \hat{x}\cdot\hat{b} & \hat{x}\cdot\hat{n} \\ \hat{y}\cdot\hat{V} & \hat{y}\cdot\hat{b} & \hat{y}\cdot\hat{n} \\ \hat{z}\cdot\hat{V} & \hat{z}\cdot\hat{b} & \hat{z}\cdot\hat{n} \end{bmatrix}. \tag{5.83}$$

Rotation of the thrust direction rate of change yields

$$\dot{\boldsymbol{u}}_R = \dot{\mathbf{D}}\boldsymbol{u}_V + \mathbf{D}\dot{\boldsymbol{u}}_V \tag{5.84}$$

where

$$\dot{\mathbf{D}} = \mathbf{D}\cdot\left(\frac{\boldsymbol{r}\times\boldsymbol{v}}{r^2}\right) \tag{5.85}$$

delivers the DCM rate of change.

The direct connection between the optimal controls and the spherical angles α and β remains to be established. The primer vector from Eq. (5.61) is rearranged to appear

$$\boldsymbol{\lambda_v} = \lambda_v \boldsymbol{u}_R \tag{5.86}$$

with the time derivative

$$\dot{\boldsymbol{\lambda}}_{\boldsymbol{v}} = \dot{\lambda}_v \boldsymbol{u}_R + \lambda_v \dot{\boldsymbol{u}}_R. \tag{5.87}$$

Recall the velocity co-state equations of motion in Eq. (5.64). The initial position co-state is then

$$\boldsymbol{\lambda_r} = -\dot{\lambda}_v \boldsymbol{u}_R - \lambda_v \dot{\boldsymbol{u}}_R - \frac{\partial \boldsymbol{f}_n}{\partial \boldsymbol{v}} \boldsymbol{\lambda_v} \tag{5.88}$$

where Eqs. (5.86) and (5.88) relate the initial position and velocity co-states to the thrust direction angles and the magnitude the velocity co-state vector and its corresponding rate of change, i.e.,

$$\dot{\lambda}_v = -\frac{1}{\boldsymbol{u}^T \boldsymbol{v}} \left[\lambda_v \dot{\boldsymbol{u}}^T \boldsymbol{v} + \boldsymbol{\lambda}_{\boldsymbol{v}}^T \frac{\partial \boldsymbol{f}_n}{\partial \boldsymbol{v}} \boldsymbol{v} - \boldsymbol{\lambda}_{\boldsymbol{v}}^T \boldsymbol{f}_n \right]. \tag{5.89}$$

The new angle variables now constitute another formulation of the 2PBVP that provides more physical intuition in constructing initial guesses and reduces sensitivity during the optimization process.

The adjoint control transformation is straightforwardly inverted by solving for the angles and their associated time rate of change as functions of the co-state variables $\boldsymbol{\lambda_r}$ and $\boldsymbol{\lambda_v}$. The magnitude of the velocity co-state is defined to be

$$\lambda_v = \|\boldsymbol{\lambda_v}\| \tag{5.90}$$

and the time derivative of this magnitude is

$$\dot{\lambda}_v = \pm \| - \boldsymbol{\lambda}_{\boldsymbol{r}}^T - \boldsymbol{\lambda}_{\boldsymbol{v}}^T \left(\frac{\partial \boldsymbol{f_n}}{\partial \boldsymbol{v}} \right) \| \tag{5.91}$$

where the sign ambiguity is resolved via the Law of Cosines:

$$\lambda_v \dot{\lambda}_v \cos\theta = \boldsymbol{\lambda_v} \cdot \dot{\boldsymbol{\lambda}}_{\boldsymbol{v}}. \tag{5.92}$$

The thrust direction frame transformation from Eq. (5.82) is inverted to

$$\boldsymbol{u}_V = \mathbf{D}^{-1}\boldsymbol{u}_R = \mathbf{D}^T\boldsymbol{u}_R \tag{5.93}$$

where the pointing direction in the frame R is given by $\boldsymbol{u}_R = \boldsymbol{\lambda_v}/\lambda_v$. The time rate of change of the thrust pointing direction in the vehicle frame is then obtained from rearranging Eq. (5.84) to

$$\dot{\boldsymbol{u}}_V = \mathbf{D}^T(\dot{\boldsymbol{u}}_R - \dot{\mathbf{D}}\boldsymbol{u}_V) \tag{5.94}$$

where the rate of change in frame R is obtained from

$$\dot{\boldsymbol{u}}_R = \frac{-\boldsymbol{\lambda_r} - \dot{\lambda}_v\boldsymbol{u}_R - (\frac{\partial \boldsymbol{f_n}}{\partial \boldsymbol{v}})^T\boldsymbol{\lambda_v}}{\lambda_v}. \tag{5.95}$$

Recalling Eq. (5.80), the angle β is obtained from

$$\beta = \sin^{-1} u_{V,3} \tag{5.96}$$

with $u_{V,3}$ the third element of the unit vector $\boldsymbol{u}_V$. Likewise, the angle α is given by

$$\alpha = \begin{cases} \cos^{-1}\left(\frac{u_{V,1}}{\cos\beta}\right) \\ \sin^{-1}\left(\frac{u_{V,2}}{\cos\beta}\right) \end{cases} \tag{5.97}$$

where both relations must be used to resolve the quadrant ambiguity. The rates of change of the angles are then provided by

$$\dot{\beta} = \frac{\dot{u}_{V,3}}{\cos\beta} \tag{5.98}$$

and

$$\dot{\alpha} = \frac{\dot{u}_{V,3} + \dot{\beta}\sin\alpha\sin\beta}{\cos\beta\cos\alpha}, \tag{5.99}$$

respectively. The inverse ACT can now be used to recover the physical thrust pointing angles from the position and velocity co-state vectors.

5.4.2 Hybrid optimization of low-thrust rendezvous options

In an indirect optimization scheme, the 2PBVP must be fully reformulated for each new objective and any new set of constraint combinations. To avoid reformulating the problem for every new objective and constraint formulation, a hybrid optimization strategy combines the low dimensionality of indirect methods with the flexibility of a direct approach. For rendezvous arcs within the tour, a sequential quadratic programming (SQP) method is then used to maximize the final mass m_f, with the additional nonlinear constraints specified by Eqs. (5.56) and (5.57). The initial spacecraft mass is specified as the reference spacecraft mass, i.e., $m_0 = m_r$. Note that the same initial condition $m_0 = m_r$ is employed for all independently generated object-to-object legs.

5.4.2.1 Introducing sequential quadratic programming

Direct optimization methods are explicitly formulated to extremize a cost function. This approach is advantageous in contrast to the reformulation as a boundary value problem that characterizes indirect schemes. Constrained direct optimization is therefore generally formulated as

$$\min J(\boldsymbol{x}) \tag{5.100}$$

subject to the constraints

$$\boldsymbol{g}(\boldsymbol{x}) \leq \boldsymbol{0} \tag{5.101a}$$

$$\boldsymbol{h}(\boldsymbol{x}) = \boldsymbol{0} \tag{5.101b}$$

$$\boldsymbol{x}^L \leq \boldsymbol{x} \leq \boldsymbol{x}^U \tag{5.101c}$$

where $\boldsymbol{g}(\boldsymbol{x})$ is an l-vector of inequality constraints, $\boldsymbol{h}(\boldsymbol{x})$ is an p-vector of equality constraints, and the state vector $\boldsymbol{x}$ is bound between lower and upper limits on each state. A maximization problem is easily converted to a minimization problem by switching the sign (±) of the cost function and all of the inequality constraints are written as in Eq. (5.101a) by switching signs on the constraints as needed. Consistent with indirect optimization, the constraints are adjoined to the cost function to create the Lagrangian function Λ, i.e.,

$$\Lambda(\boldsymbol{x}) = J(\boldsymbol{x}) + \sum_{j=1}^{l} \nu_j \{\max[0, g_j(\boldsymbol{x})]\} + \sum_{k=1}^{p} \nu_{l+k} |h_k(\boldsymbol{x})| \tag{5.102}$$

where, as before, the variables ν are Lagrange multipliers. Then, the well-known Karush-Kuhn-Tucker (KKT) conditions [124, 125] for an optimal solution $\boldsymbol{x}^*$ are:

1. The solution $\boldsymbol{x}^*$ is feasible (all constraints in Eq. (5.101) are satisfied).
2. The relation

$$\nu_j g_j(\boldsymbol{x}^*) = 0 \tag{5.103}$$

   is separately satisfied for every j and where all $\nu_j \geq 0$.

3. The gradient of the cost function and adjoined constraints vanishes, that is,

$$\nabla J(\boldsymbol{x}^*) + \sum_{j=1}^{l} \nu_j \nabla g_j(\boldsymbol{x}^*) + \sum_{k=1}^{p} \nu_{l+k} \nabla h_k(\boldsymbol{x}^*) = \boldsymbol{0} \tag{5.104}$$

   for all $\nu_j \geq 0$ and unrestricted ν_{l+k}.

These conditions ensure local optimality of the cost function either within or on the boundaries defined by the constraints.

Sequential Quadratic Programming (SQP), one type of non-linear programming (NLP) algorithm, optimizes the cost function by solving a series of sub-problems where the objective function is approximated as quadratic and the constraints are approximated as linear. The SQP method iterates the update equation

$$\boldsymbol{x}^q = \boldsymbol{x}^{q-1} + \zeta \boldsymbol{s}^q \tag{5.105}$$

where ζ dictates step size. The iteration process continues until a solution $\boldsymbol{x}^q$ satisfies the KKT conditions for constrained optimality. The first sub-problem is the determination of the search direction $\boldsymbol{s}^q$ by minimizing the quadratic function Q, that is

$$Q(\boldsymbol{s}^q) = J(\boldsymbol{x}^q) + \nabla J(\boldsymbol{x}^q)^T \boldsymbol{s}^q + \frac{1}{2}(\boldsymbol{s}^q)^T \boldsymbol{B} \boldsymbol{s}^q, \tag{5.106}$$

subject to the linear constaints

$$\nabla g_j(\boldsymbol{x}^q)^T\boldsymbol{s}^q + \sigma_j g_j(\boldsymbol{x}^q) \leq 0 \qquad j = 1, \ldots, l \tag{5.107a}$$

$$\nabla h_k(\boldsymbol{x}^q)^T\boldsymbol{s}^q + \bar{\sigma}_k h_k(\boldsymbol{x}^q) = 0 \qquad k = 1, \ldots, p. \tag{5.107b}$$

The matrix $\boldsymbol{B}$ approximates the Hessian matrix of the Lagrangian, $\nabla^2\Lambda$, and the parameters σ_j and $\bar{\sigma}$ ensure that the sub-problem possesses a feasible solution. Because of its form, the search direction sub-problem in amenable to solution via one of the various quadratic programming techniques available in Nocedal [126]. The optimal step size ζ in Eq. (5.105) is the focus of the second sub-problem and is determined such that the Lagrangian function $\Lambda(\boldsymbol{x}^q)$ is minimized. Because this sub-problem is one-dimensional, a simple line search method is employed to compute ζ [127]. Though this introduction to SQP is brief, a more thorough discussion is available in Eldersveld [128].

There are a variety of SQP implementations, but two popular algorithms are MATLAB©'s `fmincon` and the SNOPT packages developed by Gill, Murray, and Saunders [98]. This investigation uses the SNOPT algorithm because of its ease in implementation, quick computation times, and the ability to mix analytical and numerical derivatives. In addition, the SNOPT package solves the search direction and step size sub-problems internally, and the approximation matrix $\boldsymbol{B}$ is computed with no input from the user.

5.4.2.2 Initial and target states

The computation of rendezvous arcs requires the definition of an initial state from which the spacecraft departs whenever a thrust segment is initiated and a target state that serves as a matching condition for the spacecraft state vector upon arrival. This definition is accomplished by specifying the initial state $\boldsymbol{x}_I$ to be the position and velocity of a specified asteroid (or Earth, for the Earth-to-asteroid arc) that is denoted as the departure body for a particular rendezvous segment. Likewise, the target state $\boldsymbol{x}_T$ is the position and velocity of the desired arrival body. In the ephemeris point-mass model in Section 2.2.1, the states of celestial bodies at a given epoch are determined by interpolation of the HORIZONS data using a cubic spline with interpolation points at one-day intervals. For the simplified model in Section 5.2, however, an equivalent continuous path for the celestial body is determined, where the motion satisfies the natural dynamics from the sun-Jupiter CR3BP. Accordingly, for each asteroid a set of reference nodes are extracted from the HORIZONS data, transformed to the sun-Jupiter rotating frame, and supplied as the initial guess for a fixed-time multiple shooting corrections process, described in Sect. 2.4.1.3, where continuity is specified for all interior points. In this corrections scheme, the positions and velocities of the nodes are allowed to vary without constraint, so long as the resulting solution yields a continuous path for the asteroid motion. One such conversion is displayed in Fig. 5.5, with the original HORIZONS data represented by a dashed line and the reconverged continuous CR3BP trajectory plotted as the solid line. Motion for all 12 asteroids, as well as the Earth, is transitioned to the CR3BP. Once a tour trajectory is determined within the context of the CR3BP, the results are transitioned back to the point-mass ephemeris model to restore the true positions of the asteroids and the Earth.

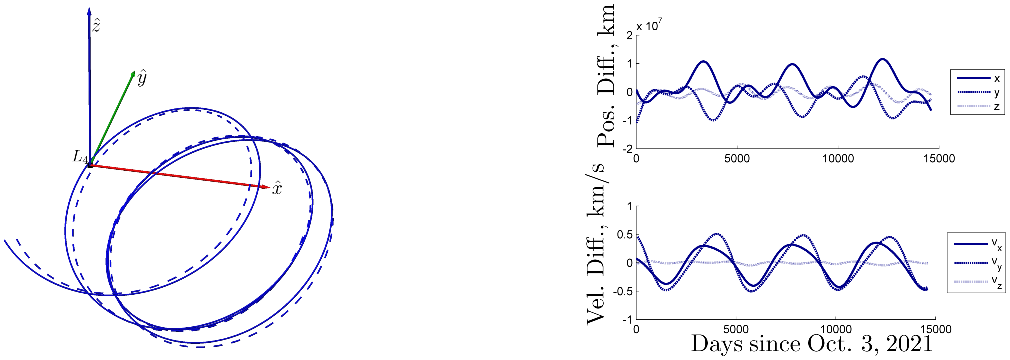

a. Asteroid track in sun-Jupiter rotating frame, ephemeris (dashed) and CR3BP (solid).

b. Deviation between CR3BP and ephemeris rotating frame components.

Figure 5.5.. Comparison of 1143 Odysseus trajectories from Oct. 3, 2021 to Oct. 3, 2061 from ephemeris data and under CR3BP dynamics

5.4.2.3 Rendezvous arc detection and computation

For even a relatively small number of asteroids, manually determining and generating all possible optimal rendezvous arcs is a laborious process. For example, for any given pair of asteroids, there are several epochs over the specified 40-year window that define a locally optimal departure state for a rendezvous arc. So, when all possible asteroid pairs are considered, hundreds of locally-optimal rendezvous arcs are available for any given thrust duration (TD). Therefore, an automated scheme that detects conditions amenable to locally optimal transfers and, subsequently, computes the corresponding point solutions is critical for rapid trajectory design.

The SQP algorithm adjusts the free variables in order to ensure that the mass objective is maximized while satisfying the constraints on asteroid arrival. The general corrections procedure defined in Sect. 2.4.1 provides a framework for addressing the nonlinear arrival constraints of the hybrid optimization scheme. Thus, the optimization problem for asteroid-to-asteroid arcs is posed as

$$\max J = m_f \tag{5.108}$$

with the free variables

$$\boldsymbol{X} = \begin{Bmatrix} \tau_0 \\ \boldsymbol{\lambda}_{\boldsymbol{r},0} \\ \boldsymbol{\lambda}_{\boldsymbol{v},0} \end{Bmatrix} \tag{5.109}$$

subject to the arrival constraints

$$\boldsymbol{F}(\boldsymbol{X}) = \boldsymbol{\psi}_f = \boldsymbol{x}_T - \boldsymbol{x}_T(\tau_0 + TD) = \boldsymbol{0} \tag{5.110}$$

from Eq. (5.57). Recall that the initial boundary conditions from Eq. (5.56) are implicitly satisfied by defining the spacecraft state at thrust initiation to the state of the departure object at the same epoch. While the SQP package SNOPT can numerically approximate required gradients, computational speed is improved by supplying user-defined values for the partial derivatives. Thus, the Jacobian for the objective function is obtained via

$$\nabla m_f = \begin{bmatrix} \boldsymbol{\Psi}(\tau_0 + TD, \tau_0)_{m,\boldsymbol{x}} \dot{\boldsymbol{x}}_{\boldsymbol{I}}(\tau_0) & \boldsymbol{\Psi}(\tau_0 + TD, \tau_0)_{m,\boldsymbol{\lambda}} \end{bmatrix} \tag{5.111}$$

where the subelements of the 14 × 14 STM relate the initial position and velocity states as well as costates to the spacecraft mass at thrust termination and $bm\dot{x}_I(\tau_0)$ is the time rate of change of the state of the departure body. Likewise, the Jacobian for the constraint vector Eq (5.110) is

$$D\boldsymbol{F}(\boldsymbol{X}) = \Big[\big(\boldsymbol{\Psi}(\tau_0 + TD, \tau_0)_{\boldsymbol{x},\boldsymbol{x}}\dot{\boldsymbol{x}}_{\boldsymbol{I}}(\tau_0) - \dot{\boldsymbol{x}}_{\boldsymbol{T}}(\tau_0 + TD)\big) \quad \boldsymbol{\Psi}(\tau_0 + TD, \tau_0)_{\boldsymbol{x},\boldsymbol{\lambda}}\Big] \tag{5.112}$$

where the STM terms relate initial changes in the spacecraft operational state to the final state at thrust termination.

Conditions likely to yield optimal transfers include low distance and low relative velocities between asteroids. One efficient strategy to detect these transfer conditions searches epochs for those that correspond to the minimum relative distance between an asteroid pair. Thus, solutions to the local optimization problem

$$\min d_a(\tau_0) = \|\boldsymbol{r}_T(\tau_0) - \boldsymbol{r}_I(\tau_0)\| \tag{5.113}$$

supply the initial guesses for the parameter τ_0 in the rendezvous problem. Thus, the problem involves only one free parameter, and a grid search readily produces all the solutions over the 40-year window of opportunity. Once the set of initial parameters τ_0 is determined, the hybrid optimization scheme is applied to generate thrust arcs connecting the paths of the asteroids. The result of this automated procedure as applied to the scenario where 8241 Agrius is the departure asteroid and 4138 Kalchas is the target is illustrated in Fig. 5.6. The positions of closest relative distance are signified by the green spheres for 8241 Agrius and the red spheres for 4138 Kalchas, with the black arcs representing the converged rendezvous arcs and the black spheres the actual departure and arrival states.

The hybrid optimization process yields a single rendezvous segment connecting two asteroids and resulting in a trajectory arc with minimum propellant consumption for a specified thrust duration. The initial and terminal states along these arcs correspond to approximate asteroid positions and velocities from the CR3BP dynamical model such that the spacecraft is delivered from the vicinity of one asteroid to that of

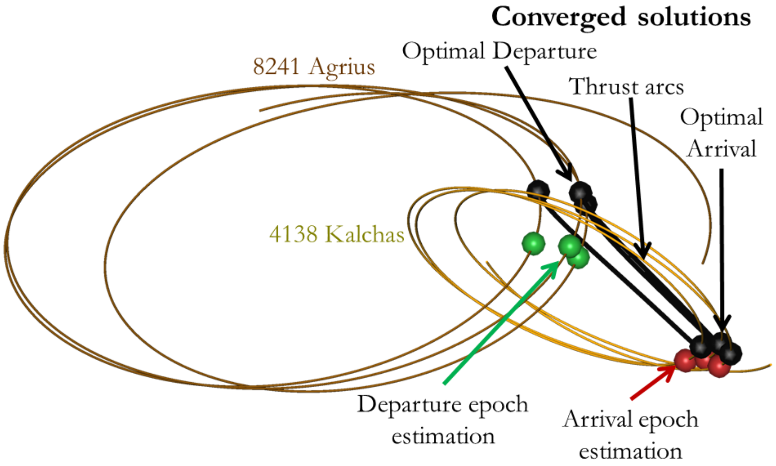

Figure 5.6.. Initial guess of the rendezvous epochs for arcs from 8241 Agrius departure (green) to 4138 Kalchas arrival (red), with corresponding rendezvous arcs (black)

another. However, once a point solution is generated for a single specified thrust duration, TD, a simple continuation scheme is applied that produces trajectory arcs over a large range of thrusting times. The continuation process updates the value of TD and uses the previously computed solution as the initial guess for the subsequent 2PBVP. The complete set of thrust arcs that is determined via the continuation scheme, termed a "family", represents a set of options for a single pre-determined asteroid-to-asteroid link within a design space relating engine operation time and propellant consumption for a spacecraft transfer. For this analysis, families of transfer arcs between any asteroid pair with thrust durations between $TD = 0.7$ and a nominal maximum $TD = 2.0$ in non-dimensional time units, incremented in steps of 0.02 non-dimensional time units, or 483 to 1379 days in 14 day steps, are produced. Some families do not cover the full range of thrust durations since the iteration process is terminated once the epoch expands to the limits of the window, i.e., Oct. 3, 2021 to Oct. 3, 2061. Note that for every thrust arc segment within these families, the initial spacecraft mass is assumed to be $m_0 = m_r = 500$ kg, or $m_0 = 1$ non-dimensional unit. (Of course, this initial mass may be adjusted in the tour construction process.) Once the independent solutions comprising the families of rendezvous arcs are computed, the initial conditions are stored for future use; this set of stored initial conditions is termed a “library”.

5.5 Search strategies: enumerated tree searches and ant colony optimization

Construction of potential survey tours is accomplished via the use of two distinct search methods. The first, an enumerated tree search, reveals all possible solutions, albeit for a pre-specified asteroid-to-asteroid thrust duration. Furthermore, the computational cost of the tree search method grows exponentially with the inclusion of additional target asteroids. In contrast, the second search method, ant colony optimization, enables the exploitation of the trade-off between thrust duration and propellant consumption that is intrinsic to the operation of VSI systems while simultaneously offering a more managable growth in computational cost. The operation of both search methods is detailed.

5.5.1 Enumerated tree search

To generate a potential tour sequence, an automated process extracts independent families of arcs from the library of solutions, selects individual rendezvous legs from within these families, and combines them into a series of thrust arcs between the asteroids and coast segments in the vicinity of the objects. This selection and joining of independent thrust arcs is performed via an enumerated tree search wherein all potential new targets are exhaustively searched. Figure 5.7 illustrates the operation of the tree search method. Note that for NP-hard problems enumerated tree searches quickly become computationally expensive and can be replaced with other search methods such as branch-and-bound.

Since there are many possible thrust arcs across any given family, and the automatic procedure extracts only one solution arc per family, a trade-off is available

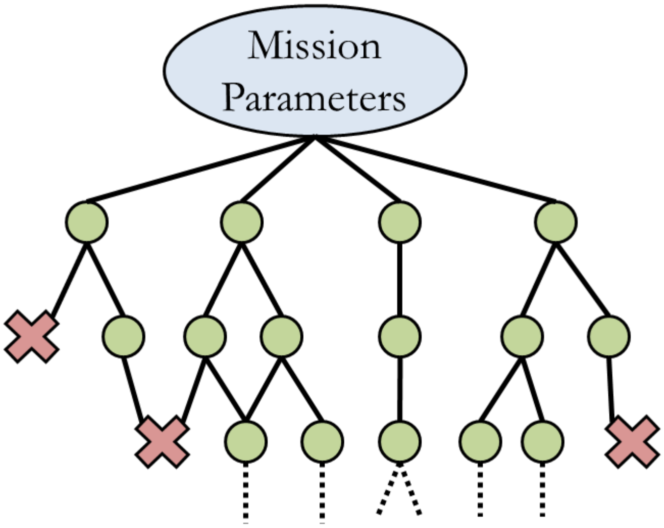

Figure 5.7.. Schema of the enumerated tree search algorithm. Note that, in general, intermediate target asteroids (green circles) or terminal asteroids (red X's) can appear on multiple paths.

between thrust duration TD, departure epoch τ_0, and arrival mass m_f. In general, m_f increases with TD while τ_0 decreases; however, it is observed that the quantity $(TD + \tau_0)$ usually increases with larger values of TD. For this investigation, the tour sequence algorithm allows the user to select one of three possible thrust duration options over all families in a potential sequence:

- maximum TD, with maximum m_f and arrival epoch as well as minimum τ_0;
- minimum TD, with the reverse result;
- median TD, with median values of arrival mass and departure and arrival epochs.

Once specific thrust arcs are selected, approximations are employed to estimate the performance metrics associated with a particular tour. For example, propellant consumption during each interval of engine operation must be incorporated into an equivalent cost corresponding to any potential tour scenario comprised of several rendezvous arc segments. Accordingly, for a rendezvous sequence built from n thrust intervals, the approximate consumption of propellant mass, m_{cons}, is computed via

$$m_{consumed} = m_0 \left(1 - \prod_{i=1}^{n} \frac{m_i}{m_0} \right) \tag{5.114}$$

where m_i is the arrival mass in kilograms at the end of the i^{th} independently generated thrust arc.[3] For feasible options, this easy to compute approximation can always be evaluated against a more rigorous model, such as an end-to-end optimization or the scaling relations in Section 5.6.3.

Since the families representing asteroid-to-asteroid transfer arcs are independently created, the selected rendezvous sequences must be evaluated to ensure they are physically realizable and satisfy mission constraints. Frequently, the two most common constraints in mission design are propellant mass and mission duration, i.e., a finite amount of mass is available and a limited opportunity usually exists for a timeline.

---

[3] For the case of impulsive maneuvers, an equivalent total trajectory cost is $\Delta v_{tot} = \sum_{i=1}^{p} \Delta v_i$ where Δv_{tot} is the total impulsive Δv and Δv_i is the equivalent value for one maneuver.

Therefore, a maximum amount of propellant is available for activities within the swarm m_p and a maximum mission duration, TOF, is specified in the automated tour design scheme. Thus, for a tour to be feasible, the estimated propellant consumption, m_{cons}, must be less than m_p and the final rendezvous must occur before $\tau_d + TOF$ where τ_d is the epoch corresponding to Earth departure. Additionally, since the goal is survey options for missions to the Trojan asteroids, a further constraint is imposed, that is, the spacecraft cannot re-visit an asteroid after departure. Ultimately, the arc selection procedure is summarized in Table 5.4. Recall that the optimization of a VSI engine requires a constraint upon either thrust duration or

Table 5.4. Arc selection procedure for tour generation.

Step	**Description**
1	Select specific desired asteroid arrival epoch and thrust duration options as well as specify asteroid swarm propellant mass m_p and end-to-end mission timeline TOF.
2	For each asteroid of interest, perform Steps 3-8.
3	Retrieve from library all thrust arc families departing from current asteroid.
4	Remove families that return to previously visited asteroids.
5	For given TD option, eliminate all families with departure epochs prior to the current departure epoch or beyond the arrival epoch $\tau_d + TOF$.
6	Estimate spacecraft mass at end of all thrust arcs and remove families where $m_{cons} > m_p$.
7	For the remaining families, update tour information to include data from new arcs.
8	Repeat Steps 3-7 until the exploration of all possible tours is complete.

propellant consumption: therefore, all Earth-to-asteroid outbound legs in this investigation possess a pre-specified duration of 3.5 years, slightly longer than the 2.7 years required for a Hohmann transfer, though this value is readily altered. Accordingly, the Earth departure epoch τ_d is easily computed once an asteroid arrival epoch is selected. The result of the sequence construction procedure is a set of potential tours with estimated propellant mass consumption values less than m_p and with total time within the swarm that is less than $(TOF - 3.5)$ years. Performance metrics include propellant consumed, swarm tour duration, coast time in the vicinity of the asteroids, and the number of asteroid encounters; specific sequences of interest are then selected for further analysis.

5.5.2 Ant colony optimization with parallel pheromone distribution

Ant colony optimization scenarios usually assume a simplified, if not static, transition option between target nodes, with an accompanying simplification in the implementation details, where this abstraction of the problem may eliminate vital characteristics of the underlying system dynamics. While the SACO algorithm detailed in Sect. 2.5.1 can, in practice, be applied to mission planning scenarios, several considerations point to a novel ACO solution approach, one that may in fact be a more true mimicry of actual ant foraging behavior than is typical of SACO.

5.5.2.1 Parallel pheromone distribution

One chief difference between spacecraft trajectory applications of ACO and more traditonal ACO scenarios is that astrodynamics problems typically involve an infinite number of potential connections between celestial objects of interest rather than a single link. Furthermore, many SACO applications either intrinsically possess easy-to-compute link costs or scenarios are readily abstracted to a simplified model whereas mission analysis and design must maintain a higher level of model fidelity in order to ensure viable resulting trajectories. Thus, rather than a sparse network with a relatively low number of analytically modeled links between nodes, astrodynamics applications typically present a very dense grid of connections, each possessing a unique but infinite trade space that generally must be constructed numerically. While large portions of these trade spaces can be eliminated due to physical, logistical, or other practical considerations, there still remains an infinite possible number of solutions due to the continuous nature of the underlying dynamics. Thus, a discretization of the search space is required, though this may still result in very large search spaces. For example, in the current investigation, roughly 36,000 individual thrust arcs are constructed computationally between asteroid pairs for a set of 12 objects over a 40-year window. However, these rendezvous arcs are grouped into 551 families characterized by the close approach epochs between asteroid pairs and offering a trade-off between thrust duration and propellant consumption.

The highly correlated nature of the asteroid-asteroid rendezvous legs within distinct families naturally leads to the concept of ACO with parallel pheromone distribution (ACO-PPD), that is, ACO wherein successful tours spread pheromone to nearby links as well. Thus, if an individual arc from a family is part of a successful tour, then some amount of pheromone is applied to solutions in the family with similar thrust duration values ("parallel" solutions), as illustrated in Fig. 5.8. Accordingly, when the ants are following pheromone trails, the potential to explore nearby solutions also exists which could offer improved performance over the previously traveled sequence. The distributed pheromone can be spread to any number of arcs within the family, although, in practice, a balance is struck between increasing the number of potential solutions to explore and maintaining a low computational overhead (i.e., if pheromone is spread to all possible arcs, the compuational cost for one ant approaches that of an enumerated tree search algorithm). The distribution over the nearby arcs can also be modeled from one of several profiles: for the current investigation, both uniform and Gaussian distributions of pheromone are considered. When normal distributions are employed, the standard deviation is assumed to be

$$\sigma = \sqrt{N_{ps}} \tag{5.115}$$

where N_{ps} is the one-sided number of arcs over which the pheromone is spread (i.e., if $N_{ps} = 5$, pheromone is placed on 11 members of the family, i.e., the traveled leg plus 5 solutions with larger TD values and 5 with lower durations). While the current implementation generates tours using pre-computed low-thrust arcs between asteroids, ACO-PPD can be readily adapted to support a diverse range of mission planning architectures.

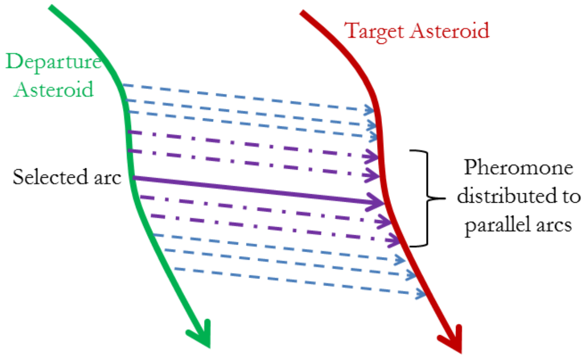

Figure 5.8.. Diagram of asteroid-asteroid family with traveled arc and pheromone distributed to nearby thrust legs.

5.5.2.2 Generation of asteroid tours

Though pheromone distribution supplies a powerful framework for extending ACO to astrodynmics applications, several implementation details remain to fully incorporate ACO-PPD to the generation of asteroid tours. Notably, link costs are often more complex for spacecraft trajectories than most SACO applications. Additionally, SACO usually assumes that all nodes must be transited for the least cost or that the optimal route from one specific node to another is desired (note that the latter case is analogous to the determination of the optimal trajectory from Earth to another planet, say Jupiter or Saturn). However, for the construction of asteroid tours, it is not feasible to visit all potential targets with one trajectory and selecting specific target asteroids *a priori* may unduly restrict preliminary explorations of the design space. In fact, the concept of an "optimal" spacecraft tour is heavily dependent on the relative weighting assigned to propellant and operations costs, the desired number of objects, relative scientific value of various targets, and many other considerations. Thus, this investigation expands SACO and ACO-PPD concepts to favor options beyond optimal route-finding, e.g., the best selection of potential targets within the context of limited resources. This implementation of an ACO-PPD strategy may, in fact, produce a better model of ant scavenging behavior than previous SACO applications.

When not actively following pheromones, ants explore by randomly selecting a previously unvisited target asteroid and tracking the first feasible family (characterized by the rendezvous leg of median thrust duration TD value) that links the current asteroid to the target asteroid. If no families linking these two specific asteroids include a feasible median TD arc, the destination asteroid is discarded and a new target is randomly selected. If all asteroids are excluded by this procedure, then the ant terminates its tour. Ant exploration behavior is triggered under the following circumstances:

- at the current node, *exploration* is selected based upon the exploration probability γ; or,
- if *following* is identified, then either no pheromone exists on arcs departing the current asteroid or none of the pheromone trails satisfy time or propellant constraints.

Using these conditions, the ants are guaranteed to continue encountering new asteroids until the limits on total time-of-flight or maximum propellant capacity are reached.

A crucial aspect of ACO is the definition of the link quality metric, i.e., $B_{i,j}$, that conveys local information to traveling ants and aids in the determination of the travel probability represented in Eq. (3.27). For asteroid tour applications, one potential metric is

$$B_{i.j} = \frac{w_j^W p_{i,j}^M}{\Delta t_{i,j}^L} \tag{5.116}$$

where w_j is the target importance, $p_{i,j}$ is the propulsive cost to travel from object i to the j^{th} asteroid, $\Delta t_{i,j}$ is the time to travel from one object to the next, and W, M, and L are weighting parameters. For Trojan asteroid tours, the target importance w_j is set equal to the scientific priorities in Table 5.3 and the propulsive cost is defined to be $p_{i,j} = m_{f:i,j}$, that is, the arrival mass along the independently computed thrust arc. Thus, the link quality of an arc is not affected by the mass consumption along previous arcs. The time metric is defined as $\Delta t_{i,j} = t_{f:j} - t_{f:i}$, that is, the difference in arrival epochs between the next asteroid and current asteroid; note that this value includes the loiter time at the current asteroid as well as the transit time between the current object and the next encounter. Thus, Eq. (5.116) is reformulated as

$$B_{i.j} = \frac{w_j^W m_{f:i,j}^M}{\Delta t_{i,j}^L} \tag{5.117}$$

where all required information is available either from the pre-computed thrust arc families or the pre-specified asteroid priority.

While SACO implementations often specify that the overall quality of a solution is a simple summation of the link costs across the sequence, other methods of defining tour quality are available. Recall that for the current investigation, the individual link quality metric $B_{i.j}$ includes the relative priorities concerning time, propellant, and target, all of which are locally important. However, the tour quality value Q that informs the update to pheromone levels can represent any combination of local and global information across the tour sequence and, hence, affords another level of control over the performance of the algorithm. Therefore, several different formulations of 'tour quality', summarized as follows, are examined:

- *Summed link quality*: This tour quality metric is consistent with many SACO implementations by summing the individual link quality corresponding to each tour via
$$Q = w_1^W + \sum_{\substack{j=2 \\ i=j-1}}^{N_e} B_{i,j} \tag{5.118}$$
where N_e is the total number of asteroid encounters. Only the merit of the first target is included as Earth-to-asteroid legs are not considered in this ACO investigation.

- *Number of encounters*: Tours are ranked solely upon the number of asteroids encountered, without regard to propellant cost or asteroid priority such that
$$Q = N_e. \tag{5.119}$$

- *Summed object merit*: Quality of tours is determined by summing the importance of the encountered asteroids by
$$Q = \sum_{j=1}^{N_e} w_j \tag{5.120}$$
where a fewer number of higher priority targets could elevate its ranking over a tour to a larger number of less important objects.

- *Combined importance and loiter time*: The importance of the asteroids is multiplied by the duration of proximity operations at the object and then summed as
$$Q = \sum_{j=1}^{N_e} w_j LT_j \tag{5.121}$$
where LT_j is essentially the loiter time, i.e. the interval spanning the arrival at the j^{th} object to departure from the same asteroid. Thus, tours that include longer durations at higher priority targets are favored. However, a maximum useful loiter time $LT_{\max}$ can be instituted such that any proximity duration above this threshold is not incorporated into Eq. (5.121).

Each of these tour quality definitions, aside from the summed link quality, allows for the tour quality to be developed independently of the local behavior of the ants. A related factor is the number of ants N_{sa} that lay pheromone trails. Any implementation where the number of pheromone laying ants is less than the total number of ants, i.e., $N_{sa} < N_a$, necessitates a ranking of the ants by their respective tour qualities Q. For ACO-PPD implemenations, a larger value for N_{sa} allows more pheromone spread and, hence, a broader survey of the design space while a lower number focuses on improvement in the few best routes.

Similar to the recognized tendency for ACO algorithms to rapidly "lock" onto known routes, ACO-PPD may concentrate ants along only a few highly favorable encounter sequences within the first few ant generations. While this behavior may allow a more thorough exploration of the continuous trade spaces associated with particular asteroid progressions, it may also neglect other advantageous target sequences. Thus, a selection criteria to favor unique series over rendezvous chains with identical orders of encounter, but possibly a different set of individual arcs, has also been included. With this option, unique successions of asteroids are placed ahead of all but the highest quality examples of repeated sequences; for example, if three of the top asteroid series include a repeated encounter progression but differing individual legs, then only the best performing example is retained and the remaining two are placed behind all the potential tours with unique asteroid orders.

Finally, seeding the initial distribution of the ants for each generation supplies another level of input into the ACO implementation process. Two methods are employed in this investigation, namely i) randomly distributing ants to seed each generation, or ii) for each ant, based upon current exploration probability γ, either place it at a random starting location or stochastically locate the ant at a starting node based upon pheromone concentrations departing the nodes. In the latter case, the probability at being placed at the i^{th} asteroid is given by

$$P_i = \frac{\sum_{j=1}^{N_p} \tau_{i.j}}{\sum_{i=1}^{N_{ast}} \sum_{j=1}^{N_{p:i}} \tau_{i.j}} \tag{5.122}$$

where N_{ast} is the total number of asteroids and $N_{p:i}$ is the total number of links with pheromone departing the i_{th} asteroid. Consistent with previous options, random assignment of the initial object favors exploration for good sequences while ant placement based upon pheromone concentration benefits the more thorough exploitation of a fewer number of sequences. Note, however, that even though an initial target is not selected *a priori*, the current implementation of ACO-PPD does require a pre-specified swarm arrival epoch.

5.5.2.3 Comparison to enumerated tree search

While this investigation does not include a rigorous benchmark comparison between ant colony optimization and other graph search methods, some predictions about ACO-PPD performance relative to enumerated tree searches can be made. Assume, as an example, that a set of 15 distinct asteroid sequences originate from 624 Hektor for the swarm arrival epoch of 2026; this set of tours, averaging nearly three asteroid encounters, is a fairly conservative representation of the average performance, in both number of tours discovered and number of encounters per tour, exhibited by an enumerated tree search scheme. [73, 75] Assuming that each pre-computed family represented in the asteroid tours contains 66 members, fully assessing each potential combination of thrust arcs within a tour requires 4356 operations. Thus, fully characterizing the trade space, that is, all possible sets of thrust arcs associated with the employed rendezvous families within all tours, associated with one initial target asteroid requires approximately 65,340 computations and, therefore, examining all 12 potential targets necessitates on the order of 784,000 operations for just one swarm arrival epoch. These numbers, of course, discount the possibility that, even for identical asteroid sequences, different combinations of individual asteroid-asteroid legs may engender or preclude further potential encounters (i.e., one set of arcs from a three asteroid sequence may enable the spacecraft to visit a fourth target, while a different combination consumes too much propellant for the spacecraft to reach any further objects). Furthermore, the number of operations to fully enumerate the tour trade space grows exponentially with each additional asteroid added to the search.

Ant colony optimization, even with distributed pheromones, offers a much more managable growth in computational cost. Assuming, as before, an average of 3 asteroids per tour, with an average of 20 members per family with pheromone, each ant requires on the order of 400 operations to create a tour. If 25 ants are used per generation (resulting in approximately 10,000 computations per generation), over 78 generations of the ACO-PPD algorithm would be required to match the computational cost of the 12-asteroid enumerated tree search performed at the same epoch (recall that the current implementation of ACO-PPD necessitates the *a priori* selection of an arrival epoch) and that assesses all possible members of each family of rendezvous solutions. This, of course, does not consider that at each asteroid several departure rendezvous families, with associated pheromones, may be assessed before the selection of the next target. On the other hand, this figure assumes that every ant always follows pheromone trails and neglects the significant computational cost savings when exploration behavior is selected (as it will be for a relatively significant proportion of any ACO run). Furthermore, the computational cost of the ACO-PPD algorithm is relatively fixed, regardless of the number of target asteroids. Thus, ACO-PPD offers significant advantage when larger numbers of asteroids are included in the tour creation process.

5.6 Mission operations: high-fidelity baseline architectures

The automated rendezvous path generation process supplies estimated trajectory performance for potential encounter sequences within the asteroid swarm. As the rendezvous costs and timings for the swarm tours are, at best, approximations confined to the Sun-Jupiter L_4 region, potential trajectories must be transitioned to higher fidelity baselines incorporating an Earth-to-asteroid transfer leg. Furthermore, recall that the pre-computed asteroid-asteroid low-thrust transfers are computed assuming a pre-specified spacecraft mass and engine power. However, since human mission planners may wish to consider a range of spacecraft parameters, scaling relationships are developed for the performance of the low-thrust propulsion system.

5.6.1 Generation of outbound Earth-to-swarm leg

For a specific Trojan tour of interest, an Earth-to-swarm segment must be included such that the spacecraft rendezvous with the first asteroid in the tour occurs at or prior to the asteroid arrival epoch specified in the sequence generation process. The computation of the Earth-to-asteroid arc consequently determines the true arrival epoch at the initial target asteroid. As previously stated, the Earth departure leg greatly benefits from the inclusion of a hybrid propulsion scheme assuming an initial departure velocity is allowed. Propellant mass is optimized by targeting a final spacecraft mass of $m_f = m_r$ while using SNOPT to minimize the spacecraft mass at Earth departure, that is m_0. However, the inclusion of a departure velocity invalidates the initial boundary condition as posed in Eq. (5.56). Position continuity must be maintained, but velocity is now constrained, i.e.,

$$\sqrt{\Delta \boldsymbol{v}_I \cdot \Delta \boldsymbol{v}_I} - V_\infty = 0 \tag{5.123}$$

where $\Delta \boldsymbol{v}_I = \boldsymbol{v}_I - \boldsymbol{v}_\oplus(\tau_0)$, such that $\boldsymbol{v}_I$ is the spacecraft initial velocity and the vector $\boldsymbol{v}_\oplus(\tau_0)$ is defined as the velocity of Earth at spacecraft departure. The departure V_∞ is selected based upon the capabilities of a chemical booster stage or hyperbolic velocity after an Earth fly-by. Thus, for the interplanetary leg, SNOPT minimizes the initial spacecraft mass m_0 subject to the constraints in Eqs. (5.57) and (5.123) and position continuity with the Earth at the initial departure epoch.

The optimization problem for NEP and SEP enabled outbound legs is therefore formulated with objective function

$$\min J = m_0 \tag{5.124}$$

as well as free variables

$$\boldsymbol{X} = \begin{Bmatrix} \tau_0 \\ \boldsymbol{v}_0 \\ m_0 \\ \boldsymbol{\lambda}_{\boldsymbol{rv},0} \end{Bmatrix} \tag{5.125}$$

and a constraint vector

$$\boldsymbol{F}(\boldsymbol{X}) = \begin{Bmatrix} \boldsymbol{x}_T^t - \boldsymbol{x}_T \\ m_f^t - m_r \\ \sqrt{\Delta\boldsymbol{v}_I \cdot \Delta\boldsymbol{v}_I} - V_\infty \end{Bmatrix} = \boldsymbol{0} \tag{5.126}$$

that includes the arrival at the target asteroid, spacecraft mass matching, and constraint on Earth departure excess velocity. Recall that the superscript t indicates the value obtained from the terminal state of a propagation. Because the initial spacecraft mass is both a free variable as well as the objective function, the objective gradient is readily realized as

$$\nabla m_0 = \begin{bmatrix} \mathbf{0}_{1,4} & 1 & \mathbf{0}_{1,6} \end{bmatrix} \tag{5.127}$$

where the subscripts i, j on the zero vectors indicate a row vector ($i = 1$) of length j. The constraint gradient is supplied by

$$D\boldsymbol{F}(\boldsymbol{X}) = \begin{bmatrix} \left(\boldsymbol{\Psi}_{\boldsymbol{x},\boldsymbol{r}}\boldsymbol{v}_\oplus - \dot{\boldsymbol{x}}_{\boldsymbol{T}}\right) & \boldsymbol{\Psi}_{\boldsymbol{x},\boldsymbol{v}} & \boldsymbol{\Psi}_{\boldsymbol{x},m} & \boldsymbol{\Psi}_{\boldsymbol{x},\boldsymbol{\lambda}} \\ \boldsymbol{\Psi}_{m,\boldsymbol{r}}\boldsymbol{v}_\oplus & \boldsymbol{\Psi}_{m,\boldsymbol{v}} & \boldsymbol{\Psi}_{m,m} & \boldsymbol{\Psi}_{m,\boldsymbol{\lambda}} \\ -\frac{\Delta\boldsymbol{v}_I^T}{\Delta v_I}\dot{\boldsymbol{v}}_\oplus & \frac{\Delta\boldsymbol{v}_I^T}{\Delta v_I}\mathbf{I}_3 & 0 & \mathbf{0}_{1,6} \end{bmatrix} \tag{5.128}$$

where the STM elements are defined as in Sect. 5.4.2.3 and the natural acceleration of the Earth, $\dot{\boldsymbol{v}}_\oplus$, is provided by the appropriate dynamical model, i.e., CR3BP or point-mass ephemeris.

The outbound phase of the trajectory design process is also automated by creating a library of pre-generated trajectory arcs using CR3BP dynamics and an NEP engine. So, point solutions for locally optimal rendezvous arcs between Earth and each of the 12 sample asteriods are computed where the departure epoch τ_d occurs within the year 2018 and the spacecraft arrives in the vicinity of the asteroid swarm 3.5 years later in

2021. Thereafter, for any specific tour, the pre-computed departure epoch is adjusted by a integer multiple of the Earth-Jupiter synodic period, that is, 398.88 days, such that the spacecraft arrives at the initial asteroid only a short time in advance of the selected starting epoch for the asteroid tour. Other mission parameters such as the Earth-departure V_∞ and the spacecraft reference mass m_r can also be readily adjusted to examine alternate launch vehicles. Reference solutions determined using default values for these parameters are scaled using the relations in Section 5.6.3 and, when necessary, re-optimized to produce trajectories satisfying these new mission requirements. Likewise, if a specific Earth launch mass is desired, the optimization method can be reformulated such that propellant consumption is specified while the Earth-to-asteroid thrust duration is optimized.

The construction of an outbound leg using a power-limited SEP system offers a challenge; the engine model switches from a constant-power regime defined by the fixed maximum engine power to a varying-power domain where the sun distance determines the available power. In this investigation, the switch between thrust regimes is accomplished by introducing an intermediate patch point along the thrust arc, where the node is defined by the state vector $\boldsymbol{\chi}_s$ and co-state vector $\boldsymbol{\lambda}_s$. Thus, two forward-propagated nodes, the first at the Earth and the second at the switch point, define the PLS Earth-to-asteroid legs. Prior to the switch point, the spacecraft engine operates with constant power $P_{\text{max}} = P_{\text{lim}}$ while beyond the switch point, the varying power is determined by $P_{\text{max}} = \frac{P_{\text{ref}}}{d_s^2}$, with the appropriate control laws and co-state equations of motion. However, this switch must occur when the power available from the sun matches the limit on maximum engine power. Accordingly, the constraint

$$\frac{P_{\text{ref}}}{d_s^2} - P_{\text{lim}} = 0 \tag{5.129}$$

is incorporated when generating trajectories using a PLS system. Recall that the symbol d_s denotes the magnitude of the displacement vector $\boldsymbol{d}_s$ from the Sun. Either a NEP or SEP enabled outbound leg seeds the estimates for the initial co-states of the nodes, while the initial guess for the state of the switching node is determined by when the seeding NEP or SEP arc satisfies the conditions in Eq. (5.129). Additional constraints on the PLS-enabled trajectory include

$$t_c + t_v - TD_{out} = 0 \tag{5.130}$$

and, for trajectories using ephemeris dynamical models, an additional timing constraint is necessary, i.e.,

$$\tau_s - \tau_d - t_c = 0 \tag{5.131}$$

where t_c is the time spent thrusting under constant power, t_v is the duration of time under varying power, TD_{out} the total thrust interval on the outbound leg, τ_s represents the switch epoch, and τ_d corresponds to the epoch at Earth departure. Continuity in the state vector is ensured by

$$\boldsymbol{\chi}_s^t - \boldsymbol{\chi}_s = \mathbf{0} \tag{5.132}$$

where $\boldsymbol{\chi}_s^t$ corresponds to the spacecraft state vector at the end of the constant-power thrust arc and $\boldsymbol{\chi}_s$ is the initial seven-dimensional state on the varying-power segment. During preliminary optimization runs, no restriction was placed on the continuity involving the co-state vector $\boldsymbol{\lambda}_s$, however, the naturally emerging optimal solution results in co-state continuity across the two thrust domains. Accordingly, the constraint

$$\boldsymbol{\lambda}_s^t - \boldsymbol{\lambda}_s = \mathbf{0} \tag{5.133}$$

is also included for PLS outbound legs, where the addition of this constraint also allows improved convergence of the numerical optimization process. This result reflects the more straightforward implementation, that is, removing the switching node and, alternately, constructing a set of equations of motion wherein the switch in engine power domain is an automatic function of the spacecraft position.

Incorporating the new variables as well as constraints into the optimization problem for PLS enabled outbound legs with the switching point explicitly included yields the free variable vector

$$\boldsymbol{X} = \left\{ \begin{matrix} \tau_d \\ t_c \\ \boldsymbol{v}_0 \\ m_0 \\ \boldsymbol{\lambda}_{\boldsymbol{rv},0} \\ \tau_s \\ t_v \\ \boldsymbol{\chi}_s \\ \boldsymbol{\lambda}_s \end{matrix} \right\} \tag{5.134}$$

and a constraint vector

$$\boldsymbol{F}(\boldsymbol{X}) = \left\{ \begin{matrix} \boldsymbol{\chi}_s^t - \boldsymbol{\chi}_s \\ \boldsymbol{\lambda}_s^t - \boldsymbol{\lambda}_s \\ \boldsymbol{x}_T^t - \boldsymbol{x}_T \\ m_f^t - m_r \\ t_c + t_v - TD_{out} \\ \tau_s - \tau_d - t_c \\ \frac{P_{\mathrm{ref}}}{d_s^2} - P_{\mathrm{lim}} \\ \sqrt{\Delta\boldsymbol{v}_I \cdot \Delta\boldsymbol{v}_I} - V_\infty \end{matrix} \right\} = \boldsymbol{0} \tag{5.135}$$

while the mass objective function is unchanged from Eq. (5.124). As with a NEP or SEP enabled outbound leg, the objective gradient is readily realized as

$$\nabla m_0 = \begin{bmatrix} \boldsymbol{0}_{1,5} & 1 & \boldsymbol{0}_{1,14} \end{bmatrix} \tag{5.136}$$

where the subscripts i, j are as before. The constraint gradient is supplied by

$$D\boldsymbol{F}(\boldsymbol{X}) = \begin{bmatrix} \boldsymbol{\Psi}_{\boldsymbol{\chi},\boldsymbol{r}}\boldsymbol{v}_{\oplus} & \dot{\boldsymbol{\chi}}_s^t & \boldsymbol{\Psi}_{\boldsymbol{\chi},\boldsymbol{v}} & \boldsymbol{\Psi}_{\boldsymbol{\chi},m} & \boldsymbol{\Psi}_{\boldsymbol{\chi},\boldsymbol{\lambda}} & 0 & 0 & -\mathbf{I}_7 & \mathbf{0}_7 \\ \boldsymbol{\Psi}_{\boldsymbol{\lambda},\boldsymbol{r}}\boldsymbol{v}_{\oplus} & \dot{\boldsymbol{\lambda}}_s^t & \boldsymbol{\Psi}_{\boldsymbol{\lambda},\boldsymbol{v}} & \boldsymbol{\Psi}_{\boldsymbol{\lambda},m} & \boldsymbol{\Psi}_{\boldsymbol{\lambda},\boldsymbol{\lambda}} & 0 & 0 & \mathbf{0}_7 & -\mathbf{I}_7 \\ 0 & 0 & \mathbf{0}_{1,3} & 0 & \mathbf{0}_{1,6} & \frac{\partial \boldsymbol{x}_T^t}{\partial \tau_s} & \left(\dot{\boldsymbol{x}}_T^t - \dot{\boldsymbol{x}}_T\right) & \boldsymbol{\Psi}_{\boldsymbol{x},\chi} & \boldsymbol{\Psi}_{\boldsymbol{x},\boldsymbol{\lambda}} \\ 0 & 0 & \mathbf{0}_{1,3} & 0 & \mathbf{0}_{1,6} & \frac{\partial m_f^t}{\partial \tau_s} & \dot{m}_f^t & \boldsymbol{\Psi}_{m,\chi} & \boldsymbol{\Psi}_{m,\boldsymbol{\lambda}} \\ 0 & 1 & \mathbf{0}_{1,3} & 0 & \mathbf{0}_{1,6} & 0 & 1 & \mathbf{0}_{1,7} & \mathbf{0}_{1,7} \\ -1 & -1 & \mathbf{0}_{1,3} & 0 & \mathbf{0}_{1,6} & 1 & 0 & \mathbf{0}_{1,7} & \mathbf{0}_{1,7} \\ 0 & 0 & \mathbf{0}_{1,3} & 0 & \mathbf{0}_{1,6} & 0 & 0 & \tilde{\mathbf{P}} & \mathbf{0}_{1,7} \\ -\frac{\Delta \boldsymbol{v}_I^T}{\Delta v_I}\dot{\boldsymbol{v}}_{\oplus} & 0 & \frac{\Delta \boldsymbol{v}_I^T}{\Delta v_I}\mathbf{I}_3 & 0 & \mathbf{0}_{1,6} & 0 & 0 & \mathbf{0}_{1,7} & \mathbf{0}_{1,7} \end{bmatrix} \tag{5.137}$$

where the submatrix $\tilde{\mathbf{P}}$ is

$$\tilde{\mathbf{P}} = \left[-\frac{2P_{\text{ref}}}{d_s^4}\boldsymbol{d}_s^T \quad \mathbf{0}_{1,4}\right] \tag{5.138}$$

and the partial derivatives $\frac{\partial \boldsymbol{x}_T^t}{\partial \tau_s}$ and $\frac{\partial m_f^t}{\partial \tau_s}$ are zero if the system of natural dynamics is time invariant. When the equations of motion are time varying, finite differencing suffices to produce these elements of the constraint gradient matrix.

5.6.2 End-to-end optimization

Transitioning any solution or design concept to a higher-fidelity regime, including a point-mass ephemeris model, is a key step for validation of the results. Given a possible asteroid tour mission, the cost as well as timing estimates and engine operation histories are obtained using the hybrid optimization scheme in the point-mass ephemeris model. Optimal point solutions computed using the CR3BP provide initial guesses for the corresponding optimal thrust arcs under the influence of the higher fidelity dynamics. The epoch parameter τ_0 directly translates between the two models of natural dynamical motion whereas the initial co-states defining the operation of the low-thrust engine are recovered via the adjoint control transformation (ACT) detailed in Sect. 5.4.1.5. For this investigation, only the gravity of the sun and Jupiter are incorporated in the point-mass ephemeris model; the gravitational effect of other celestial bodies, e.g., Mars and Saturn, are only slight perturbations on the overall motion, even along the outbound leg. The gravitational field of the Earth is likewise neglected in this preliminary investigation because the spacecraft quickly escapes the Earth sphere of influence: outside of this relatively small region, the perturbative effect of the mass of the Earth is also negligible. However, a more detailed investigation of trajectories in the Earth-moon region would be required if any of the preliminary results are transitioned to a later-stage mission design architecture.

As previously noted, the time-free optimal operation of the VSI engine drives the thrust duration to infinity while reducing the propellant consumption to zero, both for individual arcs as well as full end-to-end trajectories with thrust and coast periods. Thus, bounds placed upon the duration or propellant consumption of individual thrust arcs, as is the case when specified loiter times or transfer durations are desired, results in a separation of the end-to-end optimization process into a series of individual optimizations. For instance, optimization of the full end-to-end trajectory incorporating thrust duration constraints and spacecraft mass continuity produces a solution identical to optimizing each thrust arc independently with the corresponding TD and mass values. Therefore, for the tour within the swarm, accurate propellant costs are readily determined by incorporating the propellant consumed along previous thrust arcs into the optimization of the subsequent arcs, rather than assuming each thrust arc to be independent. For example, after arrival in the swarm, the first rendezvous arc between asteroids consumes propellant mass such that the spacecraft mass is less than 500 kg at the initiation of the second thrust arc. Accordingly, the optimization problem for the second asteroid-to-asteroid rendezvous arc possesses an 'initial' spacecraft mass equal to the arrival mass at the end of the previous rendezvous segment while an initial guess for the optimal operation is supplied by the pre-computed independent thrust arc. For all the sample cases, this initial estimation of the co-states is sufficient to ensure convergence of the new, higher-fidelity optimization process providing an updated optimal control time history and thrust profile. The propellant usage computation then continues throughout the tour in the swarm. The spacecraft mass at swarm arrival is still specified to be 500 kg and, therefore, the Earth-to-asteroid arc still targets an arrival mass of 500 kg.

5.6.3 Scaling properties of low-thrust transfer arcs

A convenient approach to generate initial guesses for the optimization process is scaling of the results from the pre-existing solutions. In this investigation, the initial conditions for the rendezvous arcs that are computed in the CR3BP and employing a NEP thruster are scaled to improve convergence in the delivery of a locally optimal solution. As demonstrated in Prussing and Conway, [62] the relationship

$$\frac{1}{m_f} - \frac{1}{m_0} = C \int_{t_0}^{t_f} \frac{a^2}{P} dt \tag{5.139}$$

advantageously links the engine power, P, and the acceleration profile, a, to the initial and final masses of the thrusting spacecraft. Using this relation in conjunction with Eq. (5.44), results in the scaled specific impulse

$$I_{sp} = \frac{2P_{\max}}{mag_0}. \tag{5.140}$$

Recall that Eq. (5.60) yields

$$\frac{\lambda_v}{\lambda_m} = \frac{m^2 a}{P_{\max}}, \tag{5.141}$$

where this form admits a scaling of either the velocity or mass co-states. Retaining an initial mass co-state equal to unity produces the following scalings for the velocity and position co-states:

$$\boldsymbol{\lambda_{vn}} = \lambda_{\boldsymbol{vn}} \boldsymbol{u} \tag{5.142}$$

$$\boldsymbol{\lambda_{rn}} = \frac{\lambda_{\boldsymbol{vn}}}{\lambda_{\boldsymbol{vo}}} \boldsymbol{\lambda_{ro}} \tag{5.143}$$

where the optimal thrust pointing direction $\boldsymbol{u}$ is preserved and the subscripts n and o indicated the scaled and original values, respectively. In addition to the construction of initial guesses, the scaling relationships are useful for rapidly examining a large variety of mission scenarios without the requirement to fully optimize the corresponding trajectories. For example, baseline solutions generated with default values can readily be scaled to satisfy the requirements of other potential scenarios or constraints. Note that, for the VSI engine model, changes in the spacecraft parameters such as mass and engine operating power do not engender corresponding changes in the physical path of the spacecraft along the thrust arc or the optimal departure and arrival epochs at the asteroids of interest. On the other hand, modifying the spacecraft mass and electrical power do render alterations to the optimal engine operation history, notably the specific impulse and the thrust magnitude, but not thrust pointing direction.

6. END-TO-END ASTEROID SURVEY TOURS - RESULTS

Tour trajectory architectures are explored for the Sun-Jupiter L_4 Trojan asteroids, specifically those enabled by an advanced electrical propulsion system. Encounter sequences directly incorporating relative scientific value and satisfying a variety of distinct mission objectives are rapidly generated via the automated design process. Potential tours of interest are then transitioned to higher-fidelity models for more detailed analysis. Several strategies aid in the automated transition of trajectory solutions to address changes in spacecraft capability.

6.1 Preliminary searches for potential survey tours

Prospective trajectories wherein a spacecraft encounter multiple Trojan asteroids are generated using the enumerated tree search as well as the ant colony heuristic. Both automated schemes estimate the performance of a robotic probe operating within the asteroid swarm by extracting and sequencing thrust arcs from the library of pre-computed transfer solutions. Preliminary paths through the swarm are evaluated upon number of asteroids accessed, relative scientific merit of the encountered asteroids, estimated propellant consumption and ΔV cost, as well as time spent in the vicinity of the targets.

6.1.1 Trajectory options arising from enumerated tree searches

Inclusion of the potential scientific merit of the individual target asteroids is included as a post-processing step in the tour generation scheme from Sect. 5.5.1. Recall that this sequencing procedure uses an enumerated tree search over a limited subset of the rendezvous arcs from the full library of pre-computed solutions, i.e., only one asteroid-asteroid leg of pre-specified thrust duration TD is evaluated per family. Potential rendezvous legs are added to tour sequences so long as they do not violate either the propellant budget of the spacecraft or limits on the mission window. The spacecraft and mission parameters used in this investigation, unless otherwise noted, are presented in Table 6.1. These values are readily altered and are used here strictly for demonstration purposes. Once a set of potential tours is constructed, the individual merits of the encountered asteroids are summed for each tour, resulting in a prospective mission priority ranking. Particular tours of interest can then be transitioned to higher fidelity models if desired.

Table 6.1. Spacecraft and tour parameter values.

Quantity	**Value**
Swarm arrival spacecraft mass (m_r), kg	500
Propellant available in swarm (m_p), kg	150
Tour window in swarm (TOF), yrs	10.5
Reference engine power ($P_{\max}$), kW	1.0
Selected arc duration from family	Median TD

Tours originating from all twelve asteroids are generated over a 25-year window of initial epochs, from 2021 to 2046, that is all tours that are 10.5 years in duration, arrive no sooner than 2021, and end operations no later than 2057 are discovered. Figure 6.1 synthesizes the results into a glyph plot representing the relative performance of each initial target asteroid. As noted in the figure, the objects are compared according to the number of tours available, the number of encounters per tour, and the relative merit ranking of potential tours. Two initial asteroids, namely 624 Hektor and 1143 Odysseus, provide good all-around performance relative to other objects when selected as the initial target, while three others (5652 Amphimachus, 7152 Euneus, and 8317 Eurysaces) provide good performance in all categories except the number of high-priority tours (that is, cumulative scientific merit of 4 or larger). What is intriguing about the latter three asteroids is that they individually possess low priority, but they seem to provide ample opportunity to transfer to other, more meritritious, asteroids within the swarm. On the other extreme, 3548 Eurybates and 8241 Agrius seem to offer the least overall options, though the high scientific priority of 3548 Eurybates does ensure that it provides a relatively large number of high merit tours.

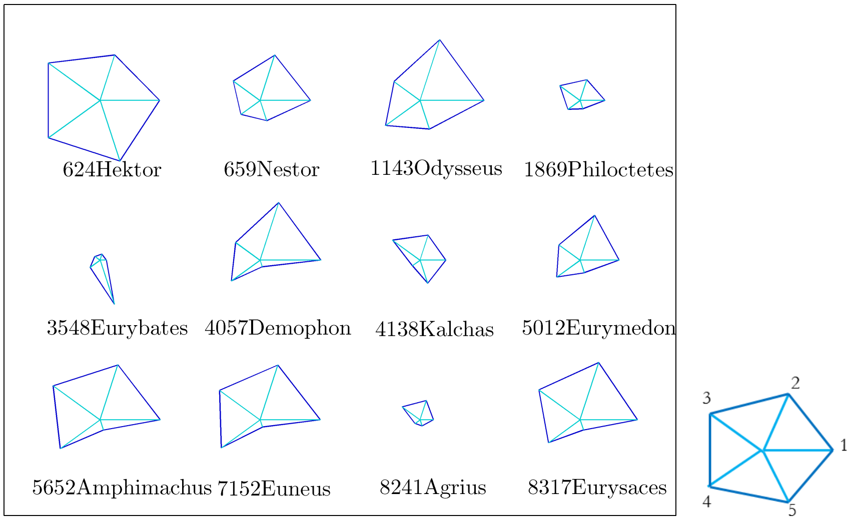

Figure 6.1.. Aggregate tree searches for all twelve target asteroids. For comparison of relative lengths, the spokes are: 1) average number of tours per year, 2) average number of tours encountering 3 asteroids, 3) average number of tours encountering 4 or more asteroids, 4) average merit of all tours, 5) average number of tours with priority 4 or higher.

Examining tours orginating from 3548 Eurybates in more detail provides further insight not only into advantages of selecting this asteroid as the initial encounter but also the peformance of the other potential targets. Averages of the number of asteroids visited per tour and the average merit of the tours over the 25-year swarm arrival window are computed and displayed in Fig. 6.2. Both averages have a cyclical pattern with a peak-to-peak period of approximately 11 years; intuitively, higher merit opportunities correspond to years when the average number of encounters per tour is approximately 3 or higher. Though not shown in this investigation, these trends in the number of encounters and merits of the tours are exhibited by tours originating at other initial target asteroids. Note that even though there are some initial epochs where only two asteroid tours are available, other swarm arrival years offer ample tours with 3 or even 4 asteroid encounters. Recalling the relative performance of 3548 Eurybates from Fig. 6.1, the inference can be made that most tours within the swarm and with the parameters specified in Table 6.1 offer encounters with at least 3 target objects.

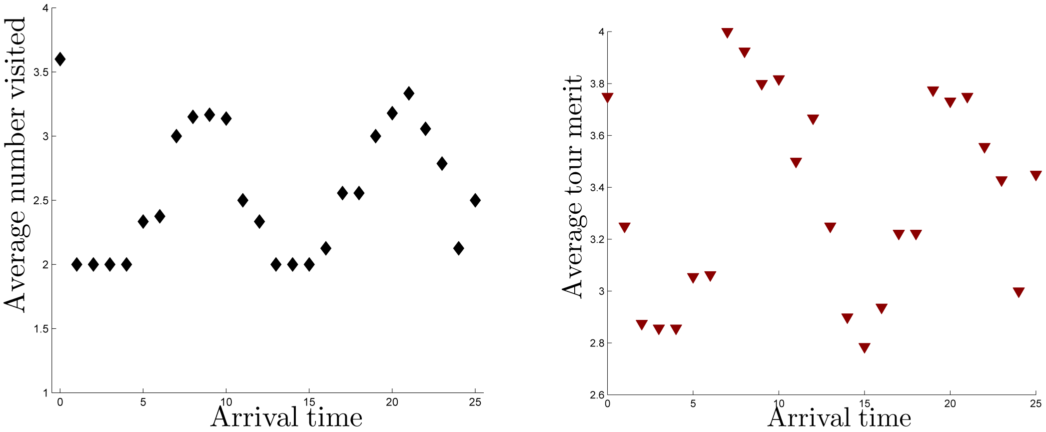

a. Average number of encounters per tour.

b. Average tour priority.

Figure 6.2.. Yearly search averages for tours originating at asteroid 3548 Eurybates, in one-year increments, from Oct. 3, 2021.

One more step in the selection of specific tours of interest is to examine the potential tours for one swarm arrival epoch; as a demonstration, the asteroid 624 Hektor is selected as the initial target and an arrival in the year 2026 is chosen. The tour generation scheme produces a set of 15 viable tours, 14 of which encounter 3 asteroids. Propellant, ΔV, and proximity operation time estimates for the tours are displayed in Fig. 6.3, where the tours have been ranked in descending order by total scientific merit. Note that propellant consumed and tour ΔV are directly related while the distribution of proximity operation times near the encountered asteroids shows a few patterns consistent with multiple potential tours using identical transfer arcs. For example, the three highest ranked tours all follow the same rendezvous leg from 624 Hektor to 3548 Eurybates and thus have the same duration spent in the vicinity of the initial target asteroid. However, each tour has a distinct tertiary target and therefore present options for duration near 3548 Eurybates and total tour propellant cost. The third ranked tour is selected for further investigation because it offers long intervals at both of the highest value target asteroids, 624 Hektor and 3548 Eurybates, and a final short duration in the vicinity of 8241 Agrius. For this tour, the spacecraft path through physical space and the thrust profiles of the VSI engine are presented in Fig. 6.4. Note the large out-of-plane motion of the tour, consistent with the relatively high inclinations of the target asteroids. On the other hand, the 624 Hektor to 3548 Eurybates rendezvous arc has a thrust profile that is roughly consistent in magnitude and is thus readily transferable to a constant specific impulse mission architecture while the second rendezvous arc could be replaced with two thrust intervals with an intermediary coast interval.

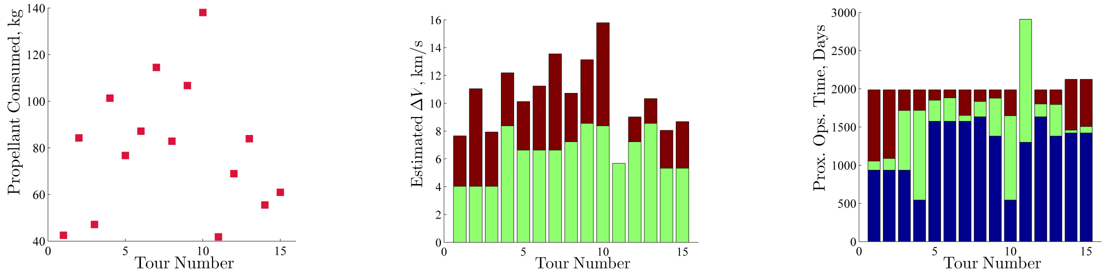

a. Propellant consumed, per tour. b. Tour ΔV, by leg. c. Prox. Ops. time, by encounter.

Figure 6.3.. Performance of tours originating from 624 Hektor with swarm arrival in 2026, median thrust duration.

6.1.2 Encounter sequences constructed via ant colony optimization

The ACO-PPD algorithm is applied to the construction of tours within the L_4 Trojan asteroid swarm; several runs are made, each with a distinct set of parameters

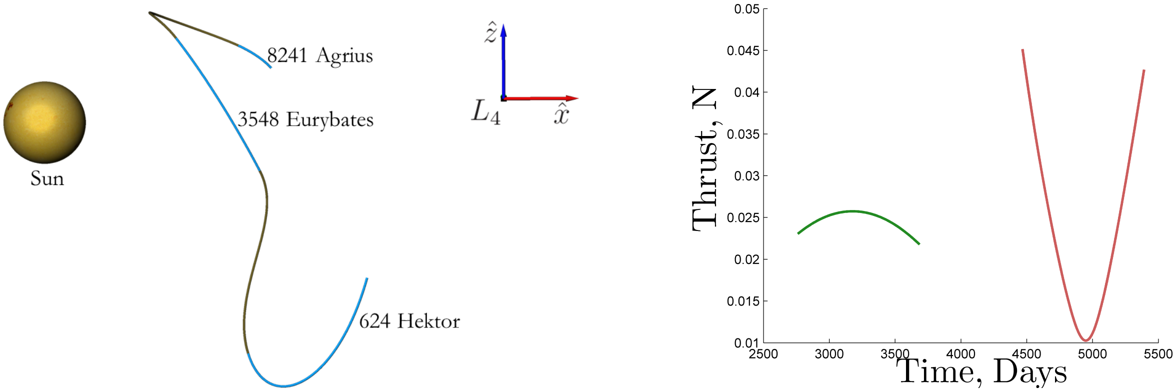

a. Trajectory, rotating frame, view from ecliptic plane. Blue coast arcs near asteroids, gold thrust arcs.

b. Thrust profiles. Time is days since 3 October 2021.

Figure 6.4.. Tour constructed using median duration thrust arcs originating at 624 Hektor and encountering 3548 Eurybates and 8241 Agrius.

so that the effect of the various options on the performance of the algorithm may be assessed. A set of parameters common to all the runs is defined in Table 6.2 while additional parameters that differ by ACO-PPD run are presented in Table 6.3. Note that, as before, these parameters for the ACO searches are selected merely to demonstrate the operation of the search method; more detailed analysis would be required to select the best search parameters for each case considered. As the goal is tours that explore the L_4 asteroid swarm, ants are specified to not return to asteroids they have already encountered. Furthermore, Case 7, which uses the combined importance and loiter time tour quality metric, has a specified $LT_{\max}$ of 517 days, or approximately 1.4 years, such that loiter times longer than this maximum value are capped at 517 days when constructing the tours.

Table 6.2. Spacecraft, tour, and ACO-PPD parameter values, common to all runs.

Quantity	**Value**
Swarm arrival spacecraft mass (m_r), kg	500
Propellant available in swarm (m_p), kg	150
Tour window in swarm (TOF), yrs	10.5
Reference engine power ($P_{\max}$), kW	1.0
Swarm arrival year	2026
Number of generations (N_g)	50
Link quality weight in link probability (β)	1
Pheromone spread size (N_{ps})	5
Number of ants to lay pheromone (N_{sa})	5
Base exploration probability (γ_{ss})	0.1
Selected arc duration from family (exploration)	Median TD

The characteristics of the highest ranked tour from each run are summarized in Table 6.4, where the different ACO-PPD parameters engender varying amounts of

Table 6.3. ACO-PPD parameter values that differ among runs.

	Case Values							
Quantity	**Base**	**1**	**2**	**3**	**4**	**5**	**6**	**7**
Number of ants (N_a)	25	20						
Pheromone distribution	Uniform	Gauss						
Link quality weights	$M = 1$ $L = 1$ $W = 0$					$M = 0$ $L = 1$ $W = 0$	$M = 1$ $L = 1$ $W = 1$	
Tour quality metric (Q)	Link Quality		Number	Merit Sum				Priority Loiter
Favor unique	Yes				No			
Ant placement	Random				Pher.			

*Empty cells indicate value is identical to base set of parameters.

divergence from the performance of the base run. Note that the row for "Merit × Prox. Ops. Time" is computed via the link quality definition in Eq. (5.121); thus, this metric provides a sense of the proportion of time spent at high potential scientific return objects. The base set of parameters, as well as Cases 1 and 2, results in the creation of a tour that encounters 5 asteriods, namely 1143 Odysseus, 4138 Kalchas, 8317 Eurysaces, 659 Nestor, and 5652 Amphimachus, within 10.5 years; note that this tour was not generated by an equivalent enumerated tree search using only single links from the rendezvous families. Thus, ACO-PPD has the potential to bring forth tours not available to schemes that do not fully access the potential trade spaces offered by rendezvous opportunities. Furthermore, the 5-asteroid sequence did not emerge from the run for Case 4, which did not favor unique encounter orders and placed ants at targets with higher pheromone concentrations, showing that certain parameter options can counter, to some extent, the reported tendency for ACO to "lock" into solutions. On the other hand, parameter sets that incorporate the target priority typically result in sequences with fewer encounters but generally higher potential for scientific return. Notabley, Cases 3, 6, and 7 generate target orders that were discovered via the simplified tree search scheme (specifically, 624 Hektor, 3548 Eurybates, and 659 Nestor for Cases 3 and 6 contrasted with 624 Hektor, 3548 Eurybates, and 8241 Agrius for Case 7), however the ACO-PPD runs do result in the selection of individual thrust arcs that tend to increase the tour quality metric above that of tours from the enumerated search. While certain sets of ACO-PPD parameters do result in similar qualitative results, each case offers a distinctly different quantitative result for the highest ranked tour (e.g., Cases Base, 1 and 2 produce the same sequence but provide different options for proximity duration and propellant consumption). The notable exceptions to this behavior are Cases 3 and 6, which generate identical tours, albeit with slightly different run times. For all sets of ACO-PPD parameters, the largest effect on the run time are the number of ants per generation (as evidenced by Case 1 that only employs 20 ants compared to all other cases that use 25 ants) and whether the parameters will favor tours with more or fewer encounters (generally, cases that produce tours with a larger number of asteroids in the sequence will require more computations). Though not an exhaustive examination of all possible combinations of ACO-PPD, spacecraft, and mission parameters, these cases do highlight the power and versatility of ant colony optimization when applied to astrodynamics scenarios.

Table 6.4. Performance of highest ranked tour from ACO-PPD runs.

	Case Values							
Quantity	**Base**	**1**	**2**	**3**	**4**	**5**	**6**	**7**
Number of asteroid encounters	5	5	5	3	4	4	3	3
Summed merit of asteroids	4	4	4	5	2.5	2.5	5	4.5
Consumed Propellant, kg	125	115	95	40	75	65	40	65
Tour ΔV, km/s	15.7	15	14	7.5	10.1	10.5	7.5	8.5
Total Prox. Ops. Time, days	750	570	450	1750	1300	1200	1750	2150
Merit × Prox. Ops. Time, days	630	470	340	2670	660	610	2670	3530
Computation time*, sec	102	77	102	90	111	99	95	85

*For Matlab 2011a in Windows 7 Enterprise with 2.00 GHz dual processors.

Two cases from the ACO survey are examined in more detail, specifically the base case and case 6. Note that all search parameters are identical for these two cases, with the exception that case 6 explicitly incorporates the relative scientific value in the link quality metric ($W = 1$) whereas the base set of parameters omits the priority ranking ($W = 0$). The ranked performance of the ants, or tours, from the last generation of the ACO search using the base set of parameters is highlighted in Fig. 6.5 while Fig. 6.6 illustrates the physical path and thrust profiles of the best performing tour. Note that the encounter sequence encounters two asteroids with known spectral type, even though scientific value was not explicitly considered in the generation of potential tours. In contrast, the tour performances at the last ACO generation and the best performing trajectory related to the 6^{th} set of parameters is displayed in Figs. 6.7 and

6.8, respectively. Note that the case that includes scientific merit in the link quality ensures that higher priority targets are accessed for longer loiter periods, even though a fewer number of asteroids may be reached over the course of operations.

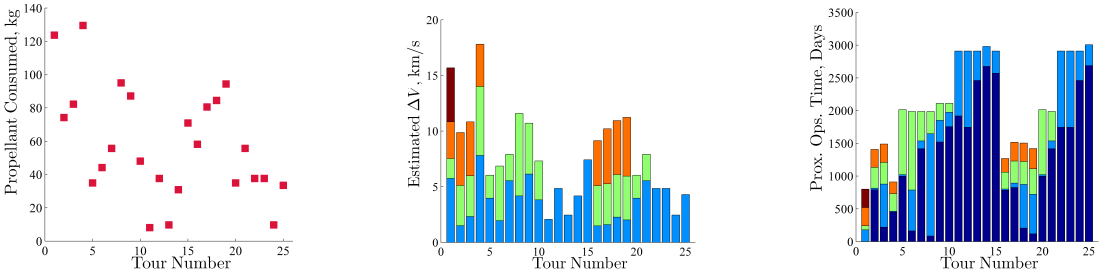

a. Propellant consumed, per tour. b. Tour ΔV, by leg. c. Prox. Ops. time, by encounter.

Figure 6.5.. Performance of tours constructed using ant colony heuristic, from Base Case, neglecting scientific merit of targets.

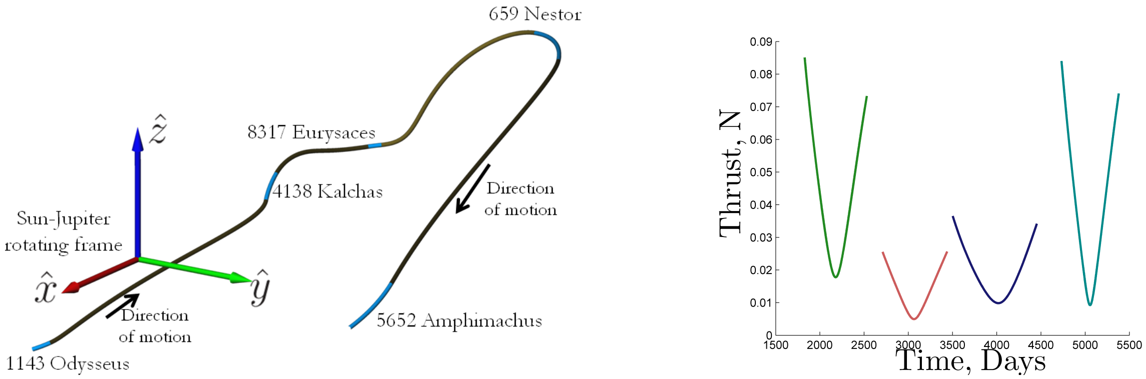

a. Trajectory, rotating frame, view from ecliptic plane. b. Thrust profiles.

Blue coast arcs near asteroids, gold thrust arcs. Time is days since 3 October 2021.

Figure 6.6.. Highest quality tour constructed by ACO-PPD, originating at asteroid 1143 Odysseus and encountering a total of 5 asteroids.

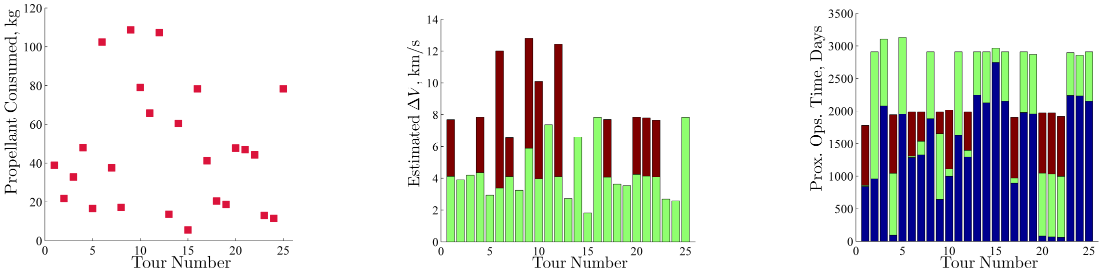

a. Propellant consumed, per tour. b. Tour ΔV, by leg. c. Prox. Ops. time, by encounter.

Figure 6.7.. Performance of tours constructed using ant colony heuristic, from Case 6, incorporating scientific merit of targets.

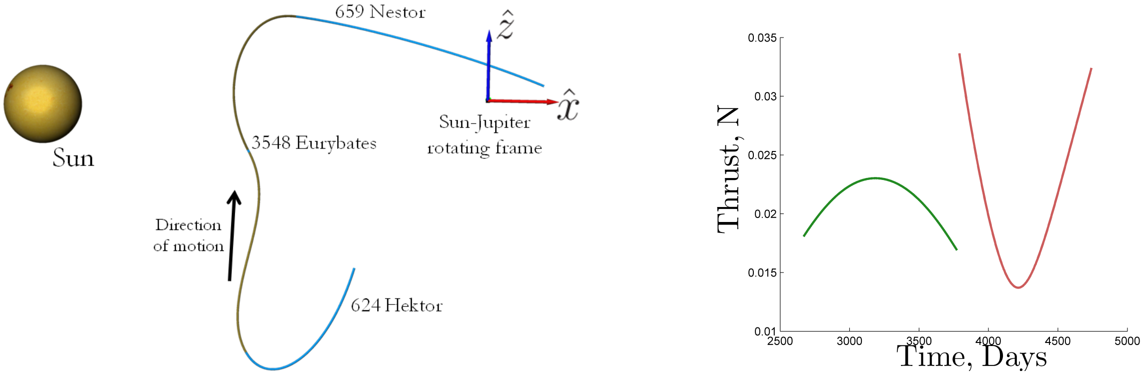

a. Trajectory, rotating frame, view from ecliptic plane. b. Thrust profiles.

Blue coast arcs near asteroids, gold thrust arcs. Time is days since 3 October 2021.

Figure 6.8.. Highest quality tour constructed by ACO-PPD, originating at asteroid 624 Hektor and encountering 3 high priority asteroids.

6.2 End-to-end trajectory options

While the pre-computed rendezvous solutions are enabled by a constant-power VSI engine, several electrical power source options are available for the low-thrust propulsion system. Furthermore, the propellant cost approximations formulated from the independently generated thrust arcs must be altered to reflect true end-to-end mass expenditures. Thus, the automated transition of prospective tours constructed using simplified dynamical models to a variety of higher fidelity regimes is examined. First, the transformation from the simplified dynamics of the Sun-Jupiter CR3BP to the higher accuracy point-mass ephemeris is considered. Then, the trade-off available between the various electrical power sources is explored. Finally, a scenario is investigated wherein the spacecraft parameters, and consequently the engine peformance histories, are scaled from the baseline values used to pre-compute the library of thrust arc solutions.

6.2.1 Baseline paths transitioned to higher accuracy natural dynamics

The automated tour generation procedure enabled by the enumerated tree search is applied to two asteroid survey scenarios. Recall that an initial target asteroid, arrival epoch, propellant mass within the asteroid swarm, mission duration, and asteroid-to-asteroid thrust arc duration must all be specified for the tree search scheme. An appropriate initial asteroid arrival epoch is determined from a grid search across a window of several years, so this arrival epoch selection is completed as a separate step in the analysis. However, the remaining constraints for the two scenarios are defined as follows:

1. Initial asteroid: 1143 Odysseus, $m_p = 100$ kg, $TOF = 10$ years, thrust arcs of median TD;
2. Initial asteroid: 7152 Euneus, $m_p = 150$ kg, $TOF = 14$ years, thrust arcs of median TD.

The mission duration TOF is pre-specified to include a 3.5 year Earth-to-asteroid leg, so the time within the swarm for the two proposed mission scenarios are defined as 6.5 and 10.5 years, respectively. The hybrid propulsion scheme detailed in Sect. 5.6.1 enables the outbound leg from Earth to the asteroid swarm for both scenarios; the constraint on Earth departure velocity is specified as $V_\infty = 7.5$ km/sec. This value is slightly lower than the departure $V_\infty = 8.8$ km/s required for a Hohmann transfer and well below the roughly $V_\infty = 10.5$ km/s needed for a 3.5 year Lambert arc. These parameters enable several potential tours for a specified arrival epoch, although only one is analyzed in each case.

6.2.1.1 Initial asteroid 1143 Odysseus, 10-year mission

The creation of a specific end-to-end trajectory that satisfies the mission requirements while enabling rendezvous with several asteroids originates with the selection of an initial asteroid arrival epoch. Combining thrust arcs from various families, as detailed in Section 5.5.1, the sequence generation algorithm is applied over a 25-year window from October 3, 2021 to October 3, 2046. During each year, the average number of asteroids visited, as well as the average merit, per potential tour is computed and plotted in Fig. 6.9. Several years possess averages encounter numbers greater than 2, indicating that these initial epochs enable tours that rendezvous with at least three asteroids. Furthermore, several years present high priority tours, signified when average tour priorities are larger than 2. Selecting the year 2025, year 4 in Fig. 6.9, for further analysis, three potential tours reach only two asteroids and three rendezvous sequences encounter three asteroids. Note that no 4-asteroid tour emerged for arrival in 2025. A three-asteroid sequence reaching 4057 Demophon and 5012 Eurymedon is selected for further analysis. An outbound leg is determined, as described in Section 5.6.1; the estimated end-to-end costs as well as departure and arrival time histories are summarized in Tables 6.9 and 6.10. Note that the spacecraft mass at arrival at 1143 Odysseus is 500 kg, thus, 84.726 kg of propellant is expended on the

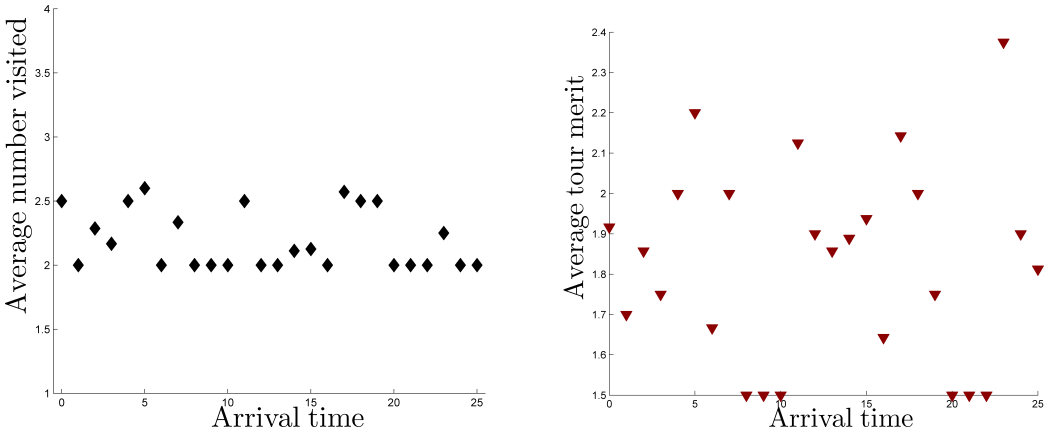

a. Average number of encounters per tour. b. Average tour priority.

Figure 6.9.. Yearly search averages for tours originating at asteroid 1143 Odysseus, in one-year increments, from Oct. 3, 2021.

outbound leg and 33.899 kg is consumed within the swarm. Thus, to complete the trajectory, roughly 20% of the spacecraft mass at Earth departure is propellant for the low-thrust engine. The remaining 66.101 kg of the mass budget that is available from m_p might enable extended missions and additional scientific instruments on the spacecraft. Additionally, the proposed trajectory allows approximately 5 months of operation in the vicinity of 1143 Odysseus and 7 months near 4057 Demophon before the final rendezvous with 5012 Eurymedon.

Table 6.5. Spacecraft propellant budget for 10-year mission with tour of 3 asteroids

	Value			**CR3BP**
Quantity	**CR3BP**	**Ephemeris**	**Units**	**Error (%)**
Mass at Earth departure	584.726	583.238	kg	+0.255
Mass at final asteroid arrival	466.101	464.983	kg	+0.240
Total propellant consumption	118.625	118.251	kg	+0.316
V_∞ at Earth departure	7.50000	7.50000	km/sec	0

Table 6.6. Epochs of interest for 10-year mission with tour of 3 asteroids

	Gregorian Date YYYY:MM:DD:HH:MM:SS	
Description	**CR3BP**	**Ephemeris**
Earth departure	2021:6:3:13:0:27	2021:6:6:5:3:33
1143Odysseus arrival	2024:12:2:22:0:27	2024:12:5:14:3:33
1143Odysseus departure	2026:5:11:19:42:18	2026:3:30:3:43:18
4057Demophon arrival	2028:11:21:0:49:52	2028:10:9:8:50:53
4057Demophon departure	2029:6:28:7:56:47	2029:8:15:6:17:58
5012Eurymedon arrival	2031:12:11:22:56:58	2032:1:28:21:18:9

In addition to a mass budget and trajectory timeline, the physical path and engine operation histories are also of interest. Accordingly, the spacecraft trajectory under CR3BP dynamics is displayed in Fig. 6.10. The Earth-to-asteroid arc is magenta, arcs where the engine is operating within the swarm are dark gold, and coasts in the vicinity of asteroids are indicated by light blue. The position of the Earth is displayed at the Earth departure epoch of June 3, 2021. Note that upon arrival within the swarm, the thrust arcs are nearly planar, a fact that contributes to the relatively low propellant expenditure. Time histories of the thrust level and the engine I_{sp} are plotted in Fig. 6.11, where the Earth-to-1143 Odysseus segment is indicated in magenta, the 1143 Odysses to 4057 Demophon arc is green, and the 4057 Demophon to 5012 Eurymedon leg is red. As apparent in Fig. 6.11, the thrust and I_{sp} levels are consistent in magnitude over all periods of engine operation, that is, in the thrust range 10-50 mN and 5,000-20,000 sec that reflects I_{sp} values. With proper adjustments for spacecraft mass and timing, this tour can serve as a reference path for trajectory design with currently available constant specific impulse engines.

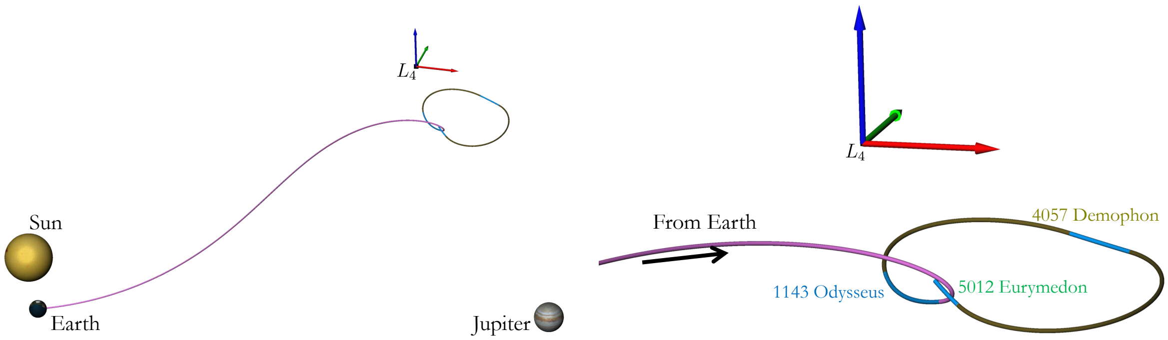

Figure 6.10.. Plot of trajectory for tour with initial target 1143 Odysseus, outbound leg (pink), thrust arcs (gold), coasts in the vicinity of asteroids (blue), in Sun-Jupiter rotating frame.

The baseline design in the CR3BP that is generated by the automated procedure is now analyzed using higher fidelity motion for the Sun, Jupiter, and the target asteroids. All thrust arcs are optimized using a Sun-Jupiter point-mass ephemeris

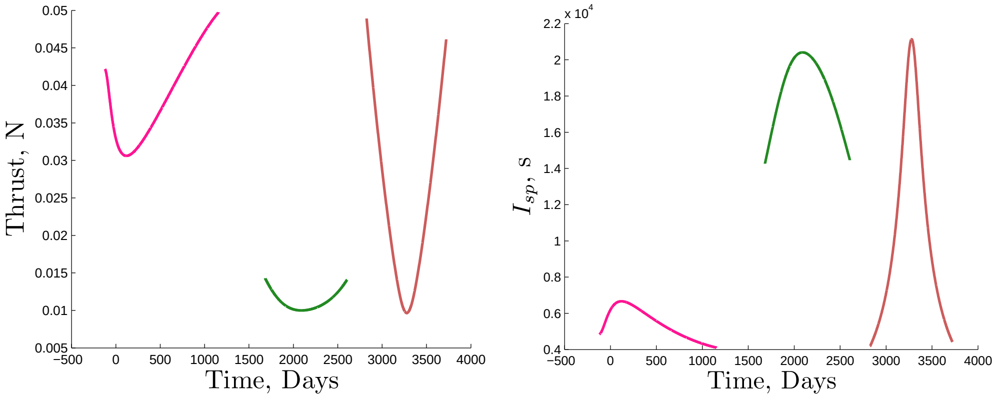

Figure 6.11.. Thrust and I_{sp} profiles for outbound leg (pink) and first (green) and second (red) asteroid rendezvous arcs for mission scenario with initial asteroid 1143 Odysseus.

model, where propellant consumed is retained from segment to segment. Thus, the initial mass of the spacecraft on the 4057 Demophon to 5012 Eurymedon leg is now the arrival mass of the spacecraft from the 1143 Odysseus to 4057 Demophon rendezvous arc. A target mass of 500 kg is retained for arrival at the initial tour asteroid, 1143 Odysseus. The results from the newly produced, higher fidelity tour are recorded in Tables 6.9 and 6.10, along with a percentage error in the propellant costs between the CR3BP and the point-mass ephemeris dynamics models. For this potential tour, the automated process accomplished in the simpler model over-estimates all reported masses, but by less than one percentage point in comparison with the higher-fidelity estimate. So, the required spacecraft mass at Earth departure is approximately 1.5 kg less than orginially estimated; the spacecraft mass upon arrival at 5012 Eurymedon is roughly 1 kg less than predicted. Overall, however, actual propellant consumed decreases by around 0.4 kg. The physical path of the spacecraft and the engine operation histories under the point-mass ephemeris model are very similar to those predicted by the automated CR3BP algorithm. The optimal departure and arrival epochs that are displayed in Table 6.10, however, can vary on the order of one to two months between the CR3BP and higher fidelity motion.

6.2.1.2 Initial asteroid 7152 Euneus, 14-year mission

Repeating the trajectory design process for the second set of mission parameters further highlights the benefits of the automated procedure. For the same 25-year arrival epoch window, the swarm rendezvous arc combination procedure produces the results in Fig. 6.12. Now, with an increased propellant budget and an expanded time of flight, a greater number of potential mission scenarios are generated; many of these sequences result in encounters with up to four asteroids. Consequently, these tours generally have higher average merit due to the additional asteroid encounter, however the relatively low scientific ranking of the initial target, 7152 Euneus, limits the priority of the individual encounter sequences. For the arrival epoch corresponding to the year 2031, there are 35 feasible tours and, within that set, there are 9 sequences that link 4 asteroids. Select an asteroid tour originating at 7152 Euneus and possessing subsequent encounters with 5012 Eurymedon, 1143 Odysseus, and 5652 Amphimachus. An end-to-end trajectory is constructed with propellant costs and a timeline represented in terms of the epochs displayed in Tables 6.7 and 6.8. As before, the reference spacecraft mass is 500 kg upon swarm arrival, so 79.309 kg of propellant is consumed on the outbound segment while 118.985 kg is used within the asteroid-to-asteroid arcs. Of the swarm mass budget of 150 kg, 31.015 kg remains to enhance mission capabilities. For this mission scenario, approximately 34% of the spacecraft Earth departure mass must be propellant. As observed in Table 6.8, the spacecraft spends about 8, 17, and 5 months in the vicinity of 7152 Euneus, 5012 Eurymedon, and 1143 Odysseus, respectively, with an arrival at 5652 Amphimachus in September 2041.

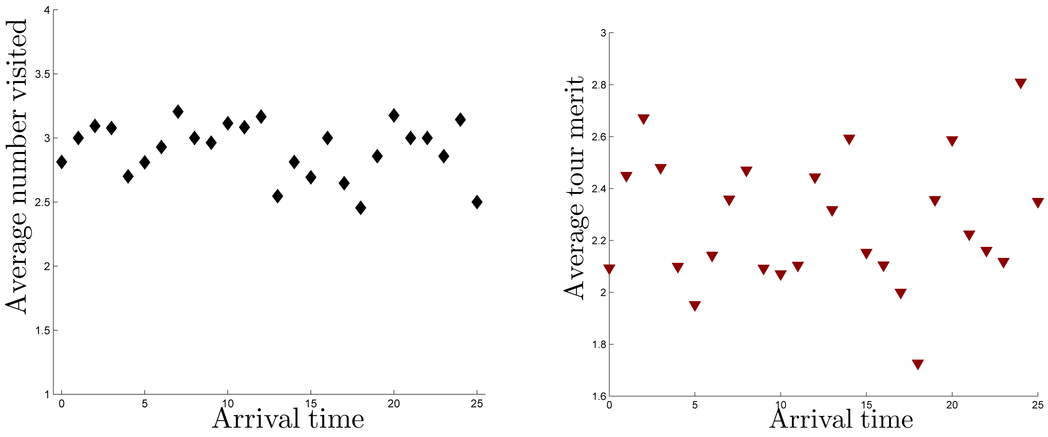

a. Average number of encounters per tour.

b. Average tour priority.

Figure 6.12.. Yearly search averages for tours originating at asteroid 7152 Euneus, in one-year increments, from Oct. 3, 2021.

The trajectory generated by the automated procedure is displayed in Fig. 6.13, where the color scheme is consistent with Fig. 6.10. The position of the Earth is displayed at the Earth departure epoch of January 12, 2028. In contrast to the ren-

Table 6.7. Spacecraft parameters for 14-year mission with tour of 4 asteroids

	Value			**CR3BP**
Quantity	**CR3BP**	**Ephemeris**	**Units**	**Error (%)**
Mass at Earth departure	579.309	584.795	kg	-0.938
Mass at final asteroid arrival	381.015	388.397	kg	-1.90
Total propellant consumed	198.294	196.397	kg	+0.966
V_∞ at Earth departure	7.50000	7.50000	km/sec	0

Table 6.8. Epochs of interest for 14-year mission with tour of 4 asteroids

	Gregorian Date YYYY:MM:DD:HH:MM:SS	
Description	**CR3BP**	**Ephemeris**
Earth departure	2028:1:12:9:9:0	2028:1:12:16:21:35
7152Euneus arrival	2031:7:13:18:9:0	2031:7:14:1:21:35
7152Euneus departure	2032:3:4:14:1:45	2032:6:11:7:10:20
5012Eurymedon arrival	2034:9:14:19:9:20	2034:12:22:12:17:55
5012Eurymedon departure	2036:2:29:19:27:13	2035:12:30:6:23:11
1143Odysseus arrival	2038:9:11:0:34:48	2038:7:11:11:30:46
1143Odysseus departure	2039:2:22:2:22:19	2039:2:19:7:46:30
5652Amphimachus arrival	2041:9:3:7:29:54	2041:8:31:12:54:5

dezvous trajectory that originates with 1143 Odysseus, the trajectories in this second scenarios are no longer nearly planar; thus, the propellant requirements are relatively higher. Time histories of thrust and engine I_{sp} values are plotted in Fig. 6.14, where the Earth to 7152 Euneus segment is magenta, and the first, second, and third asteroid-to-asteroid rendezvous arcs are green, red, and blue, respectively. As in the previous example, the thrust and I_{sp} levels are generally consistent over all periods of engine operation.

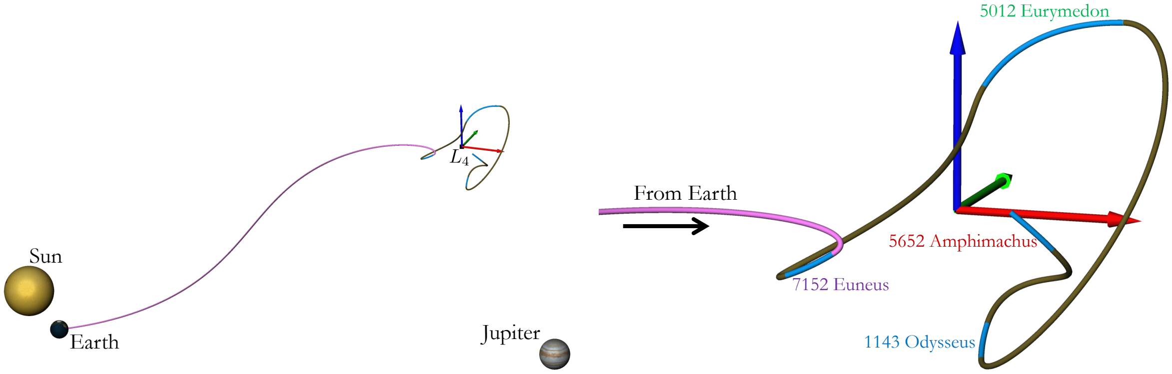

Figure 6.13.. Plot of trajectory for tour with initial target 7152 Euneus, outbound leg (pink), thrust arcs (dark gold), coasts in the vicinity of asteroids (blue), in Sun-Jupiter rotating frame.

The potential 14-year tour is re-converged in the Sun-Jupiter point-mass ephemeris model, with the results displayed in Tables 6.7 and 6.8. For this case, the lower-fidelity predictions are no longer all over-estimates, with the CR3BP predicting lower Earth departure and 5652 Amphimachus arrival masses. As before, the CR3BP results over-predict the amount of propellant needed to complete the end-to-end trajectory. As is shown in Table 6.8, the predicted and actual departure and arrival epochs vary on the order of several months. Additionally, the physical path of the spacecraft in space and the engine operation time histories under ephemeris motion are similar to those illustrated in Figs. 6.13 and 6.14.

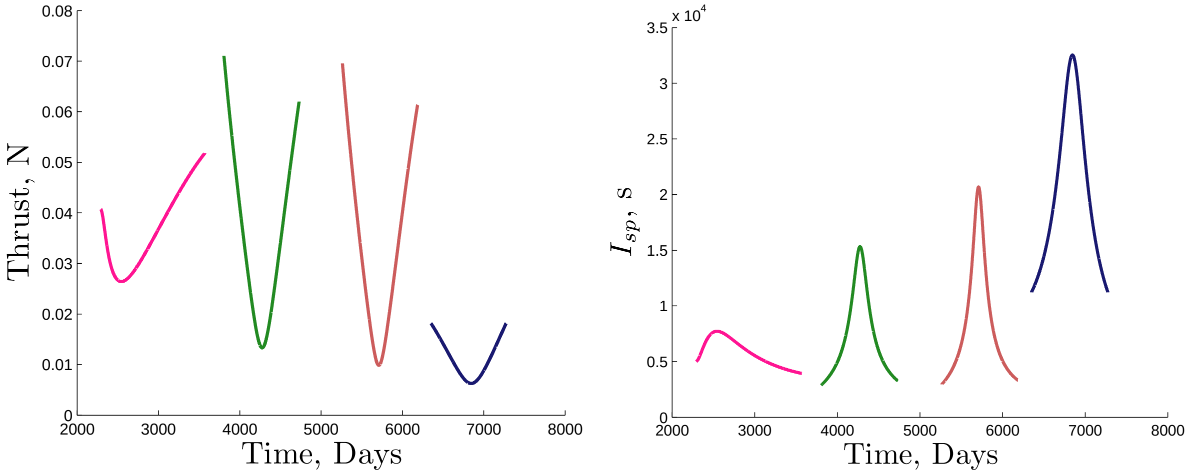

Figure 6.14.. Thrust and I_{sp} profiles for outbound leg (pink) and first (green), second (red), and third (dark blue) asteroid rendezvous arcs for mission with initial asteroid 7152 Euneus.

6.2.2 End-to-end options enabled by various electrical power sources

High-fidelity reference trajectories are constructed by incorporating a point-mass ephemeris model of gravity and three different electrical power sources for the low-thrust engine. Preliminary encounter sequences are generated via the automated tour generation procedure incorporating tree searches. Recall that arrival epoch, propellant mass within the asteroid swarm (m_p), mission duration (TOF), asteroid-to-asteroid thrust arc duration (TD), as well as initial target asteroid must all be specified. An appropriate initial asteroid arrival epoch is determined from a grid search across a window of several years, so this arrival epoch selection is completed as a separate step in the analysis. Two specific mission scenarios are considere, with the remaining constraints defined as follows:

- Initial asteroid: 1143 Odysseus, $m_p = 100$ kg, $TOF = 10$ years, thrust arcs of median TD; and,
- Initial asteroid: 4057 Demophon, $m_p = 150$ kg, $TOF = 14$ years, thrust arcs of median TD.

Note that the first mission scenario is identically defined to the first mission scenario from Sect. 6.2.1 whereas the second set of constraints for each analysis differ only by initial target asteroid. Median thrust arcs are selected for both sample mission scenarios as these intermediate thrust duration values offer a reasonable balance between propellant consumption and proximity operations duration at the asteroids. As before, the mission duration TOF includes a 3.5 year Earth-to-asteroid leg, so the time within the swarm for the two proposed mission scenarios are defined as 6.5 and 10.5 years, respectively. The constraint on Earth departure velocity is maintained as $V_\infty = 7.5$ km/s. These constraints enable several potential tours for a specified arrival epoch, although only one is analyzed in each example.

6.2.2.1 Initial asteroid 1143 Odysseus, 10-year mission

Note that the current mission scenario is identical to the architecture of interest in Sect. 6.2.1.1. Therefore, the tree search analysis peformed previously also reflects the trajectory options for this test case. The year 2026, year 5 in Fig. 6.9, is selected for further analysis, two potential tours reach only two asteroids and three rendezvous sequences encounter three asteroids. A three-asteroid sequence reaching 5652 Amphimachus and 659 Nestor is selected for further analysis. An outbound leg is constructed, as described in Section 5.6.1; the reference solution is then transitioned to three end-to-end trajectories in the ephemeris model, where each trajectory is defined in terms of the engine model, i.e., NEP, SEP, or PLS. In all cases, however, the spacecraft is constrained to an Earth-departure excess velocity of $V_\infty = 7.5$ km/s and is specfied to rendezvous with 1143 Odysseus precisely 3.5 years after departing the Earth.

The three mission scenarios along with the approximated baseline sequence are analyzed in terms of propellant consumption, mission timing, and the equivalent ΔV costs associated with the thrust arcs. The estimated end-to-end costs, as well as departure and arrival time histories, are summarized in Tables 6.9 and 6.10. As is apparent in Table 6.9, the estimated costs from the CR3BP approximation are comparable to the more accurate costs from the ephemeris NEP propagation, differing by only a few percent. For the ephemeris trajectories, note that all propulsion systems deliver approximately the same final spacecraft mass. However, each mission scenario entails a different Earth departure mass, where the NEP system requires the most propellant, the pure SEP engine the least, and the hybrid PLS thruster consumes slightly more propellant than the SEP. Also evident in Table 6.10, all potential tours possess roughly equivalent departure and arrival epochs and, accordingly, thrust and coast durations, with epochs varying on the order of days or a few weeks. Additionally, each tour allows over one year of operations in the vicinity of 1143 Odysseus, approximately 7 months of loiter time near 5652 Amphimachus, and an additional

5 months about 659 Nestor before the nominal end of the mission. The ephemeris SEP and PLS trajectories are nearly equivalent within the asteroid swarm itself, as expected since both are operating as varying-power systems during this phase of the mission. The equivalent ΔV cost for each thrust segment is computed via the definition in Eq. (5.45) where the results appear in Table 6.11. Because all mission scenarios include a nominal engine operating power equal to 1 kW while in the L_4 region, the asteroid-to-asteroid thrust arcs generate a similar amount of ΔV regardless of engine type. In contrast, the ΔVs for the outbound legs vary significantly between the engine types, where the SEP system requires the most ΔV, the NEP thruster provides the least, and the PLS engine generates an equivalent ΔV values that is approximately the average of the NEP and SEP values. Note also that the approximated sequence from the CR3BP produces ΔV estimates that closely match the higher-fidelity ephemeris NEP costs.

In addition to propellant budgets and the trajectory timeline, the physical path of the spacecraft is also of interest. Accordingly, the point-mass ephemeris spacecraft trajectories under the varying propulsion system models are displayed in Fig. 6.15 and Fig. 6.16 in the inertial and Sun-Jupiter rotating frames, respectively. The approximated trajectory that is generated by the sequencing algorithm is very similar to the NEP ephemeris trajectory and so is not displayed. The Earth-to-asteroid arc is red and dashed for the NEP thruster, the SEP arc is indicated in solid yellow, and the PLS-enabled outbound leg is solid orange. Arcs where the engine is operating within the swarm are dashed dark gold, and coasts in the vicinity of asteroids are indicated by the solid light green color. The position of the Earth is displayed at the Earth departure epoch on July 17, 2022. Note that the outbound legs for the SEP and PLS mission scenarios are very similar along the physical path traced through space.

Time histories for the engine operating parameters such as thrust, specific impulse, and electrical power are also of interest in mission analysis. These histories are plotted in Figs. 6.17, 6.18, and 6.19, respectively. The Earth-to-1143 Odysseus

Table 6.9. Spacecraft mass and propellant budget for 10-year mission with tour of 3 asteroids, various electrical power sources

	Value					**CR3BP**
Quantity	**CR3BP**	**Eph. NEP**	**Eph. SEP**	**Eph. PLS**	**Units**	**Error (%)**
Earth departure mass	584.190	582.273	546.827	549.008	kg	+0.329
Final spacecraft mass	472.883	473.584	475.469	475.469	kg	-0.148
Propellant consumption	111.307	108.689	71.358	73.540	kg	+2.409
V_∞ at Earth departure	7.50000	7.50000	7.50000	7.50000	km/s	0

Table 6.10. Epochs of interest for 10-year mission with tour of 3 asteroids, various electrical power sources

	Gregorian Date YYYY:MM:DD			
Description	**CR3BP**	**Eph. NEP**	**Eph. SEP**	**Eph. PLS**
Earth departure ($V_\infty = 7.5$ km/s)	2022:07:17	2022:07:17	2022:07:13	2022:07:11
1143 Odysseus arrival	2026:01:15	2026:01:15	2026:01:11	2026:01:09
1143 Odysseus departure	2027:03:02	2027:02:06	2027:02:06	2027:02:06
5652 Amphimachus arrival	2029:09:11	2029:08:18	2029:08:18	2029:08:18
5652 Amphimachus departure	2030:04:07	2030:04:29	2030:04:16	2030:04:16
659 Nestor arrival	2032:10:17	2032:11:09	2032:10:26	2032:10:26
Nominal mission end	2033:04:03	2033:04:03	2033:04:03	2033:04:03

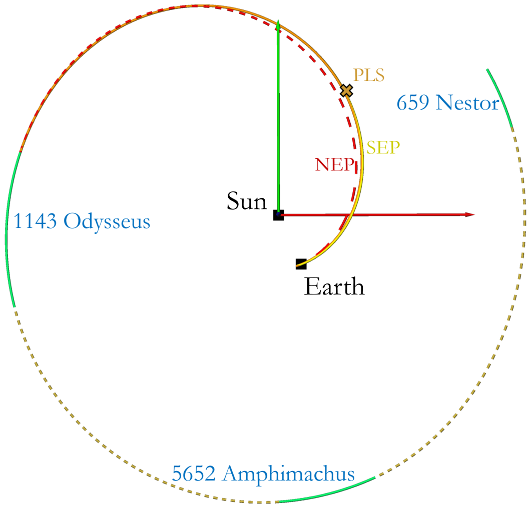

Figure 6.15.. Inertial trajectory view for tours with initial target 1143 Odysseus: outbound legs (dashed red, solid orange, solid yellow), thrust arcs (dashed gold), coasts in the vicinity of asteroids (solid green). The orange “X” marker indicates the switching point along the PLS enabled trajectory.

Table 6.11. Equivalent mission ΔV for 10-year mission with tour of 3 asteroids, various electrical power sources

	Value, km/s				**CR3BP**
Description	**CR3BP**	**Eph. NEP**	**Eph. SEP**	**Eph. PLS**	**Error (%)**
Earth to 1143 Odys. ($V_\infty = 7.5\frac{\text{km}}{\text{s}}$)	7.87554	7.82336	8.60175	8.17866	+0.667
1143 Odys. to 5652 Amph.	2.02238	1.94597	1.93721	1.93721	+3.927
5652 Amph. to 659 Nest.	3.39006	3.39160	3.40820	3.40820	-0.045

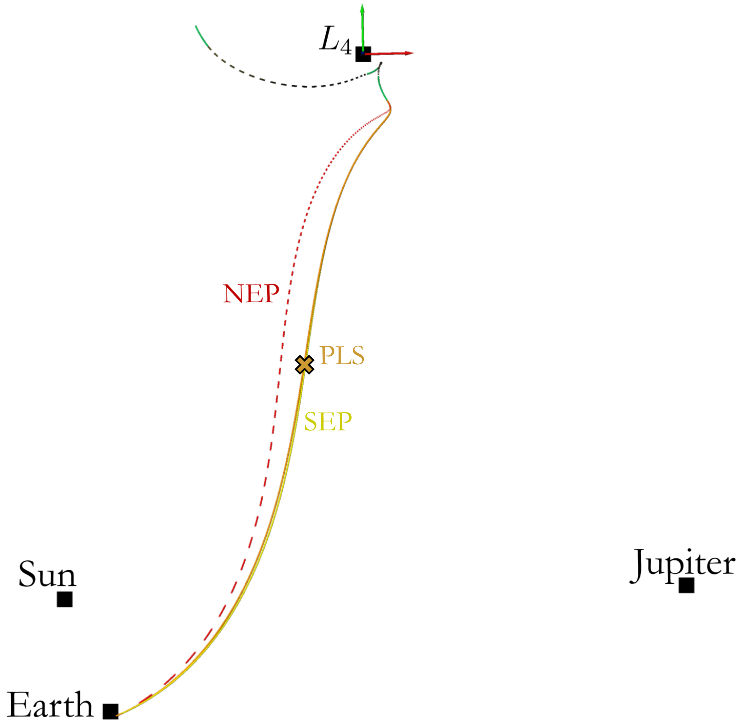

Figure 6.16.. Views of the trajectory path relative to the Sun-Jupiter rotating frame for tours with initial target 1143 Odysseus: outbound legs (dashed red, solid orange, solid yellow), thrust arcs (dashed black), coasts in the vicinity of asteroids (solid green). The orange “X” marker indicates the switching point along the PLS enabled trajectory.

segments are indicated in magenta, the 1143 Odysses to 5652 Amphimachus arc is green, and the 5652 Amphimachus to 659 Nestor leg is red. The discontinuities in the PLS outbound segment time histories are due to the switch in thrust regime. As is apparent in Fig. 6.17, each propulsion system maintains a consistent thrust-level order of magnitude across all thrust arcs. Additionally, the estimated profiles from the CR3BP sequence closely match those of the ephemeris NEP time histories. As expected from the excess power available, the SEP and PLS engines deliver large spikes in specific impluse over the relatively constant I_{sp} of the NEP thruster. The PLS and SEP systems also possess the same qualitative behavior, with large initial peaks in specific impulse and engine power and subsequent peaks in thrust magnitude along the outbound legs and, once the spacecraft is within the asteroid swarm, the engine operates at a nominal 1 kW power level. The SEP system delivers an exceedingly high initial engine power, on the order of 27 kW, however the PLS drops this high initial value to the much more feasible 4 kW. For all engine types, with proper adjustments for spacecraft mass and timing, these tours can serve as a reference paths for trajectory design with currently available constant specific impulse engines. However, as the required specific impulse values for all trajectories are above 5000 seconds, well above the capability of current electrical propulsion systems, intermediate coast arcs are likely to be inserted into the thrust legs for feasibility. Furthermore, adjusting the spacecraft mass and power parameters can also bring the optimal control histories within the capability of current systems.

6.2.2.2 Initial asteroid 4057 Demophon, 14-year mission

Repeating the trajectory design process for the second set of mission parameters further highlights the benefits of the automated procedure. For the same 25-year window of arrival epochs, the swarm rendezvous arc combination procedure produces the results in Fig. 6.20. As seen previously, with an expanded time-of-flight, a greater number of potential mission scenarios are generated; many of these sequences result in

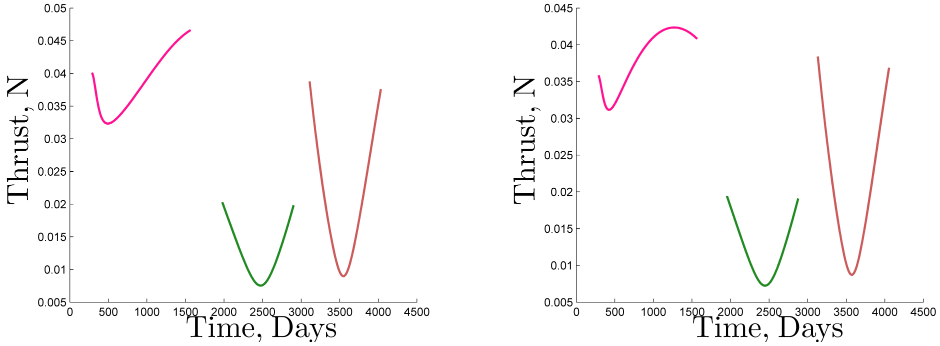

a. CR3BP

b. NEP

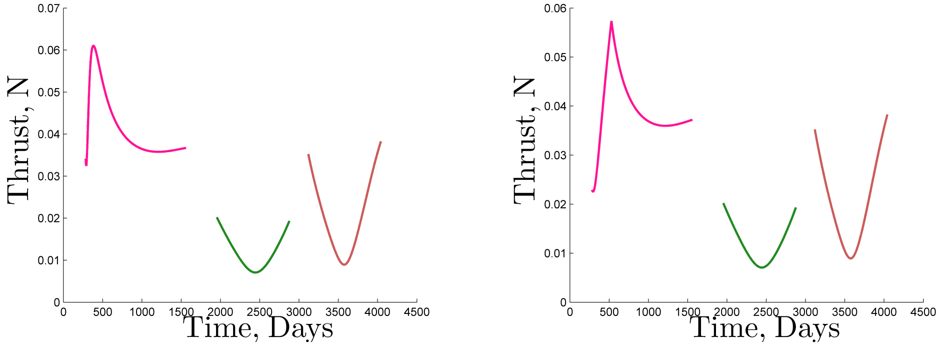

c. SEP

d. PLS

Figure 6.17.. Thrust profiles for the outbound leg (pink) as well as the first (green) and second (red) asteroid rendezvous arcs for the mission scenario given the asteroid 1143 Odysseus as the initial target within the swarm. Time is days since Oct. 3, 2021.

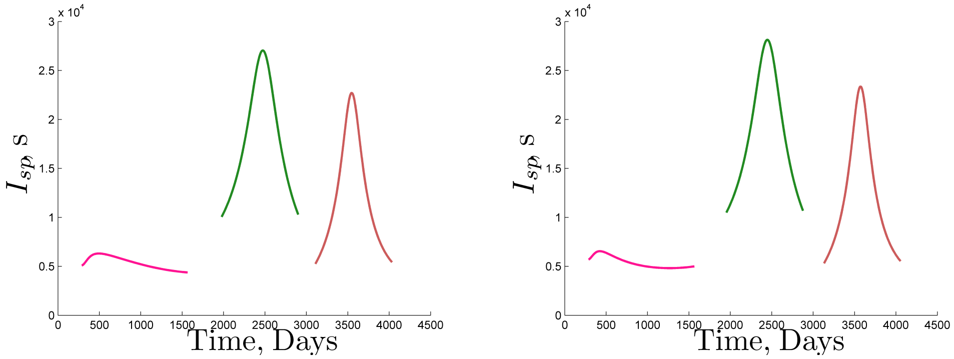

a. CR3BP

b. NEP

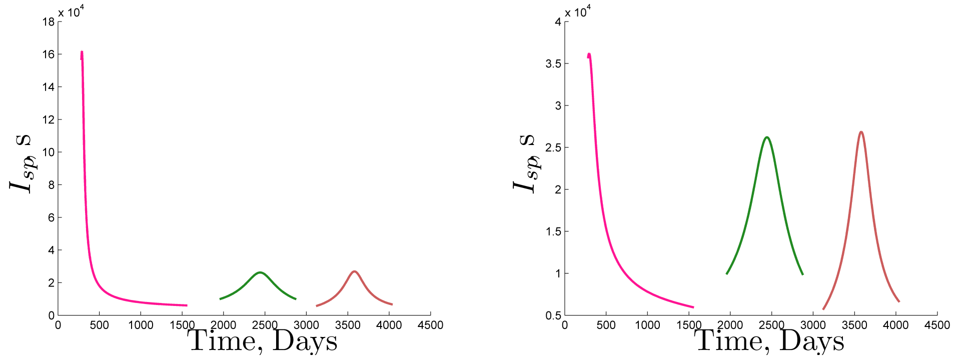

c. SEP

d. PLS

Figure 6.18.. Specific impulse profiles for the outbound leg (pink) as well as the first (green) and second (red) asteroid rendezvous arcs for the mission scenario with the asteroid 1143 Odysseus as the initial target within the swarm. Time is days since Oct. 3, 2021.

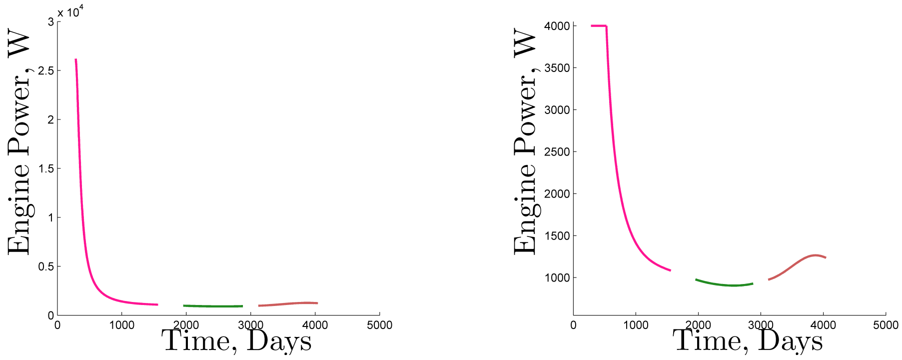

c. SEP

d. PLS

Figure 6.19.. Operating power profiles for the outbound leg (pink) as well as the first (green) and second (red) asteroid rendezvous arcs for the mission scenario with the asteroid 1143 Odysseus as the initial target within the swarm. Time is days since Oct. 3, 2021. Time histories for the NEP system and CR3BP sequence are constant at 1 kW and are not shown.

encounters with up to four asteroids as indicated by the years where the average number of asteroid encounters is greater than 3. In contrast, however, tours originating from 4057 Demophon typically have lower average merits than those initiated at 7152 Euneus, indicating less accessibility to high relative priority encounters upon departure from the initial target asteroid. For the arrival epoch corresponding to the year 2025, there are 32 feasible tours and, within that set, there are 8 sequences that link 4 asteroids. Assume that an asteroid tour is selected originating at 4057 Demophon and possessing subsequent encounters with 4138 Kalchas, 8317 Eurysaces, and 5652 Amphimachus and adjoin an Earth-to-4057 Demophon outbound leg. A set of three end-to-end, point-mass ephemeris trajectories defined by the various propulsion systems, i.e., NEP, SEP, and PLS, is constructed where, as before, the Earth-departure excess velocity is constrained to $V_\infty = 7.5$ km/s and the Earth-to-4057 Demophon thrust arc is specified to be precisely 3.5 years.

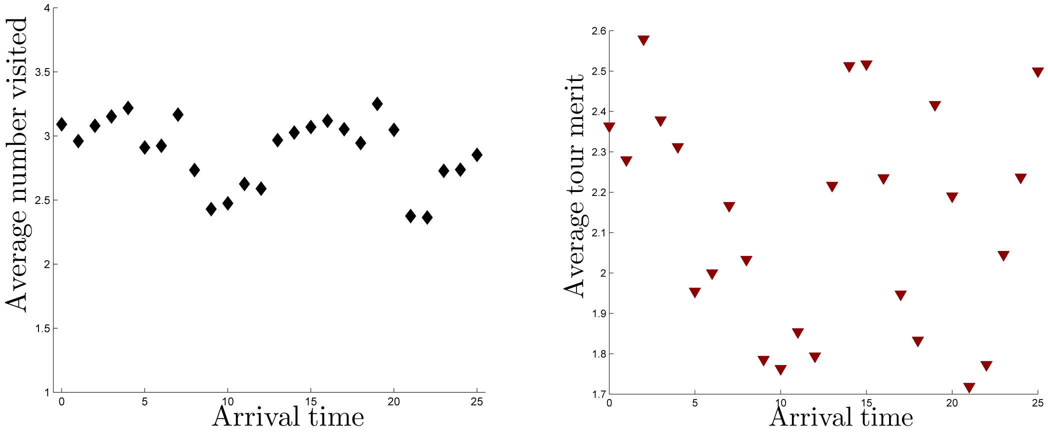

a. Average number of encounters per tour.

b. Average tour priority.

Figure 6.20.. Yearly search averages for tours originating at asteroid 4057 Demophon, in one-year increments, from Oct. 3, 2021.

The propellant consumption, mission timing, and ΔV budget for each mission scenario is summarized in Tables 6.12, 6.13, and 6.14, respectively. As with the sample tour originating with 1143 Odysseus, the propellant, timing, and ΔV estimates arising from the CR3BP sequence closely match the corresponding ephemeris trajectory enabled by a NEP system. A comparison of the NEP, SEP, and PLS ephemeris results reveals the qualitative trends observed for the mission originating with 1143 Odysseus also prevail when the initial target asteroid is 4057 Demophon. Furthermore, all ephemeris trajectories supply about 9 months of operation time in the vicinity of 4057 Demophon, over a year of loiter near 4138 Kalchas, approximately 10 months of coast with 8317 Eurysaces, and finally another 10 months near 5652 Amphimachus before the nominal end of mission operations.

The ephemeris trajectories generated by the automated procedure are displayed in the inertial and rotating frames in Figs. 6.21 and 6.22, respectively, where the color scheme is consistent with Figs. 6.15 and 6.16. The position of the Earth is displayed at the Earth departure epoch of June 5, 2021. As with the trajectories for initial target 1143 Odysseus, all three trajectories follow similar paths through space where the SEP and PLS arcs are particularly close.

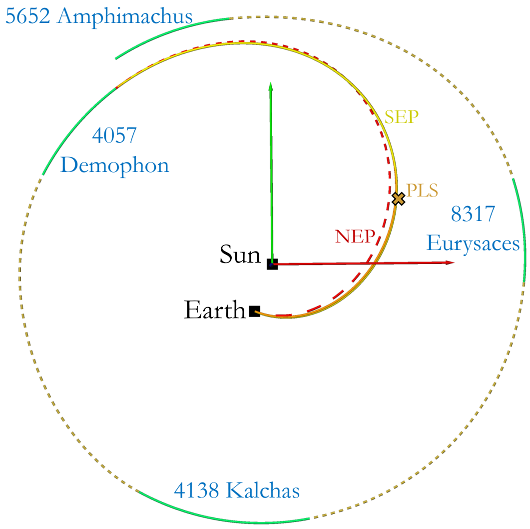

Figure 6.21.. Inertial trajectory view for tours with initial target 4057 Demophon: outbound legs (dashed red, solid orange, solid yellow), thrust arcs (dashed gold), coasts in the vicinity of asteroids (solid green). The orange “X” marker indicates the switching point along the PLS enabled trajectory.

Table 6.12. Spacecraft mass and propellant budget for 14-year mission with tour of 4 asteroids, various electrical power sources

	Value					**CR3BP**
Quantity	**CR3BP**	**Eph. NEP**	**Eph. SEP**	**Eph. PLS**	**Units**	**Error (%)**
Earth departure mass	583.986	586.691	546.696	548.593	kg	-0.461
Final spacecraft mass	447.647	447.187	447.948	447.948	kg	0.103
Propellant consumption	136.339	139.504	98.749	100.646	kg	-2.269
V_∞ at Earth departure	7.50000	7.50000	7.50000	7.50000	km/s	0

Table 6.13. Epochs of interest for 14-year mission with tour of 4 asteroids, various electrical power sources

	Gregorian Date YYYY:MM:DD			
Description	**CR3BP**	**Eph. NEP**	**Eph. SEP**	**Eph. PLS**
Earth departure ($V_\infty = 7.5$ km/s)	2021:06:02	2021:06:05	2021:05:30	2021:05:30
4057 Demophon arrival	2024:12:02	2024:12:04	2024:11:28	2024:11:28
4057 Demophon departure	2025:11:11	2025:09:22	2025:09:17	2025:09:17
4138 Kalchas arrival	2028:05:23	2028:04:03	2028:03:29	2028:03:29
4138 Kalchas departure	2028:11:25	2029:07:18	2029:07:22	2029:07:22
8317 Eurysaces arrival	2031:06:07	2032:01:28	2032:02:02	2032:02:02
8317 Eurysaces departure	2032:11:26	2032:11:20	2032:11:03	2032:11:03
5652 Amphimachus arrival	2035:06:08	2035:06:02	2035:05:16	2035:05:16
Nominal mission end	2036:04:03	2036:04:03	2036:04:03	2036:04:03

Table 6.14. Equivalent mission ΔV for 14-year mission with tour of 4 asteroids, various electrical power sources

	Value, km/s				**CR3BP**
Description	**CR3BP**	**Eph. NEP**	**Eph. SEP**	**Eph. PLS**	**Error (%)**
Earth to 4057 Demo. ($V_\infty = 7.5\frac{\text{km}}{\text{s}}$)	7.86158	7.94928	8.79683	8.30268	-1.103
4057 Demo. to 4138 Kalc.	4.64342	4.59472	4.58272	4.58272	+1.060
4138 Kalc. to 8317 Eury.	1.47900	1.72094	1.72395	1.72395	-14.059
8317 Eury. to 5652 Amph.	2.72399	2.86430	2.86731	2.86731	-4.899

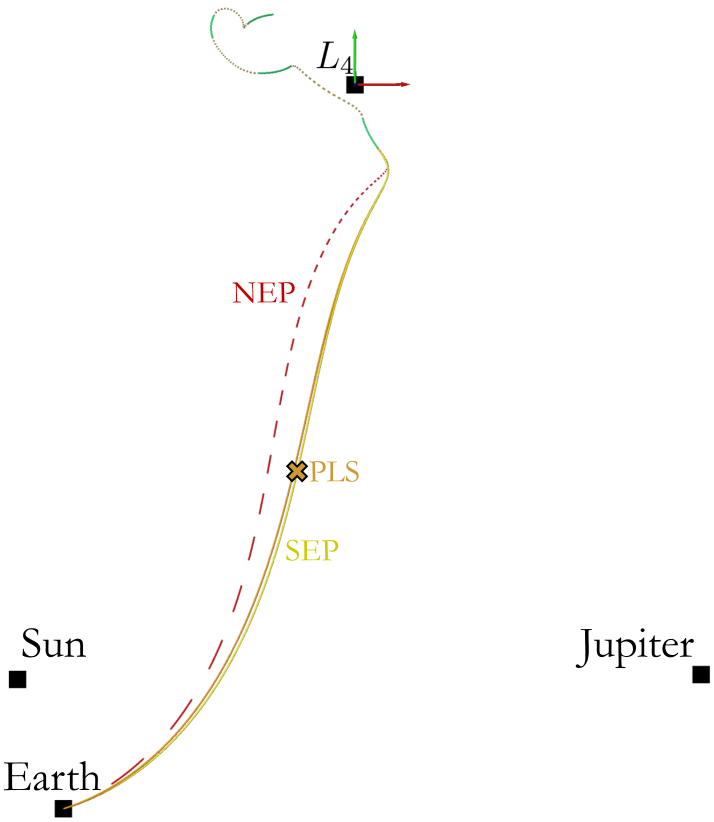

Figure 6.22.. Views of the trajectory path relative to the Sun-Jupiter rotating frame for tours with initial target 4057 Demophon: outbound legs (dashed red, solid orange, solid yellow), thrust arcs (dashed black), coasts in the vicinity of asteroids (solid green). The orange "X" marker indicates the switching point along the PLS enabled trajectory.

As in the previous example, the time histories for the engine operating parameters such as thrust, specific impulse, and electrical power are also examined, with the same qualitative differences in behavior between the electrical power sources. Figure 6.23 illustrates the time thrust and specific impulse time histories associated with the NEP ephemeris trajectory and are shown to illustrate the quantitative change in behavior for the asteroid-to-asteroid arcs of this potential tour. For all propulsion types, NEP, SEP, and PLS, the engine performance on the outbound leg is qualitatively very similar to the case with initial target 1143 Odysseus. As with the trajectories encountering 1143 Odysseus, the tours can serve as a reference paths for trajectory design with currently available constant specific impulse engines.

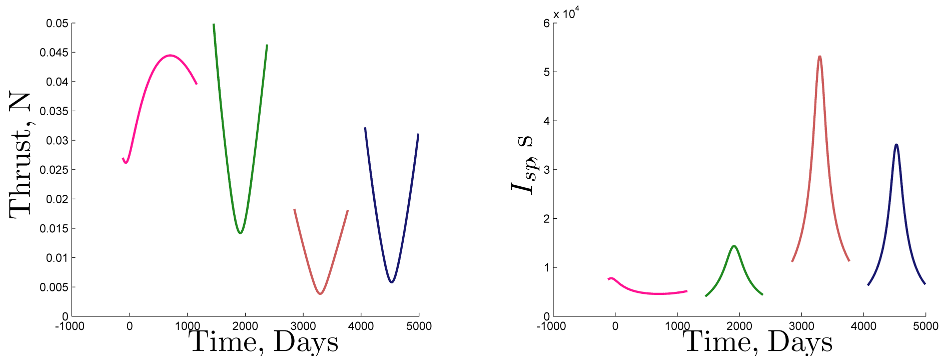

a. NEP thrust

b. NEP specific impulse

Figure 6.23.. NEP thrust and specific impulse profiles for the outbound leg (pink) as well as the first (green), second (red), and third (blue) asteroid rendezvous arcs for the mission scenario with the asteroid 4057 Demophon as the initial target within the swarm. Time is days since Oct. 3, 2021. Power time history is constant at 1 kW and is not shown.

6.2.3 Scaling of engine operation with spacecraft parameters

Though the rendezvous trajectory algorithm automatically uses the scaling relations in Section 5.6.3 to generate initial guesses for optimization, the equations are also advantageous in a rapid mission analysis scenario where full optimization runs are not feasible. For example, adjustments to a prospective baseline trajectory, especially the available engine power and the spacecraft mass upon arrival in the asteroid swarm, may be necessary or desired for iterations in a trajectory analysis procedure. However, if a large set of possible values for P_{ref} and m_r are to be considered, then trajectory computation and optimization for every scenario is prohibitively expensive. Accordingly, the scaling relationships represented in Eqs. (5.139) and (5.140) are used to rapidly approximate the performance of a specific spacecraft configuration in lieu of full optimization.

The point-mass ephemeris trajectory with initial arrival at target asteroid 1143 Odysseus in 2026 and subsequent encounters with 5652 Amphimachus and 659 Nestor, enabled by a NEP thruster, is employed as a test case for the scaling relationships. For this baseline trajectory, a new set of mission parameters is defined comprised of a spacecraft mass equal to 750 kg upon arrival in the asteroid swarm and 500 W of electrical power available to the thruster. Recall that the original analysis was performed using $m_r = 500$ kg and $P_{\text{ref}} = 1$ kW. The scaling equations are applied using the new spacecraft parameters and the baseline trajectory performance metrics; for comparison, the trajectory is also re-converged and optimized using the new spacecraft parameters. The results from the scaling procedure and the optimization process are included in Table 6.15, along with the performance metrics of the baseline trajectory. As observed in the table, even for this large difference between the baseline and the updated specifications, the approximate scaling relationships predict the actual results to within numerical error. An approximate thrust magnitude is also computed via Eq. 5.44, where this thrust magnitude incurs the same accuracy as the I_{sp} prediction.

In altering the spacecraft parameters, any potential change in the qualitative behavior of the trajectory is also a concern. The departure and arrival epochs, as well as the physical path of the vehicle, are largely unaffected by changes in the spacecraft mass and available power. In contrast, the specific impulse and thrust magnitude time histories are altered as a result of adjustments to m_r and P_{ref}, as is displayed in Fig. 6.24. The magnitude of the thrust vector is approximately doubled in response to this new set of spacecraft parameters, while the outbound leg thrust profile (magenta) trends downward for the scaled results, whereas the baseline thrust profile reacts oppositely, i.e., trends upward. Additionally, the evolution of the specific impulse is qualitatively the same for all the thrust arcs, however, the I_{sp} values are reduced by an order of magnitude.

Table 6.15. Spacecraft mass and propellant budget for 10-year mission with tour of 3 asteroids, scaled by reference mass and reference power

Quantity	**Value**			**Units**	**Error (%)**
	Optimized Reference	**Scaling Prediction**	**Scaled, Optimized**		
Reference power, P_{ref}	1	0.5	0.5	kW	–
Reference mass, m_r	500	750	750	kg	–
Earth departure mass	582.273	1301.830	1301.830	kg	0.00
Final spacecraft mass	473.584	642.487	642.487	kg	0.00
Propellant consumption	108.689	659.343	659.343	kg	0.00
Average I_{sp} on outbound leg	5371	1449	1449	s	0.00
V_{∞} at Earth departure	7.50000	7.50000	7.50000	km/s	0.00

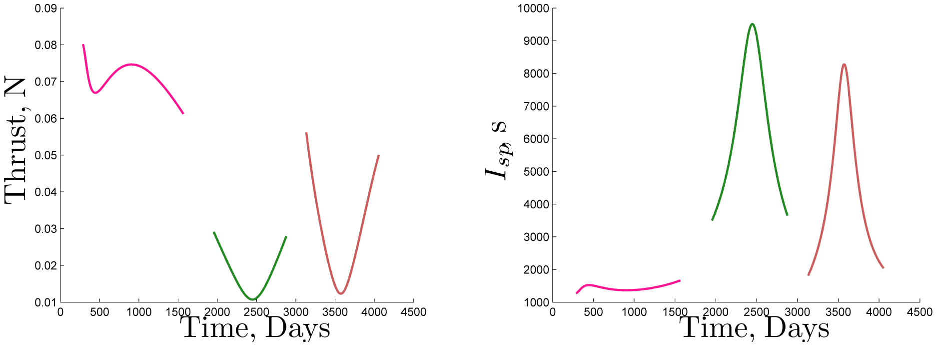

a. Thrust

b. Specific impulse

Figure 6.24.. Fully optimized thrust and specific impulse profiles for the outbound leg (pink) as well as the first (green) and second (red) asteroid rendezvous arcs for the mission scenario with the asteroid 1143 Odysseus as the initial target within the swarm and reference mass $m_r = 750$ kg and electrical power $P_{\text{ref}} = 0.5$ kW. Time is days since Oct. 3, 2021.

6.3 Trojan asteroid surveys - summary and conclusions

The general framework for automated rendezvous tour construction is applied to the analysis of robotic surveys of the Sun-Jupiter L_4 Trojan asteroids enabled by a variable specific impulse (VSI) propulsion system. The potential scientific return associated with an asteroid encounter is critical when assessed potential tour trajectories. Accordingly, the prospective merit of the target asteroids is appraised and incorporated into the design process, both as a post-processing step as well as an intrinsic component of the encounter sequence generation. A VSI engine enables the smooth adjustment of thrust magnitude and propellant efficiency without the need for thruster shut-downs and restarts. Nuclear electric and solar electric propulsion are modeled as constant- and varying-power systems, respectively, while a power-limited solar electric engine is analyzed as a hybrid system comprised of constant- and varying-power thrust regimes. Indirect and direct optimization methods are blended to produce a hybrid optimization scheme wherein mass objective functions are directly optimized using the optimization packages SNOPT and *fmincon*. Engine operation is determined via an indirect, calculus of variations optimization approach, where the constant- and varying-power systems follow distinct control laws and equations of motion. The optimization procedure is combined with an easily computed rendezvous detection criteria and employed to quickly and automatically yield a large number of rendezvous arcs between a selected set of asteroids. The independently generated asteroid-to-asteroid trajectory arcs are then rapidly sequenced into a series of thrust and coast arcs comprising several tour scenarios that satisfy a set of constraints on the trajectory. A straight-forward enumerated tree search scheme enables the rapid construction tour sequences, however computional requirements grow exponentially as asteroids are added to the set of potential targets. Furthermore, thrust arc duration must be pre-specified for the tree search method. However, since the VSI enabled transfers afford a trade-off between transfer duration and propellant consumed, a search strategy that exploits this adaptability is advantageous.

Thus, the ant colony heuristic is expanded by incorporating the laying of pheromone along neighboring thrust arcs within the pre-computed rendezvous solution families. This parallel distribution ensures that the duration-propellant trade space for each asteroid-to-asteroid rendezvous is explored and balanced with the other transfer options composing a tour trajectory. Individual tour sequences are then analyzed for propellant consumption, number of asteroids encountered, and coast durations in the vicinity of the asteroids. A hybrid propulsion arc from the Earth to the asteroid swarm and comprised of an initial Earth departure velocity and a low-thrust arc is then adjoined to the inter-asteroid sequence. Baseline scenarios of particular interest are then scaled appropriately by the desired engine type and available engine power and optimized in a higher-fidelity model. Results indicate that optimization of the individual thrust arcs is sufficient to ensure end-to-end propellant optimality: the selected engine model along with specifying bounds on the thrust durations creates an optimization problem wherein the rendezvous thrust segments can be treated independently, thus, greatly simplifying the generation of optimal trajectories.

The accuracy of the circular-restricted three-body model estimates are assessed and the qualitative and quantitative behavior of the various electrical power systems is appraised. For the sample tours that are examined in this investigation, the automated algorithm yields fuel mass estimates for constant power trajectories within 3% of the identical trajectories optimized from end-to-end in a Sun-Jupiter point-mass ephemeris model. In general, an Earth departure date is reliably predicted, while epochs corresponding to individual thrust arcs within the asteroid swarm vary on the order of a few months. Thus, the lower-fidelity circular-restricted three-body problem offers accurate estimates of mission requirements. Thrust magnitudes are generally in the tens of milli-Newtons, values that are readily achievable using current low-thrust propulsion technology. The required specific impulse of the VSI thruster, on the other hand, is typically tens of thousands of seconds or higher, well beyond the range of current engine systems; however, these high-efficiency periods be could readily be replaced with coast periods for constant specific impulse (CSI) systems.

Furthermore, the scaling relations can be easily used to scale the engine performance and spacecraft size to more resonable values while retaining sufficient accuracy for preliminary design studies. Results also indicate that optimal operation of a power-limited solar electric system implies continuity in the Euler-Lagrange co-state vectors across a switch in thrust regime, an observation that can reduce implementation time and computational overhead. This continuity also supports an assessment that the indirect optimization schemes reveal optimal paths through space, regardless of thrust systems or switches in engine operational domains. Furthermore, scaling relationships for engine operation and performance quantities offer an avenue for rapid investigation of mission scenarios and spacecraft parameters. However, the procedure is not limited by dynamical regime and is readily extended to other mission architectures.

While the automated procedure offers cost and timing estimates for specific trajectories comprising an asteroid tour mission, the algorithm also offers insight into overall mission planning. Of special advantage is the identification of favorable sequences of rendezvous arcs and corresponding ΔV costs, where the procedure predicts a likely set of asteroids and a specific order of encounter, independent of the on-board propulsion system. The search and combination procedure incorporates naturally favorable departure and arrival epochs while ensuring sufficient proximity operation duration in the vicinity of the target asteroids. Furthermore, families of thrust arcs computed using a variable specific impulse model can aid in the recognition of corresponding thrust durations that enable the use of constant specific impulse systems with a minimum of engine power cycles.

6.3.1 Asteroid surveys - recommendations for future investigation

Several avenues of investigation may enhance the capability of the automated design scheme for constructing Trojan asteroid tours. While the pre-computation of asteroid-to-asteroid trust arcs is a viable strategy when the number of targets is relatively small, computational requirements would quickly become prohibitive with even a modest growth in the number of objects of interest. Therefore, the computation of asteroid-to-asteroid rendezvous arcs on an “as-needed” basis may greatly enhance the ability of the automated procedure. Additionally, the transformation of thrust arcs enabled by the VSI engine to equivalent arcs supported by other propulsion schemes, e.g., chemical boosters or conventional constant specific impulse electrical thrusters, is of interest. Finally, multiple probes sent to the asteroid swarm may permit the exploration of a larger number of target objects or the evolution of multiple asteroids over time. Thus, schemes to coordinate the actions of multiple surveying vehicles require further development.

7. CONCLUDING REMARKS AND RECOMMENDATIONS

A general framework for the automated construction of rendezvous tour trajectories is detailed and applied to the removal of debris near to the Earth as well as robotic surveys of the Sun-Jupiter Trojan asteroids. Formulating trajectory design procedures within the context of this high-level strategy enables a systematic, encompassing approach to the automation of spacecraft tour trajectories. The trajectory design strategy is composed of four high-level functions:

1. *Mission conception*: the formulation of the mission goals and constraints;
2. *Definition of natural dynamical models*: the selection of a minimal dynamical model suitable for rapid preliminary analysis while retaining sufficient dynamical fidelity;
3. *Automated tour generation*: the automated process whereby potential trajectories are constructed, composed of three sub-tasks:
    (a) *Relative target value assessment*: determining a set of potential individual targets and assessing their relative priority, if any;
    (b) *Rendezvous computation*: computing and applying the propellant costs as well as the timing required for transfer from one object to another;
    (c) *Search strategy implementation*: the ordered selection of targets for individual spacecraft and the production of encounter sequences; and,
4. *Mission operations*: the transition of preliminary trajectory results to higher fidelity models suitable for eventual mission operations.

As illustrated by the analyses of the two distinct mission scenarios, the tour construction framework is flexible in implementation and allows for varying levels of automated operation. Each task within the context of the framework may be independently adjusted without requiring dramatic modifications in the other functions. The two scenarios examined provide unique perspectives on the implementation of the general tour construction strategy, however other mission architectures could represent equally valuable insight. For example, a tighter interrelation between the implementations of the target value, rendezvous computation, and search strategy could be beneficial for a mission scenario distinct from the illustrative examples provided. Observations relevant to each component of the tour design framework are offered.

7.1 Mission conception

Once a spacecraft mission is proposed and a associated set of goals is defined, measurable objectives are formulated such that satisfying the specific objectives also achieves the desired goals. These objectives may be adjusted over time as the mission planning proceeds from preliminary investigation to actual flight operations. The mission goals and objectives are identified to supplement existing knowledge and / or techincal capability and, therefore, the historical context of an investigation is critical. While two specific mission architectures are analyzed, the automated tour design strategy may be applied to a wide variety of spacecraft mission scenarios, from the construction of tours of planetary satellites to the support of an infrastructure for deep-space human missions. Indeed, the general framework is readily expanded to incorporate brief flyby encounters in addition to prolonged rendezvous options. Furthermore, many of the high-level concepts for the automated tour design process may also be broadly applicable outside of spacecraft operations, e.g., the path planning of unmanned aerial vehicles (UAVs), the routing of disaster recovery suppliers, and the guidance of robotic submersibles.

7.2 Definition of natural dynamical models

The definition of the mathematical model defining the natural motion of the operating vehicle as well as the target objects is fundamental to the trajectory construction process. The inverse square law of gravitation, first formalized by Newton, provides a high accuracy basis for analysis of the motion of celestial objects. In particular, the N-body model underpins the equations of motion employed by this investigation. Care must be taken, however, to ensure that any simplified dynamical model provides an adequate balance between computational efficiency and fidelity to relevant real-world effects. For example, the librating motion of the Sun-Jupiter Trojan asteroids is not captured by two-body approximations and, therefore, multiple gravitating bodies must be explicitly modeled. While not addressed during the course of this analysis, real-world phenomena such as drag and nonspherical gravitating bodies are readily incorporated into the tour design framework.

7.3 Tour generation: Relative target value assessment

Evaluating the relative desirability of particular encounters is a key task of the tour design strategy. This priority ranking can be applied to sets of objects, e.g., determining what groups of debris fragments to mitigate, as well as individual targets, e.g., preferentially encountering fragments posing a high likelihood of collision. The assignment of target value also benefits greatly from human intuition, for example assessing the potential scientific knowledge to be gained from a particular asteroid. Thus, while certain aspects of determining relative target priority benefit from automation, human-in-the-loop interaction remains a key factor.

7.4 Tour generation: Rendezvous computation

A wide variety of options exist for transferring the operating spacecraft from one target to another and accurate simulation of these capabilities is critical for preliminary analysis. The rendezvous operation is modeled using a variety of techniques, from analytical approximations to high-fidelity numerical simulations, depending on the desired precision of the cost estimates. A differential corrections procedure that is flexible in implementation ensures continuous trajectory solutions when numerical simulations are required. Optimal low-thrust rendezvous arcs in multibody regimes are computed via a hybrid optimization scheme that retains the low-dimensionality of indirect methods while exploiting the robustness of direct, gradient-based local optimization techniques. These continuous thrust arcs, enabled by a variable specific impulse (VSI) thruster, are readily computed and provide estimates of departure and arrival epoch, required propellant mass and ΔV budgets, as well as optimal engine operating conditions. Models simulating VSI engines are of value as a preliminary analysis tool due to the relative ease of application as well as insights afforded into the optimal operation of other propulsion systems, for example chemical boosters and traditional constant specific impulse thrusters.

7.5 Tour generation: Search strategy

An efficient search strategy is critical for the investigation of large design spaces, particularly those that present continuous trade-offs between control variables. While strict tree enumeration is feasible for small problems, the computational cost of such schemes grows exponentially with the growth of the design space. Therefore, evolutionary and other hueristic search algorithms are of interest. Ant colony optimization (ACO) is a meta-hueristic methods particularly well-suited to routing problems such as the construction of spacecraft tour trajectories. Additionally, ACO is flexible in implementation, from enabling searches incorporating multiple operating vehicles to the exploration of continuous trade spaces. Several enhancements to the ant colony heuristic may prove beneficial in other applications, both in astrodynamics and in other industries.

7.6 Mission operations

The transition to a flight operation regime is the final step of the automated tour construction framework. Several options are available for this transition, from the high fidelity simulation of the baseline path to the real-time adjustment of the encounter sequence. An auction and bidding scheme is demonstrated as a viable method for coordinating the actions of multiple independently operating spacecraft. This auction procedure readily adjusts and enhances the performance of reference paths constructed using the ant colony heuristic and the combination of evolutionary and auction schemes warrants further investigation. Tour trajectories of the Trojan asteroid, enabled by a low-thrust propulsion system, are readily transitioned to higher fidelity models and various options for electrical power source as well as spacecraft parameters are rapidly examined. Baseline paths employing a VSI engine may also provide novel options for trajectories using traditional propulsion technologies such as chemical boosters. Finally, while not explicitly addressed in this analysis, the incorporation of closed-loop feedback and orbit determination capabilities into the overall design and operations framework can enable completely autonomous guidance, navigation, and control of spacefaring vehicles.

Stu Beef, you've done it again!

LIST OF REFERENCES

LIST OF REFERENCES

[1] J. A. Dunne and E. Burgess, *The Voyage of Mariner 10.* Washington, DC: National Aeronautics and Space Administration, Scientific and Technical Information Office.

[2] G. A. Flandro, "Fast Reconnaissance Missions to the Outer Solar System Utilizing Energy Derived from the Gravitational Field of Jupiter," *Astronautica Acta*, vol. 12, pp. 329–337, 1966.

[3] M. A. Minovitch, "An Alternative Method for Determination of Elliptic and Hyperbolic Trajectories," tech. rep., Jet Propulsion Laboratory, California Institute of Technology, Pasadena, California, July 1961. TM-312-118.

[4] M. A. Minovitch, "A Method for Determining Interplanetary Free-Fall Reconnaissance Trajectories," tech. rep., Jet Propulsion Laboratory, California Institute of Technology, Pasadena, California, August 1961. TM-312-130.

[5] E. Rinderle, "Galileo User's Guide, Mission Design System, Satellite Tour Analysis and Design Subsystem," tech. rep., Jet Propulsion Laboratory, California Institute of Technology, Pasadena, California, July 1986. JPL D-263.

[6] A. Wolf and J. Smith, "Design of the Cassini Tour Trajectory in the Saturnian System," *Control Engineering Practice*, vol. 3, pp. 1611–1619, November 1995.

[7] J. Lygeros, S. Sastry, and C. Tomlin, *The Art of Hybrid Systems.* DRAFT, July 29 2001.

[8] Advanced Concepts Team, "Global Trajectory Design Competition." European Space Agency, `http://sophia.estec.esa.int/gtoc_portal/`, 2005–2014.

[9] B. W. Barbee, G. W. Davist, and S. Diaz, "Spacecraft Trajectory Design for Tours of Multiple Small Bodies," *Advances in the Astronautical Sciences*, vol. 135, no. 3, pp. 2169–2188, 2009.

[10] B. J. Wall and B. A. Conway, "Genetic algorithms applied to the solution of hybrid optimal control problems in astrodynamics," *Journal of Global Optimization*, vol. 44, no. 4, pp. 493–508, 2009.

[11] I. S. Grigoriev and M. P. Zapletin, "One Optimization Problem for Trajectories of Spacecraft Rendezvous Mission to a Group of Asteroids," *Cosmic Research*, vol. 47, no. 5, pp. 426–437, 2009.

[12] C. H. Yam, D. D. Lorenzo, and D. Izzo, "Low-thrust trajectory design as a constrained global optimization problem," *Proceedings of the Institution of Mechanical Engineering, Part G: Journal of Aerospace Engineering*, vol. 225, no. 11, pp. 1243–1251, 2011.

[13] J. Englander, "Evolutionary mission trajectory generator." NASA Goddard Space Flight Center Website. `http://opensource.gsfc.nasa.gov/projects/emtg/index.php`; Accessed 30 May 2014.

[14] M. Ceriotti and M. Vasile, "MGA Trajectory Planning with an ACO-inspired Algorithm," *Acta Astronautica*, vol. 67, pp. 1202–1217, 2010.

[15] A. Heaton, N. Strange, J. Longuski, and E. Bonfiglio, "Automated Design of the Europa Orbiter Tour," *Journal of Spacecraft and Rockets*, vol. 39, no. 1, pp. 17–22, 2002.

[16] A. E. Lynam, "Broad-search algorithms for the spacecraft trajectory design of Callisto-Ganymede-Io triple flyby sequences from 2021 to 2040, Part I: Hueristic pruning of the search space," *Acta Astronautica*, vol. 94, no. 1, pp. 246–252, 2014.

[17] A. E. Lynam, "Broad-search algorithms for the spacecraft trajectory design of Callisto-Ganymede-Io triple flyby sequences from 2021 to 2040, Part II: Lambert pathfinding and trajectory solutions," *Acta Astronautica*, vol. 94, no. 1, pp. 253–261, 2014.

[18] G. A. Tsirogiannis, "A graph based methodology for mission design," *Celestial Mechanics and Dynamical Astronomy*, vol. 114, pp. 353–363, 2012.

[19] D. Izzo, T. Vinkó, C. Bombardelli, S. Brendelberger, and S. Centuori, "Automated Asteroid Selection for a 'Grand Tour' Mission," in *58th International Astronautical Congress*, (Hyderabad, India), September 24-28 2007. Paper No. IAC-07-C1.7.07.

[20] E. Canalias, A. Mithra, and D. Carbonne, "End-to-End Trajectory Design for a Chemical Mission Including Multiple Flybys of Jovian Trojan Asteroids," in *AAS/AIAA Astrodynamics Specialist Conference*, (Girdwood, Alaska), pp. 1195–1212, July 31 - August 4 2011. Paper No. AAS 11-481.

[21] M. Matsumoto and J. Kawaguchi, "Optimum Trajectory for Low-Thrust Multiple Trojan Asteroid Flybys," *European space Agency Special Publications*, vol. 548, pp. 499–504, 2004.

[22] E. Perozzi, A. Rossi, and G. Valsecchi, "Basic Targeting Strategies for Rendezvous and Flyby Missions to Near-Earth Asteroids," *Planetary and Space Science*, vol. 49, no. 1, pp. 3–22, 2001.

[23] B. W. Barbee, S. Alfano, E. Pinon, K. Gold, and D. Gaylor, "Design of Spacecraft Missions to Remove Multiple Orbital Debris Objects," in *35th Annual AAS Guidance and Control Conference*, (Breckenridge, Colorado), February 3-8 2012. Paper No. AAS-12-017.

[24] J. Missel and D. Mortari, "Path optimization for Space Sweeper with Sling-Sat: A method of active space debris removal," *Advances in Space Research*, vol. 52, pp. 1339–1348, 2013.

[25] I. Newton, *The Principia: Mathematical Principles of Natural Philosophy*. Berkeley, California: University of California Press, 1999. Translation by I. B. Cohen and A. Whitman.

[26] Solar System Dynamics Group, *HORIZONS System.* Jet Propulsion Laboratory. http://ssd.jpl.nasa.gov/?horizons.

[27] H. B. Keller, *Numerical Solution of Two Point Boundary Value Problems.* Philadelphia, Pennsylvania: Society for Industrial and Applied Mathematics, 1976.

[28] D. J. Grebow, "Generating Periodic Orbits in the Circular Restricted Three-Body Problem with Applications to Lunar South Pole Coverage." M.S. Thesis, School of Aeronautics and Astronautics, Purdue University, West Lafayette, Indiana, 2006.

[29] B. Bradie, *A Friendly Introduction to Numerical Analysis.* Upper Saddle River, New Jersey: Prentice Hall, 2006.

[30] W. H. Press, S. Teukolsky, W. Vetterling, and B. Flannery, *Numerical Recipes. The Art of Scientific Computing.* Cambridge University Press, third ed., 2007.

[31] L. Shampine and H. Watts, "DEPAC Design of a User Oriented Package of ODE Solvers." SAND79-2374, Sandia National Laboratories, 1980.

[32] H. K. Kahlil, *Nonlinear Systems.* Prentice Hall, third ed., 2002.

[33] K. Ogata, *Modern Control Engineering.* Upper Saddle River, New Jersey: Prentice Hall, fourth ed., 2002.

[34] E. W. Dijkstra, "A note on two problems in connexion with graphs," *Numerische Mathematik*, vol. 1, no. 1, pp. 269–271, 1959.

[35] A. H. Land and A. G. Doig, "An Automatic Method of Solving Discrete Programming Problems," *Econometrica*, vol. 28, no. 3, pp. 497–520, 1960.

[36] D. L. Applegate, R. E. Bixby, V. Chvätal, and W. J. Cook, *The Traveling Salesman Problem: A Computational Study.* Princeton University Press, 2007.

[37] M. Dorigo, V. Maniezzo, and A. Colorni, "Positive Feedback as a Search Strategy," tech. rep., Dipartimento di Elettronica, Politecnico di Milano, Italy, 1991. Tech. Rep. 91-016.

[38] M. Dorigo and T. Stützle, *Ant Colony Optimization.* Cambridge, Massachusetts: MIT Press, 2004.

[39] E. Bonabeau, M. Dorigo, and G. Theraulaz, *Swarm Intelligence: From Natural to Artificial Systems.* Oxford, England, United Kingdom: Oxford University Press, 1999.

[40] W. Vickrey, "Counterspeculation, auction, and competitive sealed tenders," *Journal of Finance*, vol. 16, pp. 8–37, 1961.

[41] H. R. Varian, "Economic Mechanism Design for Computerized Agents," in *Proceedings of the First USENIX Workshop on Electronic Commerce*, (New York, New York), July 1995.

[42] D. J. Kessler and B. G. Cour-Palais, "Collision Frequency of Artificial Satellites: The Creation of a Debris Belt," *Journal of Geophysical Research*, vol. 83, no. A6, pp. 2637–2646, 1978.

[43] NASA Orbital Debris Program Office, "Satellite Collision Leaves Significant Debris Clouds," *Orbital Debris Quarterly News*, vol. 13, pp. 1–2, April 2009.

[44] NASA Orbital Debris Program Office, "Chinese Anit-Satellite Test Creates Most Severe Orbital Debris Cloud in History," *Orbital Debris Quarterly News*, vol. 11, pp. 2–3, April 2007.

[45] "Satellite Debris Analysis Indicates Hydrazine Tank Hit." U.S. Department of Defense Press Release, February 28 2008. No. 0146-08.

[46] NASA Orbital Debris Program Office, "Fengyun-1C Debris: One Year Later," *Orbital Debris Quarterly News*, vol. 12, pp. 2–3, January 2008.

[47] J. Liou, "An Active Debris Removal Parametric Study for LEO Environment Remediation," *Advances in Space Research*, vol. 47, pp. 1865–1876, 2011.

[48] J. P. Loftus, P. D. Anz-Meador, and R. Reynolds, "Orbital Debris Minimization and Mitigation Techniques," *Advances is Space Research*, vol. 13, no. 8, pp. 263–282, 1993.

[49] H. G. Lewis, A. E. White, R. Crowther, and H. Stokes, "Synergy of Debris Mitigation and Removal," *Acta Astronautica*, vol. 81, no. 1, pp. 62–68, 2012.

[50] C. Früh, M. Jah, E. Valdez, P. Kervin, and T. Kelecy, "Taxonomy and Classification Scheme for Artificial Space Objects," in *Advanced Maui Optical and Space Surveillance Technologies Conference*, (Maui, Hawaii), September 10-13 2013.

[51] M. P. Wilkins, A. Pfeffer, P. W. Schumacher, and M. K. Jah, "Towards an Artificial Space Object Taxonomy," in *Advanced Maui Optical and Space Surveillance Technologies Conference*, (Maui, Hawaii), September 10-13 2013.

[52] P. D. McCall, "Modeling, Simulation, and Characterization of Space Debris in Low-Earth Orbit." Ph.D. Dissertation, Florida International University, Miami, Florida, 2013.

[53] B. M. Wiegmann, "NASA's Marshall Space Flight Center Recent Studies and Technology Developments in the Area of SSA/Orbital Debris," in *Advanced Maui Optical and Space Surveillance Technologies Conference*, (Wailea, Maui, Hawaii), September 11-14 2012.

[54] K. Hicks, "Risk Prioritization for Mitigation of Debris in Low Earth Orbit." M.S. Thesis, School of Aeronautics and Astronautics, Purdue University, West Lafayette, Indiana, 2013.

[55] G. E. Peterson, "Target Identification and Delta-V Sizing for Active Debris Removal and Improved Tracking Campaigns," in *23rd International Symposium on Spaceflight Dynamics*, (Pasadena, California), October 29 - November 2 2012. Paper No. ISSFD23-CRSD2-5.

[56] M. M. Castronuovo, "Active Space Debris Removal - A Preliminary Mission Analysis and Design," *Acta Astronautica*, vol. 69, pp. 848–859, November-December 2011.

[57] V. Braun, A. Lupken, S. Flegel, J. Gelhaus, M. Mockel, C. Kebschull, C. Wiedemann, and P. Vorsmann, "Active debris removal of multiple priority targets," *Advances in Space Research*, vol. 51, pp. 1638–1648, 2013.

[58] L. M. Healy, "Lambert Targeting for On-Orbit Delivery of Debris Remediation Dust," 2014. *Journal of Spacecraft and Rockets*, doi: `http://arc.aiaa.org/doi/abs/10.2514/1.A32634`.

[59] O. de Weck, U. Scialom, and A. Siddiqi, "Optimal reconfiguration of satellite constellations with the auction algorithm," *Acta Astronautica*, vol. 62, no. 2, pp. 112–130, 2008.

[60] A. Salazar and P. Tsiotras, "An auction algorithm for allocating fuel in satellite constellations using peer-to-peer refueling," in *2006 American Control Conference*, (Minneapolis, Minnesota), June 14-16 2006.

[61] J. Hilland, R. Wessen, D. Porter, and R. Austin, "A market-based conflict resolution approach for satellite mission planning," *IEEE Transactions on Engineering Management*, vol. 48, no. 3, pp. 272–282, 2001.

[62] J. E. Prussing and B. A. Conway, *Orbital Mechanics.* New York: Oxford University Press, second ed., 2013.

[63] D. A. Vallado and W. D. McClain, *Fundamentals of Astrodynamics and Applications.* El Segundo, California: Microcosm Press / Springer, third ed., 2007.

[64] R. R. Bate, D. D. Mueller, and J. E. White, *Fundamentals of Astrodynamics.* New York: Dover Publications, Inc., 1971.

[65] H. Goldstein, J. Charles P. Poole, and J. L. Safko, *Classical Mechanics.* Boston, Massachusetts: Addison-Wesley, third ed., 2001.

[66] H. G. Lewis, R. Newland, G. Swinerd, and A. Saunders, "A New Analysis of Debris Mitigation and Removal Using Networks," *Acta Astronautica*, vol. 66, no. 1-2, pp. 257–268, 2010.

[67] Scitor, *NORAD Satellite Catalog (Public).* Joint Space Operations Center. http://www.space-track.org.

[68] R. DeHart, "NASA Robotic CARA Team Report for March 2013 A-Train MOWG," tech. rep., National Aeronautics and Space Administration, Tsukubashi, Ibaraki, Japan, March 4-7 2013.

[69] F. Chan, *Spacecraft Collision Probability.* El Segundo, California: Aerospace Press, 2008.

[70] National Research Council (U.S.) Aeronautics and Space Engineering Board, Committee for the Assessment of NASA's Orbital Debris Programs, *Limiting future collision risk to spacecraft: an assessment of NASA's meteoroid and orbital debris program.* Washington, D.C.: National Academies Press, 2011.

[71] T. N. Edelbaum, L. L. Sacket, and H. L. Malchow, "Optimal Low Thrust Geocentric Transfer," in *AIAA 10th Electric Propulsion Conference*, (Lake Tahoe, Nevada), AIAA, November 1973. Paper No. AIAA 73-1074.

[72] W. Hohmann, *The Attainability of Heavenly Bodies.* Washington, D.C.: National Aeronautics and Space Administration, 1925. Technical Translation F-44, November 1960.

[73] J. R. Stuart, K. C. Howell, and R. S. Wilson, "Design of End-To-End Trojan Asteroid Rendezvous Tours Incorporating Potential Scientific Value," in *AAS/AIAA 24th Space Flight Mechanics Meeting*, (Santa Fe, New Mexico), January 26-30 2014. Paper No. AAS-14-267.

[74] A. Rizzoli, F. Oliverio, R. Montemanni, and L. Gambardella, "Ant Colony Optimisation for vehicle routing problems: from theory to applications," tech. rep., Instituto Dalle Molle di Studi sull'Intelligenza Artificiale (IDSIA), September 7 2004. IDSIA-15-04.

[75] J. R. Stuart, K. C. Howell, and R. S. Wilson, "Automated Design of Propellant-Optimal, End-to-End, Low-Thrust Trajectories for Trojan Asteroid Tours," 2014. *Journal of Spacecraft and Rockets*, doi: `http://arc.aiaa.org/doi/abs/10.2514/1.A32748`.

[76] NASA Dawn Mission Website. `http://www.nasa.gov/mission_pages/dawn/mission/index.html`; Accessed 7 June 2013.

[77] JAXA Hayabusa Mission Website. `http://www.isas.jaxa.jp/e/enterp/missions/hayabusa/index.shtml`; Accessed 7 June 2013.

[78] "NASA's Asteroid Sample Return Mission Moves into Development." NASA OSIRIS-REx Mission Website, May 13 2013. http://www.nasa.gov/mission_pages/osiris-rex/osiris-rex-development.html; Accessed 7 June 2013.

[79] M. Brown, "Mission Concept Study: Trojan Tour Decadal Study," tech. rep., National Aeronautics and Space Administration, 2011. SDO-12348.

[80] "NASA's Asteroid Initiative Benefits from Rich History." NASA Asteroid Initiative Website, April 10 2013. http://www.nasa.gov/mission_pages/asteroids/news/asteroid_initiative.html; Accessed 7 June 2013.

[81] M. Desjean, "Missions to the Jupiter Trojans," in *40th International Conference on Environmental Systems*, (Barcelona, Spain), July 11-15 2010. Paper No. AIAA 2010-6285.

[82] C. Colombo, M. Vasile, and G. Radice, "Optimal Low-Thrust Trajectories to Asteroids Through an Algorithm Based on Differential Dynamic Programming," *Celestial Mechanics and Dynamical Astronomy*, vol. 105, pp. 75–112, October 2009.

[83] J. T. Olympio, "Optimal Control Problem for Low-Thrust Multiple Asteroid Tour Missions," *Journal of Guidance, Control, and Dynamics*, vol. 34, pp. 1709–1719, November-December 2011.

[84] T. Sakai, "A Study of Variable Thrust, Variable Specific Impulse Trajectories for Solar System Exploration." Ph.D. Dissertation, School of Aerospace Engineering, Georgia Institute of Technology, 2004.

[85] D. Goebel, J. Brophy, J. Polk, I. Katz, and J. Anderson, "Variable Specific Impulse High Power Ion Thruster," in *Joint Propulsion Conference*, (Tucson, Arizona), AIAA/ASME/SAE/ASEE, July 2005. Paper No. AIAA 2005-4246.

[86] T. W. Glover, F. R. C. Diaz, A. V. Ilin, and R. Vondra, "Projected Lunar Cargo Capabilities of High-Power VASIMR Propulsion," in *Proceedings of 30th International Electric Propulsion Conference*, (Florence, Italy), September 2007. IEPC-2007-244.

[87] K. Komurasaki, Y. Arakawa, and H. Takegahara, "An Overview of Electric and Advanced Propulsion Activities in Japan," in *Proceedings of Third International Conference of Spacecraft Propulsion*, (Cannes, France), pp. 27–39, October 2000.

[88] D. F. Lawden, *Optimal Trajectories for Space Navigation.* London, UK: Butterworths, 1963.

[89] L. S. Pontryagin, V. G. Boltyanskii, R. V. Gamkrelidze, and E. F. Mischchenko, *The Mathematical Theory of Optimal Processes*, vol. 4. New York: Interscience, 1962.

[90] M. Volle, "Optimal Variable-Specific-Impulse Rendezvous Trajectories Between Halo Orbits," in *International Symposium on Space Flight Dynamics*, (Kanazawa, Japan), Japan Society for Aeronautical and Space Sciences and ISTS, June 2006. Paper No. ISTS 2006-d-73.

[91] J. Senent, C. Ocampo, and A. Capella, "Low-Thrust Variable-Specific-Impulse Transfers and Guidance to Unstable Periodic Orbits," *Journal of Guidance, Control, and Dynamics*, vol. 28, pp. 280–290, March-April 2005.

[92] J. R. Stuart, M. T. Ozimek, and K. C. Howell, "Optimal, Low-Thrust, Path-Constrained Transfers between Libration Point Orbits using Invariant Manifolds," in *AIAA/AAS Astrodynamics Specialist Conference*, (Toronto, Ontario), August 2-5 2010.

[93] J. R. Stuart and K. C. Howell, "Trajectory Tour of the Trojan Asteroids Generated via an Optimal Low-Thrust Algorithm," in *IAF 62nd International Astronautical Conference*, (Cape Town, South Africa), October 3-7 2011. Paper No. IAC-11-C1.1.1.

[94] J. R. Stuart and K. C. Howell, "An Automated Search Procedure to Generate Optimal Low-Thrust Rendezvous Tours of the Sun-Jupiter Trojan Asteroids," in *23rd International Symposium on Space Flight Dynamics*, (Pasadena, California), October 29 - November 2 2012. Paper No. ISSFD23-IMD1-2.

[95] J. R. Stuart, K. C. Howell, and R. S. Wilson, "Automated Design of Propellant-Optimal, End-to-End, Low-Thrust Trajectories for Trojan Asteroid Tours," in *AAS/AIAA 23rd Space Flight Mechanics Meeting*, (Kauai, Hawaii), pp. 989–1005, February 10-14 2013. Paper No. AAS-13-492.

[96] G. Leitmann, *The Calculus of Variations and Optimal Control.* New York, New York: Plenum Press, 1981.

[97] O. Bolza, *Lectures on the Calculus of Variations.* New York, New York: Dover, 1961.

[98] P. E. Gill, W. Murray, and M. A. Saunders, "SNOPT: An SQP algorithm for large-scale constrained optimization," *Society for Industrial and Applied Mathematics Journal of Optimization*, vol. 12, no. 4, pp. 979–1006, 2002.

[99] D. Goldberg, *Genetic Algorithms in Search, Optimization, and Machine Learning.* Reading, Massachusetts: Addison Wesley, 1989.

[100] Y. Gao and C. Kluever, "Low-Thrust Interplanetary Orbit Transfers Using Hybrid Trajectory Optimization Method with Multiple Shooting," in *2004 AIAA/AAS Astrodynamics Specialist Conference and Exhibit*, (Providence, Rhode Island), August 16-19 2004. Paper No. AIAA-2004-4088.

[101] J. Zhang, Y. Z. Luo, and G. J. Tang, "Hybrid Planning for LEO Long-Duration Multi-Spacecraft Rendezvous Mission," *Science China Technological Sciences*, vol. 55, no. 1, pp. 233–243, 2012.

[102] M. Sentinella and L. Casalino, "Hybrid Evolutionary Algorithm for the Optimization of Interplanetary Trajectories," *Journal of Spacecraft and Rockets*, vol. 46, no. 2, pp. 365–372, 2009.

[103] Q. Dong, C. Pingyuan, and W. Yamin, "Multiple Gravity-Assisted Trajectory Optimization Using a Hybrid Method," in *2010 International Conference on Intelligent Computing and Integrated Systems*, (Guilin, China), pp. 3–6, October 22-24 2010.

[104] G. Mengali and A. Quarta, "Tradeoff Performance of Hybrid Low-Thrust Propulsion System," *Journal of Spacecraft and Rockets*, vol. 44, no. 6, pp. 1263–1270, 2007.

[105] J. Heiligers, C. McInnes, J. Biggs, and M. Ceriotti, "Displaced Geostationary Orbits Using Hybrid Low-Thrust Propulsion," *Acta Astronautica*, vol. 71, no. 2-3, pp. 51–67, 2012.

[106] R. Bevilacqua, J. S. Hall, and M. Romano, "Multiple Spacecraft Rendezvous Maneuvers by Differential Drag and Low Thrust Engines," *Celestial Mechanics and Dynamical Astronomy*, vol. 106, no. 1, pp. 69–88, 2010.

[107] T. Edelbaum, "The Use of High- and Low-Thrust Propulsion in Combination for Space Missions," *The Journal of the Astronautical Sciences*, vol. 9, no. 2, pp. 49–60, 1962.

[108] D. W. Johnson, "Optimal Orbit Insertion Strategies Using Combined High and Low Thrust Propulsion Systems." M.S. Thesis, Graduate School of Engineering, Air Force Institute of Technology, Wright-Patterson AFB, Ohio, 1997.

[109] G. Fedotov, "Possibilities of Combining High- and Low-Thrust Engines in Flights to Mars," *Cosmic Research*, vol. 39, no. 6, pp. 574–582, 2001.

[110] G. Mingotti, F. Topputo, and F. Bernelli-Zazzera, "Earth-Mars Transfers with Ballistic Escape and Low-Thrust Capture," *Celestial Mechanics and Dynamical Astronomy*, vol. 110, no. 2, pp. 169–188, 2011.

[111] S. Owens and M. Macdonald, "Analogy to Bi-Elliptic Transfers Incorporating High- and Low-Thrust," *Journal of Guidance, Control, and Dynamics*, vol. 36, no. 3, pp. 890–894, 2013.

[112] V. Szebehely, *Theory of Orbits.* New Haven, Connecticut: Academic Press, first ed., 1967.

[113] C. Lanczos, *The Variational Principles of Mechanics.* New York, New York: Dover, fourth ed., 1970.

[114] J. Stewart, *Calculus: Early Transcendentals.* Pacific Grove, California: Brooks/Cole Publishing, fourth ed., 1999.

[115] J. P. Emery, D. M. Burr, and D. Cruikshank, "Near-Infrared Spectroscopy of Trojan Asteroids: Evidence for Two Compositional Groups," 2013. *Astronomical Journal*, doi: `http://arxiv.org/abs/1012.1284`.

[116] W. Calvin, "NASA's WISE Colors in Unknowns on Jupiter Asteroids." Jet Propulsion Laboratory Release, October 2012.

[117] S. J. Weidenschilling, "Hektor: Nature and Origin of a Binary Asteroid," *Icarus*, vol. 44, no. 3, pp. 807–809, 1980.

[118] W. K. Hartmann and D. P. Cruikshank, "Hektor: The Largest Highly Elongated Asteroid," *Science*, vol. 207, no. 4434, pp. 976–977, 1980.

[119] F. Marchis, F. Vachier, J. Durech, J. Berthier, M. Wong, P. Kalas, G. Duchene, and M. van Dam, "Physical Characteristics of the Binary Trojan Asteroid (624) Hektor," in *Asteroids, Comets, Meteors*, (Niigata, Japan), May 16-20 2012.

[120] M. Broz and J. Rozehnal, "Eurybates - the only asteroid family among Trojans?," *Monthly Notices of the Royal Astronomical Society*, vol. 414, no. 1, pp. 565–574, 2011.

[121] A. E. Bryson, Jr. and Y.-C. Ho, *Applied Optimal Control.* Waltham, Massachusetts: Blaisdell Publishing, 1969.

[122] J. M. Longuski, J. J. Guzmán, and J. E. Prussing, *Optimal Control with Aerospace Applications.* New York, New York: Springer.

[123] L. C. Dixon and M. C. Bartholomew-Biggs, "Adjoint Control Transformations for Solving Practical Optimal Control Problems," *Optimal Control Applications and Methods*, vol. 2, pp. 365–381, 1981.

[124] W. Karush, "Minima of Functions of Several Variables with Inequalities as Side Constraints." M.S. Thesis, Department of Mathematics, University of Chicago, Chicago, Illinois, 1939.

[125] H. W. Kuhn and A. W. Tucker, "Nonlinear Programming," in *Proceedings of 2nd Berkeley Symposium*, (Berkeley, California), pp. 481–492, University of California Press, 1951.

[126] J. Nocedal and S. J. Wright, *Numerical Optimization.* Berlin, New York: Springer-Verlag, second ed., 2006.

[127] M. J. Box, D. Davies, and W. H. Swann, *Non-Linear Optimization Techniques.* Oliver and Boyd, 1969.

[128] S. K. Eldersveld, "Large-Scale Sequential Quadratic Programming Algorithms." Ph.D. Dissertation, Department of Operations Research, Stanford University, Stanford, California, 1991.

VITA

VITA

Jeffrey Richard Stuart was born in Anderson, Indiana on May 2^{nd}, 1986 to James and Mary Stuart. After graduation from Anderson High School in 2004, he attended Purdue University, where he graduated with a Bachelor of Science in Aeronautical and Astronautical Engineering in December 2008. During his time as an undergraduate student, he co-oped with ATA Engineering, Inc. in San Deigo, California, completing four work rotations performing structural analysis and testing. Upon graduation, he started his graduate studies in the Purdue University School of Aeronautics and Astronautics, where he worked for Professor Kathleen Howell. He received his Master of Science in Aeronautics and Astronautics in May 2011. While a graduate student, he received support as a teaching assistant in the School of Aeronautics and Astronautics, working for Prof. John Sullivan in the fluid dynamics and aerodynamics laboratory courses. He additionally received support as a NASA Space Technology Research Fellow, a Indiana Space Grant Fellow, and a Purdue Research Fellow. During summers, he worked at Dynetics, Inc. in Huntsville, Alabama (2009), The Aerospace Corporation in Chantilly, Virginia (2010-2011), and NASA's Jet Propulsion Laboratory in Pasadena, California (2012-2014). He has accepted a position as a member of the technical staff at the Jet Propulsion Laboratory in the Navigation and Mission Design System Engineering Group.